PhD-FSTM-2022-067
The Faculty of Science, Technology and Medicine

DISSERTATION

Defence held on 11/05/2022 in Luxembourg

to obtain the degree of

DOCTEUR DE L'UNIVERSITÉ DU LUXEMBOURG

EN PHYSIQUE

by

Christian Kameni Boumenou
Born on 07 July 1985 in Banka, (Cameroon)

CHARACTERIZATION OF THE SURFACE PROPERTIES OF POLYCRYSTALLINE CU(IN, GA)SE_2 USING A COMBINATION OF SCANNING PROBE MICROSCOPY AND X-RAY PHOTOELECTRON SPECTROSCOPY

Dissertation defence committee

Prof. Dr Alex Redinger, dissertation supervisor
Professor, Université du Luxembourg

Dr Sascha Sadewasser
Principal Investigator of the Laboratory for Nanostructured Solar Cells
International Iberian Nanotechnology Laboratory (INL), Braga, Portugal

Prof. Dr Phillip Dale, Chairman
Professor, Université du Luxembourg

Dr Romain Carron
Group leader, Laboratory for Thin Films and Photovoltaics
Swiss Federal Laboratories for Materials Science and Technology, Dübendorf, Switzerland

Prof. Dr Thomas Schmidt, Vice Chairman
Professor, Université du Luxembourg

Contents

List of Figures

List of Tables

Acronyms and Abbreviations

a lattice parameter

A acceptor like defect state

AFM atomic force microscopy

Al: ZnO aluminium doped ZnO

APT atomic probe tomography

BB band bending

c lattice parameter

CBD chemical bath deposition

Cd cadmium

Cd_{Cu} cadmium on copper site donor like defect

CdS cadmium sulfide

CdTe cadmium telluride

CPE cadmium pre-electrolyte

Cu copper

Cu_2ZnSnS_4 copper zinc tin sulfide

CIGSe copper-indium-gallium-diselenide

$CuInSe_2$ Copper-indium-diselenide

CGI Cu/(In+Ga) ratio

CISe $CuInSe_2$

CGSe $CuGaSe_2$

CL cathodoluminescence

D donor like defect state

DFT density functional theory

E_C conduction band edge energy

E_F Fermi energy level

E_g bandgap energy

E_V valence band edge energy

EBIC electron beam induced current

EDX energy-dispersive X-Ray

Ga gallium

GGI Ga/(In+Ga) ratio

GI grain interior

HT high-temperature

i-ZnO intrinsic ZnO

In indium

In_{Cu}^{2+} indium on copper site donor like defect

IPES inverse photoemission spectroscopy

KCN potassium cyanide

KPFM Kelvin probe force microscopy

Mo molybdenum

$MoSe_2$ molybdenum diselenide

Na sodium

NH_4OH ammonia

Ni-Al Nickel-Aluminium

ODC ordered defect compounds

PCEs power conversion efficiencies

PCE power conversion efficiency

PDTs post deposition treatments

PDT post deposition treatment

PL photoluminescence

PVD physical vapor deposition

QFLS quasi-Fermi level splitting

SEM scanning electron microscopy

SPM scanning probe microscopy

SIMS secondary ion mass spectroscopy

STM scanning tunneling microscopy

STS scanning tunneling spectroscopy

Se selenium

SLG Soda lime glass

TEM transmission electron microscopy

UHV ultra high vacuum

UPS ultraviolet photoelectron spectroscopy

V_{Cu} Cu vacancies

XRF X-ray fluorescence

XPS X-ray photoelectron spectroscopy

ZnO zinc oxide

Abstract

Polycrystalline Cu(In,Ga)Se_2 (CIGSe) exhibit excellent properties for high power conversion efficiency (PCE) thin film solar cells. In recent years, photovoltaic cells made from CIGSe reached a PCE of 23.4%, surpassing that of multicrystalline silicon photovoltaic cells. Nevertheless, the changes in surface composition and electronic properties of the absorbers after various solution-based surface treatments are still under intensive investigation and are widely discussed in the literature. In this thesis, the front, the rear surface properties as well as the impact of post-deposition treatments (PDT) on CIGSe absorbers with different elemental compositions were analyzed by scanning tunneling microscopy and spectroscopy, Kelvin probe force microscopy, and X-ray photoelectron spectroscopy.

I show that potassium cyanide (KCN) etching reduces the Cu content at the surface of Cu-rich absorbers substantially. The reduction of the Cu-content is accompanied with the formation of a large number of defects at the surface. Scanning tunneling spectroscopy measurements showed that most of these defects could be passivated with Cd ions. A semiconducting surface and no changes in the density of states were measured across the grain boundaries. In addition to the defect passivation an increase in surface band bending due to the substitution of Cu vacancies by Cd ions, which act as shallow donor defects was observed. As in the case of the front surface, the analyses carried out on the back surface of Cu-rich absorbers showed that a detrimental Cu_xSe secondary phase was also formed at the interface between the $MoSe_2$ layer and CISe absorber after growth. This Cu_xSe secondary phase at the back contact was not present in Cu-poor absorbers.

Regarding the alkali metal post-treated absorbers, I show that the occurrence of an enlarged surface bandgap, often reported on CIGSe absorbers after PDT treatment is only present after H_2O rinsing. After ammonia (NH_4OH) washing, which is always applied before buffer layer deposition, all the high bandgap precipitates disappeared and an increased amount of an ordered vacancy compound was observed.

The thesis thereby gives a comprehensive overview of the CIGSe surfaces after various chemical and post deposition treatments.

Chapter 1

Introduction

The strong increase in global warming due to the emission of greenhouse gases worries the whole world and has become one of the important topics to be closely cared off. During the recent Intergovernmental Panel on Climate Change held in August 2021, it was shown that most of the greenhouse gases (GHG) originate from human activities and that if no quick action is undertaken to reduce them, the global average warming could exceed 1.5^{o}C in the next twenty years [1]. Since the principal human activity that produces GHG is the burning of fossil fuels for electricity and heat production, transportation, buildings, etc. [2], one way to limit their emission could be the use of green energies such as solar photovoltaic (PV), wind, biomass as well as hydropower [3]. Although it is crucial to exploit all these alternative sources, solar PV is largely seen as the most promising technology for the future [4, 5]. The sun is abundant and inexhaustible. Over a year, the sun radiates to the earth roughly six thousand times more energy than that consumed by the entire world population [6]. The radiated energy can be converted into electricity via solar PVs [7]. This energy conversion is widely known to produce less CO_2 [8], which is one of the main components of GHG [2]. Furthermore, solar PV has exhibited the highest cost decline between 2010 and 2019 as compared to other renewable energy sources [9], and their worldwide capacity is predicted to be in the order of terawatt in the next ten years [5].

Albeit the global PV market is nowadays dominated by silicon solar cells [10, 11], polycrystalline Cu(In, Ga)Se_2 (CIGSe) thin film devices occupy a good place among the best candidates to produce low-priced solar electricity. The CIGSe solar cells along with their corresponding solar panels provide low production costs [12], high

performance [13], long term stability [14] and a reduced energy payback time [15]. On top of this, CIGSe absorbers exhibit excellent properties for high performance thin-film solar cells. They have at the same time a high absorption coefficient [16], a tunable direct bandgap [17] and high minority carrier lifetimes [18]. Over the last years, CIGSe devices have exhibited power conversion efficiency (PCE) exceeding 23% [19] on the laboratory scale, which already, is higher than that of multicrystalline silicon solar cells [20, 19, 21]. With such high efficiency, CIGSe devices are currently among the best thin film based photovoltaic cells [19].

Despite the CdS being largely endorsed as the efficient buffer layer for CIGSe photovoltaic cell technology, note that the actual world record PCE was acquired from the Cd-free Zn(O, S, OH) buffer layer [22]. Add this to the fact that Cd is a toxic metal element, this important breakthrough has strengthened the idea of replacing the CdS with another nontoxic Zn(O, S, OH) buffer layer without performance loss. Nevertheless, most of the high efficiency CIGSe solar cells still enclose CdS and are largely employed as a reference specimen for the appraisal of their Cd-free counterparts [23]. Consequently, the impact of Cd in-diffusion on the surface electronic properties of CIGSe absorbers investigated in the framework of this thesis is still a topic of interest in the community. The study could help to better understand the various chemical and electronic changes that happen at the surface of the CIGSe absorbers after CdS growth, their eventual impact on devices, and could serve as a reference for the future development of any other types of CIGSe based devices. Cd present in the CdS buffer layer has been reported to significantly modify the CIGSe/CdS interface [24, 25]. It substitutes Cu vacancies that exist at the very near surface of the absorber after growth and alters the doping concentration at the hetero-interface [26, 27]. This change in doping profile converts the very near surface of the film from its original *p-type* character to *n-type* forming thus a homojunction CIGSe and CdS interface [28]. Furthermore, it was shown that pre-electrolyte treated the absorbers surface with Cd substantially enhances the performance of the CdS free CIGSe solar cell devices [29].

One more crucial breakthrough that allowed achieving world record CIGSe efficiency in recent years was the post-treatment of the absorbers with heavy alkali metal elements and under a selenium environment. PCE around 22.6% was measured from the absorbers which were post-treated with rubidium fluoride (RbF) [30]. However,

the underlying reason behind this outperformance of the CIGSe solar cells after RbF post-deposition treatment (PDT) is still under intensive investigation and is widely discussed in the literature [30, 31, 32, 33, 34, 35, 36].

The objective of this thesis is first to study the surface properties of the pristine CIGSe absorbers and secondly to investigate changes in chemical and electronic properties that occur at the surface of the CIGSe after various surface treatments such as potassium cyanide etching, cadmium pre-electrolyte treatment and RbF-PDT. The idea is to correlate the surface chemical or compositional properties of the absorbers to their corresponding electronic properties like the local density of state and work-function.

Since the treatments happen at the very near surface of absorbers, high surface sensitivity characterization techniques need to be used. Therefore, scanning probe microscopy (SPM) and X-ray photoelectron electron spectroscopy are the main tools employed in this thesis. As SPM techniques are exceedingly surface-sensitive the specimens have to be clean and air exposure needs to be avoided. Hence, an inert gas suitcase, nitrogen-filled glove box ($H_2O < 1\,\text{ppm}$; $O_2 < 1\,\text{ppm}$) and an ultra-high vacuum (UHV) system were used to minimize the sample contamination to a strict minimum.
The thesis is structured as follows:

In **Chapter 2**, the basic properties of CIGSe solar cells are introduced. The stacked-layer structure of the CIGSe solar cell along with the corresponding band alignment at the CIGSe/CdS heterointerface are presented. Afterwards, the structural and electronic properties of CIGSe based solar cells, which include the lattice structure, the intrinsic *p-type* nature, the energy bandgap, and the phase diagram are discussed in detail.

In **Chapter 3**, the state of the art results acquired from the front and the rear surface of the CIGSe published in the literature is summarized. The effect of air exposure and subsequent potassium cyanide etching (KCN) has been reviewed. After this, the theory behind the diffusion of cadmium into the surface of the absorber as well as the impact of alkali metal post-deposition treatment were presented and thoroughly discussed. Furthermore, the chapter also introduces how grain boundaries (GBs) are formed in polycrystalline CIGSe and summarizes the different models that have been

proposed to explain their impact on efficiency.

In **Chapter 4**, the main characterization techniques, samples preparation and experimental details are discussed. It starts with the short presentation of SPM. Afterwards, the theory behind scanning tunneling microscopy (STM) and spectroscopy (STS), and Kelvin probe force microscopy (KPFM) together with their respective technical implementations are described. This also applies to XPS. Regarding the orther supplemental techniques such as secondary ion mass spectroscopy (SIMS), Raman spectroscopy, etc., only a short description that aims to allow readers to understand how the results were obtained is given.

Chapter 5 focuses on the impact of the Cd in-diffusion on the chemical and electronic properties of Ga free $CuInSe_2$ and Cu-rich ($Cu/In \geq 1$) absorbers. The chapter is concentrated on absorbers with Ga free and with excess Cu content, and without PDT because they present ideal properties such as excellent transport properties and small potential fluctuations [18]. The effect of the KCN etching on the chemical and electronic properties of the absorbers grown under Cu-rich conditions was also investigated. The results are compared to the ones recorded from the UHV heated samples and the findings published in literature.

As indicated earlier, one of the main objective of this thesis was to investigate the surface of pristine absorbers and to compare the outcomes to the results from the air-exposed and KCN etched absorbers. Hence, as Cu-rich absorbers exhibit Cu_xSe phase on top, they were mechanically peeled off from their original substrates and the back surface was analyzed. The results are presented and discussed in **Chapter 6**.

In **Chapter 7**, the surface properties of the pristine Cu-poor CIGSe absorbers, as well as, the effect of the cleaning process on the surface properties of the absorbers that were post-treated with NaF and RbF PDTs were investigated. The pristine CIGSe absorbers were not exposed to environment where the pressure was higher than 10^{-9} mbar before the analysis. The aim was to limit the contamination from the atmosphere, which could alter the surface properties of the obsorbers [37, 38, 39, 40].

In **Chapter 8**, the summary of the thesis and the outlook are given.

Chapter 2

Basic properties of $Cu(In,Ga)Se_2$ photovoltaic cells

This chapter starts with a short presentation of the stacked-layer structure of Mo/CIGSe /CdS/i-ZnO/ZnO:Al photovoltaic cells. Afterwards, the properties of the copper-indium-gallium-diselenide (CIGSe) materials including the lattice structure, the intrinsic p-type character, the energy bandgap, and the phase diagram are discussed in detail.

2.1 $Cu(In,Ga)Se_2$ based solar cells structure and corresponding energy band diagram

In this section, the most common device structure for CIGSe based thin film solar cells together with its corresponding energy band diagram is presented. In Fig. 2.1(a) a complete stacked-layer structure of Mo/CIGSe/CdS/i-ZnO/ZnO:Al photovoltaic cells is sketched. The sketch shows that the CIGSe solar cells consist of a superposition of different types of materials grown via various deposition techniques one on top of the other. Soda lime glass (SLG) with a few millimeter thick ($\sim 1-3\ mm$) is utilized as the substrate. The key reason behind this choice is that SLG has to some extent a positive impact on the CIGSe photovoltaic cell performance. It contains the element sodium, which was reported to substantially improve the open-circuit voltage of the CIGSe absorbers [41, 42, 43, 44] therefore the efficiency of the device, notably via the passivation of some defect states at the surface and/or the grain boundaries

[45, 46, 47, 48]. Polycrystalline semiconductors consist of grain boundaries which serve as non radiative recombination centers [37, 49].

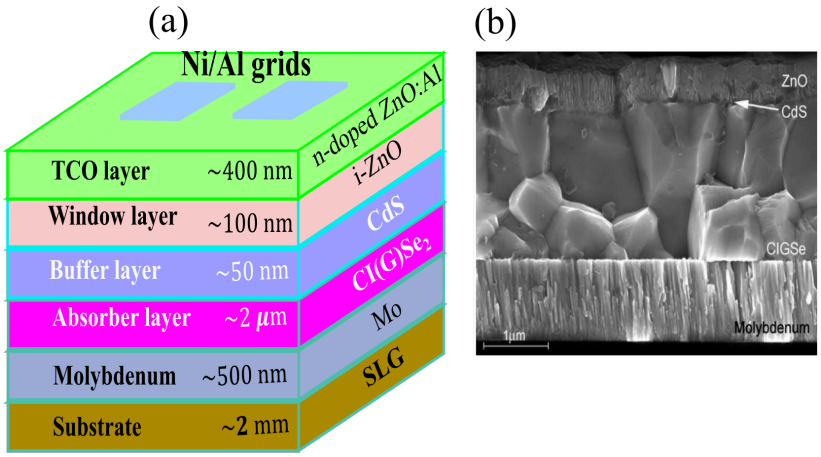

Figure 2.1: (a) Schematic representation and (b) SEM micrograph of a cross-section of a CIGSe based solar cell [50].

Nonetheless, extensive investigations are currently carrying out in order to replace the high production cost SLG [51] by other cheaper substrates such as polyimide and metal foils [51, 52]. Compared to SLG, the polyimide and metal foil substrates are flexible and lighter and have already shown more or less a similar improvement on the CIGSe absorbers. Almost similar power conversion efficiencies (PCEs) were recorded from the films grown on SLG and polyimide substrates that were post-treated with heavy alkali metals [15, 52, 53].

On top of the SLG substrate, a layer of molybdenum (Mo) with a thickness of $\sim 500\ nm$ is grown via magnetron sputtering. This Mo layer acts as a rear contact and also helps to reflect back into the CIGSe absorbers most of the non-absorbed light. Additionally, its excellent compatibility with selenium leads to a creation of a thin intermediate layer of $MoSe_2$ at the CIGSe/Mo interface [54, 55], which forms an ohmic contact with CIGSe [54, 55]. Following the Mo rear contact, a *p-type* CIGSe absorber layer is added via physical vapor deposition (PVD) by means of a multistage co-evaporation process. The optimum thickness used so far for CIGSe absorbers is $\sim 2\ \mu m$.

As in the case of CdTe or Cu_2ZnSnS_4 photovoltaic technologies, the *p-n* hetero-junction in CIGSe solar cell devices is formed right at the interface between the *p-type* CIGSe absorber and *n-type* cadmium sulfide (CdS) buffer layer. The CdS layer has a

thickness of $\sim 50\ nm$ and is grown by means of solution based chemical bath deposition (CBD). With its positive impact on *p-n* heterojunction electronic properties, the CdS film is considered as one of the most efficient buffer layer for CIGSe based solar cells. It produces a beneficial band alignment at the absorber/buffer interface [23, 27] and protects the absorber surface against sputter damage during the deposition of the window layer [56]. The first argument is ascribed to the diffusion of Cd from the CdS compound into the absorber that converts the absorber surface from *p* to *n-type* as proposed in Refs. [57, 58], and will be discussed in more detail further in this thesis.

Although most of the state-of-art cells have been achieved with a thin CdS buffer, numerous other alternative buffers along with various deposition techniques have been developed and are currently under scrutinization. The non-exhaustive list of these alternative materials and deposition methods as well as their corresponding efficiencies can be found in Refs. [22, 56]. Cd is a toxic heavy metal element, which might cause health problems including lung cancer [59] if one is exposed to it for a long time. The Mo/CIGSe/CdS multilayer is capped with a thin zinc oxide (ZnO) double window layers, which consist of an approximately 100 nm thick layer of intrinsic ZnO (i-ZnO) and a $\sim$ 400 nm thick layer of highly aluminium doped ZnO (Al: ZnO). A Nickel-Aluminium (Ni-Al) grid is grown on top of the whole stacked-layer and forms the front contact of the device.

In Fig. 2.1(b), an scanning electron microscopy (SEM) micrograph of a CIGSe solar cell is presented [50]. As described above, from the bottom to the top, all the stacked-layers are well-defined and can be clearly identified. For example, the granular structure of the polycrystalline CIGSe absorber is nicely recognized. The average grain size is approximately 1 μm and is smaller than the thickness of the CIGSe film.

Fig. 2.2 depicts the energy band alignment for a completed CIGSe photovoltaic cell device. The CdS buffer and ZnO window layers exhibit wide bandgaps of 2.4 eV and 3.3 eV, respectively. The major part of the light that reaches the CIGSe photovoltaic cells is therefore transmitted to the low bandgap CIGSe absorbers layer where the electron-hole pairs are generated. The band bending (BB) that is observed at the CIGSe/CdS hetero-junction leads to charge carrier separation. As graphically indicated, the reconstruction of the surface of the film after growth creates electronic defects states at the junction between the CdS and the absorber, which serve as re-

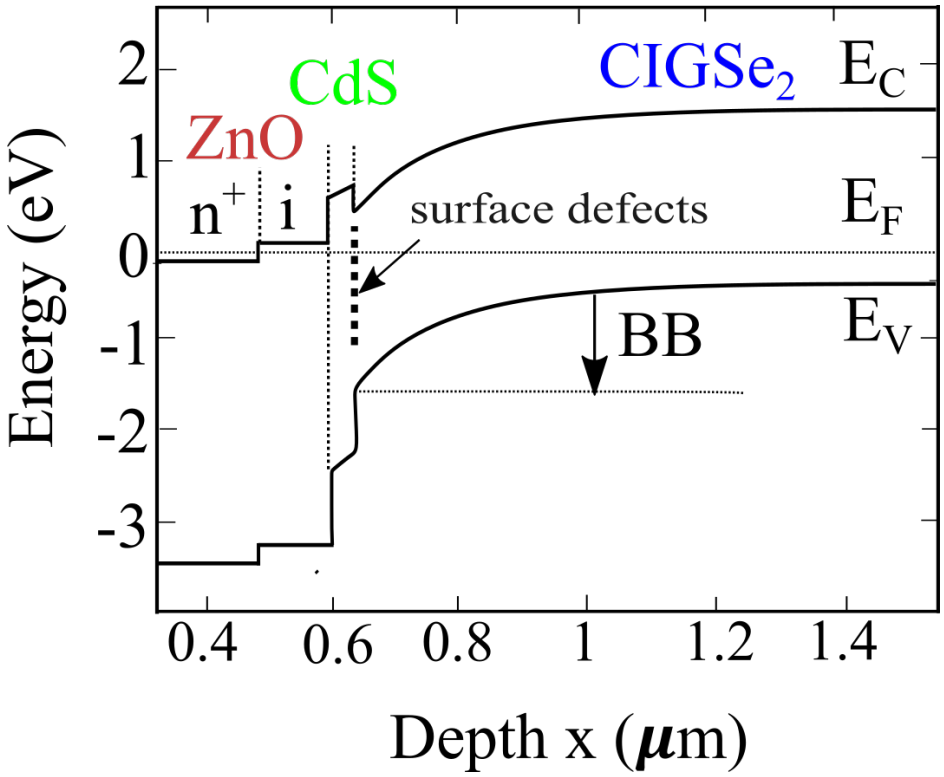

Figure 2.2: Simplified representation of the energy band diagram of a CIGSe photovoltaic cell adapted from Ref. [13], E_C, E_V, BB , E_F are the conduction band minimum, valence band maximum, band bending and Fermi energy level, respectively.

combination centers [60, 61, 62]. Hence, in-depth insight into the effect of those defect states on the CIGSe absorbers is important for the optimization of the CIGSe solar cells. The generating mechanism and different types of defects observed so far in chalcopyrite CIGSe absorbers will be summarized in the following sections.

2.2 Structural properties of Cu(In,Ga)Se_2

Copper-indium-diselenide ($CuInSe_2$) is a I-III-VI_2 ternary semiconductor that crystallizes in a tetragonal chalcopyrite structure [23, 63, 64, 65]. It is composed of a group I atom (Cu), group III atom (In) and a group VI atom (Se). To achieve a high efficiency from the solar cell made of this compound, gallium (Ga) atoms are in general added into the $CuInSe_2$ (CISe) based crystal matrix to form a quaternary $CuIn_{1-x}Ga_xSe_2$ compound. The Ga content $x = [Ga]/([Ga] + [In])$ introduced aims to enhance the CISe electronic properties, particularly, to tune its energy bandgap as will be shown in Fig. 2.4. Depending on the x ratio ($0 < x < 1$) used, the energy bandgap of the film

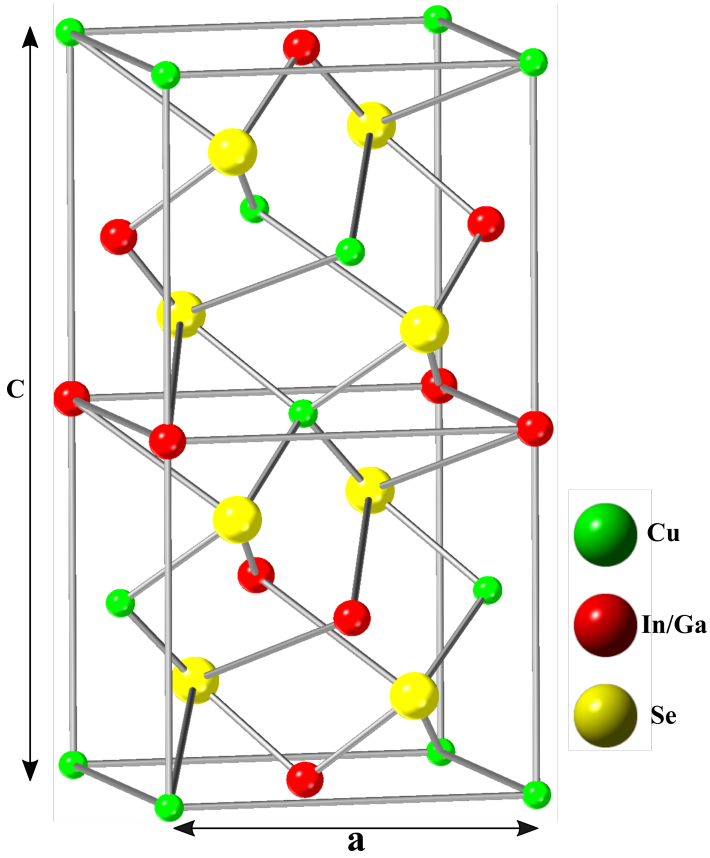

Figure 2.3: Sketch of the chalcopyrite unit cell of a CIGSe absorber adapted from Ref. [68]. The lattice constants are a and c ; Cu, In/Ga, Se elements are depicted in green, red and yellow colors, respectively.

can vary from 1.0 eV for a pure CISe absorber to 1.7 eV for a pure $CuGaSe_2$ (CGSe) absorbers [66]. During the last few years, power conversion efficiencies surpassing 20% [67] and 15% [66] on the laboratory scale were reported for $CuIn_{1-x}Ga_xSe_2$ with x vaying from 0.30 to 0.35, and CISe absorbers, respectively.

In Fig. 2.3 , a conventional unit cell of CIGSe compound where the Cu atoms are depicted in green, the In/Ga atoms in red and the Se atoms in yellow is presented. In this figure, which can be seen as a superposition of two sphalerite (zincblende) structures with the volume of unit cell about twice the size of the sphalerite structure [64, 69], each Cu and In/Ga atom are tetrahedrally coordinated to four Se atoms, whereas each Se atom is tetrahedrally coordinated to two Cu and two In atoms. The unit cell is a chalcopyrite structure where the Cu and In/Ga elements are often denoted as cations, and Se elements as anions. Conversely to sphalerite structure, the different bonding lengths between the cations and Se anions causes a distortion of the lattice

parameters a and c [70]. However, the crystal structure still remains undisturbed when the ratio of the lattice parameters c/a is 2, and linearly varies with respect to Ga concentration as given in equations $a(x) = (-0.17x + 5.782)\ \mathring{A}$ and $c(x) = (0.589x + 11.619)\ \mathring{A}$ [23].

2.3 Origin of p-type nature of Cu(In, Ga)Se_2

Unlike other semiconductors such as silicon, where extrinsic impurities are needed to tune their conductivity properties, the $CuIn_{1-x}Ga_xSe_2$ semiconductor is grown natively p-type with net doping densities ranging from $10^{15} cm^{-3}$ to $10^{17} cm^{-3}$ at ambient temperature [71, 72]. Its p-type character as can be seen in Table 2.1, which depicts a list of the most relevant defects that exist in the CIGSe matrix along with their respective formation energy is controlled by Cu vacancies (V_{Cu}).

Table 2.1: List of the most relevant intrinsic and extrinsic point defects in ternary CISe and CGSe matrix. The corresponding electronic nature of these impurities is indicated by A for acceptor-like defect state and D for donor like defect state. E_V is the energy of the valence maximum and E_C the conduction band minimum that are used to measure the acceptor defect levels and donor defect levels [73, 74], respectively. The formation entalphies ΔH of the neutral defects are extracted from references [73, 74].

Defect	**Energy**^{CGSe}**[eV]**	**Energy**^{CISe}**[eV]**	ΔH^{CGSe}**[eV]**	ΔH^{CISe}**[eV]**	**type**
$\mathbf{V_{Cu}}$	$\mathbf{E_V}$ +0.01 [73]	$\mathbf{E_V}$ +0.03 [73]	0.66 [73]	0.60 [73]	**A**
$\mathbf{V_{III}}$	$\mathbf{E_V}$ +0.19 [73]	$\mathbf{E_V}$ +0.17 [73]	2.83 [73]	3.04 [73]	**A**
$\mathbf{Cu_{III}}$	$\mathbf{E_V}$ +0.29 [73]	$\mathbf{E_V}$ +0.29 [73]	1.41 [73]	1.54 [73]	**A**
$\mathbf{III_{Cu}}$	$\mathbf{E_C}$ −0.49 [73]	$\mathbf{E_C}$ −0.25 [73]	4.42 [73]	3.34 [73]	**D**
$\mathbf{Cu_i}$	$\mathbf{E_C}$ −0.21 [73]	$\mathbf{E_C}$ −0.20 [73]	3.38 [73]	2.88 [73]	**D**
$\mathbf{In_{Cu}^{2+}}$	/	$\mathbf{E_C}$ −0.34 [73]	/	1.85 [73]	**D**
$\mathbf{Cd_{Cu}}$	$\mathbf{E_C}$ −0.06 [74]	$\mathbf{E_C}$ −0.00 [74]	−0.51 [74]	−0.90 [74]	**D**

With its lowest formation energy, V_{Cu} as compared to other point defects are the most dominant defects present in CIGSe. Accordingly, their acceptor-like nature is responsible for the p-type character of CIGSe [75]. However, it important to note that

in case of the CIGSe grown under Cu-poor conditions, the V_{Cu} easily form together with In_{Cu}^{2+} donors like a neutral defect pair $2V_{Cu}^{-}$+In_{Cu}^{2+} [76]. This implies that because of self-point defects compensation a neutral CIGSe absorber can also be synthesized. But, this is as a whole not the case. The lowest formation energy of V_{Cu}^{-} will always induce a small excess of V_{Cu}, which leads to a *p*-type nature of CIGSe.

Cd_{Cu} extrinsic donor defect shows a negative formation energy, which indicates that it is easily formed after the CdS buffer layer deposition. With its energy close to the conduction band minimum, it acts as shallow donors and is considered as the cause of the type inversion of the CIGSe surface [77, 78, 79]. As a result, while the bulk electronic properties of CIGSe film is *p*-type doped material after the deposition of CdS, the very near surface is *n*-type.

2.4 Bandgap of Cu(In,Ga)Se_2

$CuIn_{1-x}Ga_xSe_2$ is a direct bandgap semiconductor material [80]. The bandgap energy E_g varies continuously with respect to x [81, 82, 83] and can be tuned from about 1.04 eV (for a pure CISe absorber) to about 1.7 eV (for a pure CGSe absober). The mathematical formulation of the variation of E_g as a function of x is given in equation (2.1) [84, 83], and the corresponding graphical representation in Fig. 2.4 [85].

$$E_g = (1-x)E_g(CISe) + xE_g(CGSe) - bx(1-x) \tag{2.1}$$

In equation (2.1), b varies from 0.15 eV to 0.24 eV [86] and is commonly called optical bowing coefficient, and x refers to the Ga content.

Fig. 2.4 shows that adding Ga elements into a crystal matrix of CISe influences especially the conduction band of the compound. While the valence band edge energy remains more or less unaffected [85], the conduction band edge energy strongly shifts towards the vacuum level leading to an increase of the energy bandgap. This different behavior is ascribed to the interaction among the atomic orbitals that exist in CIGSe chalcopyrite type semiconductor materials. In these materials, the valence band edge/maximum is determined by the hybridization of cation Cu-*d* and anion Se-*p* orbitals [75] and the conduction band minimum consists of In/Ga-*s,p* orbitals. Therefore, inserting Ga in $CuInSe_2$ should as shown in Fig. 2.4 affect only the conduction band minimum and not the valence band maximum.

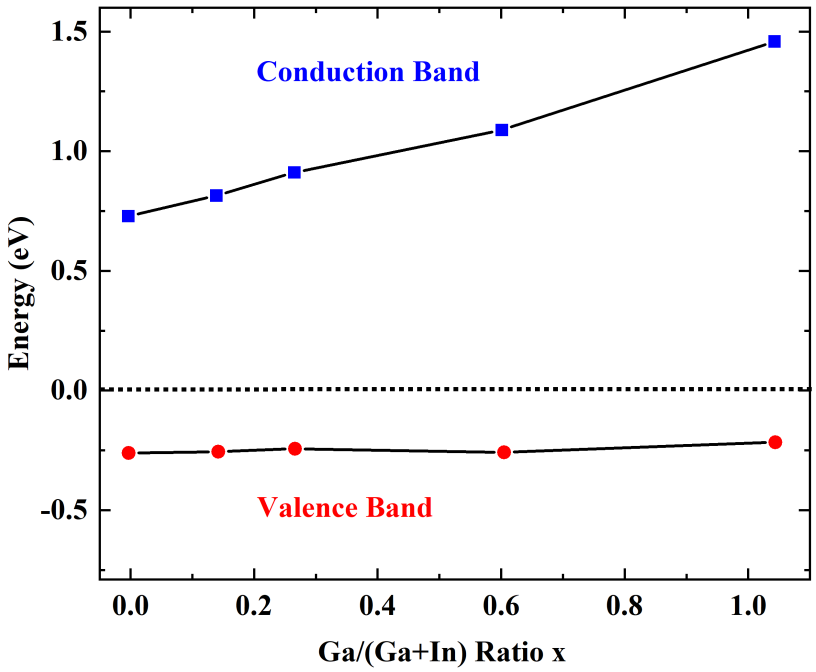

Figure 2.4: Variation of the bandgap energy with respect to $x = Ga/(Ga+In)$ adapted from Ref. [85]. The full red circles represent the change in valence band edge energy E_V, whereas the full blue rectangles represent the change in conduction band edge energy E_C.

However, the position of the valence band maximum and hence the energy bandgap also depend on the Cu content. In a crystal with a high Cu content, the strong interaction between the Cu-d and Se-p orbitals shifts the valence band maximum up towards the conduction band inducing a reduction of the band gap energy [87]. Conversely, in a Cu deficient compound, this interaction is reduced and hence an increase of the energy bandgap is observed [88]. Consequently, the Cu-depleted CIGSe compounds exhibit higher bandgap energy [87, 89, 90] as compared to stoichiometric ones.

2.5 Phase diagram of $Cu(In,Ga)Se_2$

To properly synthesize CIGSe thin films, an in-depth knowledge of the growth mechanisms of the material is crucial. One aide to designing growth processes is a phase diagram, which is a graphical representation of different phases that can be formed in an alloy.

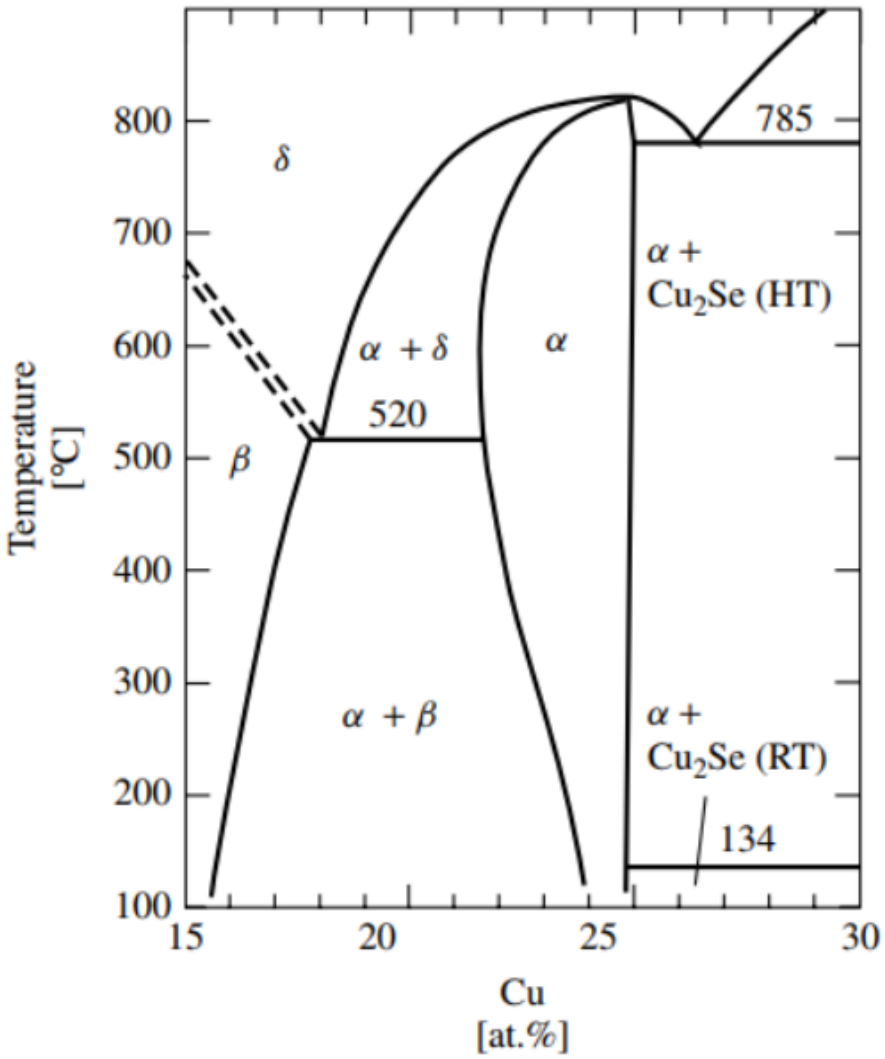

Figure 2.5: Phase diagram of chalcopyrite $CuInSe_2$ adapted from Ref. [91]. The x-axis depicts the atomic ratio of Cu, whereas the y-axis displays the growth temperature in Celsius. The chalcopyrite $CuInSe_2$ phase is designated by α. The δ phase is the elevated-temperature chalcopyrite compounds and β phase is an ODC. Cu_2Se exists at both ambient and elevated-temperature phase.

In Fig. 2.5, a reproduced phase diagram of CISe along the In_2Se_3-Cu_2Se pseudo binary with respect to Cu content and temperature is depicted [91]. The graph is shown for the Cu content varying from 15 at.% to 30 at.%, where a Cu content of 25 at.% corresponds to a stoichiometric composition (Cu /In=1). The diagram is divided into different phases labeled as α that represents the chalcopyrite CISe, β that is the ordered defect compounds (ODC) $CuIn_3Se_5$ phase [92] and δ that is the high-temperature (HT) sphalerite phase. The α-phase exists as a single phase for Cu

contents ranging from about 23 at.% to 25 at.% and for temperatures up to 800°C. In this compositional range, the chalcopyrite CISe structure is formed and remains as a single phase with a Cu content tolerance of about 3 at.% leading to a significantly Cu -poor CISe compound. The single α phase region for CISe is relatively narrow at low temperature and widens towards the In-rich side at higher temperature (500°C). This temperature of around 500°C is the optimum temperature at which CIGSe films are usually grown. At 500°C, although both over stoichiometric also called Cu-rich (Cu /In>1) and Cu -poor (Cu /In<1) films can be synthesized, it important to note that so far, the best device-quality are obtained from Cu -poor films with a bulk Cu content that varies from 22 at.% to 24 at.%.

For a Cu concentration ranging from 16 at.% to 23 at.%, the CISe phase coexists with a $CuIn_3Se_5$ phase. The two phases crystallize in a similar lattice structure and differ only from the number of the inherent defect states present in their crystal matrix. The $CuIn_3Se_5$ ODC phase contains a defined number of V_{Cu} and antisite defects In_{Cu} [76], which are absent or limited in $CuInSe_2$ matrix. As in the case of the α-phase, for Cu content below 16 at.%, the β phase is stable and also exists as a single phase.

The investigations carried out in this thesis are conducted on two different types of CIGSe films: the Cu-rich CISe film and the Cu-poor CIGSe film. The Cu-rich CISe film is produced with a bulk Cu/In ratio of ~ 1. This Cu/In value corresponds to a Cu content of ~ 25 %, which, as shown in the phase diagram (Fig. 2.5), falls within the α single phase region. Regarding the Cu-poor CIGSe film, three samples with a Cu/(In+Ga) ratio (CGI) of ~ 0.96, ~ 0.95, and ~ 0.85 are analysed. The films with a CGI of ~ 0.96 and ~ 0.95 crystallize as previously stated in the single α phase whereas the one with the CGI of ~ 0.85 consists of a mix of the chalcopyrite CIGSe phase and $Cu(In,Ga)_3Se_5$ ODC phase (Fig. 2.5), and corresponds to a Cu content of ~ 21 at.%.

Chapter 3

Surface properties of Cu(In, Ga)Se_2 based photovoltaic cells

In this chapter, most of the important studies carried out on both the front and the rear surface of CIGSe based solar cells hitherto are reviewed. The chapter is divided into three main parts. In the first part, the effect of air exposure and chemical etching on the front surface electronic properties are presented and widely discussed. Additional to this, the change due to cadmium in-diffusion mechanism and alkali metal post deposition treatments (PDTs) are also summarized. The second part focuses on the rear surface electronic properties. In the third part, the electronic activity and the current standpoint of the GBs in CIGSe are introduced.

3.1 Front surface properties of Cu(In,Ga)Se_2

In the CIGSe technology, the front surface of CIGSe is of high importance since it interacts directly with the CdS buffer layer. This very thin layer composed of few monolayers of materials is the main part of the film that forms together with the CdS buffer layer, the heterojunction in a CIGSe device. Therefore, any contamination due to air exposure, changes in composition due to the surface reconstruction or due to changes as a result of surface chemical treatments will strongly affect the performance of the whole device. It is well known from the literature that, as one of the main elements that compose the CIGSe compound, In or Ga oxidizes easily when they are exposed to air [93, 94], forming hence a thin oxide detrimental layer at the surface of

the film.

Several cleaning procedures including potassium cyanide (KCN) etching, ammonia (NH_4OH) rinsing, and hydrochloric acid rinsing have regularly been used to remove those oxide layers from the top surface of the non-stoichiometric films as well as the Cu_xSe secondary phase from the surface of over stoichiometric CIGSe. In this section, the state of the art of effect of air exposure and chemical treatments on the electronic properties of CIGSe surfaces are summarized. Moreover, changes in surface properties due to the in-diffusion of cadmium into the front surface of the film and to the alkali post-deposition treatments are also thoroughly discussed.

3.1.1 Impact of air exposure and chemical etching on Cu(In, Ga)Se_2 surface electronic properties

Since several steps such as synthesizing the CIGSe film inside the physical vapor deposition (PVD) machine and depositing the CdS buffer layer by means of chemical bath deposition (CBD) have to be followed in order to prepare a CIGSe solar cell, exposing the film to air during the fabrication of the CIGSe device cannot be circumvented. The PVD system in which the absorbers are usually synthesized is not in most of the cases connected to the glovebox where the CdS buffer deposition is performed. Consequently, transferring the CIGSe absorbers from the PVD to the glovebox leads to air exposure which induces the formation of a thin layer of oxides [95, 96, 97] at the surface of CIGSe as already stated. To avoid the impact of this surface oxidation on CIGSe solar cell devices, various methods like Ar-ion sputtering process, the deposition of a thin Se protection layer on top of the films and KCN etching the film after air exposure have been developed [98, 99, 100]. The Ar-ion sputtering process has been reported to preferentially remove Se from CIGSe thin films [101] altering, thereby, the surface chemical composition [64]. Furthermore, the formation of metallic Cu and In in connection with the Ar-ion sputtering was also observed in the chalcopyrite compounds [64]. Although, Se layer protects the surface from oxidation and can be easily removed via an annealing process in vacuum or ultra vacuum chamber [102], one of the main disadvantages of this approach is that the vaporisation of Se can significantly contaminate the vacuum chamber. The KCN etching approach seems to be the most popular technique used hitherto to remove oxides from the surface of

the CIGSe samples [98, 100]. Various work suggested that KCN washing successfully cleaned the contaminations [64, 103] and restore the initial quasi Fermi-level splitting of the films [96]. The changes in surface electronic properties generated by exposing the absorber to air are reproduced, and the loss in surface workfunction measured after air exposure is recovered [64]. The results suggest that KCN etching does not degrade the absorbers properties [96]. Hence, it can be used to produce cleaner surfaces for surface sensitive analyses [103, 104]. Furthermore, KCN etching is compulsory for over stoichiometric deposited absorbers since it helps to wash away the Cu_xSe secondary phases, which precipitate on top of the CIGSe layer during growth [105]. Nevertheless, Elanzeery *et al.* demonstrated in Ref. [106] that KCN washing also introduces additional defects in the near-surface of the absorbers. The authors showed that the induced defects can be passivated by post-treating the sample with alkali elements, InSe or Se at elevated substrate temperatures [106]. Besides, early study on CISe revealed that KCN cleaning might also alter the surface composition via withdrawal of copper [107]. The impact of those surface treatments on the electronic properties of the films might not be fully understood and is further investigated in this thesis. In order to correlate the local density of states of the KCN etched absorbers to compositional changes, the samples were critically investigated with scanning tunneling microscopy (STM) and spectroscopy (STS) and X-Ray & Ultraviolet photoemission spectroscopy (XPS/UPS). The results are compared to the findings that exist already in literature [37, 39, 40, 108, 109].

3.1.2 In-diffusion of cadmium into the $Cu(In,Ga)Se_2$ front surface

The cadmium element present in the CdS plays an important role during the manufacture of a CIGSe based solar cell device. Photoelectron spectroscopy analyses showed that Cd ions favorably modify the energy band diagram at the CIGSe/CdS interface [24, 25]. The findings were supported by high resolution atom probe tomography and energy dispersive x-ray spectroscopy measurements [79, 110, 111] where it was shown that cadmium diffused into the surface of the absorber and substitute copper vacancies, modifying thereby the doping concentration in the surface region [26, 27]. The surface of the absorbers is *n-type* doped [29] and a homojunction is formed between

the absorber and the buffer layer [28]. The results were promoted by the theoretical study developed in Ref. [74]. Persson *et al.* showed that cadmium atoms replacing copper vacancies act as shallow donor defects [74]. Moreover, it was also demonstrated that pre-treated the CIGSe with Cd ions significantly improve CdS free buffer layer solar cells [29].

The theoretical investigation describing the diffusion mechanism of these Cd atoms into an over stoichiometric $CuInSe_2$ compound as well as into its corresponding ordered defect compound (ODC) Cu-poor $CuIn_5Se_8$ has been developed and is proposed in [112, 113]. Kiss *et al* utilized ab-initio density functional theory (DFT) to analyze the correlation between the diffusion procedure of cadmium dopants with the copper content of $CuInSe_2$ thin film materials. Details of the theoretical approaches and a thorough discussion of the results can be found elsewhere [112, 113]. The authors calculated the formation energies of Cd defects in $CuInSe_2$ and showed that the most stable energy configuration for Cd impurities is to substitute Cu elements. The result suggests that after the growth of CdS buffer layers, some Cd elements diffuse into the surface of the film and occupy Cu vacancies as indicated above. However, the authors pointed out that the diffusion path for the Cu-rich and poor specimens is significantly different.

In the case of Cu-rich $CuInSe_2$ absorbers [Fig. 3.1(a-c)], their calculations exhibited that the most favorable diffusion path is to transfer the Cd atom from the Cu site defect into a Cd interstitial defect. An illustrative schematic of this situation together with the activation energy approximated to be around $\sim 2.13\,\mathrm{eV}$ is displayed in Fig. 3.1(a) where the blue arrow highlights the migration path [23]. The lattice structure of an absorber including a Cd atom at an interstitial position is shown in Fig. 3.1(b). From the interstitial position [Fig. 3.1(b)], Kiss *et al*'s findings revealed as depicted in Fig. 3.1(c) that Cd elements can easily diffuse along the hexagonal channels formed by three anions and three cations of the $CuInSe_2$ structure [23]. The activation energy in this particular case is a bit lower and was estimated to be $\sim 0.23\,\mathrm{eV}$.

In the case of Cu-poor $CuIn_5Se_8$ absorbers [Fig. 3.2(a-d)] where a profuse number of Cu vacancies (V'_{Cu}) is present [Fig. 3.2(a)], a Cd atom is first inserted into one of the V'_{Cu}, and a Cu atom is kicked out from its original site leaving behind a new Cu vacancy [Fig. 3.2(b]. The exchange pathway is highlighted by the green arrow

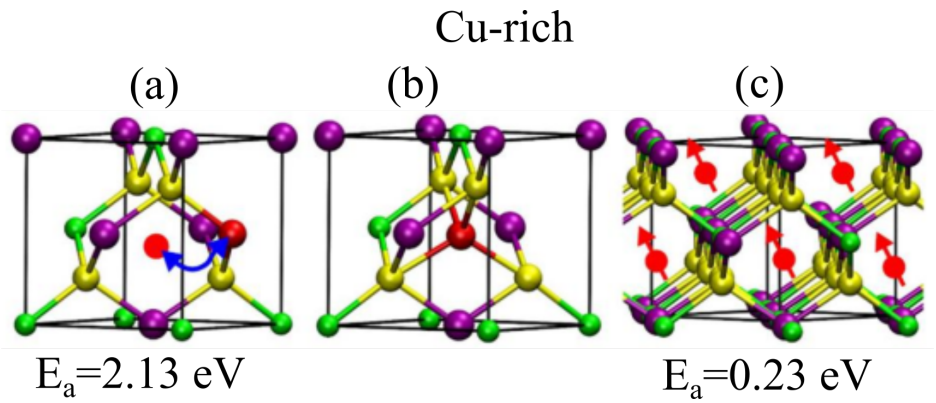

Figure 3.1: Schematic representation of the in-diffusion of Cd extrinsic defect in Cu-rich CISe thin film absorbers adapted from Ref. [23]. The Cd extrinsic defect is depicted in red, the Cu, In and Se elements are shown in green, purple and yellow colors, respectively. (a) shows the situation where a Cd_{Cu} impurity in a Cu site moves (blue arrow) to a Cd_i interstitial position as shown in (b). From the the interstitial position, the Cd can diffuse via the hexagonal channels in CISe [(see red arrow in the image (c)] [23].

in Fig. 3.2(b) and the activation energy is $\sim 0.94\,\text{eV}$. Afterwards, the Cd impurity squeezes into this newly created Cu vacancy as shown by the orange arrow in Fig 3.2(c) and resketched in Fig. 3.2(d). For this second migration, the activation energy was approximated to $\sim 0.45\,\text{eV}$. In a Cu-poor absorber, the diffusion of the Cd atom is realized just by successively repeating the above described reaction. Experimental proofs of the Kiss *et al* calculations are shown in [23].

Therefore, it is clear that for both non stoichiometric and over stoichiometric CISe specimens, the Cd atom diffuses into the absorber not only via grain boundaries but also via the Cu vacancies. However, the impact of this in-diffusion of Cd atoms on the surface electronic properties of the film and thereby on the CISe device efficiency is still not fully understood yet.

Furthermore, efficient tuning of the electrical properties via in-diffusion of Cd into the absorber matrix was reported to be facilitated by an inherent copper depletion of the surface of non stoichiometric $CuInSe_2$ [58, 111], which has yielded to be the finest composition for powerful photovoltaic cells [18]. Nevertheless, it is important to emphasize that a major part of these investigations was performed on Cu-poor absorbers, where it is proved that the near-surface region is copper depleted [111, 58].

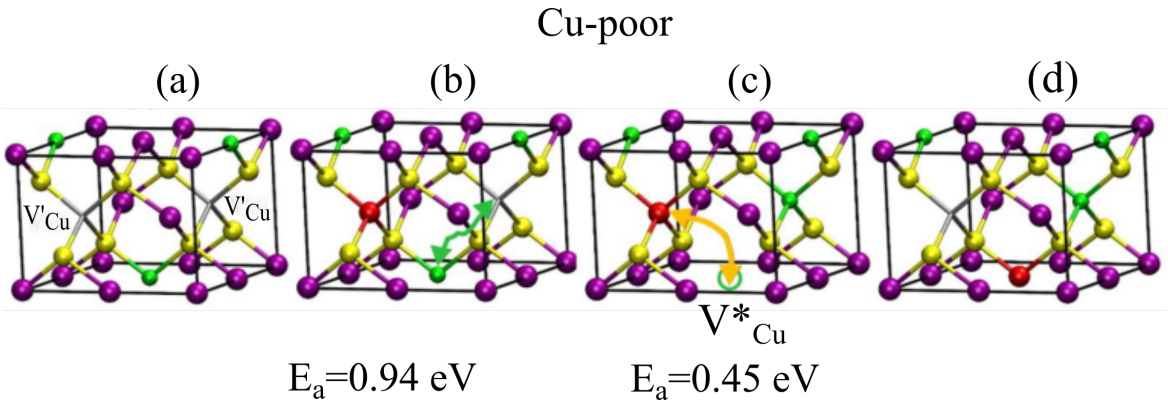

Figure 3.2: Schematic representation of the in-diffusion of Cd extrinsic defect in Cu-poor $CuIn_5Se_8$ thin film absorbers adapted from Ref. [23]. The Cd extrinsic defect is depicted in red, the Cu, In and Se elements are shown in green, purple and yellow colors, respectively. (a) shows a lattice structure of a absorber under the Cu-poor configuration; (b) presents a Cd atom in one of the Cu vacancy, and the situation where one Cu atom is to moving from its initial position to a vacancy position (green arrow) leaving behind a V^*_{Cu} vacancy; (c) Cd squeezes into a V^*_{Cu} (yellow arrow); (d) shows the situation where Cd is in V^*_{Cu}. [23].

For the absorbers that have grown under Cu-excess, which exhibit reduced efficiency in the final CIGSe devices and present fewer Cu vacancies, the favorable influence of cadmium, which is nicely archived for non-stoichiometric absorbers, may be absent. In order to fill this gap, the effect of Cd in-diffusion on the electronic properties of the over stoichiometric CISe films is thoroughly scrutinized in this thesis. The results are presented and widely discussed in Chapter 5.

Since the impact of the Cd in-diffusion is restricted to the very near surface of the absorbers, highly surface-sensitive techniques have to be employed. If GBs need also to be investigated, the tool has to present a high spatial resolution, as well. Hence, scanning probe methods are ideal as they grant us to analyze the surface properties of semiconductors with nanoscale resolution (See Chapter 4). Especially, Kelvin probe force microscopy (KPFM) was used regularly to investigate band alignment at the grain boundaries [48, 114]. Additionally, the influence of Cd in-diffusion was scrutinized on Cu-poor absorbers with KPFM [108]. The results exhibited that the diffusion of Cd into the GB considerably reduces the band bending at the grain boundaries [108].

STS of polycystalline CISe revealed crucial pieces of information into the film

properties anterior to the CdS growth [37, 40, 115], like the reduction of the density of defect states at the GBs and heat-induced surface passivation. Wide bandgap fluctuations were measured with STS on epitaxially deposited absorber [116]. In the present thesis, STM and STS data published heretofore are extended. Thereafter, the alteration of the grain boundaries and surface properties due to Cd in-diffusion is thoroughly explored and discussed (See chapter 5).

3.1.3 Impact of alkali post deposition treatment

Post-treating the surface of CIGSe with alkali elements has been demonstrated to be an efficient way to improve the performance of the CIGSe photovoltaic cells. During the last decades, the PCEs in the laboratory exceeding the 20% efficiency benchmark due to diverse PDTs with alkali elements was reported [77]. The PDTs change the chemical composition at the surface and alter the deposition of the CdS. The open-circuit voltages are boosted and the minority carrier lifetimes are enhanced [117, 118], which indicates better passivation of the junction defects and/or better bulk properties. This beneficial effect was observed for the first time in the early 1990s when a small amount of Na provided by SLG substrate was found to considerably improve the structural properties of the absorber during growth along with a superior device performance [41]. Since that discovery, investigating the role of Na in CIGSe has attracted the attention of many researchers and has become one of the key topics to be closely analyzed in the field of CIGSe based solar cells. Several studies [119, 120, 121, 122, 123, 124] have been carried out and published on that topic. More specifically, Cabellero *et al.* [119] reported that Na accelerates the formation of a $MoSe_2$ layer [125] at the CIGSe back surface, which is known to significantly enhance the electrical transport properties across the $MoSe_2$/ CIGSe back interface [119, 125]. Additionally, an increase of the net carrier concentration after adding Na elements into the CIGSe bare absorber was also reported [120]. Few years ago, numerous models involving the creation of acceptors such as the antisite defect $Na_{In/Ga}$ [101, 126], elimination of the antisite donor defect In_{Cu} [127], and neutralization of donor like V_{Se} [128] to justify the increase in holes density after post-treating the film with Na or after their out-diffusion from the SLG glass substrate were suggested in the literature. Regarding the neutralization of donor like V_{Se} vacancies, for example, Ruckh *et al.* showed in Ref. [128] that this effect

takes place through a chemisorption of oxygen atoms in connection with the surface oxidation, which is known to be accelerated by the presence of Na. This argument was further promoted in Ref. [45] where it was shown that oxygen in a V_{Se} donor site (O_{Se}) acts as a shallow acceptor with a defect energy of about $\sim$ 130 meV. Despite these findings and thorough investigations, the impact of Na PDTs on CIGSe solar cells might not be fully understood. Especially, since PDTs increase the complexity of the process and the influence of Na on the film properties might also have changed.

Although the debate regarding the favourable effect of Na in CIGSe solar cells is still ongoing, others alkali elements such as potassium (K), rubidium (Rb), and cesium (Cs) as well as their fluoride compounds were recently found to increase even more the performance of the devices. Their theoretical and experimental effects on CIGSe absorbers are discussed in more detail in [30, 127, 129, 130, 131]. Since the best PDT treated CIGSe solar cell (PCE $\sim$ 22.6% [30]) has been achieved from films that were treated with RbF [30], only the impact of RbF post-deposition treatments on CIGSe is summarized in the following section.

As indicated earlier, the underlying reason behind the high performance of the RbF-PDT CIGSe solar cells is still under intensive investigation and is widely discussed in the literature. While some findings show an increase in both V_{oc} [30, 31, 32] and fill factor (FF) [31, 32, 33] others rather show an increase in V_{oc} and a decrease in FF [34, 35, 36], suggesting that the power conversion efficiency of the RbF-PDT CIGSe device may depend on the amount of RbF deposited or on how the bare absorbers have been prepared. Depending on the deposition procedures, notably on the Cu concentration in the bulk, the surface chemical composition of the film can be significantly different. A formation of a thick layer of $RbInSe_2$ extraction current barrier at the hetero-interface [132, 133] was reported from the absorber with the bulk CGI of about $\sim$ 0.8, and was proposed as the main origin of the reduced FF largely discussed so far in the literature [134]. At the same time, the modification of the energy band diagram at the interface between the CIGSe and CdS buffer after RbF-PDT has also been reported to improve the V_{oc} [33] of the devices. It was shown by Maticius *et al.* in Ref. [134] that this enhancement in V_{oc} depends again on the amount of the CGI present in the absorber. The authors proposed as depicted in Fig. 3.3 that, contrarily to the film with a CGI of about $\sim$ 0.8 where a thick layer of $RbInSe_2$ that covers the entire

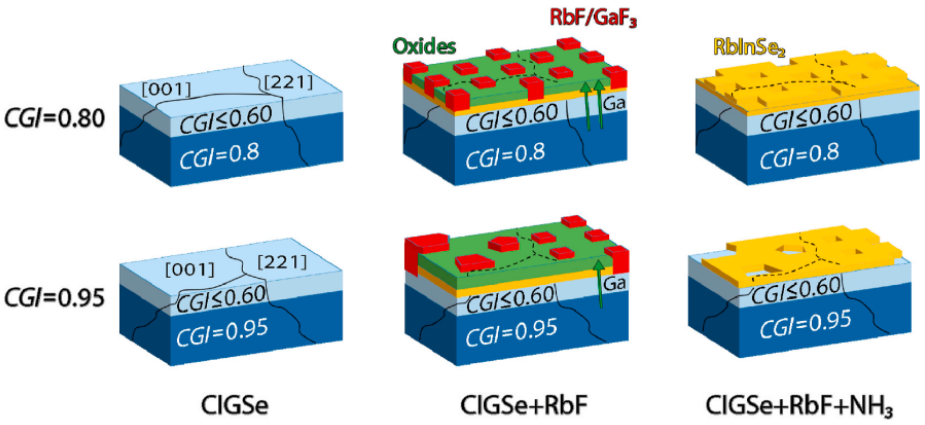

Figure 3.3: Model explaining the diffusion processes and the formation of $RbInSe_2$ secondary phase at the surface of the CIGSe proposed by N. Maticiuc *et al.* in Ref. [134] before (left column), after RbF-PDT (middle column), and after RbF-PDT + ammonia (NH_4OH) rinsing, for the film with the bulk CGI of about 0.8 (top row) and the one with the CGI of about 0.95 (bottom row). The oxides layer refers to agglomerations originated from hydroxides and carboxides as well as to metal oxides. The grain orientations were determined by means of electron beam scattered diffraction (EBSD).

surface of the absorber is measured, on the surface of the absorber with the CGI of about $\sim$ 0.95, a formation of a very thin and uneven distributed layer of $RbInSe_2$ is formed, which suggest that in order to see the real influence of RbF-PDT on the PCE of CIGSe devices the use of an appropriate bulk CGI is crucial. The RbF-PDT beneficially affects the superior device characteristics of CIGSe solar cells grown on samples with close-to-stoichiometry composition and deteriorates the ones of the CIGSe devices prepared on samples with high Cu vacancies [133]. Consequently, in this thesis only RbF-PDT CIGSe absorbers with a bulk CGI higher or equal to 0.95 are investigated. On those types of absorbers, a reduced interface recombination [135, 136] in line with the additional downward band bending at the CIGSe absorber surface and a flat conduction band alignment upon interface formation with CdS buffer [33] were reported.

In Fig. 3.3, a model explaining the diffusion processes and how the $RbInSe_2$ secondary phase is formed at the surface of CIGSe film after RbF-PDT is proposed [134]. Two samples grown under the same conditions but with different Cu-concentrations,

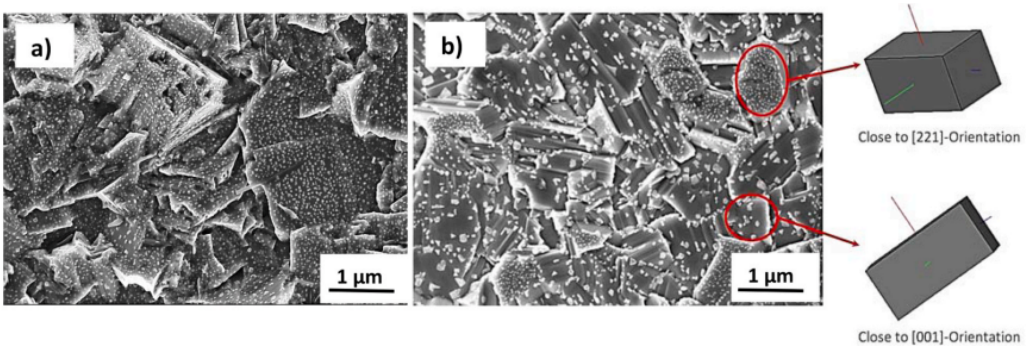

Figure 3.4: Morphological images of the RbF-covered CIGSe surfaces: (a) CIGSe film with the lower bulk CGI content (CGI = 0.8) and (b) the one with the higher bulk CGI (CGI = 0.95). The samples were explored as post-treated meaning without any rinsing step. On the right hand side, the EBSD data showing the distribution of the Rb-containing phase as a function of the grain orientations [134].

which have been treated with RbF elements were used to discuss the effect of nominal CGI on the lateral distribution of the Rb alkali metals at the surface of the CIGSe films. As can be seen, the surface of the two sets of bare absorbers is strongly Cu-depleted (with CGI < 0.6). The surface CGIs are similar for the both series of CIGSe absorbers and independent of the bulk composition. Both RbF free absorbers show a Cu-depleted nanolayer of about $\sim 100\,\mathrm{nm}$. However, after the RbF-PDT, the authors demonstrated (results not shown here) that the reduction of CGI on the surface depends on the nominal CGI composition and is stronger in the case of the film with the lower bulk CGI (CGI = 0.8) where a higher amount of Cu-vacancies is expected. While a few nanometer of RbF-containing particles are evenly distributed at the surface of the film with the lower Cu-content (Fig. 3.3 upper row), non-evenly distributed islands were found on the one with the higher CGI (CGI = 0.95) (Fig. 3.3 lower row). On the higher CGI absorbers, the distribution of the RbF-containing islands depends on the orientation of the grains. They are denser and more uniform on grains with [221] orientation whereas on grains with [001] orientation they are less denser and uniformly distributed. As shown in Fig. 3.4, the grain orientations indicated here have been determined via a combination of a SEM and electron backscatter diffraction data acquired from the same absorbers.

In Fig. 3.4, the surface of the film with lower Cu-content is uniformly covered with RbF containing particles when on the surface of the sample with higher Cu-content the

formation of islands with different size and density depending on the CIGSe facets are found, as indicated above. These findings are similar to the study carried out by Witte *et al.* [137], where it was shown that the deposition of the CdS buffer layer on top of PDT-free absorbers depends on the orientation of the CIGSe grains [137]. The former author's results exhibited that the CdS are not uniformly spread across the surface of the sample. A dense and uniform precipitate was found on [001] oriented grains, whereas a poor coverage of [221] oriented grains was observed after the growth of the CdS buffer layer. This disparity between the two facets was ascribed to the lower surface energy of the facet with the [221] orientation. In contrast to the reported results in Ref. [137], a more uniform coverage of the absorber layers after CdS was found on samples with RbF-PDT [138, 139].

On the other hand, as compared to the RbF-PDT sample with higher Cu-content, a more pronounced formation of a GaF_3 secondary phase, which are removed after ammonia rinsing were detected at the surface of the RbF-PDT sample with lower Cu-content (Fig. 3.3). Additionally, a higher surface Ga/(In+Ga) ratio (GGI) ratio was measured after the removal of GaF_3 and can be attributed to the incorporation of Rb in the CIGSe matrix, which act as a driving force for Ga diffusion from the bulk of the absorbers towards the surface [134]. The surface GGI values of ~ 0.45 and ~ 0.25 suggesting an accumulation of Ga at the surface of RbF-PDT absorbers were measured for the absorber with lower and higher Cu-contents, respectively. This high value of GGI (GGI ~ 0.45) measured at the surface of the RbF PDT-absorber with lower copper content can be one of the causes of its worse performance. A surface GGI value of ~ 0.3, which ensures a favourable flat conduction band alignment at the buffer interface is so far considered as the ideal value to fabricate good solar cells [140].

Proper analysis of the real change in surface chemical composition due to the RbF-PDT alkali metals as well as their impacts on grain boundaries electronics properties requires the use of high surface sensitive and high spatial resolution characterization methods like X-ray/ultraviolet photo electron spectroscopy (XPS/UPS), secondary ion mass spectroscopy (SIMS), transmission electron microscopy (TEM), atomic probe tomography (APT), Kelvin probe force microscopy (KPFM), scanning tunneling microscopy (STM) and spectroscopy (STS) and etc. SIMS and XPS measurements carried out on low temperature co-evaporation CIGSe absorbers with RbF-PDT revealed

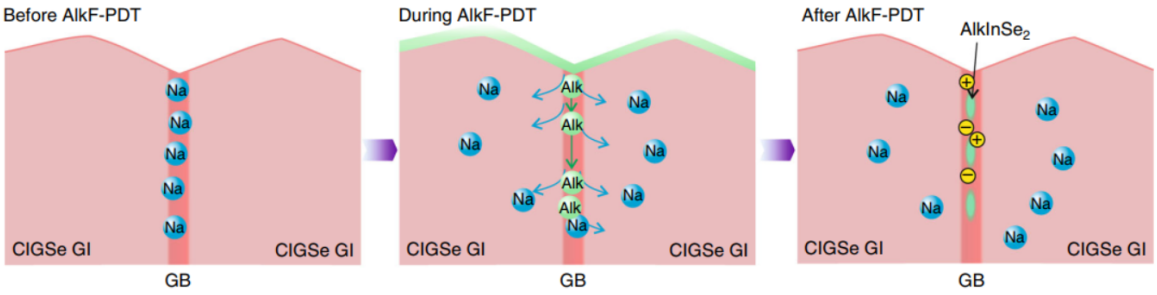

Figure 3.5: Simplified representation of the displacement of sodium to the grain interior by the heavier alkali metals after PDT and the possible formation of new compounds and charged defects at the grain boundaries [48].

a Cu-depleted surface [32]. Moreover, TEM and X-ray fluorescence (XRF) study performed by Schöppe *et al.* have shown the presence of Rb at the grain boundaries (GBs) and at the Mo/CIGSe rear interface [141]. Raghuwanshi *et al.* demonstrated via APT studies that the CdS buffer layer interface is In rich and Cu depleted [142]. These changes in elemental composition at the interface between the CIGSe absorber and CdS buffer layer of the sample with RbF-PDT was reported to not affect its surface band gap [34]. Hauschild *et al.* showed by means of XPS/UPS and inverse photoemission spectroscopy (IPES) that compared to the findings relayed by Pistor *et al.* [143] where an increase in surface energy bandgap of the absorber was measured after potassium fluoride (KF)-PDT, no change in surface bandgap is measured after RbF-PDT [34]. Additionally, higher amount of Rb (1.5 at %) and lower amount of Na and K (< 0.5 at%) was measured at GBs as compared with previous studies performed on non PDT samples, which presumably indicate the substitution of Na by K and Rb at GBs. In line with the TEM and XRF measurements carried out by Schöppe *et al.*, Rb was also found at the Mo/CIGSe interface[141]. Furthermore, a pronounced Cu depletion was measured at GBs and no Rb were detected inside the grain interiors. In this particular analysis, the concentration of Rb in the CIGSe grain interior was found to be lower than the detection limit of APT [141]. KPFM studies showed that compared to the samples with Na and K PDTs, CIGSe with Rb displayed higher and a more homogeneous workfunctions over the surface of the film [48]. In the same study, the alteration of the GBs elemental composition was also analyzed. The authors emphasized as can be seen in Fig. 3.5 that during the PDT, the heavier alkali metals such as Rb diffuse into the grain boundaries and displace the lighter Na

into the grain interior (GI), leading thus to the formation of charged defects and/or alkali-$InSe_2$ (alk$InSe_2$) phases at GBs [42]. The grain boundaries are partially passivated and the Na elements occupy the Cu vacancies within the grain interior inducing an increase of the net doping concentration of the film [42, 144]. Further pieces of information regarding how GBs are formed in CIGSe and different models suggested in literature in order to explain their impact on CIGSe are proposed in section 3.3. In addition, a short overview of GBs in CIGSe is also presented.

To the best of my knowledge, heretofore there is not STM/STS data acquired from the CIGSe sample with RbF-PDT available in the literature. In order to fill that gap, the surface properties of CIGSe RbF post-treated absorbers was systematically analyzed with STM/STS. The results are supplemented with KPFM, XPS, SIMS, and Raman spectroscopy data obtained from the same samples.

3.2 Rear surface properties of Cu(In, Ga)Se_2

Unlike the front surface of CIGSe where the utmost layer of the absorber interacts directly with the CdS buffer layer, the rear surface is the part of the absorber that forms together with the Mo layer the $MoSe_2$/CIGSe back contact interface in a CIGSe device. Therefore, it also plays an important role in CIGSe solar cells.

One of the breakthroughs that led to high PCE was the introduction of a Gallium back-gradient at the rear contact of the CIGSe solar cells [145, 146]. The formation of Gallium back-gradient considerably reduces the recombination rate at the Mo/$MoSe_2$ back-contact and enhances the performance of the graded CIGSe devices [145, 146]. Nonetheless, optimizing the $MoSe_2$/CIGSe interface is still under intensive investigation. It suffers from low optical reflectivity and exhibits high recombination velocity [147], which indicates that efficient passivation strategies have to be developed if one would like to obtain high performance CIGSe photovoltaic cells. This is particularly true for ultra-thin photovoltaic cells [148] where bandgap grading is not achievable.

In contrast to the front surface, to investigate the back surface properties of the CIGSe solar cells, the film has to priorly be lifted off from the Mo-coated SLG substrates. At present, there are several interesting reports based on the buried $MoSe_2$/CIGSe interface, which exhibit that the absorber could effectively be exfoli-

ated from the rear contact [54, 149, 150]. This facilitated the employment of surface-sensitive techniques such as XPS/UPS to analyze compositional and electronic variations at the back contact of the CIGSe absorbers. The findings showed an accumulation of Ga at the rear contact [151] and that the rear surface of $CuInS_2$ was Cu-depleted despite the fact that it was grown under Cu-excess conditions [150]. TEM exhibited an in-diffusion of Cu into the Mo layer [152] and APT analyses revealed an increased Cu and Ga content in the first 50 nm of the CIGSe films (measured from the rear contact) [153]. For the case of $CuGaSe_2$ it was shown via TEM investigation that Cu_xSe precipitations could also be present in the bulk of the sample [154]. The existence of the Cu_xSe precipitates in the bulk of absorber was already at that time speculated to be the reason for the low performances of over stoichiometric grown absorber layers. Nevertheless, up to now, the common agreement in the CIGSe research field is that absorbers that are grown under Cu- excess have a precipitate-free bulk with Cu_xSe on top, which can be washed away via KCN [155].

So far, much less is known about the spatial variations of the electronic properties on the nanoscale of the rear contact. Kavalakkatt *et al.* used a combined electron beam induced current (EBIC) and cathodoluminescence (CL) technique [147] to show that for a number of films the electronic landscapes of GBs vary with the absorber compositions and there is no straight link between the CL signal measured and the collection efficiency. For low symmetry GBs, CL analyses revealed a reduced signal, which suggests an enhanced amount of impurities at the GBs. In addition, there are some KPFM analyses available [156] on $CuGaSe_2$, which demonstrated that most of the GBs revealed downward band bending in the order of $\sim$ 50 meV compared to the grain interiors. Moreover, a signature of Ga was detected on the Mo-surface. Heretofore, there is no scanning probe microscopy (SPM) data for CISe that exist in the literature.

In the CIGSe community, it is known that Cu-concentration is extremely important [18, 100]. High efficiency CIGSe solar cells are made from the absorbers that are synthesized under Cu-poor conditions (Cu/In<1) [100]. The Cu-poor absorbers present higher V_{OC} and quasi-Fermi level splitting (QFLS) compared to absorbers with Cu/In>1 [100]. For CISe films without Ga, the difference in QFLS between Cu-poor and Cu-rich samples is tiny [96, 157]. Nevertheless, in line with Ga containing

films, the efficiency is higher for Cu-poor than for Cu-rich solar cells. In the case of over stoichiometric films, the surplus of Cu precipitates as copper selenide secondary phase on top of the CISe samples. A subsequent KCN etching [107, 150] cleans the copper selenide, thus generating a film with a stoichiometric bulk composition. The KCN cleaning, nonetheless, also has some unfavorable impacts on the composition and impurities in the front surface region [106, 158]. The study of the back surface hence offers a great opportunity to analyze stoichiometric films, which were not chemically treated with KCN.

In chapter 6, CISe films deposited under Cu-excess conditions and subsequently KCN etched were exfoliated from their original substrates and critically scrutinized using SPM methods such as STM and STS and KPFM. The local density of states was examined by STS and compared to analyses carried out on the front surface [37, 39, 40, 158], while changes in workfunction of the absorbers were investigated by KPFM in order to compare the finding to $CuGaSe_2$ results available in literature [156]. Furthermore, XPS and energy-dispersive X-Ray (EDX) analyses were employed to study the surface and bulk compositions, and the effect of the exfoliating process on quasi-Fermi level splitting was analyzed with photoluminescence (PL) imaging. At last, an x-ray diffraction tool was used to analyze the formation of secondary phases in the CISe absorber layers.

3.3 Grain boundary properties in Cu(In, Ga)Se_2

A polycrystalline semiconductor is a material incorporating a multitude of grains, which have various sizes and are randomly oriented. In such a material, crystallites are connected one to another and the interface that separates two adjacent grains is called the grain boundary (GB). GBs interrupt the long-range order provided by the periodicity of the crystal [145] and induce thereby a distortion of the lattice and the formation of dangling bonds. This local perturbation of the crystal structure leads to a distribution of defect states at GBs in polymaterials [159, 160]. The defect states eventually result in an electronic charge that, in turn, is compensated by a space charge region surrounding the GB [161]. With these localized charges, grain boundaries even though they are only localized to a few atomic layers in between

two misaligned crystalline grains may significantly affect the electrical properties of a polycrytalline semiconductor.

Unlike polycrystalline silicon (Si) [162, 163] and gallium arsenide (GaAs) [164, 165] solar cells where it is proven that the presence of GBs negatively affects the conductivity of the materials, limiting thereby the performance of the whole device, polycrystalline CIGSe based solar cells, despite containing a profuse number of GBs have reached excellent power conversion efficiencies. This high performance of CIGSe solar cells may lead forthwith speculating that in contrast to Si or GaAs semiconductor materials, GBs are electrically inactive [166] in CIGSe thin film solar cells. However, it is important to point out that despite the thorough exploration of the role of GBs in high PCE-CIGSe devices, the physics underlying their electronic properties is still at the heart of controversial discussions [37, 167, 168, 169, 170]. While some researchers suggest that GBs could improve solar cell efficiency, some others rather claimed their harmful effects on the device performance. In the following sections, the most relevant models proposed in the literature to elucidate the electronic activity of GBs as well as the current standpoint of the GBs in CIGSe are presented and are discussed.

3.3.1 Atomic relaxation model

To describe the electronic activity of GBs in CIGSe absorbers, Yan *et al.* [169] used this model for the first time in 2007 to demonstrate that twin boundaries ($\Sigma 3$) in polycrystalline CIGSe materials are electrically benign. The study was conducted via first principle density functional theory calculations, which is one of the more powerful theoretical approaches to explore the density of states of semiconductor materials. The authors showed that in opposite to CdTe, where dislocation cores at GBs create deep level defects [171, 172], no signature of such defect states was found at twin-GBs in CIGSe. The finding was found to be independent of the exact bonding configuration and was ascribed to a sturdy repulsion between Se atoms [169]. The fact that it is hard to form Se-Se wrong bonds at GBs in CIGSe materials leads to a large atomic relaxation at the GB region [169]. Due to this atomic relaxation, the defect levels shift down into the valance band, leaving behind a semiconducting GB region without deep level defects inside the bandgap. As the GB region is free of charged defects, no band bending or variation in workfunction as shown in Fig. 3.6 is observed between them

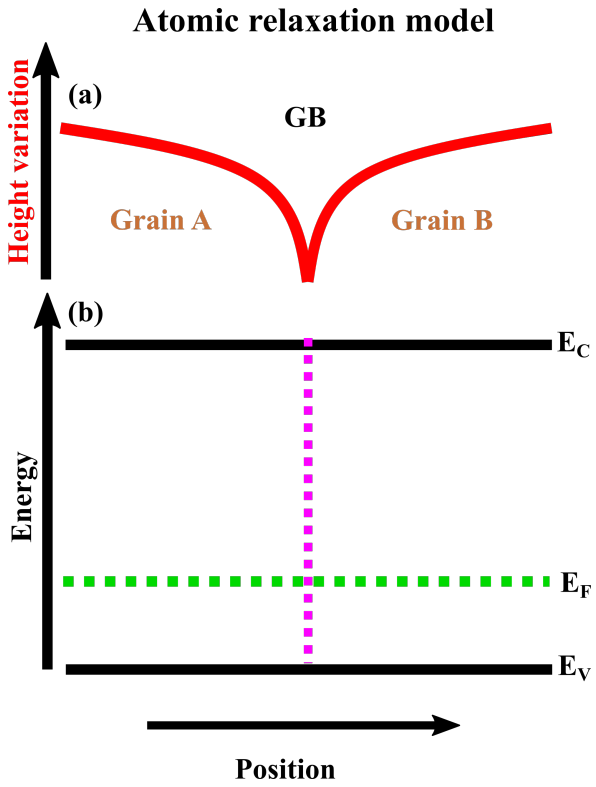

Figure 3.6: Band alignment in the neighborhood of twin-GBs in CIGSe absorbers adapted from Refs. [46, 64]: (a) 1D representation of two adjacent CIGSe grains, in this particular case named Grain A and Grain B with one grain boundary between them; (b) a sketch of the corresponding energy band diagram showing the E_C, E_V and E_F. The vertical purple dots highlight arbitrary defect states which are present at the GB [64].

and the adjacent grain interiors. Based on this, Y. Yan *et al.* reported that GBs are electrically inactive and consequently are not harmful for the solar cell performance.

3.3.2 Structural barrier model

The structural barrier model was developed by Person *et al.* [167, 173] to show as graphically displayed in Fig. 3.7 and will be discussed below that the behavior of the energy band diagram at the interface between the GBs and grain interiors (GIs) in CIGSe chalcopyrite materials depends on the atomic structure of GBs. Similar to the Yan *et al.* studies, the calculations were also performed via first principle density functional theory but this time by considering the atomic structure of (112) and $(\overline{1}\overline{1}2)$ polar facets [174], which in CIGSe community are known to be cation terminated and

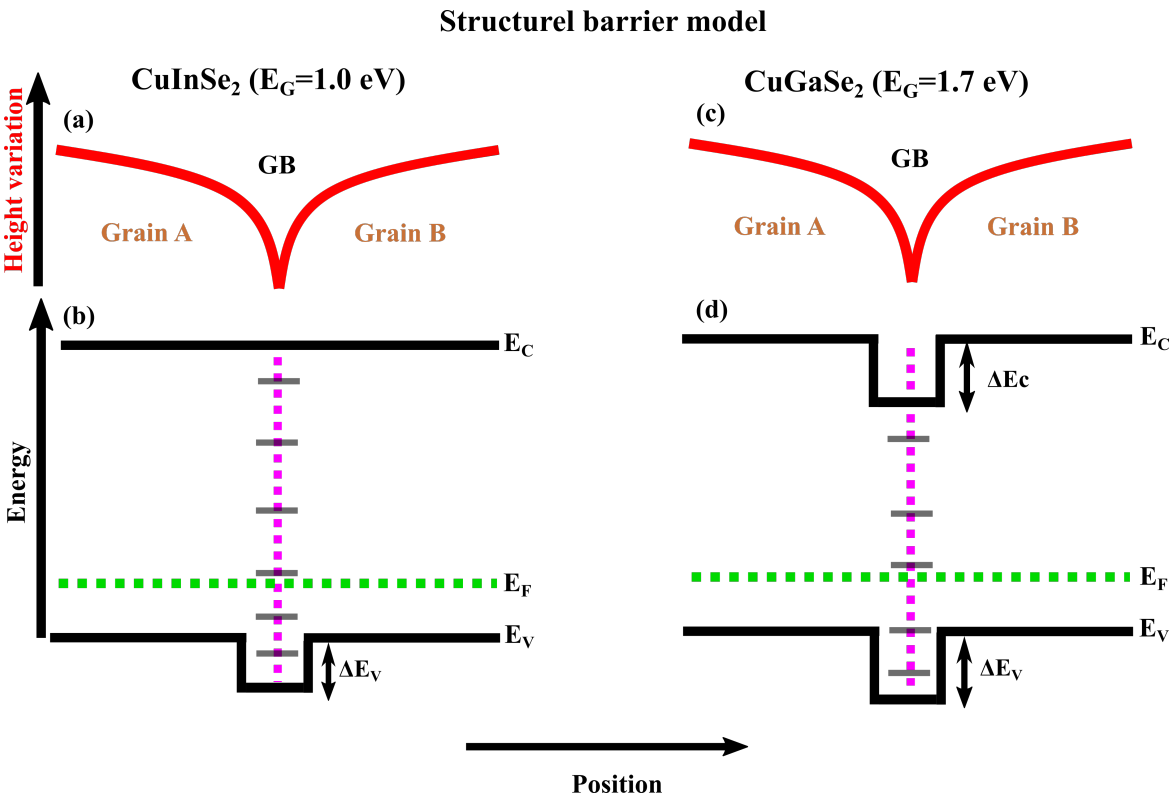

Figure 3.7: Band alignment in the neighborhood of (112) GBs in CIGSe absorbers adapted from Refs. [46, 64]: (a) and (c) 1D representation of two adjacent CIGSe grains (Grain A and Grain B) with one grain boundary between them; (b) and (d) are the sketch of the corresponding energy band diagram showing the E_C, E_V and E_F. The vertical purple dots highlight arbitrary defect states which are present at the GB [64].

anion terminated [58, 174], to model GBs. In their work, Person *et al.* assumed in one case that GBs are cation terminated and in another case that they are anion terminated. In the case of cation terminated (112) GBs, they showed as can be seen in Fig. 3.7(b) and (d) that the interface between the GBs and grain interiors exhibits a valence offset of $\Delta E_V \sim 0.2\,\text{eV}$ and $\sim 0.5\,\text{eV}$ for $CuInSe_2$ and $CuGaSe_2$, respectively. The ΔE_V offset across the interface between GB and GI (GB/GI) measured was ascribed to a reduction of the repulsive interaction between Cu-d and Se-p states at GBs, induced by the Cu-depleted of the (112) facets. Moreover, the conduction band maximum offset (ΔE_c) across the GBs/GIs interface as well as the width of the band offsets were also analysed. The findings showed a significant $\Delta E_c \sim 0.5\,\text{eV}$ at GBs of $CuGaSe_2$, whereas a negligible ΔE_c offset was observed at GBs of $CuInSe_2$. The

width of all band offsets was found to be only few atomic layers. In the case of anion terminated ($\overline{112}$) GBs, no such variation was found at the GBs/GIs interface. An almost flat conduction band maximum and valence minimum was calculated across the interface between GBs and GIs, and was speculated to be in connection with the charge compensation mechanism at the ($\overline{112}$) facets, which do not include the formation of Cu vacancies. In CIGSe chalcopyrite materials the (112) polar facets are Cu-depleted, while III-on-Cu defect states are preponderant on the ($\overline{112}$) ones [58, 174].

The valence band offset observed at the cation terminated GBs is an potential barrier that hinders holes from arriving into the GB region. Consequently, the electron-hole recombination is reduced at GBs and pathways for fast electron transport are created. A conduction band offset meanwhile attracts electrons to the GBs, thus causing a charge separation at the GB interface, which again reduces recombination at GBs. Person *et al.*'s work leads to believe that it is in favor of solar cell performance to reduce the presence of ($\overline{112}$) GBs in CIGSe absorbers. Compared to (112) GBs, ($\overline{112}$) GBs do not exhibit any electronic band offset and are accordingly not favorable for solar cell efficiency.

3.3.3 Electronic barrier model

The electronic barrier model was first developed in the early 1971 to describe the electronic activity of GBs in *p*-type polysilicon films [161, 162]. Later on, it was for the same purpose applied by Fisher *et al.* in [175, 176] to II-VI semiconductor materials, and thereafter to *p*-type CIGSe chalcopyrite compounds [71, 177, 178, 179]. The model was built up focusing the main interest on the configuration of GBs, which is the location of encounter of two grains, i.e a region in polycrystalline materials that exhibits much-distorted lattice structures and pronounced dangling bonds. Due to this atomic disordering, GBs are the preferential regions where a large number of charge defect states are localized. These localized charges alter the electronic band structure inducing thus a difference in workfunction or a formation of a potential barrier at the interface between the GB and the GIs. Hence, the nature (positive or negative) of defect states localized at a GB determines whether the energy band diagram across the GBs will bend down or up. In other words, the change in workfunction measured

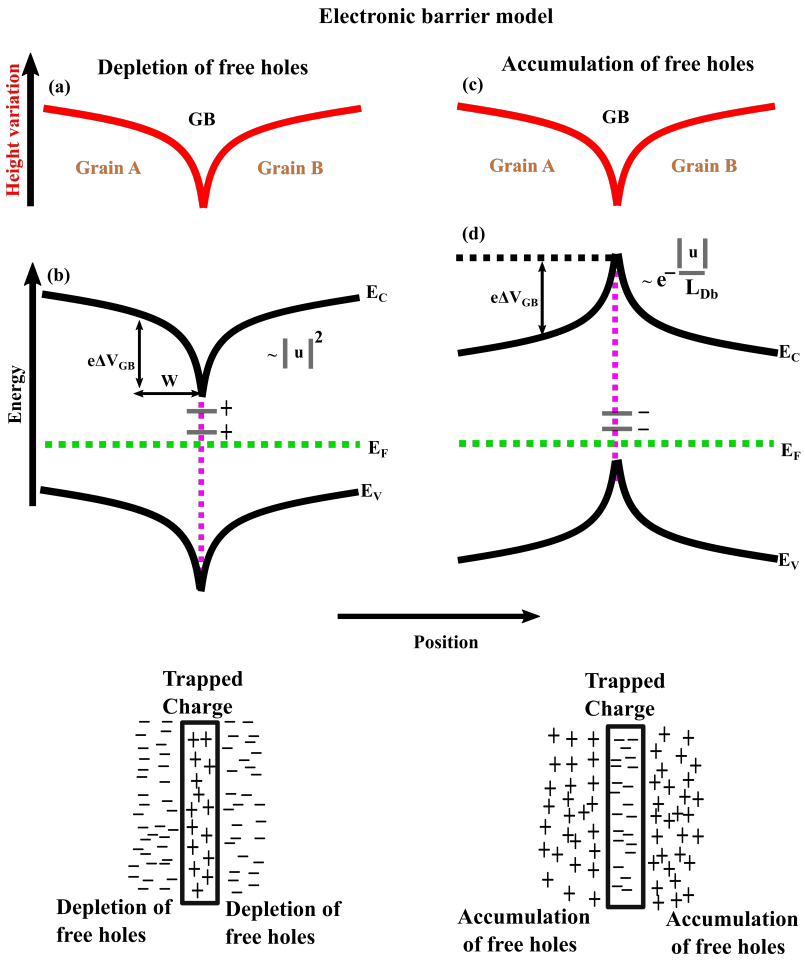

Figure 3.8: Band alignment in the neighborhood of charged GBs in CIGSe absorbers adapted from Refs. [46, 64]: (a) and (c) 1D representation of two adjacent CIGSe grains (Grain A and Grain B) with one grain boundary between them; (b) and (d) are the sketch of the corresponding energy band diagram showing the E_C, E_V and E_F in the case of the positive and negative charged trapped at a GB, respectively. The vertical purple dots highlight arbitrary defect states which are present at the GB [64].

across the GBs/GIs interface depends on the sign of the charge which is trapped at a GB.

In the case of *p*-type CIGSe chalcopyrite semiconductors, the two main configurations adopted to describe how the sign of the charge trapped at a GB alters the band diagram across the GBs/GIs interface are depicted in Fig. 3.8(b) and 3.8(d). In Fig. 3.8(b), the configuration assuming that positive charges are trapped at a GB is presented, while Fig. 3.8(d) depicts the one assuming that rather negative charges are trapped.

In the positive trapped charges situation, free holes are repelled from the near GB region, and ionized acceptors that counterbalance the positive charge at the GB are formed. As a consequence, a hole-depleted space charge region (SCR) causing the band diagram to bend down at the GB is observed [Fig. 3.8(b)]. The resulting potential barrier can be evaluated using the Poisson equation [180]:

$$\epsilon\epsilon_0 \frac{\partial^2 V_{GB}(u)}{\partial u^2} = -\rho(u) \tag{3.1}$$

where u is the coordinate with $u = 0$ the exact location of the GB, $V_{GB}(u)$ is the potential distribution across the SCR, $\rho(u)$ is the charge density in the SCR, ϵ_0 is the dielectric constant, and ϵ is the dielectric permeability of the p - CIGSe material. Considering that the band diagram displayed in Fig. 3.8(b) is under thermal equilibrium conditions [49] and the following boundaries conditions [64]: $\frac{\partial V_{GB}(u)}{\partial u}|_{u=w} = 0$ and $V_{GB}(u = w) = 0$, two-time integration of equation (3.1) can be written as:

$$V_{GB} = \frac{qN_A}{2\epsilon\epsilon_0}(|u| - w)^2 \tag{3.2}$$

Here N_A is the net doping density, q is the elemental charge, and w is the width of the space charge region.

In the negative trapped charges situation, an opposite scenario is observed. A negative charge is trapped at a GB and free holes that counterbalance the trapped charge are accumulated in the near GB region. This compensation mechanism leads to a formation of an upward band bending towards the GB, i.e a creation of a positive potential barrier at the SCR (Fig. 3.8(d)). By taking into account only the majority carriers (holes) and assuming that small potential barriers exist at the SCR, the potential distribution across the GB can be approximated from [46, 114, 181]:

$$tanh\left(\frac{qV_{GB}(u)}{4k_BT}\right) \cong tanh\left(\frac{qV_{GB}(u=0)}{4k_BT}\right) exp\left(-\sqrt{2}\frac{|u|}{L_{Db}}\right) \tag{3.3}$$

where $L_{Db} = \sqrt{\epsilon\epsilon_0 k_B T/e^2 N_A}$ is the Debye-length, and $u = 0$ is the location of the GB.

As mathematically expressed in equations (3.2) and (3.3), the potential across a GB/GI in p-poly CIGSe depends on the nature of the charges that are trapped at GBs. The positive charges GBs exhibit a quadratic potential dependence, whereas the potential distribution follows an exponential function in the case where negative charges are trapped at a GB.

From Equations (3.2) and (3.3), the potential barrier width was evaluated [64, 114]. The calculations reveal similar widths for both negative and positive potential barriers ΔV_{GB}. Baier *et al.* showed that for typical charge carrier density in the range of $10^{15} cm^{-3}$- $10^{17} cm^{-3}$ [71, 64, 114], potential variations in the range of 100 - 400 mV, the barrier widths in order of 35 - 85 nm are obtained [64].

In CIGSe, the existence of these two types of potential barriers at a GB and their impact on the resulting solar cell efficiency have been thoroughly explored. It is believed that instead of forming a positive potential barrier, having a negative potential barrier at GBs, i.e a downward band bending at GBs, is beneficial for cell performance. When a downward band bending is formed at a GB, the majority carriers (holes) are repelled from the near GB region and reflected toward the grain interior, while electrons are attracted to the GBs. As a result, a hole depleted pathway conduction leading to a reduction of the electron-hole recombination rate at GBs takes place in the CIGSe material.

3.3.4 Electronic & tunneling barrier model

The electronic & tunneling barrier model could be defined as a combination of the structural model and electronic barrier model. Additional to the above described models (subsection 3.3.2 - 3.3.3), Azulay *et al.* [182] and Hafemeister *et al.* [170] proposed it to explain further the potential landscape around the GBs in chalcopyrite thin films [182, 170]. From their analyses carried out on polycrystalline and bicrystal CIGSe films using in the first case conductive atomic force microscopy [182] and in the latter case combined Kelvin probe force microscopy and Hall measurements [170], the authors postulate as shown in Fig. 3.9 that both a potential barrier for holes and a downward band bending can simultaneously exist at a GB in CIGSe. They showed that a potential barrier with a few nm wide and several hundred mV deep, and a downward band bending of about 100 mV can be observed. In fact, Hafemeister *et al.*'s findings revealed that the Hall resistance measured at a GB in CIGSe varies as a function of temperature. In order to explain this observation, the transport mechanism across the GBs was simulated and the results showed the existence of a narrow hole tunneling barrier at some GBs in CIGSe, which had not explicitly been highlighted in the original structural barrier model.

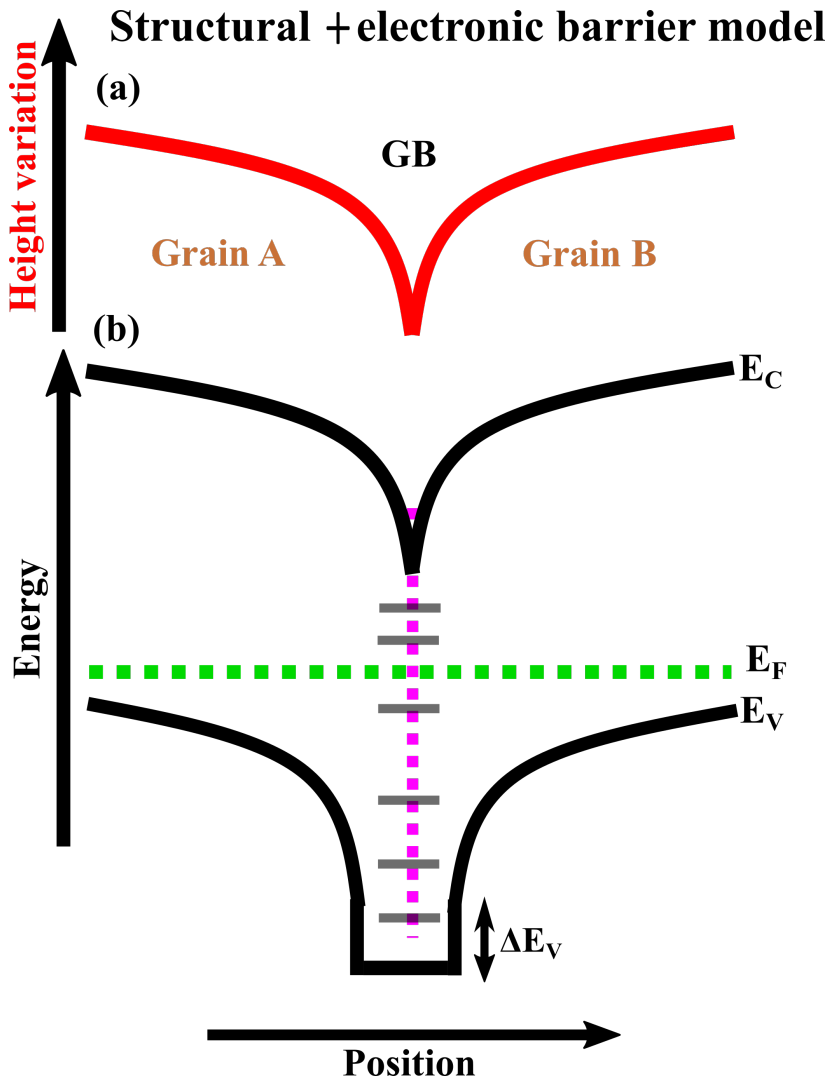

Figure 3.9: Band alignment in the neighborhood of GBs in CIGSe absorbers adapted from Refs. [46, 64]: (a) 1D representation of two adjacent CIGSe grains (Grain A and Grain B) with one grain boundary between them; (b) is the sketch of the corresponding energy band diagram showing the the E_C, E_V and E_F. The vertical purple dots highlight arbitrary defect states which are present at the GB [64].

3.4 Current standpoint of the grain boundaries in $Cu(In,Ga)Se_2$

The presence of GBs and consequently their impact on the CIGSe based solar cells performance have attracted significant research interest in recent decades and have been widely investigated. In order to gain more insight into the electronic activity of grain boundaries in CIGSe, various theoretical approaches, simulations methods, and

experimental techniques were recently developed. Until now, the findings obtained are still under intensive debate and some of them are even contradicting. In this section, the summary of the progress made heretofore in understanding the grain boundaries electronic properties in CIGSe is briefly presented. For a broad knowledge about the physics underlying the grain boundaries as well as their implications in CIGSe based solar cells, readers are strongly recommended to refer to the review studies proposed in [46, 49, 183].

The experimental investigation of the electronic properties of GBs in CIGSe has started in early 2002 [71, 184]. In fact, in 2002, Schuler *et al.* [71] demonstrated for the first time by means of Hall measurements that similar to polycrystalline Si [161] solar cells, grain boundaries also exhibit a potential barrier for majority carriers in polycrystalline CGSe solar cells. Schuler *et al.*'s findings were later supported by KPFM data [168, 178, 185] where a potential barrier ascribed to charged defects at GBs between ~ 100 and $\sim 170\,\mathrm{mV}$ and the depletion width of $\sim(42 \pm 9)\,\mathrm{nm}$ were estimated. Unlike the polycrystalline case, Siebentritt *et al.* showed that rather a neutral potential barrier for majority carriers exists across a twin grain boundary in epitaxially grown CGSe [184]. Although these findings were already predicted by the structural model (section 3.3.2), the experimental valence band offset ΔE_V of $\sim 30\,\mathrm{meV}$ reported by Siebentritt *et al.* was roughly 16.7 times lower than the theoretically expected value [173]. Hafemeister *et al.* [170] explored deeper this discrepancy between the experimental and theoretical values of ΔE_V by means of temperature dependent Hall resistance measurements. The authors found out that in addition to the 30 meV valence band offset observed by Siebentritt *et al.*, a narrow ($\sim 0.96\,\mathrm{nm}$) neutral hole barrier of $\sim$ 170 meV [184] is also present at twin GBs in CGSe. Nevertheless, the value obtained is still lower than the theoretical one.

The impact of such a valence band offset ΔE_V on the cell performance was largely investigated as well. Several two-dimensional device simulation methods and experimental models have been proposed in that respect. The two dimensional device simulation data presented in Refs. [186, 187, 188, 189, 190] point out an improvement of the performance of the solar cell with increasing ΔE_V. Already at that time, solar cells efficiency above 19% was anticipated for an ΔE_V of at least 300 meV. However, these findings are in contradiction with the ones proposed by Rau *et al.* [49] where it

is demonstrated that the internal valence band offset is unlikely the exclusive reason for the low grain boundaries activity in CIGSe thin films. Yan *et al.* later confirmed Rau *et al.*'s analyses by showing that not all GBs are Cu-depleted in CIGSe thin film absorbers [191]. The authors showed by means of combined transmission electron microscopy high resolution $z-$ contrast imaging and nanoprobe x-ray energy dispersive spectroscopy that there is not depletion of Cu at (112) GBs in CIGSe films [191]. Based on their results, they reported that (112) GBs do not exhibit a valence band offset. As a result, Yan *et al.* [169, 192] suggested the atomic relaxation model (section 3.3.1) as the best model to explain the electronic benign properties of GBs in CIGSe.

It is known that the symmetry of grain boundaries also impacts their electronic properties. By means of KPFM measurements, a smooth surface potential was observed across $\Sigma 3$ GBs in epitaxially grown CIGSe, whereas a potential barrier of $\sim$ 90 meV was detected at $\Sigma 9$ GBs within the same absorber [170]. Similarly, electron beam induced current measurements exhibited differences in carrier recombination mechanism between $\Sigma 3$ GBs and non- $\Sigma 3$ GBs [193, 194], which again confirm the dependency of GBs properties with their symmetries.

The variation of the potential across the GBs, i.e a band bending is seen hitherto as a consequence of charged defects as discussed in [161, 162]. Therefore, depending on the sign of the defect states, the band can bend up or down. However, it is essential to emphasize that, even here, the results are still on a controversial discussion, no consensus has been found yet. Both a downward band bending [168, 169, 170, 178, 179, 182, 185, 195, 196] and an up band bending [193, 197] have been regularly reported at GBs in CIGSe. A downward band bending of $\sim$ 100- 200 meV was measured at GBs in CGSe by Sadewasser *et al.* [185]. Similar studies reproduced on CIGSe [179] showed that band bending at GBs in CIGSe varies with the concentration of Ga added. A downward band bending of $\sim$ 150 meV was observed at GBs of the films with $x \sim 30\%$, while for higher Ga content films a flat band was observed [179]. These results suggest that additional Ga included in the CISe matrix does not only tune the energy bandgap of the whole absorbers but also alter the energy band diagram at GBs. Alike changes at GBs were observed when CIGSe absorbsers are post-treated with the alkali metals. After an alkali post-deposition treatment, the elemental composition at GBs is altered leading to an additional defect state or a formation of an alk$InSe_2$ phase at GBs [42, 48].

To further explore the alteration of grain boundary properties, Romero *et al.* used electro-assisted scanning tunneling microscopy to analyze the transport mechanism across GBs in CIGSe as a function of the Ga ratio [198]. As already indicated in Ref. [179], the authors showed both low and high Ga ratios exhibited a transport barrier and no transport barrier at GBs in CIGSe, respectively.

Despite profuse studies carried out until now, a general consensus regarding the influence of band bending on CIGSe solar cell performance does not exist yet. Understanding the real effect of band bending at GBs in CIGSe is one of the main topics that are nowadays closely investigated in the CIGSe research community. While Taretto *et al.* reported that the presence of a downward band bending at GBs in CIGSe will be harmful to the cell efficiency [186, 187, 188], the study carried out by Jiang *et al.* revealed their beneficial impact on the solar cell performance [178, 179]. Although the presence of GBs in CIGSe causes an increase in the short circuit current, it also reduces the open-circuit voltage leading thus to their harmful effect on the solar cell efficiency [186, 187, 188].

In this thesis, the electronic properties of GBs is analyzed by means of combined KPFM and scanning tunneling microscopy and spectroscopy. The findings are supplemented with the change in elemental composition acquired by using X-ray photoelectron spectroscopy or ultraviolet photo electron spectroscopy.

Chapter 4

Characterization techniques and sample preparation

This chapter discusses the characterization techniques, the sample preparation and the experimental details.

4.1 Characterization techniques

This section focuses on the main experimental tools that were employed to analyze the surface properties of the samples investigated in the framework of this thesis. It starts with an introduction to scanning probe microscopy (SPM), which represents the main characterization technique. Thereafter, the theoretical and working principles of X-ray photoelectron spectroscopy (XPS) as well as a brief presentation of secondary ions mass spectroscopy (SIMS) and Raman spectroscopy all used as supplemental characterization methods are presented.

4.1.1 Scanning probe microscopy

SPM refers to a wide range of tools that can be used to probe the surface properties of a sample on the nano-scale. In principle, the techniques employ a very sharp tip close or in direct contact with the sample surface to investigate the topography, surface mechanical and electrical properties of metallic, semiconducting and insulating materials. Since its working principle is derived from that of scanning tunneling microscopy (STM) and atomic force microscopy (AFM), the theoretical background of STM and

AFM is first introduced. Afterwards, the technical implementation of STM and AFM along with their corresponding derivative techniques is described.

Scanning tunneling microscopy

STM is the very first SPM technique that allowed researchers to image both the topography and the electronic properties of the surface of a sample with atomic resolution. The technique was established in 1981 by Gerd Binnig and Heinrich Rohrer at IBM Research Laboratory in Switzerland [199]. Five years later, the authors were awarded with the Nobel Prize in Physics for their discovery. At present, STM is widely used in nanotechnology and nanoscience. The tool is employed in various research fields such as physics, chemistry, materials science, biology, and medicine [200].

The fundamental concept of STM is based on the quantum mechanical tunneling effect, a phenomenon in which a particle tunnels through a potential energy barrier. This is forbidden in the framework of classical mechanics and can only be explained considering the wave-particle duality described in 1924 by L. de Broglie and experimentally proved in 1927 by C. Davisson *et al.* [201]. A schematic representation of the quantum mechanical tunneling effect is depicted in Fig. 4.1(a). The potential energy barrier V_0 is finite and is assumed to be higher than the total energy of the particles E, and the barrier width (L) to be only in order of a few angstroms ($\sim$ 0.3 - 1 nm [200, 202]).

In such a configuration, it can be shown via the use of the Schrödinger equation that although the wavefunction of the particle is gradually attenuated when tunneling through the potential barrier [Fig. 4.1(a)], the probability for it to exist in region III is non-zero [204]. This attenuation of the wavefunction when penetrating a potential barrier depends on the transmission probability, which in turn, depends on the energy of the particle, the width, and the height of the potential barrier. The model is forbidden by the laws of classical mechanics. In the classical case, as the total energy of the particles is lower than the barrier height (V_0), the particles that move from region I to region II will not have enough energy to overcome the barrier located at z=0. Hence, at the position z=0, the particles will all be reflected back into region I and will not pass through the potential barrier (region II) as shown in Fig. 4.1(b).

In the quantum mechanical case, a particle can be considered as a wave and the

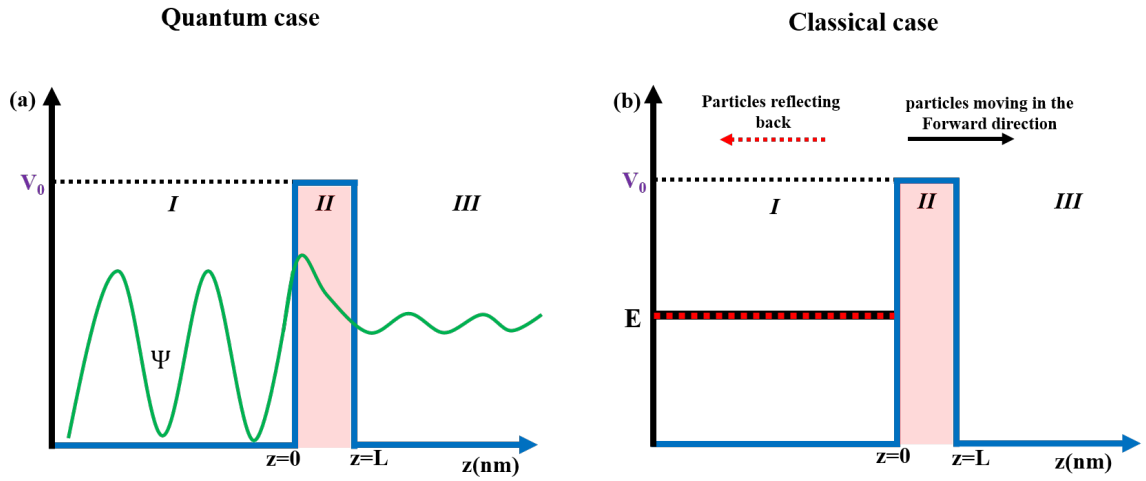

Figure 4.1: (a) simplified schematic representation of the quantum tunneling effect showing exponential decays of the electrons when penetrating a potential barrier adapted from Ref. [203]. The wave function of the electron is represented by the green curve (ψ), the width, and the height of the potential barrier by L and V_0, respectively. (b) represents the situation where a classical mechanics approach is applied. I, II, and III are region I, region II and region III, respectively

situation depicted in Fig. 4.1(a) can be described by a one-dimensional Schödinger equation. The wavefunction of a particle in regions I, II, and III [Fig. 4.1(a)] is expressed as followed [202].

$$\psi = \begin{cases} \psi_I = Ae^{i\lambda z} + Be^{-i\lambda z} & \text{for} \quad z < 0 \\ \psi_{II} = Ce^{-\gamma z} + De^{\gamma z} & \text{for} \quad 0 \leq z \leq L \\ \psi_{III} = Fe^{i\lambda z} & \text{for} \quad z > 0 \end{cases} \tag{4.1}$$

Where $\lambda = \sqrt{2mE/\hbar^2}$ and $\gamma = \sqrt{2m(V_0 - E)/\hbar^2}$ are the wave vectors, m the mass of the particles, and A, B, C, D the complex numbers, which can be calculated using the properties of the wavefunction [202]. In region I, A stands for the amplitude of the incoming wave and B represents the part of the incoming wave that is reflected at z=0. In region II, C is the amount of the wave that penetrates the potential barrier, and D is the part that is reflected at z=L. In region III, F refers to the amplitude of the final part of the wave that was transmitted. Two key points deserve to be emphasized here. The existence of the wavefunction in the forbidden region (region II), which clearly illustrates that in contrast to classical mechanics, a part of the wave

tunnels through the potential barrier. In addition, the first term of the function ψ_{II} shows an exponential decay of the wave through the barrier as indicated above. The transmission probability (T) from region I to III also called the transmission factor is the ratio of the probability density of the transmitted wave and the one of the incoming wave. It can be evaluated via the following formula [202]:

$$T = \frac{|\psi_{III}|^2}{|\psi_I|^2} = \frac{|F|^2}{|A|^2} = \frac{4\lambda^2\gamma^2}{(\lambda^2+\gamma^2)^2 sinh^2(\gamma L) + 4\lambda^2\gamma^2} \tag{4.2}$$

T is one of the important parameters to be considered when talking about the quantum mechanical tunneling effect. It depends on the total energy of the particle, the height, and the width of the potential barrier, which all define whether the tunneling probability is high enough to be measured experimentally or not.

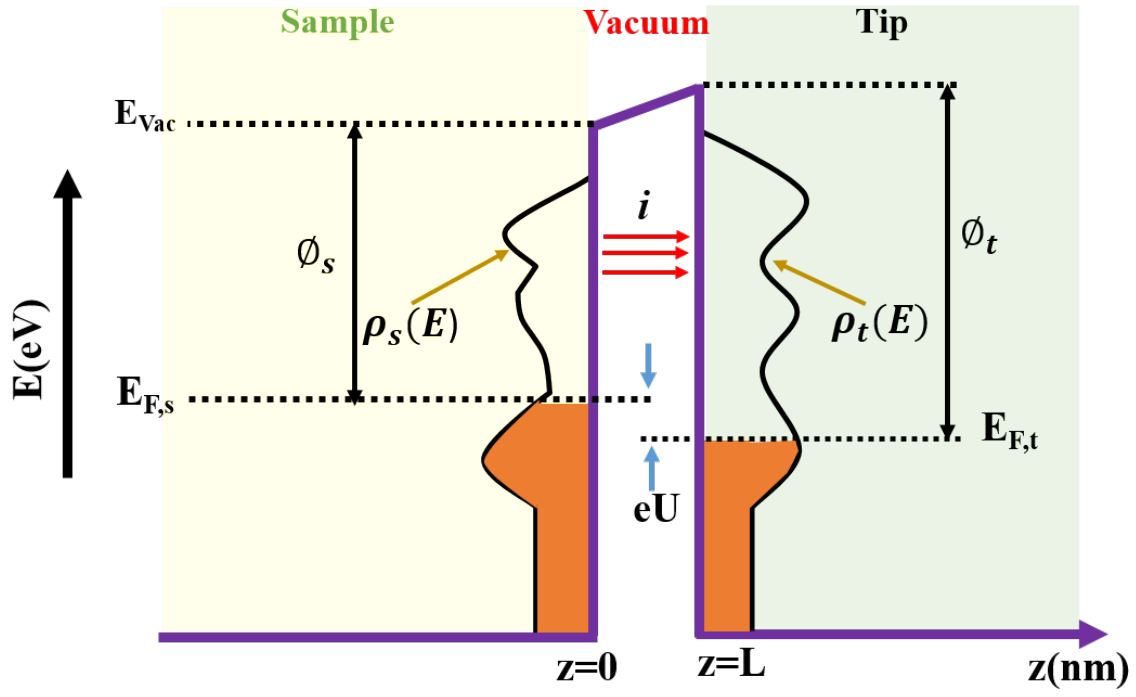

Figure 4.2: Sketch of the tunneling current between the tip and sample using a one-dimensional metal-vacuum-metal tunneling junction approach adapted from Refs. [203, 205]. ϕ_s and ϕ_t is the workfuntion of the sample and the tip, respectively. ρ_s and ρ_t the corresponding density of states and i the tunneling current when a voltage is applied.

STM applies the model described in Fig. 4.1(a) to measure the topography and electronic properties of a sample. The basic principle consists of bringing a sharp

metallic tip very close (~ 1 nm) to the surface of a sample. Thereafter, a DC voltage applied between the tip and the sample leads to a measurable tunneling current. If region I is considered as the sample surface and region III the tip, the tunneling current between the tip and the sample can also be modeled using a one-dimensional metal-vacuum-metal tunneling junction [202, 203, 205], as shown in Fig. 4.2. The model is built assuming that the workfunction (ϕ), which is defined as the energy that one needs to provide in order to remove an electron from a material into a vacuum ($\phi = E_{vac} - E_F$), of the sample is lower than the one of the tip. In Fig 4.2, ϕ_s and ϕ_t are the workfuntions of the sample and the tip, respectively. ρ_s and ρ_t are the corresponding density of states at an energy E, and i the tunneling current when a voltage is applied. As the Fermi energy of the sample is higher than that of the tip, *i.e*, as the sample density of occupied states is higher than that of the tip, if a negative voltage is applied to the sample and a positive to the tip, a current will flow from the sample to the tip.

From the model displayed in Fig. 4.2, the theoretical formula of the tunneling current between the sample and tip was established and is expressed in equation (4.3) [206, 207]. The calculations were introduced by Bardeen in 1961 [206] and were later on extended by Tersoff and Hamann [207] who successfully used them to model the current flowing between a flat metallic surface and a tip.

$$I = \frac{4\pi e}{\hbar} \int_0^{eU} \rho_t(E - eU)\rho_s(E)T(L, \phi, U, E)dE \tag{4.3}$$

With T being the transmission factor.

$$T(L, \phi, U, E) \approx exp\left[-2L\sqrt{\frac{2m}{\hbar^2}}\left(\frac{(\phi_t - E + eU)^{\frac{3}{2}} - (\phi_s - E)^{\frac{3}{2}}}{\phi_t - \phi_s + eU}\right)\right] \tag{4.4}$$

Equation (4.3) shows that the tunneling current between the sample and tip is the convolution of the density of states of the sample, the density of states of the tip, and the transmission factor. As a free-electron metal tip is commonly used to explore the sample in STM, the density of states of the tip can be considered as a constant [203, 205], although this is often not the case. Furthermore, if a very small voltage is applied between the tip and the sample [203, 205], and slight variation in workfunction over the sample surface (change in workfunction less than 100 meV [208]) is measured, the transmission factor can also be considered as a constant. Then, equation (4.3) can

be simplified [203, 205]:

$$\frac{dI}{dU} \approx \rho_s(eU) \tag{4.5}$$

Equation (4.5) shows that the variation of the tunneling current recorded during STM measurements as a function of the applied voltage can be used to approximate the surface density of states (DOS) of the samples. The technique is called scanning tunneling spectroscopy (STS) and has been widely employed to estimate the surface density of states of semiconducting samples [37, 38, 39, 40]. Its working principle will be described below. For an ideal semiconductor material, the dI/dU is zero in the bandgap and non-zero in the conduction and valence bands, which indicates that with STS the bandgap of a semiconducting surface can be measured. The technique might be very useful for the CIGSe solar cell technologies since it can allow researchers to investigate the semiconducting-like properties of the near-surface of the absorbers before the growth of the CdS buffer layer. Furthermore, with its excellent lateral resolution (lateral resolution less than 0.1 nm [199]), STS is a nice tool to study the surface and grain boundary properties in polycrystalline CIGSe. It was already used to demonstrate that the surface of Cu-poor CIGSe that was etched with KCN is metallic and exhibits reduced density of defect states at grain boundaries as compared to grain interiors [37].

STM combines equations (4.3) and (4.5) to image the topography and surface density of states of a sample. While the tunneling current acquired is used to measure the morphology of the sample, its numerical differentiation as a function of the applied voltage is employed to approximate the density of states.

In practice, the setup employs several components including a piezo driver with a very sharp and cleaned conductive tip attached to it, a distance controlling unit, and a computer to explore and acquire the information from the sample surface. The tip aims to scrutinize the sample surface, the piezo driver to control the plane position (x,y) and the tip-sample separation (z), and the distance controlling unit to approach the tip near the sample.

Technically, to image the surface topography and also measure the density of states of a sample, the STM system operates either in constant-height mode or in constant-current mode. In the constant-height mode, the tip is kept at a specific height and

the tunneling current between them is recorded while raster scanning line by line the contour of a sample surface. In contrast, in the constant-current mode the current is maintained constant while adjusting and recording the vertical position of the tip. Although both modes can be used to image the surface properties of a sample, one of the big disadvantages of using the constant-height STM mode is that during this mode the system is strongly affected by the thermal drift and the piezo creep when the measurements are carried out at ambient temperature. With these disadvantages, it is hard to map the DOS of a sample due to the long duration of the measurements, which should be at least 12 h if one would like to have a dI/dU image with an acceptable spatial resolution. The thermal drift due to the heating of the microscope will distort the image. Besides, as the absolute height is kept constant during the whole measurements, this mode is not adequate to explore the properties of polycrystalline samples where the surface is rougher and presents various grains and grain boundaries, which are randomly oriented. Analyzing such samples in constant height STM mode will damage the tip or induce its alteration due to the large topographic changes when scanning over the sample surface. Consequently, the constant height STM mode is recommended to be used for the very flat surfaces and to be performed at low temperatures.

Since the samples analyzed in the framework of this thesis have polycrystalline properties with peak to peak roughness of up to 1 μm, constant-current STM mode (CCM) appears as the most suitable method to be used in order to investigate their surface properties.

A sketch showing the working principle of the constant-current STM mode is depicted in Fig. 4.3. To run the measurements, the user has to initially preset a value for the current via a computer interface. This initial current is called the current-setpoint (I_{set}) and is the current that the setup must keep constant during the whole exploration of the area of interest. The computer communicates the current setpoint to the electronic system, which via an auto-approach gradually moves the piezo driver down (according to the z-axis) till achieving the preset current setpoint. The measurements then start by scanning line by line the region of interest and acquiring the variation in height as a function of position to map the topography of the sample. To measure the variation in height over the surface, the setup first measures the tunneling

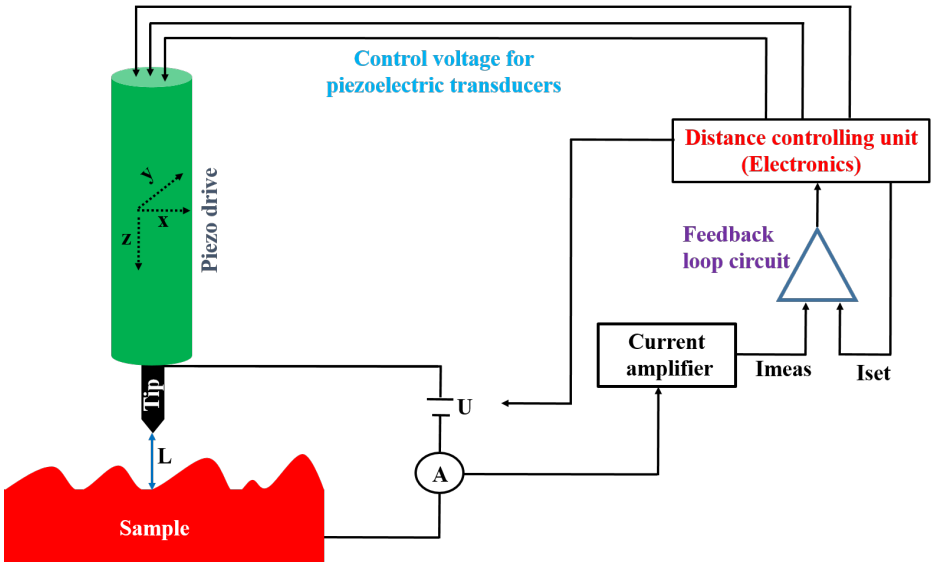

Figure 4.3: Schematic representation of the working principle of STM. U is the dc applied voltage and L the distance between the tip and sample

current (I_{meas}) between the tip and the sample at each specific (x, y) position, and compares the value obtained via a feedback loop to the current value that was set initially (current-setpoint). If the difference between the measured current and the preset current is non-zero, the feedback vertically adjusts the position of the piezo driver until I_{meas}- I_{set} becomes zero. The voltage applied to the piezo driver to cancel I_{meas}- I_{set} is then recorded and displayed on a computer as the topography of the sample surface.

Scanning tunneling spectroscopy

As previously indicated, to measure the density of states of a sample with STS, the tunneling current between the tip and the sample has first to be recorded for a specific range of applied voltage. Afterwards, the density of states is obtained by numerical differentiation of the current with respect to the applied voltage U. To do so, at each specific (x, y) position or pixel a ramp voltage (see Fig. 4.4) needs to be applied to the tip-sample junction. For each area of interest, a grid with a well-determined number of pixels is defined and a range voltage is set (U_{start} and U_{end}). The ramp voltage has to be higher than the bandgap in the case of semiconductor materials if one would like to resolve their bandgaps. At every single pixel, the voltage is ramped from U_{start} to U_{end} and the *I-U* current spectra are acquired. For a semiconductor material, in order

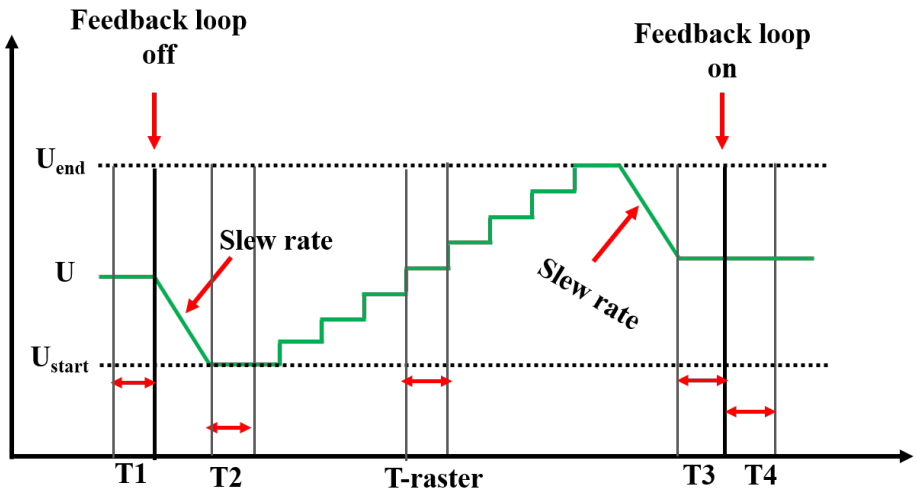

Figure 4.4: Principle of the acquisition of a single point spectroscopy data. T1, T2, T3 and T4 are the different waiting time. T-raster is the time distance between two consecutive data points of the *I-U* signal

to see the bandgap of the material the ramp voltage has not only to be large but also U_{start} should be negative when U_{end} is positive or the way around because the Fermi position corresponds to the zero voltage. The data are acquired by scanning line by line or pixel by pixel the surface of a sample. During the acquisition of the very first line data, the feedback loop is switched on and the topography information is recorded. After this, the tip is moved back to its initial position and the feedback loop used for maintaining a constant current for topography imaging is switched off in order to keep constant the tip-sample separation while acquiring the *I-U* spectrum. A schematic representation of how an *I-U* signal is obtained is shown in Fig. 4.4. At the waiting time T1, the gap voltage U employed while recording the topography signal changes to U_{start}, after that the tip moves (with a predefined slew rate) to T2 where the system gets ready to perform the first point spectroscopy. It is important to note the use of appropriate T1 and T2 is crucial for the stabilization of the measurements. Using inappropriate values for these parameters induce artifacts in the *I-U* signal. After T2, the ramp voltage is applied and the first single point spectroscopy is recorded. The T-raster is the time distance between two consecutive data points of the *I-U* signal. After recording the first *I-U* signal, the feedback loop is switched on at T3 and additional time T4 is needed before the tip passes to the next pixel where the same algorithm will be repeated. The repetition of the above described procedure

all over the surface of the region of interest will enable the acquisition of the current imaging tunneling spectroscopy (CITS) data, which afterwards can be numerically differentiated as function of voltage for density of states mapping or spectra. In Table 4.1, an example of CITS parameters used in the framework of this thesis is given.

Table 4.1: CITS parameters used to investigate the surface of CIGSe.

U_{start}	U_{end}	slew rate	T1	T2	T3	T4	T-raster	points
V	V	V/s	ms	ms	ms	ms	ms	a.u
-2	2	18	150	10	10	200	3	200

Atomic force microscopy

Since the tunneling current is the quantity that is measured in STM, the technique only works for semiconductor or metallic materials. It could not be used to investigate the topography of thick insulating materials. Hence, to overcome this limitation and thereby also explore the surface properties of insulators, AFM was developed in 1986 [209]. The method is based on the force interaction between the tip and the specimen and was successfully employed to analyze the properties of both conductor [210] and insulator surfaces [211] on the atomic scale. A schematic representation showing how AFM works is displayed in Fig. 4.5. The tool uses a sharp tip attached to a flexible cantilever to explore the properties of a sample. The tip interacts with the specimen. A laser beam from the diode is reflected off from the rear surface of the cantilever and the reflected light is measured with a photodetector. When the tip scans the surface of the sample, the interaction force that exists between the tip and the sample causes the cantilever to deflect. The cantilever deflections are detected by a photodiode and are used to map the surface properties of the sample.

The measurements can be carried out in several modes such as the contact mode, the tapping mode, and the noncontact mode. These different operations modes are visualized in Fig 4.6. The curve is divided into three main parts. The first part represents the region where the tip and the sample are brought in contact. It is also called the repulsive regime and is highlighted by green color in Fig. 4.6. The second part (region highlighted in yellow) commonly called the attractive regime is the region

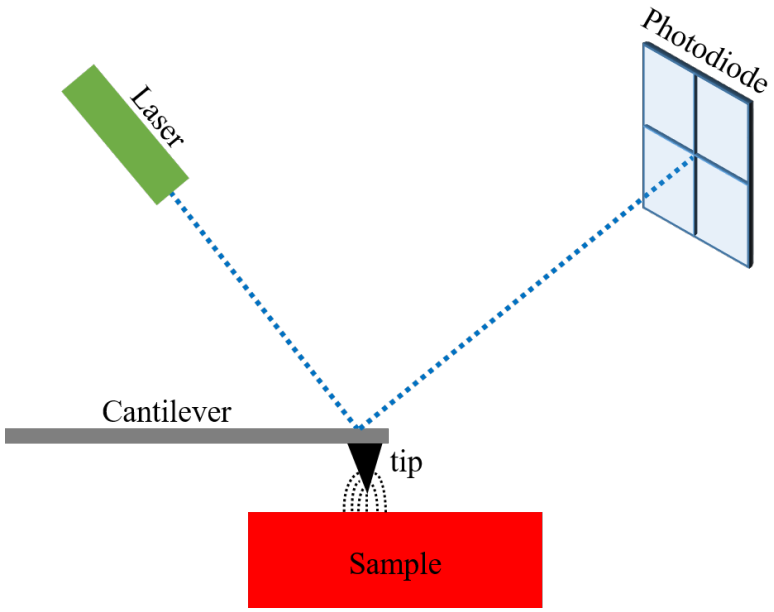

Figure 4.5: Schematic of the beam-deflection in the atomic force microscopy setup.

where the tip-sample separation is a bit larger (L ∼1 nm). The third part is the region between the attractive and repulsive regimes.

In contact mode (CM) - AFM, the setup works in the repulsive regime. The probe and the specimen are in perpetual contact while the probe scans the sample surface. Thereby, by keeping a constant tip-sample separation or a constant force between the tip and the specimen, and recording the change in height of the probe deflection while scanning the contour of the area of interest, the surface topography of a sample can be acquired. The mode works perfectly on soft materials like polymers but one of its main disadvantages is that as the probe is in direct contact with the sample during the whole measurements, the sample can be damaged or the tip can easily be broken.

In tapping mode (TM) - AFM, the measurements are conducted in the both repulsive and attractive regimes. The probe vibrating at or close to its natural resonance frequency is brought near the sample and regularly touches it at different specific intervals. When the tip approaches the sample surface, the vibrating amplitude varies due to changes in the force that exists between the tip and the sample. These changes in amplitude, while keeping the resonance frequency of the cantilever constant, are recorded and used to determine the surface topography of a sample. Although the mode is less destructive compared to the CM - AFM [212], as the tip intermittently

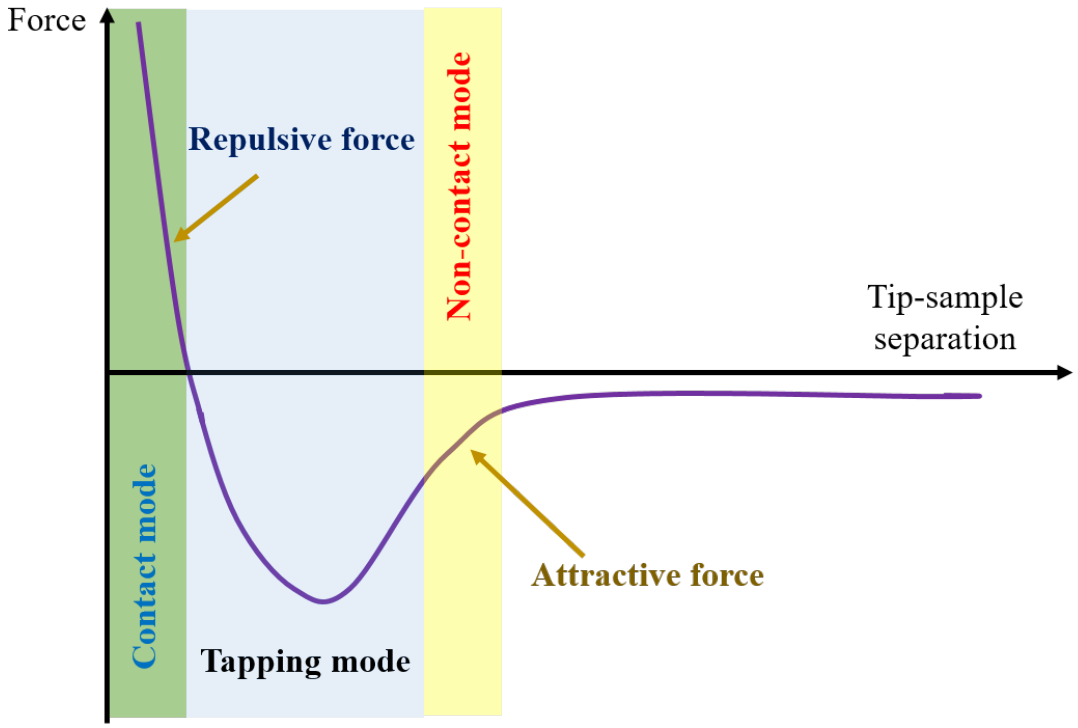

Figure 4.6: Variation of the interaction force between the tip and the sample as a function of the tip-sample separation along with the corresponding AFM operation mode adapted from Refs. [202, 212].

touches the sample surface, the probability to break it or to damage the sample is not zero.

In Noncontact (NC) - AFM (also called dynamic mode), the measurements are carried out in the attractive regime. In this mode, the tip oscillates a bit far away from the sample surface and does not touch the sample during the measurements, which suggests that the probability to break the tip or damage the sample during NC - AFM is reduced compared to CM and TM - AFM. Since NC - AFM is the AFM mode used in the framework of this thesis, its theoretical background and basic working principle are discussed in more detail in the following. Detailed information regarding the CM and TM - AFM can be found in Refs. [202, 212].

As indicated above, the NC - AFM operates in the dynamic mode. The cantilever is mechanically excited and its natural resonance frequency f_0, which depends on both the spring constant k and the mass m of the cantilever can be written as [202, 212, 213]:

$$f_0 = \frac{1}{2\pi}\sqrt{\frac{k}{m}} \tag{4.6}$$

Due to the force acting between the tip and the sample, when the tip approaches the sample the vibration amplitude of the cantilever changes inducing thereby a change in spring constant of the cantilever [213].

$$k' = k - \frac{\partial F_{ts}}{\partial z} \tag{4.7}$$

where $\frac{\partial F_{ts}}{\partial z}$ is the force gradient that interacts between the tip and the sample and z the distance between the tip and the sample.

Taking this into account, the resonance frequency can be re-written as :

$$f' = f_0 \sqrt{1 - \frac{1}{k}\frac{\partial F_{ts}}{\partial z}} \tag{4.8}$$

Equation (4.7) and (4.8) clearly show that the spring constant as well as the corresponding resonance frequency are not constant anymore. The two quantities depend on the force gradient between the tip and the sample. If the force gradient is small compared to the natural spring constant of the cantilever [214, 215], equation (4.8) will become:

$$f' = f_0 \left(1 - \frac{1}{2k}\frac{\partial F_{ts}}{\partial z}\right) \tag{4.9}$$

This leads to:

$$\Delta f = f' - f_0 = -\frac{f_0}{2k}\frac{\partial F_{ts}}{\partial z} \tag{4.10}$$

The variation of the resonance frequency (Δf) is proportional to the force gradient between the tip and the sample. The topography is being built up by keeping Δf constant.

To use this change in frequency Δf of the cantilever to measure the surface topography of a sample, two distinct NC - AFM modes can be employed: the amplitude mode (AM) and the frequency modulation (FM) mode. In the AM-mode, the change in the vibration amplitude induced by Δf is measured and is used to map the topography of the sample [216], whereas, in the FM mode, the Δf itself is directly quantified [217]. Although the two modes can be employed to study the surface properties of a sample, note that FM mode provides a higher accuracy and better lateral resolution [215], especially, when the measurements are performed in vacuum as it is the

case in this thesis. The mode is highly sensitive to tip-sample force interaction and presents a better signal-to-noise ratio [217]. Thus, frequency modulation is the NC operation mode employed in the framework of this thesis. While the noncontact FM - AFM mode is used to measure the topography, the noncontact FM - kelvin probe force microscopy mode is employed to measure the workfunction of the samples. However, in contrast to AFM where the cantilever is mechanically excited and the Van der Waals (VdW) force is quantified, the electrostatic force is measured in KPFM. The cantilever is electrically excited to disentangle the VdW force from the electrostatic and thereby avoiding the crosstalk between the topography and workfunction signals. In the next section, a model describing how the workfunction is acquired in KPFM is presented. Afterwards, the theoretical and technical implementation of this powerful tool, which allows simultaneous mapping of the topography and workfunction with nanometer resolution are introduced.

Kelvin probe force microscopy

In KPFM, the workfunction of a sample surface is measured by first acquiring the contact potential difference (CPD) between a sharp conductive tip and a sample. The technique was developed in 1991 [218] and was broadly used to measure, with nanoscale resolution, the workfunction of semiconductor surfaces [219, 220, 221] and several other semiconductor devices [222, 223]. In Fig. 4.7, a model showing how the CPD is determined in KPFM is displayed. In Fig. 4.7(a), the tip and sample with different workfunction are not in electrical contact. Their vacuum positions are identical and the workfunction of the sample is assumed to be lower than that of the tip. Therefore, if both materials are electrically brought into contact, electrons will flow from the sample to the tip until the Fermi levels are aligned. The charges transferred between them create a potential difference also called contact potential difference V_{CPD} at the tip/sample interface as can be seen in Fig. 4.7(b). The resulting contact potential difference is proportional to the workfunction difference between the tip and the sample and can be compensated by applying an external DC reverse voltage [Fig. 4.7(c)] [224].

$$V_{CPD} = \frac{\phi_s - \phi_t}{e} \tag{4.11}$$

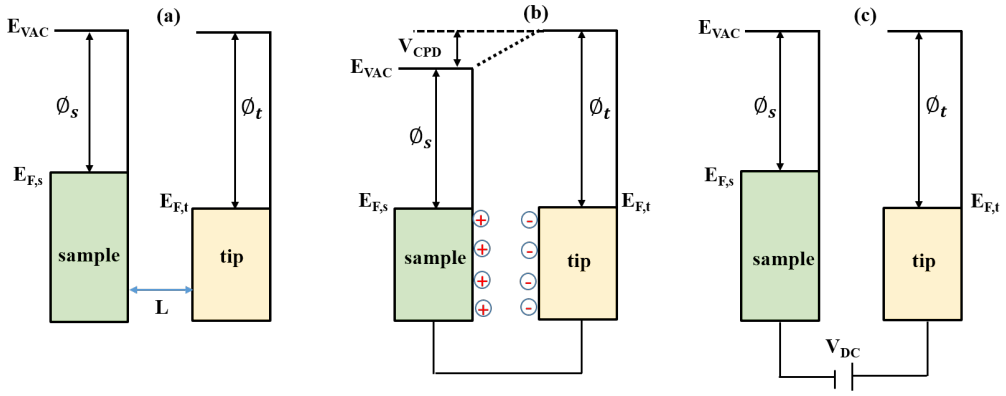

Figure 4.7: A model describing how the contact potential difference (CPD) is measured in KPFM adapted from Ref. [224]. (a) sample and tip are not in contact, (b) the two materials are brought in contact and a CPD is created between them, (c) an external DC reverse voltage (V_{DC}) is applied between the sample and the tip to cancel the CPD. When CPD= 0 V the V_{DC} applied to cancel it is recorded and is employed as a feedback signal to map the workfuntion difference between the tip and the sample. $E_{F,s}$, $E_{F,t}$, E_{VAC}, ϕ_s and ϕ_t are the Fermi level of the sample, the Fermi level of tip, the vacuum level, the workfunction of the sample, and the workfunction of the tip, respectively.

ϕ_s, ϕ_s and e are the workfunction of the sample, the workfunction of the tip and the elementary charge, respectively.

The external DC voltage (V_{DC}) applied to cancel the V_{CPD} is recorded as the workfunction difference between the sample and the tip. Thus, if the workfunction of the tip is known, the one from the sample can be extracted using equation (4.11).

There are two fundamental ways of applying a DC voltage in order to measure the CPD between the sample and the tip in KPFM: The AM mode and the FM mode KPFM [215]. In the AM mode KPFM, the electrostatic force between the specimen and the tip is minimized, while in the FM mode the electrostatic force gradient is minimized [225].

As previously indicated, FM - KPFM is the operation mode employed in the framework of this thesis. The technique provides credible workfunction values and better lateral resolution [226, 227] as compared to AM - KPFM. During the analyses, the results are less affected by the measurement artifacts due to the large size of the cantilever [226, 227]. The CPD obtained is recorded right underneath the tip apex

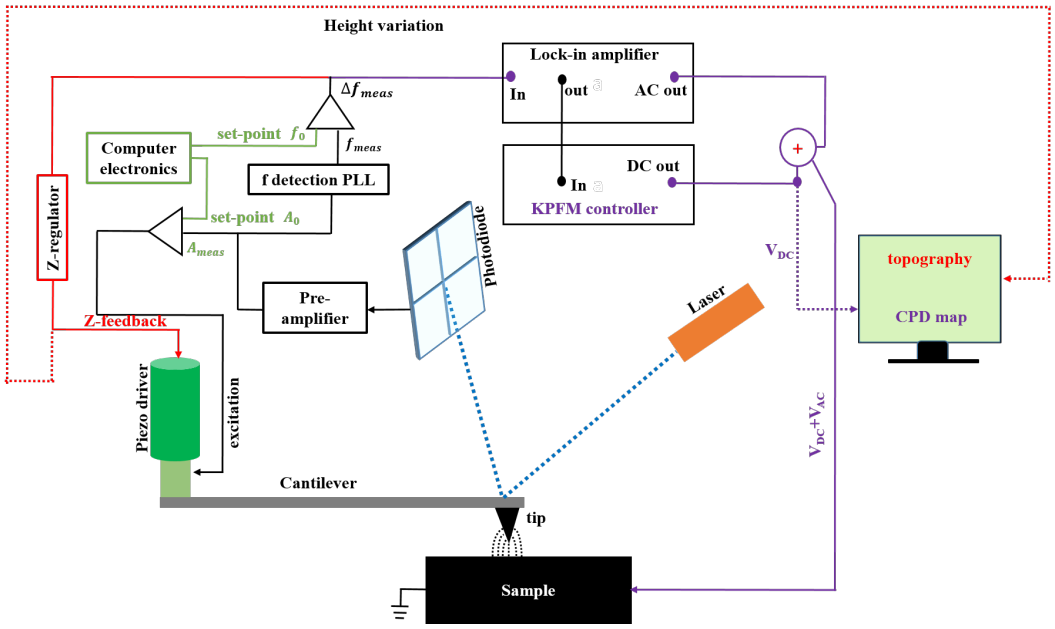

Figure 4.8: Simplified schematic showing how the FM - AFM topography and KPFM workfunction map are measured in this thesis. The sketch is adapted from Refs. [64, 228]

[226, 227]. Hence, by replacing the VdW force F_{ts} in equation (4.10) by the electrostatic force F_w obtained after applying a combination of DC and AC voltages between the tip and the sample and after considering the sample-tip system as a parallel plate capacitor, Δf in KPFM can be written as [215, 225]:

$$\Delta f \approx \frac{\partial F_w}{\partial z} = \frac{\partial^2 C}{\partial z^2}(V_{DC} - V_{CPD})V_{AC}\sin(wt) \tag{4.12}$$

Where $\frac{\partial^2 C}{\partial z^2}$ is the second derivative of the capacitance and $V_{AC}\sin(wt)$ the AC voltage that was applied to electrically excited the tip.

The frequency variation Δf expressed in equation (4.12) is the quantity that is measured in frequency modulation operation mode KFPM. As can well be seen, when the external reverse DC voltage applied is equal to the contact potential difference V_{CPD}, the amplitude of Δf oscillating at w becomes zero, which suggests that the force gradient that was acting between the tip and sample was nullified. Therefore, the V_{DC} applied to cancel the force gradient is recorded and is displayed as the workfunction difference between the sample and the tip. A simplified schematic showing how the FM - AFM topography and KPFM workfunction map are acquired in this thesis is depicted in Fig. 4.8.

For the FM - AFM measurements, the cantilever is mechanically excited a few μm away from the sample surface and its fundamental resonance frequency f_0 and set-point amplitude A_0 are detected. When it approaches the sample and starts to interact with the sample surface, the VdW force acting between the tip and sample causes the cantilever to deflect inducing thereby a shift of its resonance frequency as well as a change in the oscillation amplitude, as shown in equation (4.10). All these changes will therefore vary the location of the laser beam on the position sensitive detector (PSD). The new position of the laser is detected as an input signal, *i.e*, the measured amplitude A_{meas} and frequency f_{meas}, and is later on amplified via a pre-amplifier. Afterwards, while the measured amplitude A_{meas} is compared to the preset value A_o and is maintaining constant using an amplitude regulation system, a phase-locked-loop (PLL) measures the difference between the f_{meas} and f_0 (f_{meas}-f_0) and send the values obtained to a feedback loop, which varies the piezo driver until f_{meas}-f_0 becomes zero. This variation will induce a change in height of the piezo materials, which is acquired and is displayed on a computer as the topography image of the sample.

For the FM - KPFM measurements, except for the fact the cantilever is electrically excited and an additional look-in amplifier is needed to apply external voltages (AC+ DC) to the cantilever in order to quantify the contact potential difference, the approach is similar. The lock-in amplifier records the measured Δf from the PLL as input data and sent it to the KPFM controller unit, which acting as a feedback loop in this case continuously applied a DC voltage to cancel the lock-in amplifier out signal. The resulting DC voltage applied is then recorded and is displayed on a computer as the workfunction difference between the tip and the sample.

4.1.2 X-ray photoelectron spectroscopy

In this section, the theoretical and working principles of XPS is shortly presented. For a broad knowledge about the XPS technique, readers are highly recommended to refer to works presented in Refs. [229, 230, 231]. XPS is based on the photoelectric effect, a phenomenon where an electron is released from the specimen after interaction with light of energy much higher than its binding energy and the workfunction of the sample. In this method, a sample is bombarded with an X-ray source. The X-ray photons interact with the material and transfer their energies to core electron. The

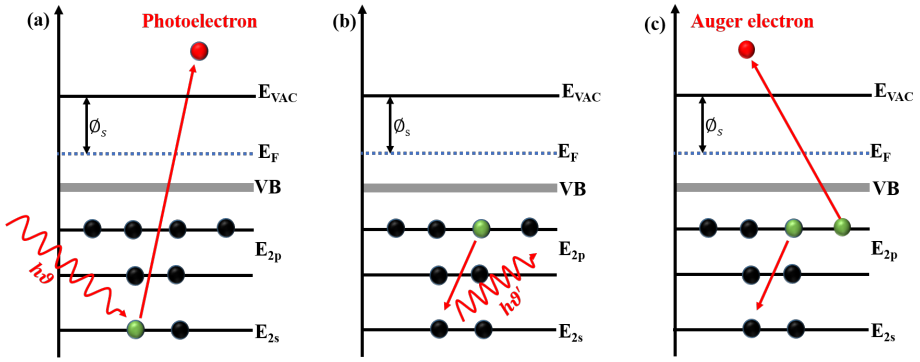

Figure 4.9: Schematic representation of how a photoelectron and how an Auger electron are generated in XPS adapted from Ref. [229]. (a) extraction of a photoelectron from the sample, (b) relaxation of another electron from a higher energy core level and emission of a photon with energy $h\nu'$ and (c) creation of an Auger electron.

electrons with enough energies escape the atom and the sample as shown in Fig. 4.9(a). In Fig. 4.9(a), the green, black and red spheres stand for the holes, the electrons, and the escaped electrons also called photoelectrons. The kinetic energy (KE) of the ejected photoelectrons can then be measured and its corresponding binding energy (E_B) determined via the following formula [229, 230].

$$KE = h\nu - E_B - \phi_s \tag{4.13}$$

In equation (4.13), h is the Planck constant, ν is the frequency of the photon, and ϕ_s is the workfunction of the sample. As the binding energy of electrons is element dependent, measuring the E_B of electrons can help to determine the elemental or chemical composition of the sample. After the emission of a photoelectron, another electron from a higher energy core level can relax into the hole left behind releasing thereby new photon energy $h\nu'$, as depicted in Fig. 4.9(b). This newly created photon energy can then be transferred to another core level electron (the Auger electron), which is also emitted from the sample, as depicted in Fig. 4.9(c).

Practically, the released photoelectrons are detected and counted by a spectrometer. During the measurements, the spectrometer and the specimen are in electrical contact, the Fermi positions of the two materials are aligned as graphically shown in Fig. 4.10 [229, 230, 231]. The alignment of the Fermi levels leads to a reduction of the energy that an electron has to overcome to reach the detector by $\Delta\phi = \phi_{sp} - \phi_s$, where

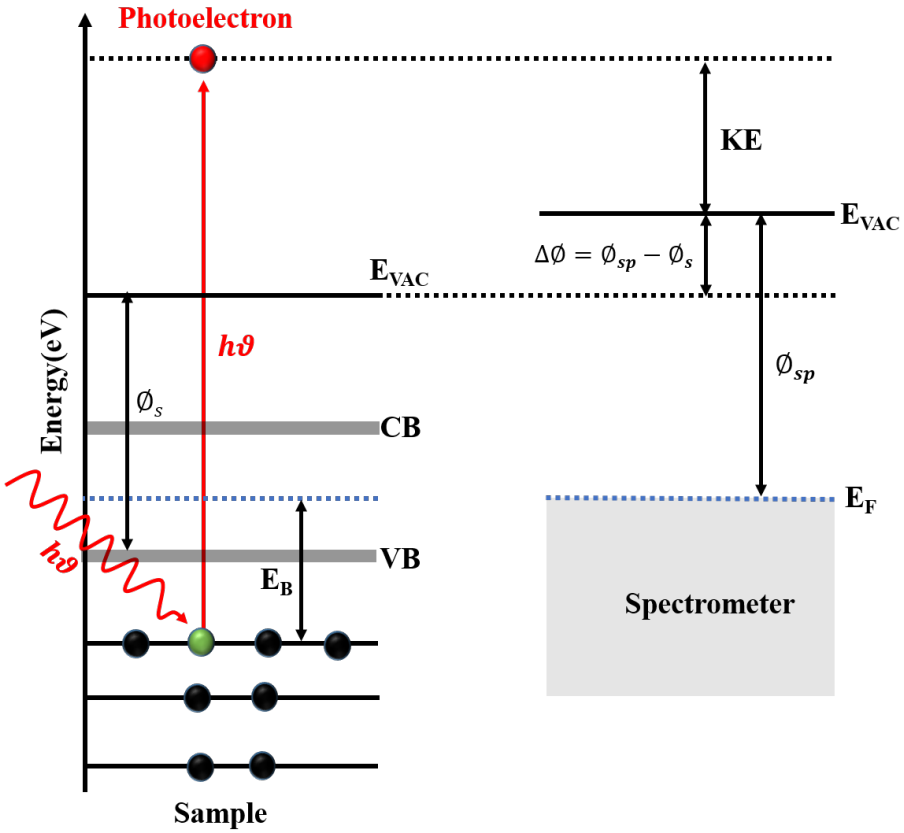

Figure 4.10: Simplified representation of XPS system when the sample and the spectrometer are in electrical contact adapted from Ref. [229].

ϕ_{sp} is the workfunction of the spectrometer [229, 230, 231]. Introducing the variation $\Delta\phi$ of the workfunction in equation (4.13) gives:

$$KE = h\nu - E_B - \phi_{sp} \tag{4.14}$$

Equation (4.14) is the theoretical formula that is applied while running XPS analyses. As can well be seen, if the workfunction of the spectrometer is known, the kinetic energy of the sample can be measured. In general, Cu, Ag, and Au metal samples are used to calibrate the spectrometer or to determine ϕ_{sp}. After measuring the workfunction of the spectrometer, it can be assumed to remain constant as long as the spectrometer is kept in ultra high vacuum (UHV) [231].

Basic working principle of XPS

As indicated above, in XPS, photoelectrons escaped from the sample after interacting with the x-ray source. Those photoelectrons are then detected and counted depending

on their kinetic energy. The instrument consists of an X-ray tube and a spectrometer, as shown in Fig. 4.11. Two main X-ray sources are commonly used. The Mg Kα source with an incident energy of 1253.6 eV and the Al Kα source with an incident of 1486.6 eV. Once the x-ray irradiates the sample, a part of it is lost in form of heat, whereas the other part is transferred to core level electrons in the sample. Afterwards, electrons with an energy higher than their binding energies and the workfunction of the sample escape from the sample. The released electrons are detected and their corresponding kinetic energies are measured by a spectrometer, which is composed of electron optics, a kinetic energy analyzer, and a detection system (CDD camera). The optics aim to decelerate the incoming electrons, the analyzer (composed of one inner and one outer hemisphere) to select electrons as a function of their kinetic energy, and the detector to count the incoming electrons. Combining the kinetic energies

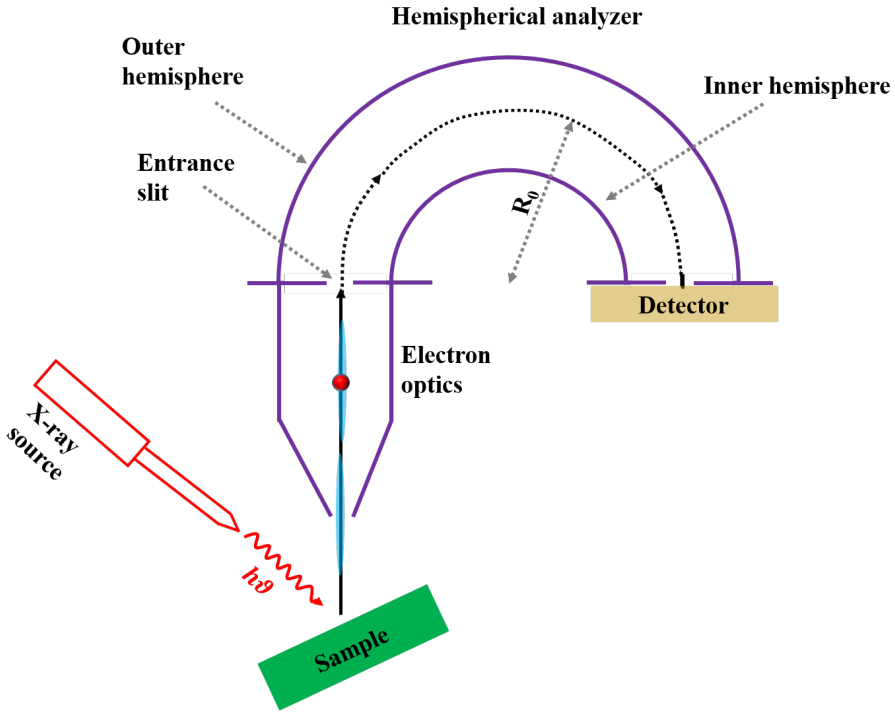

Figure 4.11: Schematic depiction of an electron spectrometer along with the x-ray source.

recorded and the total number of electrons acquired, the valence band offset as well as the chemical composition of the sample can be determined [229, 230, 231]. After experimentally acquiring the valence band spectra, a linear extrapolation approach can be used to extract their numerical values [40]. Concerning the quantification, the

experimental spectrum of the core level element of interest has to be fitted using an appropriate function. Before fitting, a background subtraction of the signal originating from the inelastic scattering electrons is needed [229]. After the fitting process, the area as well as the binding energy position of the fitted curve are extracted and used to estimate the samples chemical composition [229].

The chemical sensitivity of XPS technique makes it one of the most suitable tools to investigate the change in the elemental and chemical composition of samples containing several elements such as CIGSe. XPS has been already used to explore the changes in valence offset and elemental composition of the bare CIGSe and the CIGSe samples after various chemical treatments such as KCN etching [98], the growth of the CdS buffer layer [34], or after the alkali PDT treatments [32, 134, 232, 233].

4.1.3 Secondary ion mass spectroscopy & Raman spectroscopy

As indicated earlier, to better understand the SPM results, supplemental analyses with the SIMS and the Raman techniques were carried out. With both methods, the different elements and segregated phases that exist at the specimen surface were studied.

As its name indicates, during the SIMS measurements, secondary ions (positive or negative) escaped from the samples are used for the exploration of the surface composition. The basic principle can be described as followed. The primary ions (PIs) with energy in order of a few keV are shot into the sample [234]. Due to the interaction of PIs with the specimen, secondary ions with diverse masses related to the elements present in the sample are created and detected by a mass spectrometer. As each measured mass corresponds to one specific element that exists at the surface of the sample, their reconstruction can be used to map the sample surface composition. Further information regarding the SIMS technique can be found in [234, 235].

The Raman method is based on inelastic scattering of the light while interacting with a sample. When light interacts with a specimen, it can be scattered at the same energy as the incoming light or at a different wavelength than the incoming light [236]. The latter case is used in Raman measurements to determine the different segregated phases that exist at the surface of a sample. During the analyses, if the sample exhibits various phases, the setup will detect different wavelengths with each

of them that corresponds to one specific precipitate present at the sample surface. Hence, depending on how many wavelengths are obtained the number of phases can be measured. The tool was widely used to study the different compounds present at the surface of the bare or PDT CIGSe samples [138, 237].

4.2 Sample fabrication

The solar cell absorbers that are analyzed in the framework of this thesis are polycrystalline CIGSe. They are deposited on molybdenum-covered SLG substrates via a physical vapor deposition system and by using a co-evaporation process. The investigations are carried out on three types of samples: the over stoichiometric CISe samples, the Cu-poor CIGSe pristine samples as well as the Cu-poor CIGSe that were post-treated with NaF and NaF+RbF. The stoichiometric samples also called Cu-rich samples refer to CIGSe, which have a Cu/(In+Ga) or Cu/In ratio for Ga free samples higher than one [100], whereas the CIGSe is considered as Cu-poor absorbers when this ratio is lower that one [238]. The CISe samples were grown via single-stage co-evaporation process at a nominal substrate temperature of 580°C (as estimated with a pyrometer) and the Cu-poor pristine and PDTs treated samples using multistage low temperature (∼450 °C) co-evaporation process. The PDT treatments were performed *in - situ* and directly after the deposition of the CIGSe absorber. The NaF samples were prepared by evaporating NaF into the CIGSe matrix (for 20 minutes) at a substrate temperature of ∼ 280 °C and in the Se atmosphere [52]. A similar procedure was followed for NaF+RbF PDT samples. However, in this case, the samples were first post-treated with NaF and thereafter with RbF. Details of the deposition process and PDT treatments can be found elsewhere [52, 100, 238, 239].

Since the aim was to investigate the surface and grain boundary properties of the samples, the Cu-rich CISe absorbers were etched with KCN in order to remove the Cu_xSe secondary phase from the front surface. In addition, to study the rear surface properties of the samples, they were mechanically exfoliated from their original substrates. In order to remove the residual fluoride from the surface of samples of NaF and NaF+RbF samples, the films were rinsed with distilled H_2O and 1 molar solution of NH_4OH, respectively.

The following sections focus on sample preparation and measurements details.

4.3 Experimental details

4.3.1 Sample preparation

- **KCN etching of the front surface of Cu-rich CISe**

The Cu-rich CISe films investigated in this work were grown in the Laboratory for Photovoltaics of the University of Luxembourg. In order to wash away the Cu_xSe secondary phase from the front surface, the absorbers were etched with KCN (10 wt% KCN in H_2O, 300 seconds) and extensively cleaned with distilled water in line with literature [106]. Pinholes observed in the absorber layer after KCN cleaning [see Fig. 5.1(b)] exhibit that the Cu_xSe precipitates have been washed away with the treatment. With the surface still covered with deionized water, the absorbers were immediately introduced in an N_2-filled glovebox ($H_2O < 1$ ppm; $O_2 < 1$ppm). However, before introducing the samples into the glovebox, they were first dried into the glovebox anti-chamber by pumping and refilling it several times with N_2 to ensure that the resulting surface was free or at least had a low amount of oxygen and contamination from ambient conditions. Afterwards, a suitable vacuum suitcase was used to transfer the samples into the UHV SPM machine without any longer exposing them to air. The alike approach was followed for the XPS and PL analyses. Furthermore, to investigate the impact of Cd in-diffusion on the electronic properties, the KCN etched absorbers were chemically treated with Cd ions. To conduct the treatment, 2 mM of $CdSO_4$ were dissolved in 1.5 M ammonia (NH_4OH). Afterwards, the solution was poured into a double jacketed glass reactor preheated to 67 °C. Thirty seconds later, the KCN etched films (which were cleaned extensively with H_2O) were introduced into the mixed solution for three minutes. The treatment is called cadmium pre-electrolyte treatment (CPE) in the framework of this thesis. Subsequently, the absorbers were removed from the CPE solution and were also extensively rinsed with distilled H_2O and transferred in the SPM, PL, and XPS spectrometer machines following a procedure similar to the one described above. Concerning the UHV annealing process, it was carried out as detailed in Ref. [40]. The samples were annealed to 280°C and in the time of heating, the base pressure in the UHV machine did not surpass 2×10^{-9} mbar.

- **Exfoliation of the rear surface of Cu-rich CISe**

In order to analyze the rear surface of the Cu-rich CISe, the samples were exfoliated from their original substrates. A schematic representation showing how the peel off process was done is displayed in Fig. 4.12. The absorbers were glued to clean fluorine doped tin oxide covered SLG substrates using an UHV well suited Ag epoxy glue.

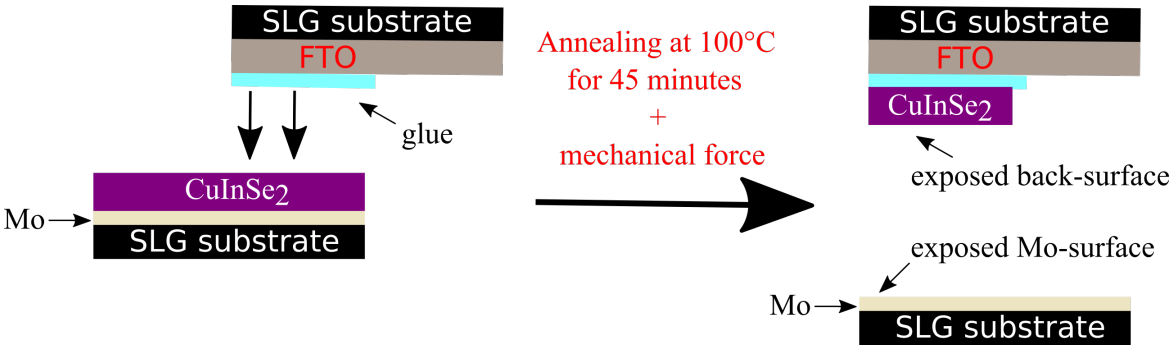

Figure 4.12: Schematic representation of the peel off process of the CISe films. First, a fluorine doped tin-oxide covered glass substrate was glued on top of the CISe films. After heating and application of mechanical force an exfoliation at the $MoSe_2$/CISe interface could be achieved. The peel off was performed in a N_2 filled glovebox to avert oxidation. *The Figure was extracted from the Boumenou et al. paper [208] and was reproduced with the permission of the Wiley © 2020.*

Afterwards, they were cured in air on a hot plate at ∼100 °C for 45 minutes and were introduced into a nitrogen filled glove box ($H_2O < 1$ ppm; $O_2 < 1$ ppm) where they were mechanically peeled off. After the exfoliation process, the samples were investigated using a combination of STM/STS, KPFM, XPS, energy dispersive X-ray (EDX), photoluminescence (PL), and X-ray diffraction (XRD) characterization methods. The samples were transferred from the N_2 filled glovebox to the SPM system via a vacuum suitcase without exposing them to air. The alike approach was applied to the XPS study. PL and EDX analyses were carried out in ambient conditions therefore a minuscule air exposure could not be bypassed. For the PL investigations, the time between exfoliating and measuring was roughly ten minutes.

Regarding the XPS analyses, the films were glued in Luxembourg and then shipped to Münster in an N_2-filled and hermetically sealed sample container. The absorbers were anew introduced into a N_2 filled glovebox, which was attached to the UHV

machine. The films were exfoliated in this box and immediately transferred into the XPS system. Hence, the rear surface was exposed to N_2 just for a few minutes. Since only one sample could be loaded at a time, the Mo-surface was retained in N_2 and transferred into UHV the next day.

- **Cleaning of the CIGSe PDT samples**

The NaF and NaF+RbF samples explored in this thesis were grown at the Swiss Federal Laboratories for Materials Testing and Research (EMPA) using multistage low temperature coevaporation process. Immediately after growth, they were shipped in a nitrogen sealed transport box to the scanning probe microscopy (SPM) laboratory of the University of Luxembourg and were introduced into a N_2 filled glove box ($H_2O \leq 1$ ppm, $O_2 \leq 1$ ppm) within the same day to minimize any exposure to air or moisture. In Luxembourg, to remove the residual fluoride from the surface, the samples were inserted in a N_2 purged glove bag, attached to the load lock of the glovebox and were consecutively rinsed with distilled water and 1M diluted solution of ammonia. The purging procedures conducted by pumping and refilling the glove bag with N_2 were performed several times to make sure that at the end the bag will be free of oxygen or any other contamination from ambient conditions. After rinsing the samples, they were directly transferred back into the N_2 filled glove box and were prepared for the STM/STS, XPS, KPFM, SIMS, and Raman measurements.

4.3.2 Measurements details

Before moving forward, note that all the STM/STS, as well as the XPS/UPS measurements detailed in the following, were conducted in a variable temperature ultra-high vacuum system with a base pressure in the 10^{-11} mbar range. The STM/STS analyses were performed employing chemically-etched tungsten tips, which were cleaned in-situ on a clean Au substrate prior to the investigation of each sample. The XPS system was calibrated on clean single-crystal metal surfaces anterior to the investigations of the samples. Al K_α and He I&II sources were employed for the XPS and UPS, respectively. To measure the workfunction of the samples, tips were calibrated on a highly oriented pyrolytic graphite (HOPG) sample. To ensure that the workfunction of the tips did not change during measurements, the calibration was done before and after

each analysis. Furthermore, the compensated DC voltage was applied to the sample for the KPFM measurements conducted in UHV and to the tip for the ones carried out in N_2.

- **Analysis details of the front surface of CISe**

The local density of states was acquired at several different spots with a scan size varying from 1 to 5 μm. At each area of interest, a 100x100 grid was defined and the DC voltage was ramped from 1.5 V to -1.5 V to measure the local current curves and thereafter derived the local density of states [203, 205]. The elemental composition was measured with XPS using a calibrated Axis Ultra DLD X-ray photoelectron spectrometer. Additionally, the films were sputtered with argon ions with an incident energy of 500 eV inside the XPS machine and re-measured in order to compare the surface and bulk chemical composition. The ion fluence (1×10^{14} ions/mm^2) was chosen such that roughly 5 nm of material was removed from the sample. After sputtering, the findings exhibited a small amount of metallic In, while the Se and Cu binding energies values were unaltered. The quantification reported in Chapter 5 does not involve this metallic contribution of In. However, the compositions obtained after taking into account the metallic In are presented in the Appendix for a comparative study.

The valence band position of the sample after various treatments was studied, as well. The absorbers were sent in N_2 filled shipping box from Luxembourg to Münster. In Münster, they were analyzed with a commercial UHV machine from SPECS equipped with a PHOIBOS 100 hemispherical analyzer.

The PL analyzes were conducted at room temperature. A Laser source with a wavelength of 660 nm, as well as, an incident excitation power of $\sim$10 mW and with a spot size of $\sim$ 2.6 mm were employed. The absorber was climbed on a transfer arm and was inserted into a cryostat, which was pumped down to $\sim 10^{-6}$ mbar. Carrying out PL measurements in such conditions allows acquiring the optical properties of the sample without exposing them to air.

- **Analysis details of the rear surface of CISe**

EDX investigations were carried out on both the front and rear surfaces of the films in order to compare the surface composition of the samples to their bulk compositions.

The measurements were performed at 20 kV, 15 kV, 7kV and 5kV acceleration voltage, and the sample compositions were derived via the well-established ZAF approach [240] without standardization.

Grazing incidence X-ray diffraction investigations were conducted at an incident angle of 1° in a parallel beam configuration. To perform the analyses, the absorbers were first KCN etched in order to remove the Cu_xSe precipitates from the front surface. Afterwards, they were peeled off following the procedure described above.

The effect of the peeling-off process and the Ag epoxy glue on the optoelectronic properties of the absorbers were studied. The measurements were carried out using a custom-built PL imaging system. The area of interest analyzed was $\sim$ 2×2 cm^2 and a pulsed laser source with a wavelength of 532 nm were employed. An InGaAs camera with a high quantum efficiency in the range of 800 nm to 1600 nm was used to collect the emitted PL spectrum. In order to evaluate the PL quantum efficiency and the quasi Fermi-level splitting of the sample before and after cleaving, the system was calibrated to absolute photon numbers.

- **Analysis details of the PDT CIGSe absorbers**

The density of states (DOS) was achieved via current imaging tunneling spectroscopy (CITS) maps at diverse regions of the samples with the aim to get representative data. The measured areas vary from 600×600 nm^2 to $2 \times 2\,\mu$m^2. For each CITS map, a grid of 150 × 150 pixels was set out and the local current-voltage spectra $(I-U)$ were recorded while the feedback loop was switched off. While the DC applied voltage was ramped from +1.3 to - 4 V to probe the surface properties of the water rinsed samples, it was swept from -2 to +2 V after rinsing the sample with ammonia. Subsequently, the DOS, which is proportional to dI/dU [203, 205] was extracted by numerical differentiation of the current I with respect to the applied voltage U. Regarding the XPS measurements, an Al K_α x-ray source was used to investigate the change in the chemical composition of samples. To determine the binding energy position of photoemission peaks, the experimental spectra of each element of interest were fitted using the same background and Voigt function with a constant full with half maximum (FWHM). To examine the E_B of In enclosed in the as grown, the water and ammonia rinsed samples, for example, a same background, FWHM and Voigt function were used to fit their respective measured signals. KPFM measurements were

carried in the N_2 environment. The analyses were performed with a Nanoscope V AFM setup operated in FM mode. SIMS measurements were carried out at the Luxembourg Institute of Science and Technology, in Luxembourg, using the Helium Ion Microscopy Secondary Ion Mass Spectrometry (HIM-SIMS) system. We concentrated on the HIM-SIMS setup since it provides as compared to standard SIMS analyses a high lateral resolution (resolution less than 20 nm) [241]. In addition, due to its excellent surface sensitivity [241], the comparison between the results obtained with this powerful technique and to SPM and XPS ones, which are the primary tools employed in the framework of this thesis is favored. For the Raman results, the measurements were conducted in air. The signals were obtained with a Renishaw inVia spectrometer. A laser with a wavelength of 442 nm along with an incident power density of $\sim 700\,\mu\mathrm{W}.\mu m^{-2}$ were used.

Chapter 5

Electronic and compositional properties of the front surface of stoichiometric $CuInSe_2$: The effect of cadmium pre-electrolyte treatment

An in-depth understanding of the changes in surface composition along with their implications on the overall device performances is important for the optimization of CIGSe solar cells. Hence, it is largely accepted in the literature that the presence of cadmium diffusing from the CdS side into the CIGSe, alters the near-surface composition of CIGSe absorbers and thereby improves the junction quality and the power conversion efficiency (PCE). The theoretical explorations [112, 113] and experimental proofs [23] demonstrating that this diffusion process is performed via Cu vacancies present in CIGSe are summarized in section 3.1.2. Nevertheless, as indicated above, the influence of this in-diffusion of Cd atoms on the surface electronic properties of the absorber and thus on the over stoichiometric CISe solar cell might not be fully understood.

In this chapter, the question of whether the absence of Cu-depletion is an intrinsic property of a Cu-rich absorber and how the removal of a Cu_xSe secondary phase via KCN etching alters the Cu-content at the surface are first addressed. Thereafter, the

effect of Cd in-diffusion on the surface electronic properties of the films is critically discussed and is compared to the results achieved from the UHV annealed samples. To investigate the morphology of the samples after KCN etching, a few SEM micrographs were quickly measured and are depicted in section 5.1. This is followed by section 5.2 where changes in surface density of states after different treatments such as KCN etching, cadmium pre-electrolyte treatment (CPE) and ultra high vacuum (UHV) annealing are presented. Furthermore, changes in surface composition and valence band offsets are depicted in sections 5.3 and 5.4, respectively. Section 5.5 focuses on the influence of CPE on the bulk properties of CISe and the last section focuses on the discussion and brief summary of the chapter.

Before moving forward, it is important to highlight that the chapter is a faintly altered version of Boumenou et al.'s article published in Physical Review Materials [158] and was reproduced hither with the permission of the American Physical Society © 2020.

5.1 SEM micrographs

Fig. 5.1 shows a cross-sectional view (a) and plane view (b) of a Cu-rich CISe absorber layer prior to the cadmium pre-electrolyte treatment investigated in this chapter. As

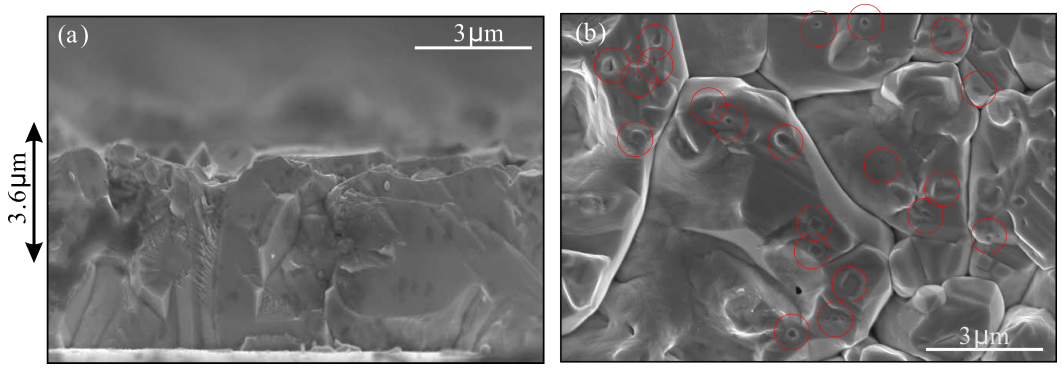

Figure 5.1: SEM micrographs of a Cu-rich absorber etched with KCN. (a) cross-section and (b) plane view. The red circles in (b) depict the positions of the Cu_xSe secondary phase prior to etching.

can be seen, the CISe sample is polycrystalline with well-defined grains and grain boundaries. The film thickness exceeds $3\,\mu$m with peak to peak roughness of up to $1\,\mu$m. In Fig. 5.1(b) clear holes with a diameter of several hundred nanometers can be

observed. These depressions are characteristic of a Cu-rich layer that has been etched with KCN [105]. A characteristic feature of a Cu-rich absorber layer is the extremely large grains of up to 5 μm.

In the following, the study carried out on the front surface of this sample after different chemical treatments such as potassium cyanide etching, cadmium pre-electrolyte treatments, and ultra-high vacuum annealing is presented.

5.2 Electronic properties of the chemical treated CISe surface

5.2.1 Impact of the cadmium pre-electrolyte treatment on the surface density of states

Since the samples analyzed in this section were grown under Cu-excess where a thin Cu_xSe detrimental layer is formed at the surface of the absorbers after the growth, measuring them prior to the KCN etching was not possible. Thereby, they were etched with KCN and were extensively rinsed with distilled water before the measurements. Details of the cleaning process can be found in section 4.3.1.

Fig. 5.2 displays STM topography images of the same absorber after KCN etching [Fig. 5.2(a)] and after CPE treatment [Fig. 5.2(e)]. The corresponding dI/dU-CITS maps at different applied voltages are shown in Fig. 5.2(b-d) for the KCN etched and Fig. 5.2(f-h) for the CPE treated sample. All images were optimized to have the best possible contrast, as indicated by the scale bar below each sub-figure. In Fig. 5.2(b-d) the dI/dU-CITS maps of the KCN etched samples show pronounced granular inhomogeneities, which manifest themselves by changes in the contrast between different grains and within individual grains. Moreover, a reduced dI/dU value at the grain boundaries (GBs) compared to the grain interiors at U=0 V is observed [Fig. 5.2(c)]. These observations are in agreement with the published results by Mönig et al. [37], who attributed the reduced dI/dU contrast to a reduced defect density at the GBs. In a subsequent publication [40] the effect of UHV annealing has been studied and it was found that the inhomogeneities are reduced and the distinct dI/dU contrast at the GBs has disappeared. It was cross checked if the samples analysed in this

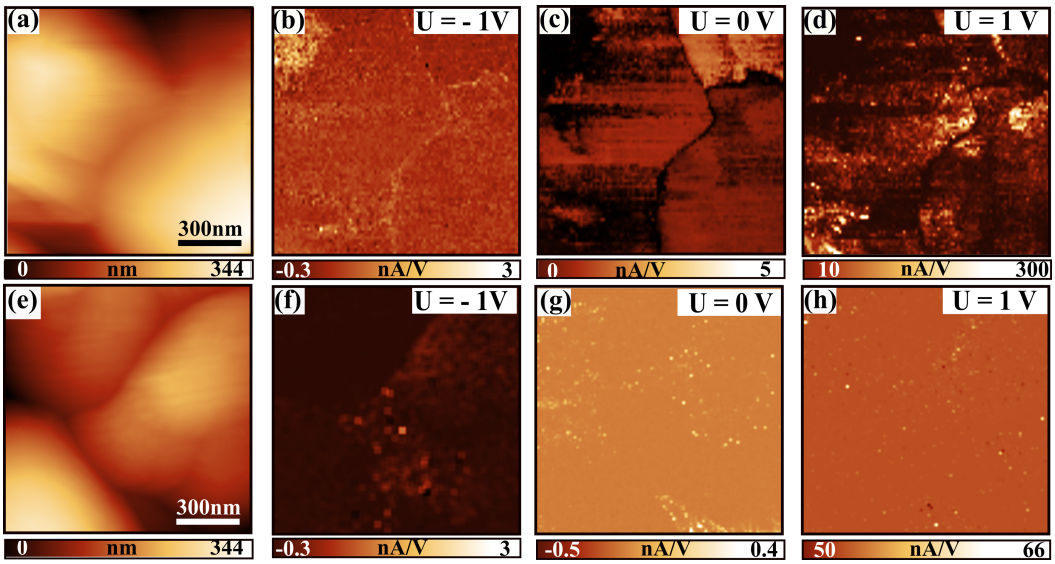

Figure 5.2: (a) STM topography of a KCN etched CISe sample, (b)-(d) dI/dU-CITS maps of the same area at -1 V, 0 V and 1 V. (e) STM topography of the CPE-treated sample, (f-h) dI/dU-CITS maps at -1 V, 0 V and 1 V. Note that the contrast of each image has been optimized as indicated by the scale bar below each image. All measurements have been carried out at the same current setpoint of 1 nA at U=1.5V prior to each dI/dU measurement.

work show a similar transition and the findings confirmed that even on Cu-rich KCN etched absorber surfaces, the inhomogeneities are reduced and the GB contrast has disappeared after UHV annealing. A detailed discussion of this observation can be found in the Appendix (see section A.1). Furthermore, the findings are also in good agreement with the others results reported in literature [37, 40]. This is somewhat unexpected since the samples explored in this particular case were grown under Cu-excess, whereas most of the literature results published so far have been obtained on Cu-poor material. Nevertheless, in Ref. [39] Cu-poor (CGI = 0.78) and Cu-rich (CGI = 1.05) materials have been compared with STM and it has been shown that Cu-rich material exhibits less granular inhomogeneities and no reduced dI/dU contrast at the grain boundaries. This is not in line with the findings presented here. However, as it will be shown below, the stronger KCN etching has converted the stoichiometric surface into a Cu-poor surface and consequently, the excellent agreement between these measurements and the published results on Cu poor absorber could be anticipated. This is already a very important outcome since it exhibits for the very first time that

KCN etching is a valuable tool to form a Cu-depleted surface, despite the fact that the growth has been carried out under Cu-excess.

In Fig. 5.2(f-h) the changes in the local density of states after the CPE treatment are presented. The first focus is on the image at U=0 V [Fig. 5.2(g)], which is indicative of the density of states at the Fermi-level. The dI/dU contrast compared to the KCN etched film is reduced by approximately a factor of 5 (see scale bar below the images), which corroborates that Cd^{2+} ions effectively reduce the number of defects at the surface. Moreover, the grain boundary contrast has completely disappeared. At positive and negative voltages some grain to grain variations are observed [Fig. 5.2(f) and (h)]. However, the magnitude has been greatly reduced compared to the KCN etched case. From these measurements, it asserts that the passivation effect of the CPE treatment is, as displayed in Fig. 5.3, similar to the UHV annealed samples despite the fact that the surface treatment is very different. Fig. 5.3 shows

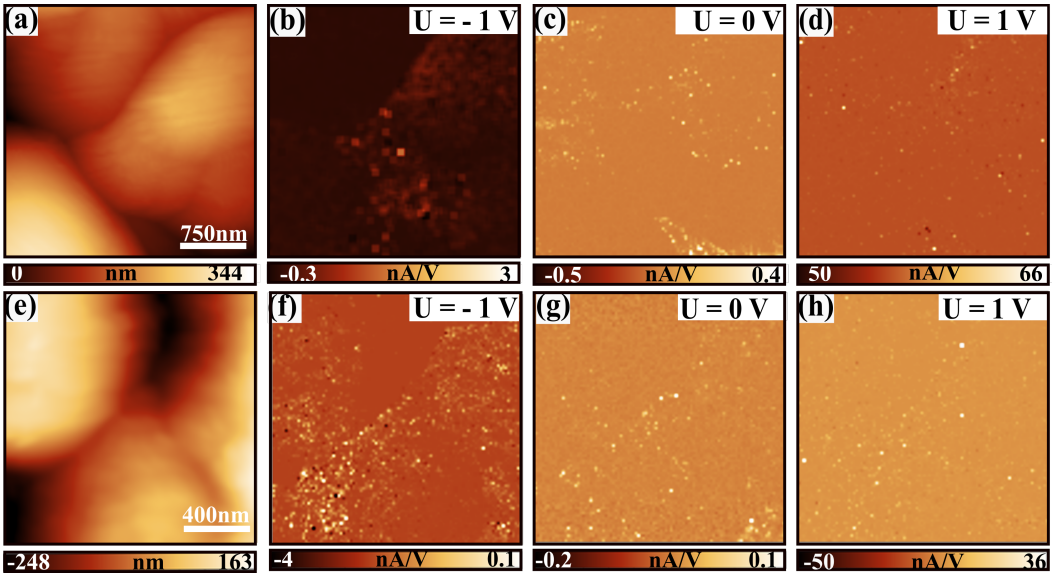

Figure 5.3: STM/STS measurements performed on a Cd-treated (a-d) and UHV annealed (e-h) sample. In both cases, the dI/dU contrast is strongly reduced as compared to the KCN etched one which is shown in 5.2(b-d). Please note that Fig. 5.3(a-d) is the reproduced data displayed in Fig. 5.2(e-h) and was re-showed here just for comparative study purposes.

the dI/dU-CITS maps at difference specific voltages, extracted from the CPE treated (b-d) and UHV annealed (f-h) samples. The respective topography images of the two absorbers are depicted in Fig. 5.3(a),(e). It is important to stress that the films

were synthesized in the same process and were both KCN etched. Only sample (e-h) underwent a subsequent heat treatment in order to passivate the surface. The dI/dU graphs exhibit a similar passivation effect for the heated and CPE treated samples. Even the magnitude of the fluctuations is reduced by a similar value (compare the scale bars of the dI/dU maps).

The result was reproduced for a number of different spots on several samples with different tungsten tips. The extracted dI/dU curves of several spots of one sample are presented in Fig. 5.4(a) for the KCN etched film and Fig. 5.4(b) for the Cd^{2+} treated sample. The curves in Fig. 5.4 represent averaged dI/dU-curves, i.e. an average of the 100×100 CITS map acquired for each spot. In agreement with the dI/dU-CITS maps presented in Fig. 5.2, a finite conductance (dI/dU), which is strongly reduced after the Cd^{2+} treatment is observed at the Fermi-energy for the KCN etched samples (shaded region in both graphs of Fig. 5.4).

The presented results in Fig. 5.2 are therefore considered to be independent of the spot chosen and are generally applicable. The scattering of the dI/dU curves observed at positive and negative applied voltages is ascribed mostly to changes in the workfunction of the tip and the sample and will be discussed in more detail later in this chapter. The important point at this stage is that there is undoubtedly a change in the density of states at the Fermi level between the KCN and CPE treated samples, which yields a metallic dI/dU curve for the KCN etched sample ($dI/dU(E_F) > 0$) and a semiconducting one for the CPE treated ones ($dI/dU(E_F) \sim 0$).

To further analyze the difference in electronic properties between GBs and grain interiors of the samples after different treatments, the dI/dU average curves extracted from the vicinity of a GB of the KCN etched sample, the ones from the heated and CPE treated samples are depicted in Fig. 5.5. Fig. 5.5(a) represents the average density of states curves extracted from the vicinity of a GB of the etched sample and Fig. 5.5(b) the ones extracted from the Cd treated and UHV annealed samples, as well as, from Ref. [40]. The image with the blue triangles, red and grey dots inside Fig 5.5(a) are cut out from the density of states map of KCN etched sample [Fig. 5.2(c)]. The blue, red, and grey curves are extracted directly from the GB, adjacent to the GB and on the grain, respectively. In line with the surface density of states map displayed in Fig. 5.2(c), a finite conductance and reduced density of defect states at GBs [see

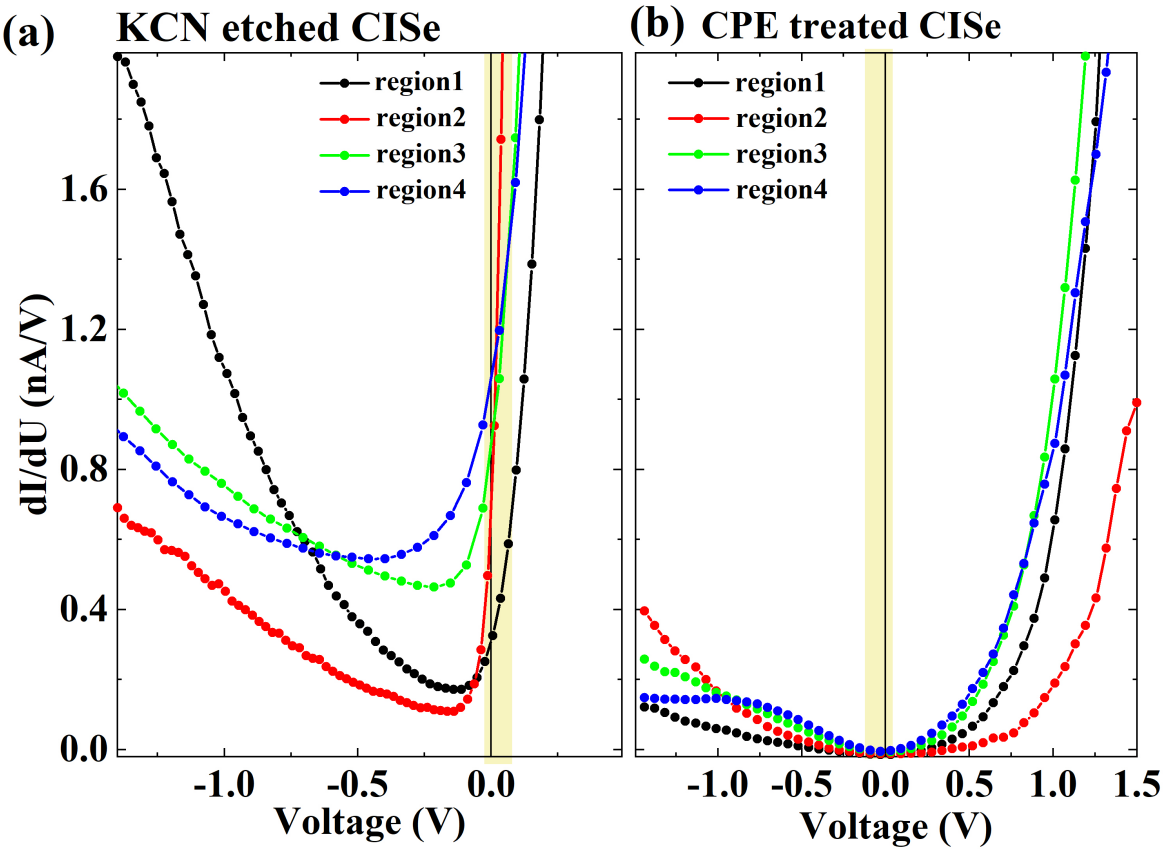

Figure 5.4: dI/dU curves of several spots extracted from (a) the KCN etched sample and (b) CPE treated sample. The different regions indicate that these measurements have been conducted at different positions of the sample, which were at least 1 mm far away from each other in order to see if the results are representative. A spot denotes a microscopic region, similar to the topography images in Fig. 5.2, which consists of several grains including grain boundaries.

the cyan ellipse on Fig. 5.5(a)], which strongly reduced after UHV annealing and after the Cadmium treatment [Fig. 5.5(b)] are obtained at the Fermi-energy for the KCN etched sample. The UHV annealed and CPE samples averages density of states curves display a semiconducting like characteristic with E_F located at the midgap.

As indicated above, the dI/dU-curves are influenced by changes in the workfunction of the sample and the tip. In fact, the measurements presented in this chapter have been carried out at a specific current setpoint. In the present case, a current setpoint of 1 nA was chosen for all the measurements. The tunneling current depends on the product of density of states of the sample and the tip and on a term, which is known as the transmission coefficient, which in turn depends on the tip sample

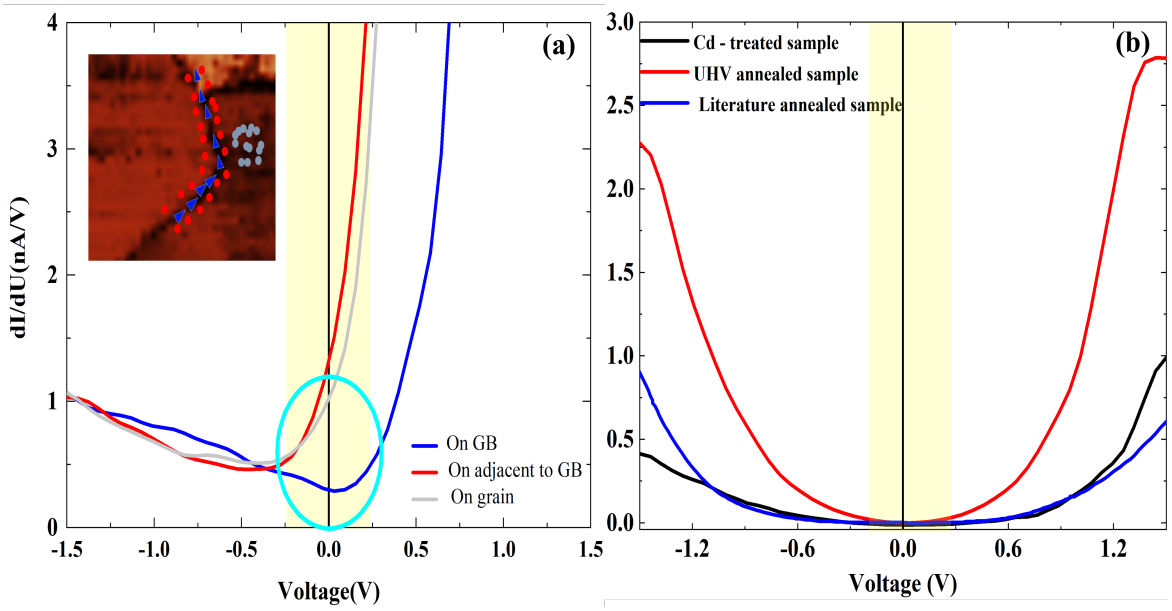

Figure 5.5: dI/dU curves extracted from the vacinity of a GB of the KCN etched sample (a) and (b) the one from the UHV annealed and CPE treated samples. All measurements have been carried out at the same current setpoint of 1 nA and at U= 1.5 V prior to each dI/dU measurement.

distance, the shape of the tip apex and the workfunctions of the tip and the sample [see equation (4.4)]. In all of the measurements presented in this work, the tip and sample workfunction may vary, which changes this transmission coefficient. Since the tunneling setpoint needs to stay constant (in our case I= 1nA), the feedback loop has to adjust the tip sample distance. This means that if changes in workfunction between the different samples/spots occur the dI/dU curves have been measured at slightly different distances. For an ideal semiconductor, the density of states in the bandgap is zero and it increases sharply at the conduction band (CB) and valence band (VB). The onset in the dI/dU curves at the band edge is therefore determined by the position where the tunneling current exceeds the noise level of the current amplifier. Since the tunneling current depends exponentially on the tip sample distance, the CB and VB onsets depend on the tip sample distance and consequently a change in the workfunction during the CITS maps alters these onsets. In a single measurement the workfunction of the tip is assumed to be constant and variations in the transfer function are therefore only related to changes in the workfunction of the sample. However, on different spots, the tip workfunction can not be considered to be constant anymore

and the changes in the transmission coefficient are increased further. Therefore, the variations in the curves presented in Fig. 5.4 and 5.5(b) is attributed to changes in the workfunctions of the tip and the sample. This fact also makes it difficult to extract the bandgap of the material, based on the measurements presented above.

Nonetheless, the results of the heat and CPE treatments are compared to the Mönig *et al.* findings [40]. In Fig. 5.5(b), the blue curve corresponds to the curve extracted from Ref. [40], the black and red ones are from the Cd-treated and from the annealed sample, respectively. The CPE treated and the literature curves look very similar, whereas the UHV annealed sample seems to have a somewhat smaller bandgap compared to the two others. As stated previously, all three curves display a semiconducting like characteristic with E_{F} located almost at the midgap. In Ref. [40] the STS data was supplemented with ultra-violet photoemission spectroscopy and inverse photoemission spectroscopy, which can be used to estimate the valence and conduction band onset. They deduced a value of $1.5 \pm 0.2\,\mathrm{eV}$, which is consistent with most of the CISe literature where a bandgap widening of the surface is assumed. Since the CPE treated sample measured here exhibits a very similar dI/dU curve than the Cu poor sample in Ref. [40], this is considered as an indication that the surface bandgap is also similar. This is in-line with the explanation model proposed below where a very similar surface is assumed for the Cu-poor UHV annealed and the CPE treated sample. The annealed sample is however somewhat different and the measurements indicate a smaller bandgap. This is also consistent with the above mentioned model that reveals that heating a stoichiometric absorber, which was treated with KCN removes most of the Cu vacancies at the surface.

In order to better understand these variations in the local density of states over the surface of different samples, they were further analyzed with the XPS. The changes in elemental composition and valence band offsets after each chemical treatment were measured and the results will be presented in the following.

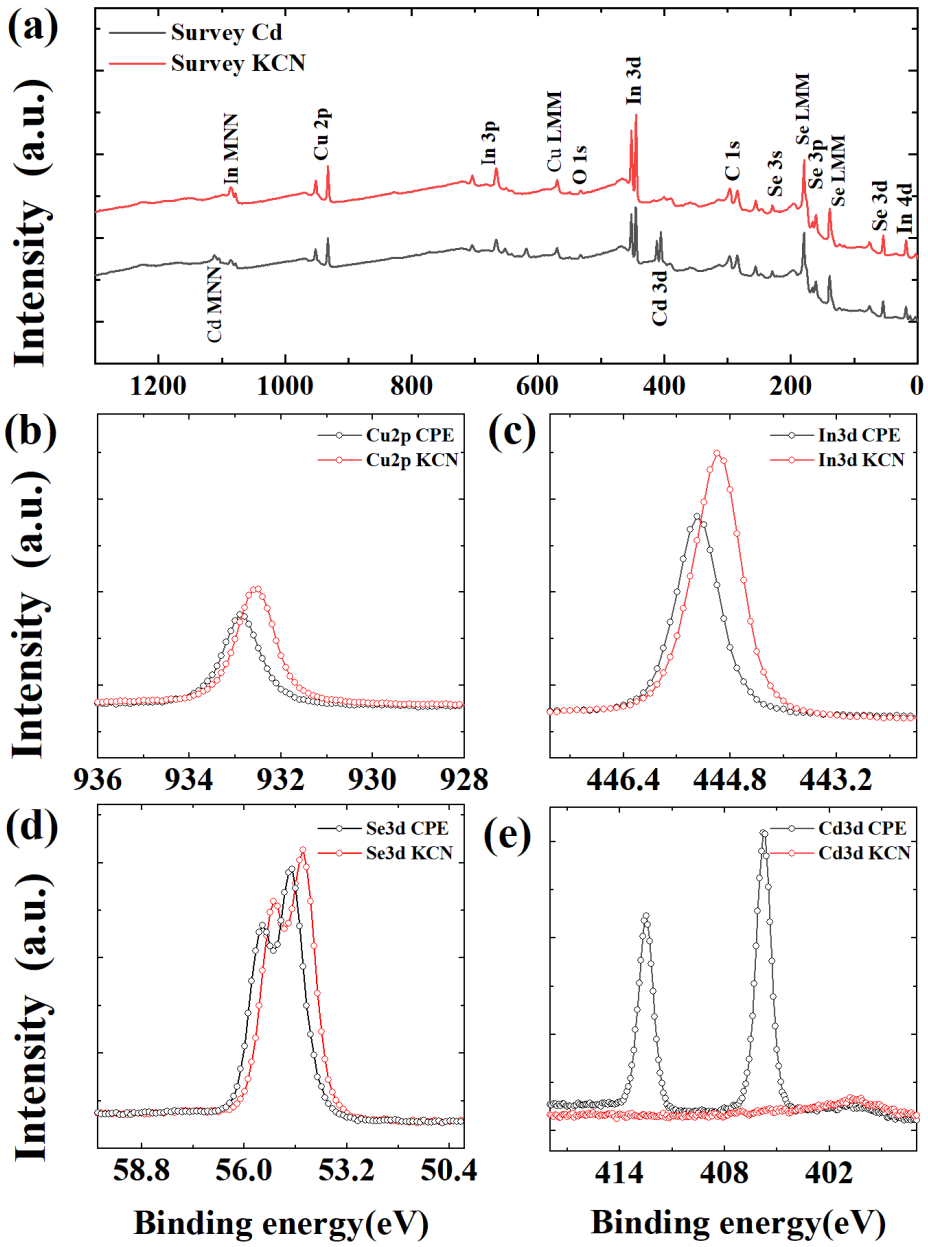

Figure 5.6: a) XPS survey spectra of the KCN and CPE treated samples ; (b-e) Individual spectra of each element. The intensity of the Cu and In peaks have been normalized to the In $3d5/2$ in order to highlight relative compositional changes.

5.3 Changes in surface composition after various chemical treatments

In Fig. 5.6 the surface composition of the KCN etched and Cd^{2+} treated samples are presented and the calculated elemental surface compositions are summarized in table 5.1. In Fig. 5.6(a) the two survey spectra are depicted and the XPS peaks of individ-

ual elements of interest are presented in Fig. 5.6(b-e). In addition to the elements in the CISe matrix, some oxygen atom was found on the absorber surfaces [Fig. 5.6(a)]. The presence of oxygen seen here is attributed to water absorption, resulting from the chemical treatment or a slight surface oxidation. The determination of the elemental composition in table 5.1 has been done without taking into account the carbon signal, where the quantification is difficult due to an overlap with the selenium Auger lines. The Cu $3p$ line was considered for the quantification since its corresponding peak is closer in energy to the other elements of interest, which means that the information depth is similar. Nonetheless, alike quantification was also done considering the Cu $2p$ line and is reported in the Appendix (see section A.2). All interpretations are independent of the choice of the Cu XPS-line. In the present case the information depth of XPS is of the order of 6-8 nm since all the XPS peaks that are considered are below 500 eV in binding energy. This also means that all the changes in composition are averages over this characteristic distance. As can be seen in table 5.1 the KCN etched

Table 5.1: Surface composition of CISe samples after various treatments, as measured via XPS. The following peaks have been used for the quantification: Cd $3d$, Cu $3p$, In $3d$, O $1s$, Se $3d$. The sputtering for both treatments was constant and approximately 5 nm of material has been removed.

sample	Cd [at%]	Cu [at%]	In [at%]	O [at%]	Se [at%]	Cu/In
CISe KCN etched	0.0	17	26	6	51	0.65
etched & sputtered	0.0	22	26	0.0	52	0.84
CISe Cd^{2+}	10	16	18	7	49	0.87
Cd^{2+} & sputtered	1	22	25	0.0	52	0.88

sample exhibits a strong Cu-depletion at the surface. The Cu/In ratio is 0.65, which is much lower than the expected value of one. After sputtering, thereby removing approximately 5 nm of material, the Cu/In ratio increases (Cu/In= 0.84), which corroborates that the bulk is closer to the expected stoichiometric value of Cu/In=1. This depletion of Cu elements is ascribed to the strong KCN etching, which removes some Cu from the near surface region in accordance with Auger depth profiling measurements [242].

In the present case, it was assumed that the absolute accuracy of the compositional measurements with XPS is of the order of 1 at%, neglecting preferential sputtering, ion beam induced diffusion, errors in the sensitivity factor and compositional variations at the grain boundaries compared to the bulk. Taking all these simplifications into account, the measured ratio after sputtering is reasonably close to the expected stoichiometric value. After sputtering, the oxygen has almost completely disappeared, which corroborates that this element was only present at the very top surface. From these measurements it concludes that the KCN treatment does not only remove the Cu_xSe secondary phase but it also removes some Cu from the near surface region of the absorber. Similar observations have also been reported in literature [103, 104], albeit less pronounced, presumably due to a different KCN concentration. The KCN etching thereby forms a Cu-poor surface on a stoichiometric absorber, which has been shown to be beneficial for device performance of stoichiometric CISe absorbers [242]. In a subsequent step the KCN etched film has been treated with Cd^{2+}. The findings reveal an additional In depletion (reduction of $\sim 30\,\%$) compared to the KCN etched sample. The result suggests that additional indium is removed from the top surface and the Cu content is slightly reduced (see Fig. 5.6(b) and table 5.1). After sputtering, the Cu/In ratio are similar to the values obtained from the KCN etched samples (within the error of the measurement) showing that there was not much inter-diffusion of these elements during the CPE treatment. The residual Cd after sputtering could arise from ion beam induced intermixing or due to some Cd that has diffused into the bulk during the CPE, presumably along the grain boundaries in accordance with findings reported in Refs. [79, 110]. A slight reduction of the selenium concentration is also observed after Cd^{2+} as depicted in Fig. 5.6(d), although these changes are close to the experimental error of the technique.

In XPS, a change in binding energy of a specific element indicates a change in the chemical environment whereas a shift of all elemental lines is indicative of surface band bending in the case of a semiconducting surface. The XPS measurements on the KCN and CPE treated absorbers shown in Fig. 5.6(b-e) exhibited a shift in the binding energy of all elements of approximately 300 meV, which immediately shows that there is a change in surface band bending. In addition to the collective shift of the XPS peaks, a change in the chemical environment of the selenium elements

and difference in valence band offsets between the KCN etched and CPE were also measured and will be presented below.

5.4 Valence band onset for KCN and CPE treated absorbers

In Fig. 5.7(a,b) a peak deconvolution of the Se $3d$ peaks is presented. The binding energy of 54.4 eV is close to the tabulated values of CISe (between 54.0-54.5 eV) [243]. The values given here refer to the highest peak of the Se doublet, i.e. the Se $3d_{5/2}$ for the KCN etched film. In the case of the KCN treated samples, it is found that approximately 95 % of the selenium atoms are in one oxidation state (i.e. CISe), whereas 5 % exhibit a smaller binding energy (i.e. a different oxidation state). For the present discussion, this peak is denoted as defective CISe since the selenium environment is distinct from the ideal case where only a single chemical environment for the Se is present. The outcome displays a shift of 0.7 eV to lower binding energy compared to the CISe environment. It is important to note that Hunger et al. [244] have measured a similar peak on $CuInSe_2$ surfaces, which were oxidized or selenium decapped. Upon Cd^{2+} treatment the amount of this defective peak increases substantially from approximately 5 % to 10 %. This indicates that some of the selenium atoms in the near surface regions bind to Cd. Again, a slight shift of the peak position of the defective peak to higher binding energies ($\sim 0.1\,eV$) is measured, which corroborates that new chemical bonds have been formed which were not present on the KCN etched sample. Hunger et al. [244] have observed a similar change in the low energy doublet after the CPE treatment on Cu poor absorbers. XPS data of CdSe exhibit a peak position of 54.1 eV [243], i.e. slightly lower than CISe, which is in accordance with our observations. The Auger parameters of both In and Cu do not change within the resolution limit of the XPS (see table A.4 in the Appendix). The Auger parameter deduced from the $Cd3d_{5/2}$ peak equals to 786.5 eV in excellent agreement with the tabulated values of CdSe and also in agreement with Hunger et al. [244] who concluded that the majority of the Cd binds to the selenium atoms, presumably only in the first monolayer. They have shown that NH_4OH cleaning of a CISe surface selectively removes oxidized indium, which leaves vacancies and selenium dangling bonds at the top surface, which

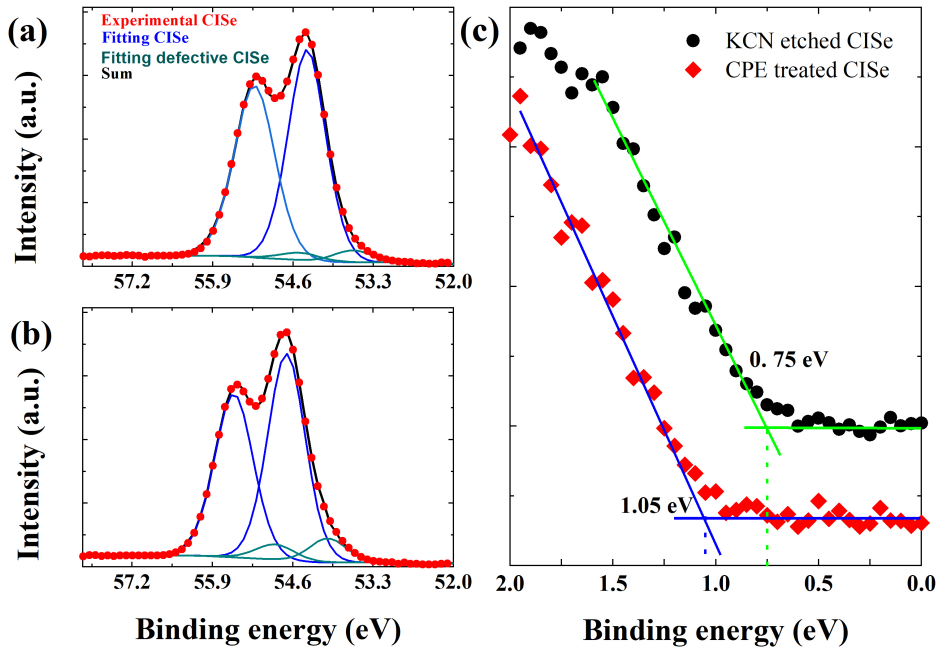

Figure 5.7: (a) Se $3d$ XPS peak of the KCN etched sample. The two main peaks correspond to the Se $3d_{3/2}$ and Se $3d_{5/2}$ contributions. Reasonable fitting can only be achieved if two chemical environments for the Se are used. The blue curve corresponds to the Se in the CISe matrix whereas the green curve represents the Se atoms that are in a different oxidation state. (b) Se $3d$ XPS peak of the CPE treated sample. The colors of all the lines are equal to Fig. 5.7(a). Note that the defective contribution is increased in the CPE case. (c) Valence band onset for the KCN and CPE treated samples measured via XPS. A comparison to UPS measurements on the same absorber can be found in the supplementary information. The KCN etched data has been shifted vertically to improve the visibility

can then be filled with Cd [244]. This interpretation would be in agreement with our observations where the chemical environment of the selenium atoms change upon Cd^{2+} treatment whereas the chemical environment of Cu and In does not change within the resolution limits of the XPS. Due to the water cleaning after the chemical treatment it is hard to disentangle residual water adsorption from indium-oxide formation on top of the KCN etched samples.

Furthermore, the valence band position of the two samples [Fig. 5.7(c)], as well as the one of UHV annealed (Fig. A.2), were investigated with high-resolution XPS at low binding energies. A comparison to UPS measurements is presented in table 5.2, which yields very similar results.

Table 5.2: Comparative study of the valence band position of the Cu rich CISe samples after various treatments such as KCN etching, CPE treatment and UHV annealed. Both XPS and UPS surface sensitive characterization techniques were used to performed the measurements. The XPS data were acquired with an Alkα source and the UPS data with an He-II source. The values denote the distance of the Fermi-level to the onset of the valence band as deduced via linear extrapolation.

sample	XPS-Alkα	UPS-HeII
KCN etched	0.75 eV	0.77 eV
KCN UHV annealed	1.08 eV	1.06 eV
CPE treated	1.05 eV	1.06 eV

The Fermi-level equals to zero binding energy in the spectrum and the valence band position is deduced via linear extrapolation as shown in Fig. 5.7(c). A shift of 0.3 eV of the valence band position is seen between the KCN etched and the CPE treated absorber. This shift is a direct consequence of band bending since it was shown above [Fig. 5.6(b-e)] that all the other XPS peaks at higher binding energies exhibit a similar energetic shift. From the measurements it is concluded that the CPE treated samples exhibit downward band bending. The distance between valence band and Fermi-level is larger than 1 eV, which suggests that the CPE treated sample is type inverted, i.e. the majority carriers at the surface are electrons whereas the majority carriers in the bulk are holes. It is essential to point out that the Fermi-level is still well inside the bandgap since Cu-poor absorbers exhibit a larger surface bandgap [40]. As it will be shown below, this type inversion has also important consequences for the interpretation of the tunneling spectra.

The measurements show that after UHV annealing a similar band bending effect is observed and the value of the valence band is very close to the one after the CPE treatment (1.08 eV compared to 1.05 eV). This result makes a lot of sense considering the fact that a very similar passivation effect of the UHV and CPE treated samples was observed in the STM data. The XPS measurements show that in both cases a substantial downward band bending is induced which eliminates the metallic like conductivity in the STS spectra. The similarity between the two treatments (CPE vs.

UHV annealing) suggests that they have the same origin.

Finally, to examine the impact of these Cd ions on the bulk electronic properties of the sample, some Photoluminescence (PL) measurements were performed on the same samples and the results are presented in the following section.

5.5 Influence of the cadmium pre-electrolyte treatment on the bulk properties of CISe absorbsers

In Fig. 5.8 the PL spectra of the KCN etched and the Cd^{2+} treated sample are depicted. The spectra are plotted on a logarithmic scale in order to better visualize small changes. Only a small change in intensity as a result of slight differences in the light in/out coupling or optical adjustments can be detected. Although the samples

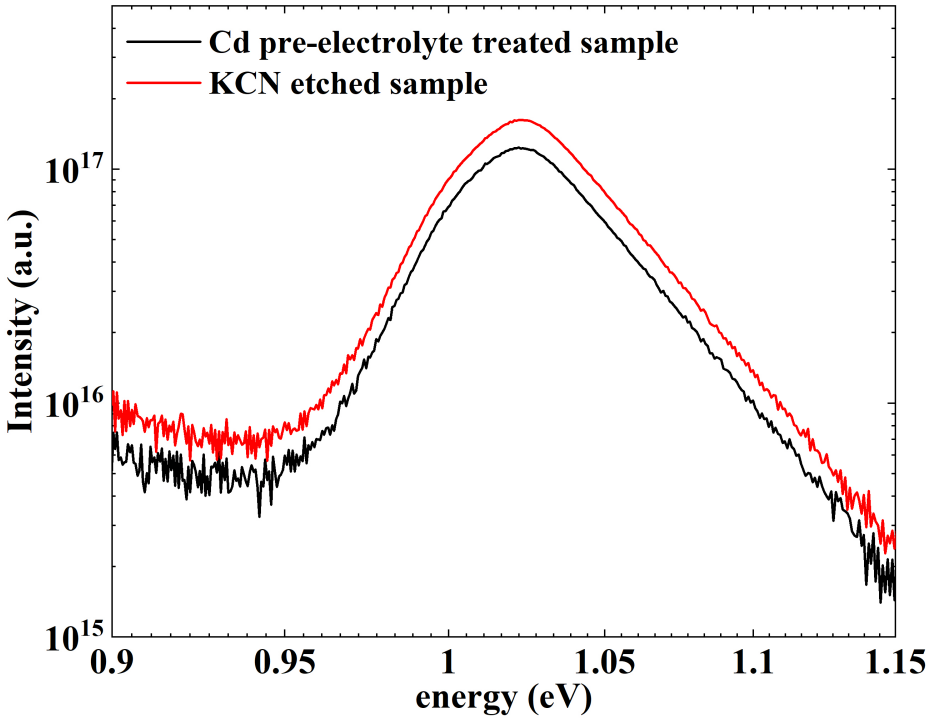

Figure 5.8: PL spectra of both KCN etched and Cd pre-electrolyte treated samples. The red and dark curves are extracted from the KCN and Cd treated samples, respectively. The measurements were carried out at room temperature in an evacuated cryostat under nominally the same excitation conditions.

have been measured the same day with exactly the same settings without air exposure, the focus had to be re-adjusted for each sample since only one sample could be placed

on the sample holder inside the evacuated cryostat. The changes in intensity by less than a factor of two are well within the error of the measurement. However, it is crucial to recall measurements that have been reported by Mönig et al. [109] who showed that the metallic dI/dU curves can be changed to a semiconductor like dI/dU curve if the sample is illuminated with laser light. They used a laser intensity of 30mW/cm^2, which is much lower than the $188\,\text{mW/cm}^2$ used in this study. Consequently, the PL measurements are not sensitive to changes in the surface state density since the high number of injected electron hole pairs will screen those states very effectively. From these measurements it is concluded that the surface treatment does not change the radiative recombination in the bulk of the sample and the changes in the surface state density are masked by the generated electron hole pairs.

5.6 Discussion and summary

In the following, an energy band diagram is constructed and a discussion aiming to determine, which defects are responsible for the observed changes in the surface density of states is proposed. Thereby, in the first part of this section, the key findings presented above are briefly summarized and the second part focuses on the interpretation of the results.

Recap of the key findings

- The STM measurements show a substantial improvement of the electronic quality of the CISe surface after the Cd^{2+} treatment suggesting an efficient surface and grain boundary passivation.

- Despite the Cu-rich growth conditions (stoichiometric bulk (Cu/In=1) with an additional Cu_xSe on the surface), KCN etching leads, not only to the removal of the Cu_xSe secondary phase but also to a strong Cu-depletion right at the surface, which gradually changes back to the stoichiometric composition after removal of a few nanometers, as shown by the XPS measurements on the sputtered CISe surface. This suggests that there is a large amount of Cu vacancies present in the near surface region due to KCN etching.

- XPS and UPS measurements corroborate that there is a type inversion upon CPE

treatment in analogy to UHV heating. This finding shows that type inversion is a crucial ingredient to understand the STS measurements. Moreover, the CPE treatment produces the same effect as UHV annealing of KCN etched samples. The STM and the XPS/UPS data show the same trend for both treatments.

- PL measurements show that the bulk recombination is not affected by the CPE treatment. The high intensity photon flux is likely to screen most of the surface states at the surface.

- The XPS measurements suggest a further reduction of the Indium content after the CPE treatment compared to the KCN etched case. This finding suggests that at least a part of the Cd ions will be incorporated at indium sites, which is a direct consequence of the removal of indium-oxides/hydroxides in the NH_4OH aqueous solution. This observation is in line with reference [244].

Interpretation of the results

The model that is proposed in the following needs to be compatible with the five points mentioned above. In general, charge neutrality needs to be guaranteed at the surface and in the bulk of the semiconductor. In the presence of band bending, the charge in the space charge region Q_{SC} needs to be compensated by surface charges Q_{S}, i.e. $Q_{\mathrm{SC}} + Q_{\mathrm{S}} = 0$. Additionally a dipole layer that is present at the surface may alter the local vacuum level. It is emphasized that the dipole layer itself does not contain a charge. However, the dipole layer may influence the surface chemistry, which in turn leads to a change in the number of surface charges.

The discussion starts with the KCN etched case [Fig. 5.9(a)]. In Fig. 5.9(a) a defect denoted as E_{D1} is considered to be located above the Fermi-level E_{F}. It has a certain energetic width, which is at least of the order of $\mathrm{k}_B\mathrm{T}$. In the sketch, it assumes that this broadening has a Gaussian distribution. Additionally, at the surface charge neutrality needs to be assumed. Due to air exposure and subsequent etching with KCN, the number of defects at the surface is quite large. This is a reasonable assumption, taking into account the large compositional changes and oxygen contamination after KCN. In order to explain the STM data, it is assumed that the charge neutrality level is located above the Fermi-level. This leads to the formation of positive surface charges Q_S, which is compensated by a negative space charge Q_{SC}, resulting in downward

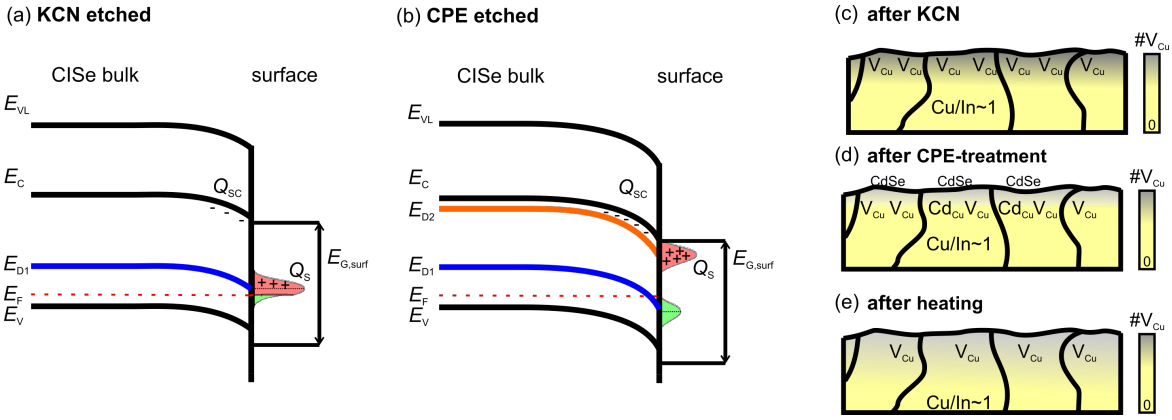

Figure 5.9: (a) band diagram of the KCN etched surface. E_{VL}, E_{C}, E_{F} and E_{V} denote the vacuum level, the conduction band, the Fermi-level and the valence band. The space charge is denoted as Q_{SC} and Q_{S} is the number surface charges. On KCN etched samples a large number of defects located at E_{D1} gives rise to the high conductance at E_{F}. The surface bandgap is labeled as $E_{\mathrm{G,surf}}$ and is slightly larger than the bulk bandgap, (b) The CPE treated sample exhibits much less defects at E_{D1} and an increased number of donor like defects at E_{D2}, which are empty. (c)-(e) sketch of the evolution of the defects at the surface due to (b) KCN, (c) Cd^{2+} and (d) heating in UHV.

band bending. From the XPS measurements only, the surface bandgap cannot be measured. Consequently, it is difficult to directly corroborate that this assumption is correct. However, other measurements on Cu-poor materials have shown that the surface bandgap is approximately $1.5 \pm 0.2\,\mathrm{eV}$ [40], which renders the interpretation of a small downward band bending plausible.

Due to the broadening of the defect E_{D1} the states above E_{F} will be empty and the ones below are filled. The empty states above E_{F} will lead to a large tunneling conductance at positive sample biases since there the current is determined by the tunneling of electrons from the occupied tip states into empty surface states. Since the number of states right at E_{F} is large a finite conductance is observed and the position of the conduction band is masked.

After the CPE treatment an increase in downward band bending is measured suggesting that the number of positive surface charges needs to increase. Due to the larger band bending E_{F} completely crosses the defect level E_{D1}, as depicted in Fig. 5.9(b). Since the defect thereby moves below E_{F}, all available states at E_{D1} are filled with

an electron and consequently, this defect will not contribute anymore to the tunneling conductance at positive bias voltages, as in Fig. 5.9(a). The density of this defect needs to be much lower, as compared to the KCN etched case since otherwise E_{F} will be very close to E_{D1} (i.e. Fermi-level pinning at E_{D1}). A reduction of E_{D1} is however not enough to explain the experimentally observed changes. Positive charges at the surface still need to be considered in order to explain the type inversion. For this aim, two possible scenarios are availables.

(a) In accordance with theory, one can assume that Cd-ions, which are adsorbed at the surface during the CPE treatment fill Cu-vacancies. It is known from XPS that the surface is Cu-depleted and consequently this assumption is well justified. Cd on Cu defects ($\mathrm{Cd_{Cu}}$) are known to form shallow donors [245] as shown in Fig. 5.9(b). Since they are located well above E_{F} they are empty, i.e. positively charged and induce strong band bending as observed in the XPS/UPS data.

(b) The XPS data have also emphasized that some of the Indium is replaced by Cd and probably a thin CdSe forms at the surface. This CdSe layer could be the origin of the enhanced downward band bending. In contrast to scenario (a), this does not include a change in the amount of Cu vacancies.

Now, the proposed passivation mechanisms in the context of UHV annealing, which has a similar effect on passivation and surface band bending in the absence of Cd ions needs to be discussed. In Fig. 5.9(e) the UHV annealing is sketched. As discussed before, the absorbers exhibit a Cu-poor surface with a stoichiometric bulk. Consequently the heat treatment will level out some of the gradient that is present after the KCN treatment, i.e. the number of Cu vacancies are reduced. This is in analogy to the CPE treatment where the number of Cu vacancies are reduced due to Cd incorporation. This interpretation is in-line with the XPS measurements by Broker et al. [39] who also observed an increase in the Cu concentration upon UHV annealing for Cu-rich material.

Here it is shown that the Cd treatment has a similar effect as the heat induced passivation as discussed above, by incorporating Cd atoms into Cu vacancies. From the preceding discussion it becomes clear that scenario (a) is more probable than scenario (b) since it is not straightforward to explain the passivation of the CISe via heat treatment with a CdSe layer as there is not Cd involved in this treatment. Therefore

scenario (a) is the most probable explanation, which allows us to explain the UHV- and the CPE-treatment.

One still needs to discuss the insensitivity of the surface treatment on the PL measurements. The electron and holes generated by the laser beam will screen the high density of surface states and consequently the changes in the surface state density does not translate in a measurable change in the PL yield. Moreover, PL essentially measures bulk properties and the change in the surface defect density will only be visible indirectly due to an increase in the surface recombination velocity, which needs to change by a few orders of magnitude in order to see a strong change in the PL [246].

Another important result of the present study is the change in the dI/dU contrast at the grain boundaries before and after Cd^{2+} treatment. It can clearly be seen that the lower defect density at the grain boundaries after KCN treatment is not visible any more after the surface has been exposed to Cd ions or heat. This extended the model proposed in Ref. [37] where the reduced defect density at the grain boundaries has been identified as a characteristic of the CISe grain boundaries. The absence of a pronounced grain boundary contrast at positive voltages also allows us to exclude a large change in workfunction between the grain boundaries and the grain interior. This is a direct consequence of the fact that the dI/dU is proportional to the product of the density of states of the sample, tip and the transmission function where the latter one is proportional to the workfunctions of the sample and the tip. The absence of a contrast a positive bias voltages is therefore a good indication that there is no band bending at the grain boundaries after the Cd-treatment. However, the incorporation of Cd ions at the grain boundaries and into the near surface region of the grains leads to a collective inversion of the CISe surface.

In this chapter, it is shown that the surface and the grain boundary signatures of the KCN etched CISe surface change significantly due to a Cd pre-electrolyte treatment. The grain boundary contrast vanishes and the surface inhomogeneities are reduced. The positive effect of the Cd^{2+} treatment can be traced back to a passivation of Cu vacancies via Cd^{2+} ions. A direct consequence of the CPE treatment is an inversion of the surface in analogy to the UHV heat treatment, which has already been discussed in the literature. The beneficial effect of the CPE treatment is probably one of the reasons for the success of CdS in CISe thin film solar cells. Moreover, it is demonstrated that

a strong KCN etching produces a Cu-poor surface with a stoichiometric bulk, which has been identified as one of the important ingredients for high efficiency CISe solar cells.

It is well known from the literature that CIGSe films grown under Cu-rich conditions always have a detrimental Cu_xSe secondary phase at the front surface. In fact, this thin layer of the Cu_xSe phase is highly conductive and may cause a short circuit in the CIGSe final device. The results presented above revealed that removing the Cu_xSe phase by KCN etching as it is done in most of the cases in literature makes the surface of the absorber become highly defective. Therefore, to circumvent carrying out the measurements on this high defective surface, over stoichiometric CISe samples investigated above were mechanically peeled off from their original substrates and the rear surface properties were examined. The reason is that it is the only way to measure the surface of Cu-rich films which have not been KCN etched. In the next chapter, the findings acquired from that study are presented. It is shown that the Cu_xSe phase does not only form at the top surface of the Cu-rich films but also at the back surface.

Chapter 6

Electronic and compositional properties of the rear surface of stoichiometric $CuInSe_2$: The formation of Cu_xSe secondary phase

Extensive knowledge and subsequent optimization of the contact layers in thin film solar cells are of high importance in order to reduce the amount of non-radiative recombination and thereby improve device performance. In Chapter 5, the influence of KCN etching and Cd in-diffusing on the front surface properties of CISe were studied. In this chapter, the back surface of absorbers grown using the same recipe was investigated. The procedure detailing how the sample was exfoliated can be found in section 4.3.1 (Fig. 4.12). The objective is to investigate the surface of the Cu-rich CISe (Cu/In=1) that was not KCN etched and to compare the outcomes to the results recorded from the top surface.

In section 6.1, the topography images along with the corresponding surface density of states (DOS) data, as well as, the XPS survey spectra acquired from the Mo-surface and CISe back-surface are presented. These results are followed by the quasi-Fermi level splitting (ΔE_F) of the same samples measured before and after peeling off process, and a calculation showing how the variations in the workfunction can affect the DOS

curves. The section 6.2 shows the workfunction measurements carried out with KPFM where a slight increase compared to the grain interiors of the workfuction is measured at the grain boundaries. In section 6.3, the element composition measured at various excitation voltages and changes in chemical composition are evaluated, and section 6.4 is based on a discussion and a brief summary of the chapter.

As in the case of chapter 5, please note that this chapter is part of Boumenou et al.'s paper published in Progress in Photovoltaics: Research and Applications [208] and was reproduced here with the permission of the Wiley © 2020.

6.1 The $MoSe_2$/CISe surface

Fig. 6.1(a) shows a representative STM image of the rear-surface of a Cu-rich CISe absorber. The surface is very flat with a RMS roughness of 8 nm. The locations of the grain boundaries are well visible in the image as they exhibit a slightly lower height than the grain interior. The large grains are covered with tiny little grains, which are observed in all of the images analyzed in this chapter. Furthermore, some deep holes (black contrast) were observed, which were likely to be caused by pinholes in the absorber layer prior to or during the peeling process. In Fig. 6.1(b) the corresponding STM image of the Mo-side is presented, where no indications of grain boundaries were found. The surface was covered with small precipitates, which had an extension of approximately 70 nm.

In order to corroborate that the absorber peeled at the $MoSe_2$/CISe interface, XPS measurements were carried out on both samples (back-side and Mo-side) and the scans are presented in Fig. 6.1(c). On the back-side all the peaks of the CISe matrix were detected, i.e. Cu, In, and Se. Contrary, the Mo-side did only show peaks that are related to Mo and Se in the survey scan. At a later stage of the chapter, high-resolution scans will be discussed in more detail. In contrast to the survey scan presented in Fig. 6.1(c) a very small amount of Cu was observed on the Mo side, whereas no traces of In was found. The XPS measurements corroborated that the absorber cleaved exactly at the $MoSe_2$/CISe interface in accordance with previous reports [147, 156, 150] due to the formation of a $MoSe_2$ layer during synthesis, which is known to be a Van der Waals solid where exfoliation is feasible. The higher oxygen signal at the Mo-side was likely

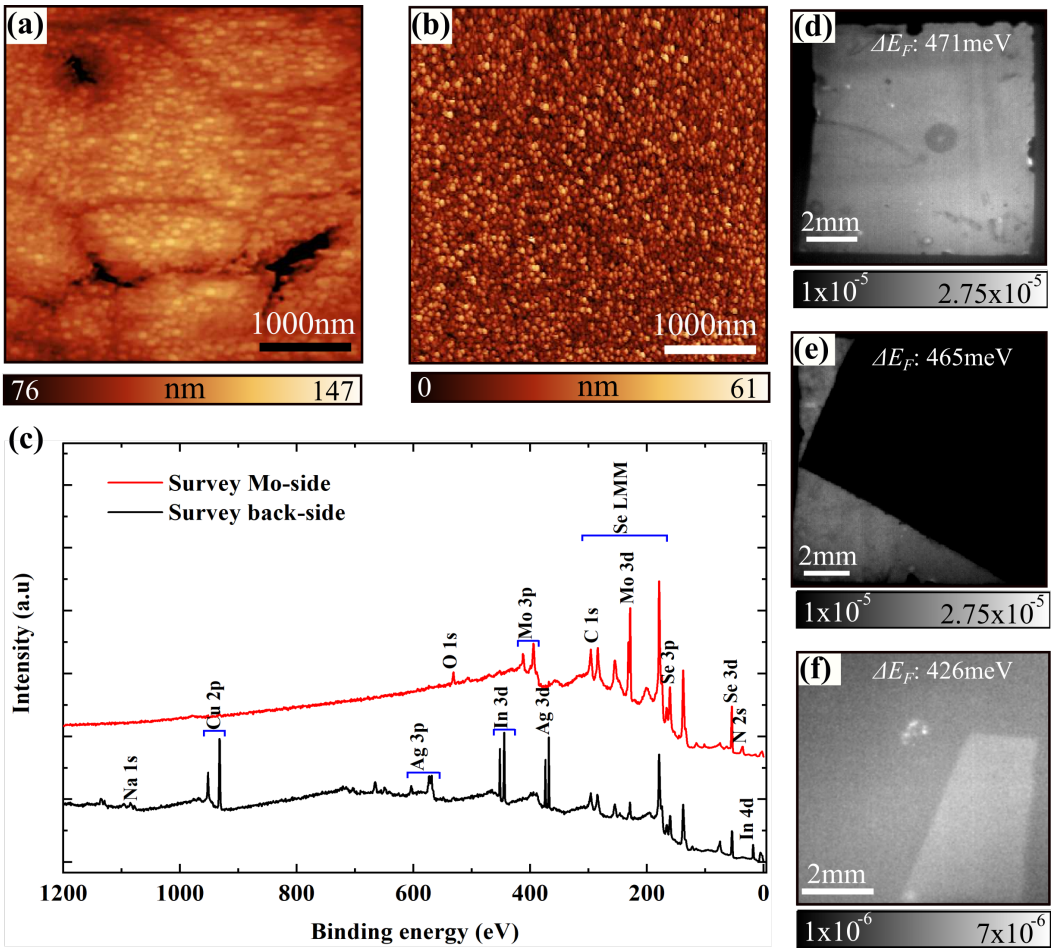

Figure 6.1: (a) STM image of the back-surface of the CISe absorber. (b) STM image of the exposed $MoSe_2$ surface after cleaving. Scan parameters: I= 1nA, U= -2V, (c) XPS survey scan. Important to note is the absence of the Cu and In peaks on the Mo-side and the absence of Mo on the backside. High-resolution scans will be discussed at a later stage of this report. (d) PL mapping of the absorber top-surface before cleaving and gluing (e) top-surface of the CISe absorber after exfoliation. The dark region is where the CISe absorber was removed from the substrate. (f) PL image of the exfoliated part. The PL image was performed via illumination from the rear-surface. (d)-(f) the PL yield indicated on the scale bar is given in PL quantum yield, which was converted to a quasi-Fermi level splitting ΔE_F via equation (6.1).

to be caused by the longer storage time of this sample compared to the back-side. As only one sample could be loaded at a time, the Mo-surface was kept in N_2 and was analyzed the day after measuring the back-surface.

Additionally, some Ag was also found in the XPS spectra and are ascribed to the

glue that was present at the edges of the exfoliated absorber due to the small size of these samples [see Fig. 6.1(f)]. Complementary EDX measurements showed that the Ag concentration in the bulk is lower than 1 at%, which is within the experimental error of the machine, considering the close distance of the In and Ag L-lines (In_L: 3.286 keV vs Ag_L: 2.984 keV). In order to check if the absorber layer was still intact after the peeling process, PL imaging measurements were carried out before the gluing and after the peeling process and the results are presented in Fig. 6.1(d)-(f). The scale bar is given in units of PL quantum yield (PLQY), which is defined as the quotient of the PL yield (photons/cm$^2 \cdot$s) emitted from the sample Y_{out} to the impinging photon density Y_{in} generated by the laser. This quantity can then be used to extract the quasi Fermi-level splitting ΔE_{F} of the absorbers via equation (6.1) [247].

$$\Delta E_F = \Delta E_F^{rad} + k_B T \ln \left[\frac{Y_{\text{out}}}{Y_{\text{in}}} \right] \tag{6.1}$$

ΔE_F^{rad} refers to the maximum achievable V_{OC} in the absence of non-radiative recombination. In this case the bandgap of the absorber is 1.0 eV, which translated to ΔE_F^{rad}=749 meV [248, 249]. The remaining constants in equation (6.1) are the temperature T at which the sample was measured and the Boltzmann constant k_B. From the measurement right after KCN etching, a ΔE_{F} of $\sim 471\, meV$ (measured by illuminating the front side of the CISe) which is a typical value for Cu-rich $CuInSe_2$ absorbers was obtained [96, 157]. After the gluing process and the subsequent liftoff the non-cleaved part of the absorber did not change significantly and ΔE_{F}=465 meV was very close to the fresh case (still measuring the front-side of the CISe absorber). The result of the back-surface, which is presented in Fig. 6.1(f) shows a somewhat reduced ΔE_{F} of only 426 meV. This showed that the gluing and exfoliation procedure had a negative impact on the opto-electronic properties of the absorber layer. However, it is important to note that the absorber was still intact and ΔE_{F}=426 meV was only 39 meV lower, which ruled out extensive metallic in-diffusion of Ag that would have increased non-radiative recombination massively. It is also essential to note that the roughness of the exposed back-contact was extremely low, in contrast to the front-surface, which may also have altered the reflection coefficient of the impinging laser light and thereby the re-absorption probability of the emitted photons, which also has an impact on PLQY [250]. From this analysis, it is clear that the peeling process of the

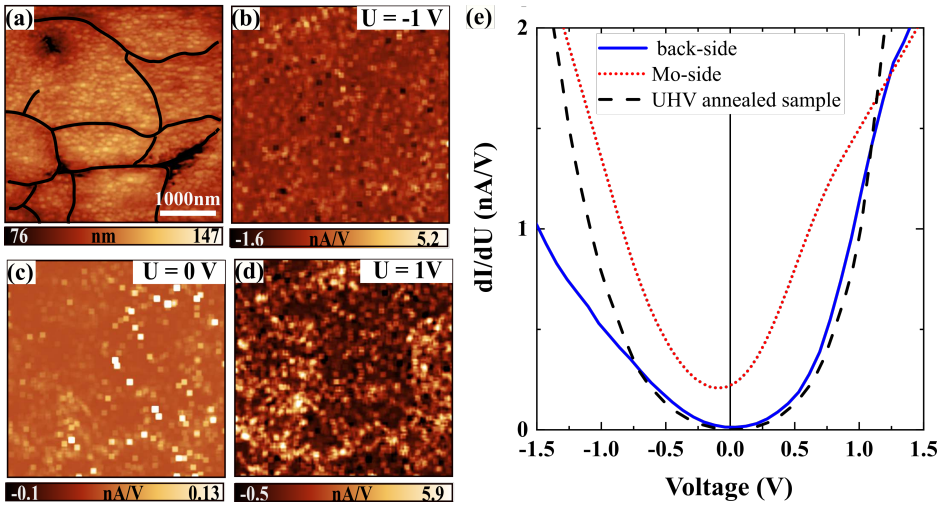

Figure 6.2: (a) STM topography image of the back-surface of the CISe absorber layer. The black lines highlight the position of the grain boundaries. (b)-(d) dI/dU-CITS maps at different applied voltages of the region shown in Fig. 6.2(a). The measurements were performed at a tunneling set-point of 1 nA, and the voltage was changed from -2V to +2V. The blue solid, red dotted and black dashed curves displayed in (e) represent the average density of states extracted from the back-side, Mo-side, and the UHV annealed front-surface.

back-surface was successful and that this procedure did not deteriorate the absorber much and an in-depth analysis of the back-surface with scanning probe techniques was well justified.

In Fig. 6.2(a) the visible grain boundaries of Fig. 6.1(a) are highlighted together with the dI/dU-CITS maps at different applied voltages [Fig. 6.2(b)-(d)]. In all three cases (U=-1V, U=0V, and U=1V) the maps are relatively featureless. The results are not in agreement with top-view measurements on potassium cyanide etched CISe samples presented in Chapter 5 and other air-exposed CISe results previously reported [39, 37, 158]. Especially, no distinct grain boundary contrast at U=0V could be observed, which indicated that the density of states at the grain boundaries was similar to the grain surfaces. The measurements showed some similarity to absorbers after UHV annealing, where a passivation of the defect states at the Fermi-level (U=0V) was observed [39, 40, 158]. Since the CITS maps at all specific voltages were featureless (no lateral variations), an average dI/dU curve from the scanned region, shown in Fig. 6.2(a) was extracted. The curve is shown in Fig. 6.2(e) as a solid line together

with a measurement on the Mo-side (see Fig. 6.1(b)) and one that was measured after heat-induced passivation on the front surface of a CISe absorber synthesized with the same process in the same physical vapor deposition system [158].

The first thing to note is that the UHV annealed sample and the measurement from the back-surface were very similar. The parts at positive voltages were almost identical whereas the curves at higher negative applied voltages were different. This variation is attributed to a difference in density of states of the tip, which was certainly not identical in the two measurements. Important however, was the excellent agreement of the valence band and conduction band onsets. The Fermi-level, which is located at U=0 V was very close to mid-gap, in agreement with the UHV annealed case [40, 158]. However, the valence band and conduction band edges were not sharp and there was substantial tailing into the bandgap region. A possible reason for this will be discussed later in the chapter.

The measurements on the Mo-side, which mainly consisted of $MoSe_2$ were different. A finite conductance was measured at E_F. Furthermore, the Fermi-level was closer to the conduction band, which points towards n-type doping in agreement with UPS measurements [54]. The finite conductance at E_F was an indication that the Mo-side had a lot of defects and explained why a well-defined semiconducting gap as expected for $MoSe_2$ has not been resolved.

The absence of a clear grain boundary contrast in STS on the back-side is somewhat surprising since it was shown via a combined electron beam induced current (EBIC) and cathodoluminescence (CL) study that carrier collection efficiency and the CL yield were different at distinct grain boundaries. STS measurements presented here do not support this interpretation. However, one needs to keep in mind that the information depth was very different for EBIC/CL (several hundred nanometers) and STS ($<$ 1 nm). Furthermore, the oxygen content may have been very different. In the present study, the cleaving was carried out in a glovebox preventing air exposure. This is usually not done for EBIC/CL measurements, which are much less surface sensitive. Another question to be discussed is the sensitivity limits of the STS measurements to detect changes in workfunction. This can conveniently be done using the fact that the tunneling conductance can be approximated by the following formula [205]: $\frac{dI}{dU} \propto \rho_S(E)T(L,U,E) \equiv DOS(E)$.

This equation assumes that the density of states of the tip ρ_t is constant for all applied voltages and that the voltage dependence of the tunneling coefficient T is small and can be neglected. The density of states of the sample is denoted with ρ_s. The tunneling coefficient depends on the workfunction of the tip ϕ_t and the sample ϕ_s, the tip-sample separation L and the tip radius R and is given by [205]:

$$T(L,\phi_{s,t},U,E) \approx \exp\left[-2(L+R)\frac{2}{3}\sqrt{\frac{2m}{\hbar^2}}\cdot\left(\frac{(\phi_t - E + eU)^{3/2} - (\phi_s - E)^{3/2}}{\phi_t - \phi_s + eU}\right)\right] \tag{6.2}$$

Assuming that the density of states of the sample ρ_s is not changing if the workfunction of the sample varies, its effect on the dI/dU can be simulated via: $(dI/dU)_{\phi_{s,B}} = (dI/dU)_{\phi_{s,A}} \frac{T_{\phi_{s,B}}}{T_{\phi_{s,A}}}$ where the subscripts A,B denote the regions of different surface workfunctions at constant density of states of the sample and of the tip.

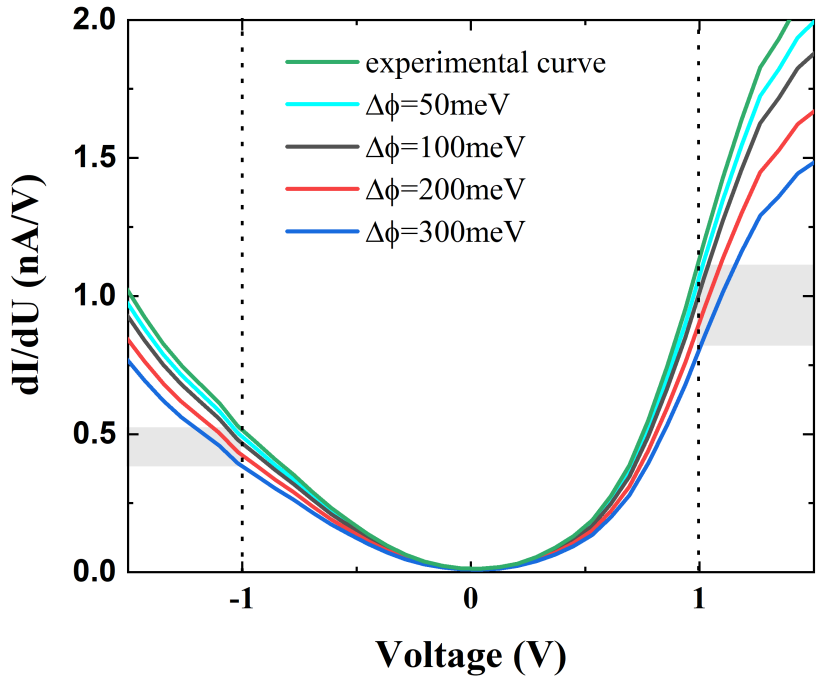

Figure 6.3: Influence of a change in the sample workfunction ϕ_s on dI/dU assuming a constant density of states of the sample ρ_s and of the tip ρ_t. A tip sample separation L=5Å , a tip workfunction ϕ_t=4.5 eV and a tip radius R=1 nm were assumed for the calculations. The workfunction difference depicted in the figure is given by: $\Delta\phi$=$\phi_{s,A}$-$\phi_{s,B}$. The shaded regions highlight the changes in conductance at a voltage of ±1 V, which corresponds to the voltages shown in Fig. 6.2(b),(d).

Fig. 6.3 illustrates how the variations in the workfunction change the dI/dU curve

assuming a constant density of states ρ_s of the sample. In the present study, the experimental dI/dU curve was not symmetric, which led to a larger change at positive voltages than at negative ones. Overall, it is observed that the curve at positive voltages is influenced mostly by the changes in workfunction. However, it is important to note that a large variation in the workfunction is needed in order to see an effect in the STS spectra. From the graph (Fig. 6.3) one can conclude that at least 100 meV difference is required to see a clear change in the experimental dI/dU-curves. This observation is confirmed by the Kelvin probe force microscopy (KPFM) measurements carried out on the same sample.

6.2 Variation of the workfunction across the rear surface of $CISe_2$ as measured with KPFM

KPFM is one of the most powerful tools to analyze, with nanoscale resolution, the change in electronic properties of semiconductor surfaces. The technique is more sensitive to changes in the workfunction than STS [214]. Therefore, it was chosen to further investigate the change in workfunction across the rear surface of the sample. The results are presented in Fig. 6.4 where a topography image [Fig. 6.4(a)] and a CPD map [Fig. 6.4(b)] are depicted. As indicated earlier, the CPD map is related to the workfunction via equation (6.3).

$$V_{CPD} = \frac{\phi_s - \phi_t}{e} \tag{6.3}$$

Consequently, the brighter regions in the CPD map corresponded to regions with higher workfunctions, assuming a constant workfunction of the tip. In the topography image one again observed the grain boundaries as slightly lower regions, in agreement with the STM measurements. Furthermore, very small dots are also observed on the rear-surface. The contact potential difference map showed, in contrast to STS a slightly higher contrast at the grain boundaries. A line profile along such a grain boundary is shown in Fig. 6.4(c). The shaded area in the graph highlights the grain boundary region. The result shows a decrease of the topography by approximately 10 nm, together with an increase in the workfunction of approximately 40 meV. This anti-correlation was observed on all grain boundaries in the image. Comparing this

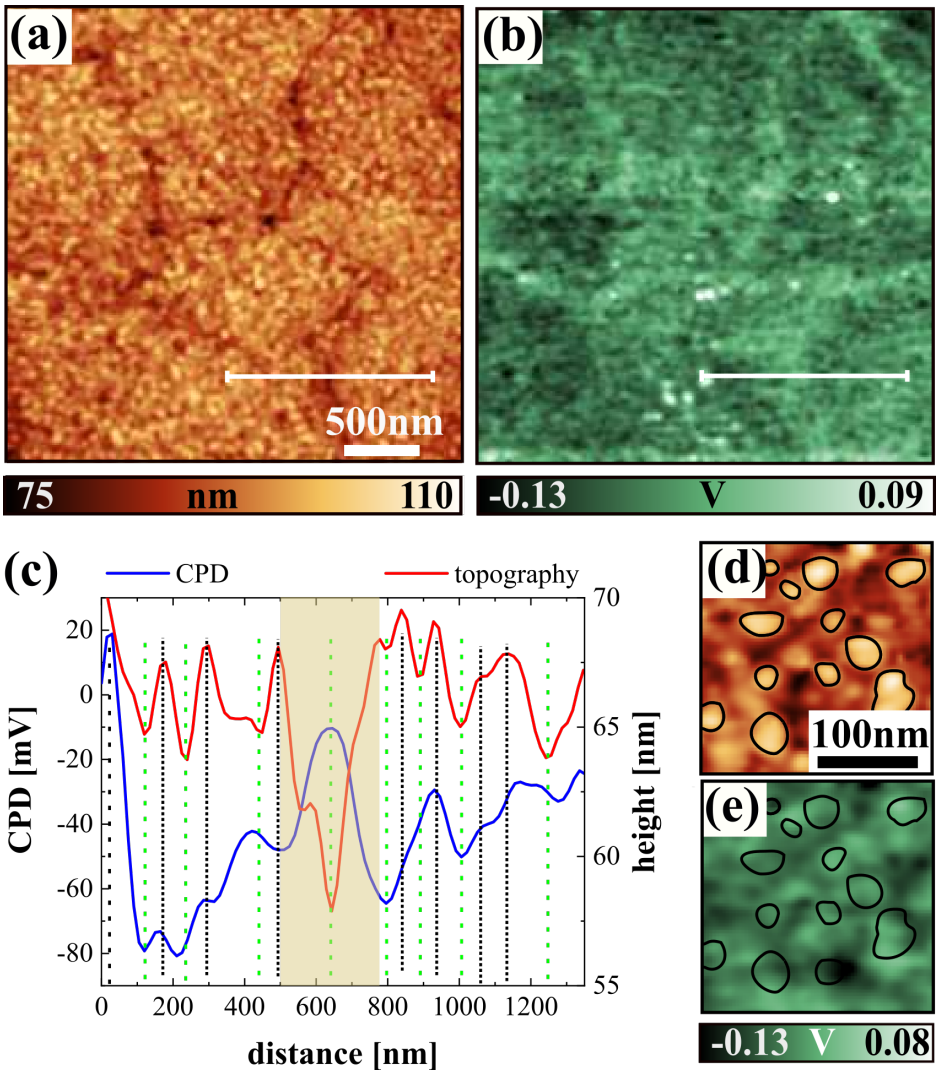

Figure 6.4: KPFM measurements carried out at the back-side of a Cu-rich CISe absorber. (a) surface topography image, (b) surface potential map, (c) line profiles as indicated in (a),(b). The shaded area highlights the grain boundary region. The green dashed lines indicate local minima in topography whereas the dashed black lines show local maxima in the topography line-scan. (d),(e) topography and CPD map of the small precipitations. Some regions are highlighted in both images to correlate the topographic information to the workfunction variations.

result to the STS measurements (Fig. 6.2) and the calculations (Fig. 6.3) it is clear that values of grain boundary band bending of approximately 40 meV were too small to be detected in STS.

However, one important aspect still needed to be discussed in more detail. A careful inspection of the density of the small dots that cover the complete back-surface showed

that, at the grain boundaries the density seemed to be slightly lower [see Fig. 6.1(a) and Fig. 6.4(a)]. It is therefore important to analyze if the changes of the dot density at the grain boundaries were responsible for the observed workfunction changes. At least the dots seemed to have an impact on the workfunction since variations in CPD were also seen on the grain surfaces. The line profiles in Fig. 6.4(c) showed that the variations were approximately 20 mV - 30 mV in the area outside of the shaded region. In Fig. 6.4(c) all the prominent minima in the topography are indicated by green dashed lines whereas the maxima are highlighted with black dotted lines. For both situations (maxima or minima) in the topography, corresponding CPD variations were measured in both directions. The findings exhibited no direct correlation between the maxima and minima in topography and CPD. Hence, it is deduced that the dots are not the main reason for the systematic changes in the workfunction that is observed at the grain boundaries. However, a thorough analysis revealed that the dots do have an impact on CPD across the surface of grain interiors albeit not always in the same direction [Fig. 6.4(d) and (e)].

To explore the elemental composition of the sample and mainly the one of those dots measured with both KPFM and STM/STS, the sample was analyzed with EDX and XPS and the results are discussed in detail below.

6.3 Elemental composition at the rear-surface

Table 6.1 summarizes the elemental compositions that were measured with EDX and XPS. The EDX measurements were acquired at 20kV, 15kV, 7kV and 5kV in order to gain some insights into the compositional changes as a function of depth. On the other hand, Table 6.1 also contains the measurements carried out at 20 kV on the front-side of the absorber after KCN etching for a comparative study. This measurement can be considered as a reference since an etched stoichiometric CISe absorber layer should exhibit a Cu/In ratio of 1 in the bulk in agreement with the results presented here. The systematic error for the elemental concentration is at least 1 at% for an EDX measurement and consequently the small deviations from the expected values were well within the error of the measurement technique. Although the systematic errors in EDX are large, changes in the composition at varying acceleration voltages

Table 6.1: Elemental composition of the rear surface of CISe samples, as measured via EDX and XPS. EDX and XPS analyses were acquired on large areas (compared to the grain size) in order to get representative averages. EDX values in brackets were measured after KCN etching of the back side. All samples were etched on the front side prior to the peel off process. All measurements performed on the back side were carried out in one session to limit the error bar. The measurements on the front side were done with another SEM machine and different systematic errors may influence the absolute numbers.

EDX composition [at%]	Cu	In	Se	Cu/In			
Back-side (20kV)	24 (24)	25 (25)	50 (50)	0.9 (0.9)			
Back-side (15kV)	28 (28)	24 (24)	48 (48)	1.2 (1.2)			
Back-side (7kV)	30 (30)	24 (24)	46 (47)	1.3 (1.3)			
Back-side (5kV)	32 (30)	23 (23)	45 (47)	1.4 (1.3)			
Front-side (20kV)	25	24	51	1.0			
XPS composition [at%]	Cu2p	In3d	Se3d	Cu/In	Na1s	Mo3d	O1s
Back-side	29	17	42	1.7	0.5	/	11
Mo-side	1	0	36	/	0.3	38	24

are much less susceptible to large errors if the quantification is done with the same characteristic X-ray lines. Consequently, the measurements performed at different acceleration voltages suggested that the Cu-content is slightly higher at the back-contact region. However, EDX measurements are not surface sensitive enough to analyze compositional changes in the near surface region. XPS measurements are much more surface sensitive ($\sim$ 6-8 nm) than EDX measurements which are entirely bulk sensitive at the used acceleration voltages (information depth $\sim$ 0.1-1 μm at 5 kV-20 kV acceleration voltage). Interestingly, the Cu concentration, as deduced via XPS was much higher close the interface with a Cu/In ratio of 1.7. This was a clear indication that excess Cu was present at the back-contact and further strengthens the EDX results. At the Mo-side a small amount of Cu was measured and no In was detected, which corroborated that there was no CISe remainders on the Mo-side. The Mo/(Se+O) ratio is 0.6, which points towards a $MoSe_2$ layer, partially oxidized due to the rather long storage time of this substrate in the glovebox before introduction

into the XPS system. The oxygen concentration was more than doubled compared to the back-side absorber, which was introduced directly after the exfoliation. However, residual oxidation of the substrate prior to the growth process cannot be excluded and may also have contributed to the higher oxygen content.

In the following, some high resolution scans of the individual elemental transitions acquired via XPS are presented and discussed. In Fig. 6.5(a) the Cu $2p$ line of the back-side and of the Mo-side are shown. The binding energy of 932.4 eV was in excellent agreement with the reported values for $CuInSe_2$ [243]. The Auger parameter, which

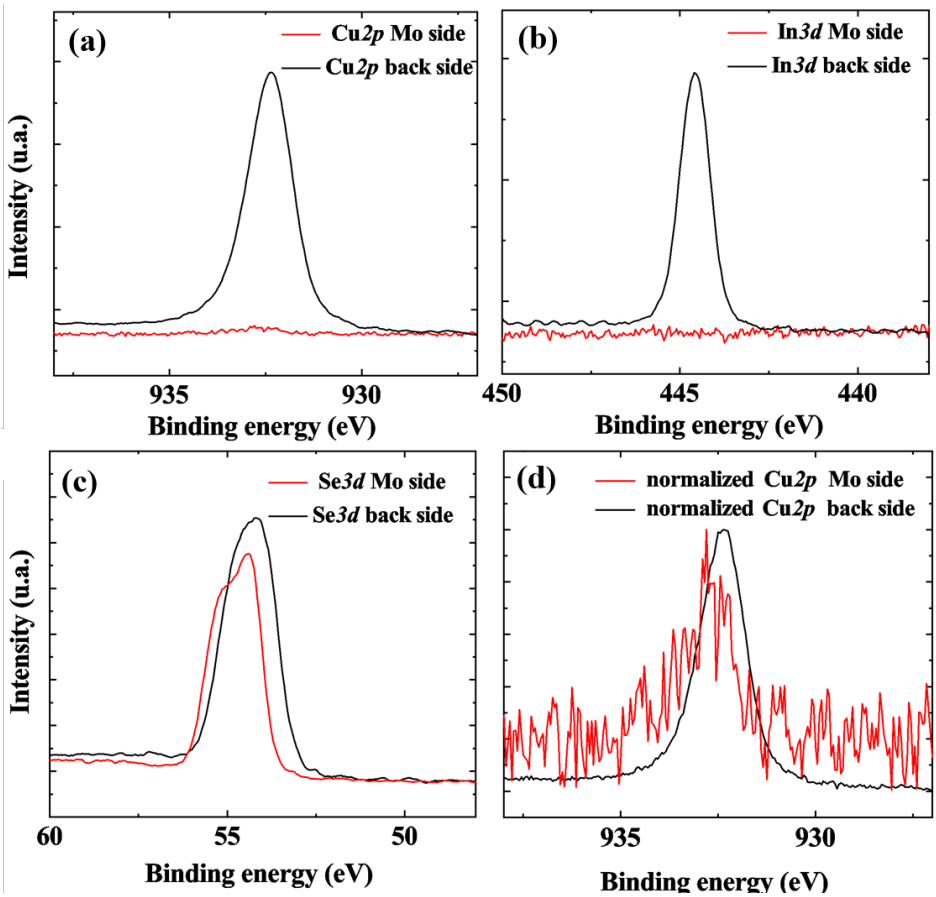

Figure 6.5: (a-d) High resolution XPS analyses of the rear surface and the Mo surface (a) Cu $2p$, (b) In $3d$, (c) Se $3d$, (d) normalized Cu $2p$ curves depicted in (a).

is only sensitive to the chemical environment and not to changes in binding energy as a result of different band bending, was 1849.7 eV, which was also in good agreement with CISe [243]. The Cu concentration at the Mo-side was only 1 % (see Table 6.1). In Fig. 6.5(d) the Cu $2p$ spectra were normalized to the peak maxima in order to improve the visibility. Within the error of the measurement no significant shift in

the binding energy was seen and the Auger lines were too weak to estimate an Auger parameter. The In 3*d* lines are presented in Figure Fig. 6.5(b). The binding energy was in accordance with the reported values [243] and almost no signature of Indium was observed at the Mo-side. This showed that the detected Cu that was measured on the Mo side is not bound to CISe. The Se 3*d* lines are depicted in Fig. 6.5(c). A clear shift in the binding energy was visible when comparing the two substrates. On the back-side the Se $3d_{5/2}$ was located at 54.2 eV whereas on the Mo-side the value was located at 54.4 eV. The shift towards higher binding energies was attributed to a change in the chemical environment of the Selenium from a CISe matrix on the back-side to a $MoSe_2$ matrix on the Mo-side. The measured value of the binding energies were in agreement with reported values [243, 251]. The elemental composition of the $MoSe_2$ (Table 6.1) was not equal to 2 and the large amount of oxygen was likely to influence the $MoSe_2$ concentration measured here. For both surfaces the Na concentration was on a similar level with approximately 0.5 %.

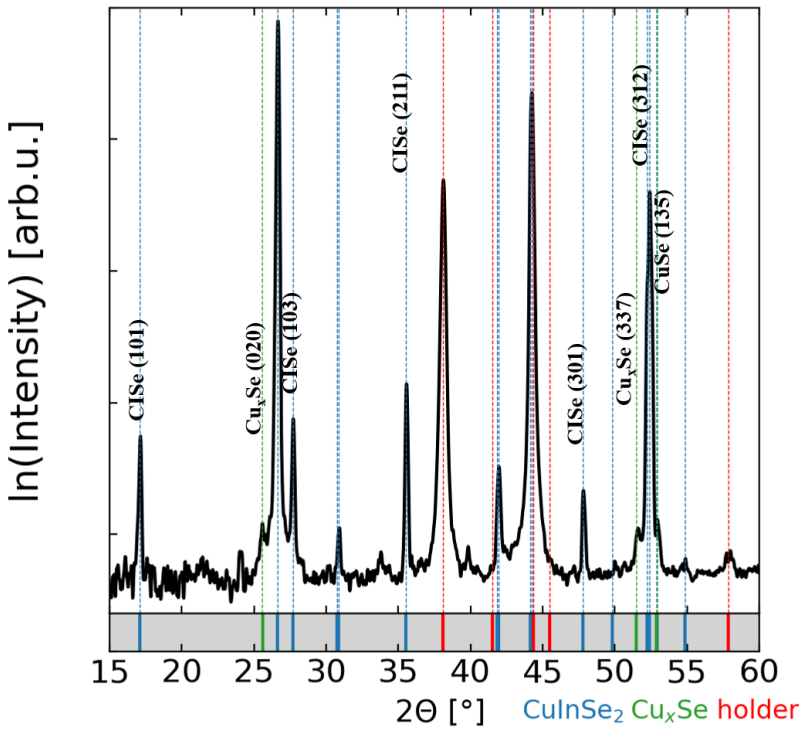

Figure 6.6: Grazing incidence XRD measurement performed on a peeled absorber (the front-side of the absorber was etched whereas the back-side was not). The peaks highlighted by blue, green and red vertical lines are from the CISe, Cu_xSe secondary phase and the holder, respectively.

The XPS and the EDX measurements strongly suggested that there was excess Cu at the back contact of the absorber layer. In order to corroborate the existence of a Cu_xSe secondary phase, grazing incidence X-Ray diffraction was used. The results are presented in Fig. 6.6. It needs to be emphasized that this absorber layer was KCN etched before the peeling process in order to make sure that all the Cu_xSe detected in the diffractogram originated from precipitates in the bulk or from the back contact. The findings revealed a peak located at 25.6° and additional shoulders

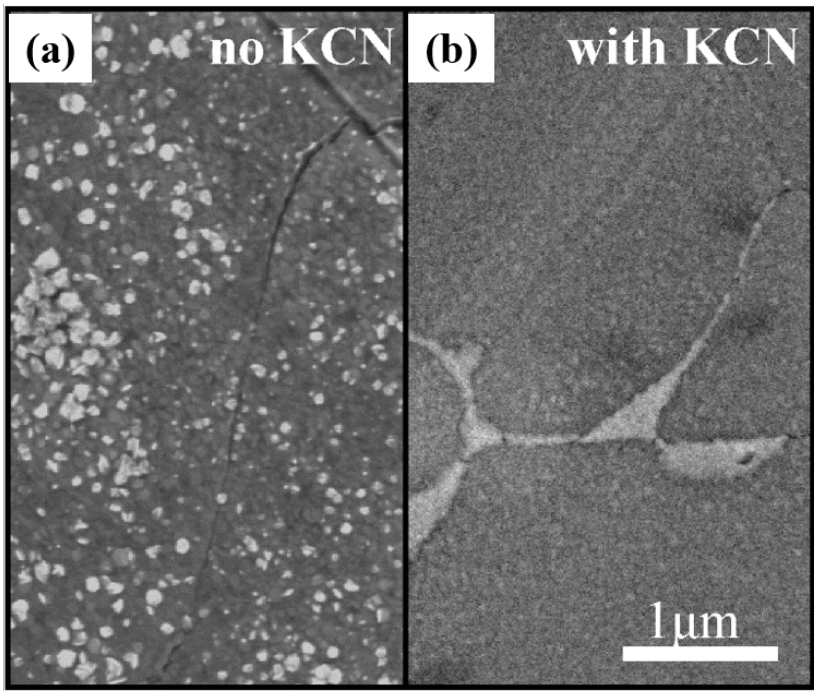

Figure 6.7: SEM micrograph of the back-side of the CISe absorber: (a) prior to KCN etching. (b) identical absorber after KCN etching.

around the (312) CISe peak at 52.39°, which were also reported to originate from Cu_xSe [155, 252]. Consequently, the XRD data confirmed that precipitations exist in Cu-rich absorbers, despite the fact that the front surface was etched with KCN prior to the peel off process. In Fig. 6.7(a) and (b) high resolution SEM measurements are presented, which show the morphology of the CISe back side prior to KCN etching and after KCN etching.

The small white grains completely disappeared after KCN etching and furthermore, substantial changes was observed at the grain boundaries. The brighter contrast in SEM as shown in Fig. 6.7(b) is not indicative of an accumulation of material but rather due to a higher secondary electron yield at the grain boundaries, i.e. a different

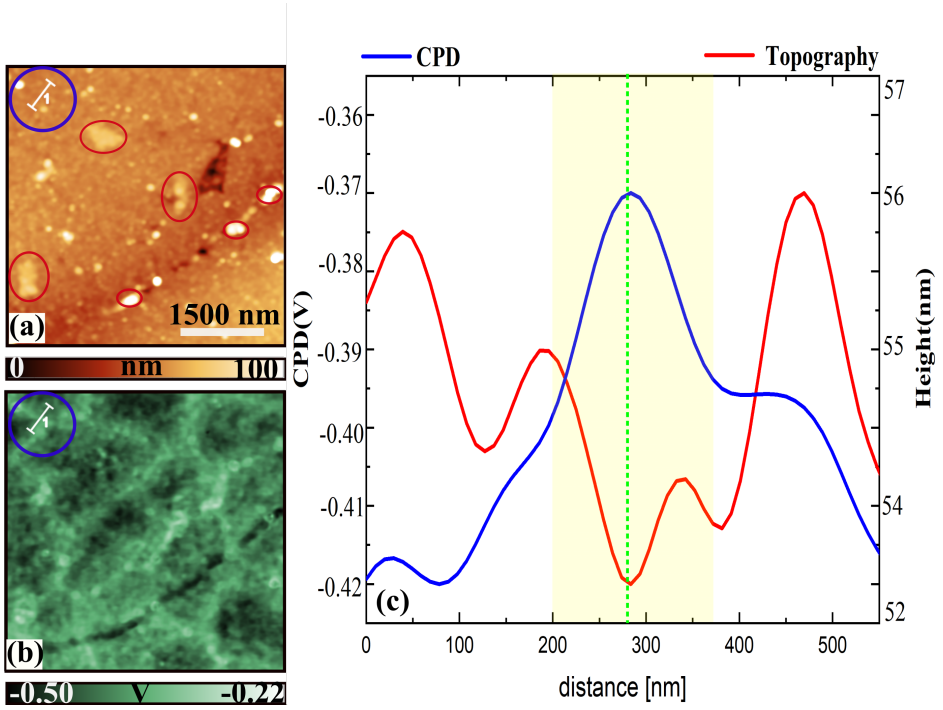

Figure 6.8: KPFM measurements carried out at the back-side of a KCN etched Cu-rich CISe absorber. (a) surface topography image, (b) surface potential map, (c) line profiles as indicated in (a),(b). The shaded area highlights the grain boundary region.

electron affinity or workfunction. Currently, it assumes that the etching rate at the grain boundaries was enhanced, suggesting that there was a larger amount of Cu_xSe present compared to the absorber back-surface. The small grains in Fig. 6.7(a) are attributed to Cu_xSe precipitates, which were removed during the KCN etching process. EDX measurements performed on the same sample showed a reduction of the Cu/In ratio from 1.4 to 1.3 due to the removal of a Cu_xSe secondary phase.

To further analyze the higher contrast observed at GBs of the etched sample, it was analyzed with KPFM. The result is shown in Fig. 6.8 where the topography image, the workfunction map as well as line profiles extracted from a GB [blue circles in Fig. 6.8(a) and (b)] are depicted in (a), (b), and (c), respectively. The topography image is featureless, no grain boundary signatures are resolved. The white particles see on its surface are ascribed to the residual Cu_xSe_2 phase which is left at the surface of the film after KCN etching. In line with the SEM measurements, a variation in the CPD contrast was also observed at GBs with KPFM confirming thereby that changes in the contrast between GBs and grain interiors measured with the SEM are due to difference in workfunction.

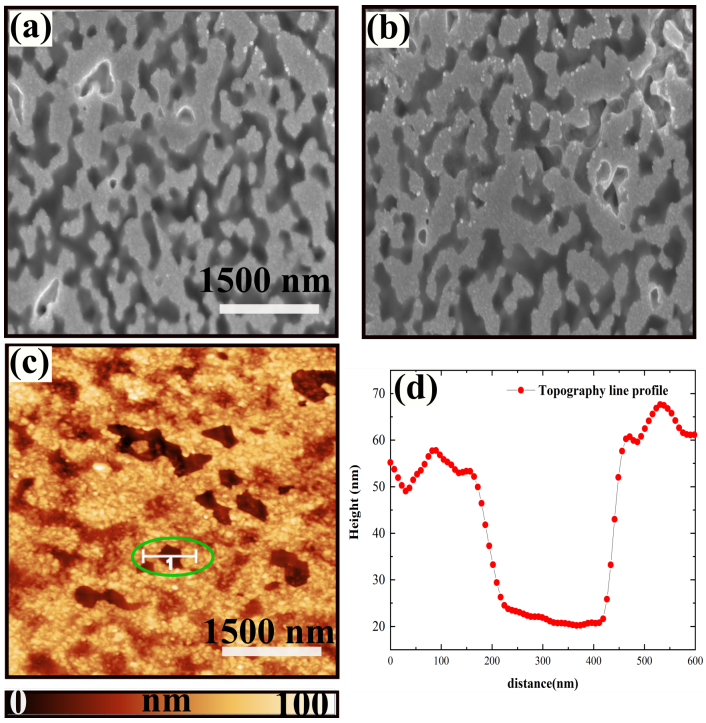

Figure 6.9: SEM measurements acquired in (a) before KCN etching and in (b) after KCN etching. The corresponding AFM image is presented in (c) and a line profile showing a cavity of $\sim$ 35 nm deep in (d). The line profile is extracted from the region indicated by the green circle in (c).

Alike SEM and EDX measurements were conducted at the rear surface of Cu-poor CISe before and after KCN etching for a comparative study. The results are depicted in Fig. 6.9 and the elemental composition in Table 6.2.

The micrographs showed no significant change after KCN etching suggesting that contrarily to the film grown under over stoichiometric conditions the backside of Cu-poor CISe is Cu_xSe free. Both images show the presence of voids of $\sim$35 nm deep [Fig 6.9(c) and (d)] over the surface, similar to the ones measured at the surface of UHV annealed Cu-poor CIGSe [253]. Although some very small dots are seen on the AFM image, note that in contrast to results acquired from the rear surface of Cu-rich CISe, the backside of Cu-poor film is unaffected by the KCN etching. This suggests as can be seen in Table 6.2 where a similar elemental composition was recorded before and after KCN treatments that tiny dots observed here are not Cu_xS secondary phase. The elemental composition measured before and after KCN etching is similar.

Table 6.2: Elemental composition of the rear surface of Cu-poor CISe samples, as measured via EDX. EDX measurements were acquired on large areas in order to get representative averages. EDX values in brackets were measured after KCN etching of the backside. All samples were etched on the front side prior to the peel off process. All measurements performed on the backside were carried out in one session to limit the error bar.

EDX composition [at%]	Cu	In	Se	Cu/In
Back-side (20kV)	25 (25)	27 (27)	48 (48)	0.9 (0.9)
Back-side (15kV)	27 (26)	26(26)	47(48)	1.0 (1.0)
Back-side (7kV)	27(27)	28(26)	45 (47)	1.0 (1.0)
Back-side (5kV)	29 (29)	24(24)	47(47)	1.2(1.2)

6.4 Discussion & summary

The following list summarizes the key findings of the preceding sections.

- The back-side of stoichiometric CISe absorber showed an increased concentration of Cu in the region close to the interface. XRD measurements showed small amounts of a Cu_xSe phase, which could be removed with a subsequent KCN etching of the back-side as evidenced by high resolution SEM micrographs.

- A weak upward band bending of approximately 40 meV was measured at the grain boundaries with KPFM.

- The STS data were similar to the results obtained on UHV annealed CISe absorbers. However, there was still substantial tailing highlights by a gradual decrease of the dI/dU curves into the bandgap region and the absence of sharp conduction and valence bands.

- The Fermi-level was mid-gap, similar to the absorbers surfaces after UHV annealing [40, 158].

- For the Mo-side, E_F was closer to the conduction band and a finite conductance was measured at E_F, which pointed towards a high number of defects in the $MoSe_2$ or very high doping levels.

The most intriguing finding is certainly the high concentration of Cu at the absorber back-side and a non-negligible concentration on the Mo-side. XRD and SEM measurements corroborate that a very thin layer of Cu_xSe formed at the $MoSe_2$/CISe interface due to the Cu-rich growth conditions. This finding is not in accordance with reports on Cu-rich $CuInS_2$ where the back surface did show an indium enrichment [150] and no indication of a Cu_xS phase. To the best of our knowledge there are no reports available where the back-surface of a Cu-rich CISe absorber was investigated with XPS measurements. However there is a lot of literature available for the Cu-poor material. In accordance with TEM measurements [152] of the back-surface a $MoSe_2$ layer which included some Cu was measured. However, no Cu_xSe secondary was observed in their studies. Furthermore, XPS and UPS measurements of the Cu-poor CIGSe/$MoSe_2$ interface also excluded a Cu_xSe secondary phase. They observed an accumulation of Ga and Cu at the rear contact, in accordance with APT measurements [153].

The present investigation shows that Cu-rich Selenium based absorbers exhibit different surface and back-surface compositions compared to the absorber bulk. The Cu-rich growth conditions trigger the precipitation of a Cu_xSe secondary phase, which is not present in Cu-poor material and which segregates at both interfaces. In the STM and AFM data presented here, one can observe that both sides of the rear-interface were covered with very small grains in the order of several tens of nanometers. The result shows a correlation of the workfunction with the grains although it is not straightforward to observe one distinct value. It rather seemed like randomly oriented small grains that exhibit slightly different workfunctions. The small grains and their variations in workfunction on the grain surfaces ($\sim$20 meV) are assigned to Cu_xSe. This conclusion was drawn on the basis of our XPS and EDX measurements, which showed a clear increase in Cu at the back-side of the CISe absorbers and the XRD measurements that showed that residual Cu_xSe was present in the absorber layer. From XRD it is hard to rule out that there was no Cu_xSe present in the bulk of the absorber. However, the EDX and SEM measurements confirm that at least a part of the Cu_xSe was present at the rear-side.

The workfunction changes at the grain boundaries that are measured in this study are inverted compared to results reported by Marron et al. [156]. However, these investigations were performed on Cu-poor $CuGaSe_2$. The differences can be assigned

to a different Cu concentration at the grain boundaries, which favours upward band bending for the case of Cu-rich material and downward band bending for Cu-poor material as exhibited by the investigations performed at the surface of Cu-poor materials. KCN etching of the back-side of Cu-rich film showed an increased etching rate at the grain boundaries compared to the surface, which was attributed to a larger amount of Cu_xSe at the grain boundaries.

Another important point that needs to be discussed further are the STS results. Based on the XPS findings the back-surface of the CISe were partially covered with Cu_xSe. In the present study the focus was on large area scans where the dI/dU maps averaged over large areas covered with a large number of small grains. This fact may explain the rather undefined band edges that are observed in the dI/dU average curve. High resolution STS measurements are necessary to disentangle the signal from the small grains from the one of the underlying substrate. At present this was not possible due to the duration of the CITS scans (approximately 15 hours), which imposed very strict limits for the maximum allowed temperature drift during STS measurements.

Finally, the implications of the formation of Cu_xSe phase at the rear surface of a film on the device performance need also to be discussed. The measurements presented above corroborate that Cu_xSe precipitations do not only form at the front contact but also at the rear-surface under Cu-rich growth conditions in CISe. The interface recombination velocities are likely to be higher than for a pure $MoSe_2$/CISe interface since the $MoSe_2$ is a layered material with pure Van der Waals bonding along the growth direction, i.e. no dangling bonds. It is likely that the Cu_xSe secondary phase makes the interface worse and thereby reduces the PCE of the final device. Furthermore, band bending is different than in Cu-poor $CuGaSe_2$. Although at present it is difficult to disentangle the influence of the Ga/In from the different Cu content, the results still showed the composition has important consequences for the properties of the grain boundaries as also described in a recent APT study for $CuInS_2$ [254]. The reported measurements showed an increased concentration of Cu at the grain boundaries in Cu-rich $CuInS_2$. If a similar behavior is assumed here, i.e a similar grain boundary chemistry in Cu-rich CISe, excess Cu would segregate out at all interfaces (front, back and grain boundaries) with distinct opto-electronic properties compared to the Cu-poor absorbers. The SEM measurements performed before and after KCN etching of

the back side are in line with these observations since a preferential etching of the grain boundaries was also observed.

In summary, it was shown that for stoichiometric CISe absorbers the rear-surface exhibited an accumulation of Cu, which is assigned to a Cu_xSe secondary phase. This is in contrast to Cu-poor CIGSe where a Cu and Ga enrichment were measured. With KPFM, a slight upward band bending of approximately 40 meV which because of its reduced value could not be measured with STS was measured at the grain boundaries. The density of states of the rear-surface was similar to that of the UHV annealed absorbers. This finding must be taken into account when discussing why Cu-rich material does not perform well in solar cells compared to Cu-poor absorbers. The detrimental Cu_xSe secondary phase, which can be etched off on the front-side is also present at the rear-surface, increasing thereby the back-surface recombination velocity. In the absence of a suitable back-surface field, this may be very detrimental for device performance. Finally it is important to note that it is likely that similar processes occur in other selenium based absorbers layers such a $Cu_2ZnSnSe_4$ where Cu-poor growth conditions are also mandatory to reach the current record power conversion efficiencies.

Chapter 7

Impact of NaF and NaF+ RbF alkali elements on the surface properties of Cu(In, Ga)Se_2: The formation of ODC phase

Cleaning the CIGSe surface after alkali-metal post deposition treatment (PDT) is one of the important steps that need to be filled in order to achieve high power conversion efficiency. For that purpose, numerous washing strategies including distilled water rinsing [233] and diluted ammonia rinsing [32, 134, 135] were developed and are widely used in the CIGSe community. Although different alkali elements such as sodium (Na), potassium (K), cesium (Cs) and rubidium (Rb) were all found to significantly improve the performance of CIGSe solar cells, the best PDT treated CIGSe solar cell was obtained from an absorber that had undergone RbF. After treating the CIGSe with RbF PDT, a PCE exceeding 22 % was measured and was mainly assigned to the enhancement of both the open circuit voltage (Voc) and the fill factor (FF) of the film after the treatment [30]. Despite the various studies that were carried out in order to explain this outperformance, the influence of RbF treatment on CIGSe surface electronic properties is still unclear. Several mechanisms were proposed, including the formation of a thin $RbInSe_2$ secondary phase [132, 232] which in some cases acts as an extraction current barrier at the hetero-interface, or the creation of an additional downward bend bending right at the interface between the CIGSe film and CdS buffer

[33, 34] as well as the formation of a strong Cu and Ga depleted surface after RbF PDT were suggested but are still under ongoing debate. In fact, having a thick layer of $RbInSe_2$ was reported to be detrimental to the device performance, whereas a formation of a thin layer of such material at the CdS/CIGSe interface was found to be beneficial for the solar cell [133]. This suggests that the effect of RbF on the CIGSe based solar cells is not elucidated yet.

To shed more light on the impact of the NaF and RbF PDTs on CIGSe surface properties, combined KPFM, XPS, STM/STS, SIMS, and Raman techniques were employed to systematically investigate the properties of CIGSe samples, which were post-treated with NaF and RbF. Three samples were considered for the study: an as grown non-air exposed sample, a NaF and a NaF + RbF as PDT deposited samples. Additionally, the influence of rinsing with the distilled water and with the diluted ammonia solution on the NaF and NaF+RbF CIGSe treated samples was examined and discussed in detail. For this purpose, in the following the as grown non-air exposed CIGSe film will be called "Rf-CIGSe", the CIGSe PDT treated with the NaF the "NaF" and the CIGSe PDT treated with the NaF+RbF the "RbF". Details of sample preparation and how measurements were carried out can be found in section 4.3.

The chapter is divided into two main parts. In the first part (section 7.1), the surface properties of the as grown non-air exposed CIGSe (Rf-CIGSe), *i.e*, absorbers that have not been in contact with air, and which were not KCN etched were analyzed. The findings are compared to the reported results acquired from the CIGSe surface, which was exposed to air and etched with KCN. The second part (section 7.2) focuses on the investigation of the surface electronic properties of NaF and RbF samples. Here, the question about how the cleaning process affects the topography, the workfunction values, the chemical composition, and the surface electronic properties of the NaF and NaF+RbF PDTs will be addressed. The last section focuses on the discussion and brief summary of the chapter.

7.1 Surface properties of as grown non air-exposed and non chemical treated Cu(In, Ga)Se_2 absorbers

In this section, the STM/STS and KPFM results recorded from the surface of Rf-CIGSe are presented. The SEM micrograph, the PL spectrum as well as the elemental composition of the film are reported in the Appendix, in Fig. A.3 and Table A.6, respectively. After the deposition of the Rf-CIGSe absorber via PVD (pressure $\sim 10^{-9}$

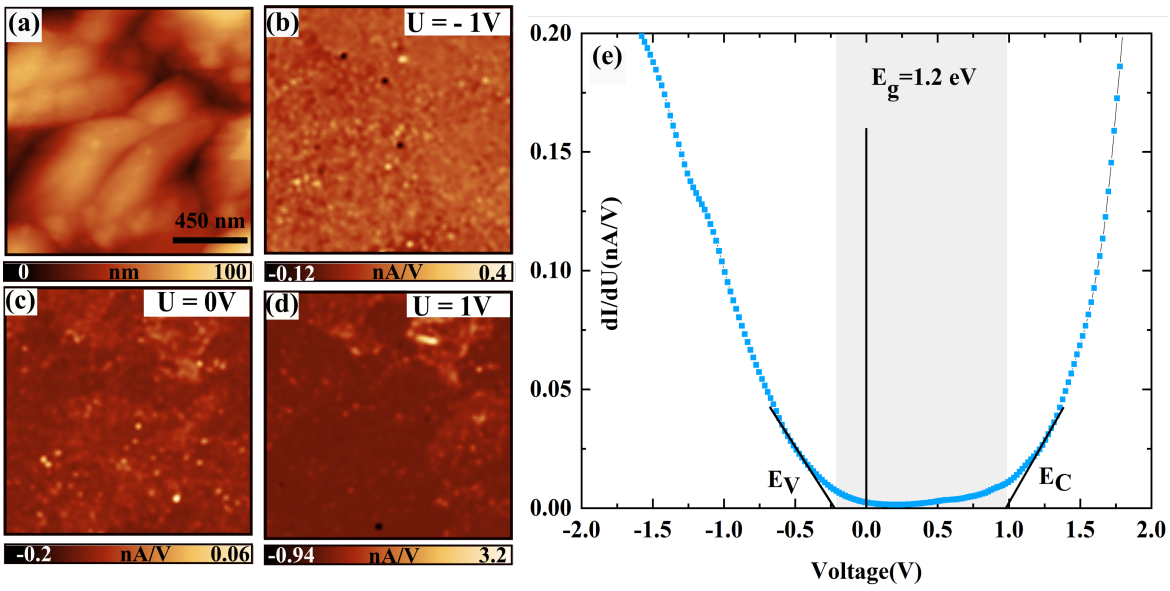

Figure 7.1: a) STM topography image presenting well defined grains and grain boundaries; (b)-(d) dI/dU-CITS maps extracted at different specific voltages, in this case at $-1\,V$, $0\,V$ and $1\,V$; (e) average dI/dU curve extracted from the region with the lower contrast[(d)]. The measurements were carried out with the V-gap of $-2V$, the current setpoint of 0.2 nA and the ramp voltage was from $-2\,V$ to $2\,V$.

mbar), the sample was immediately moved into a suitable vacuum suitcase, with a base pressure of $\sim 10^{-9}$ mbar, from there into the SPM machine to reduce the surface contamination. In Fig. 7.1, the STM topography image showing different grains and grain boundaries [Fig. 7.1(a)], the corresponding dI/dU- CITS maps extracted at different specific voltages [Fig. 7.1(b)-(d)] as well as the dI/dU average curve from the regions with the lower contrast in (d) [Fig. 7.1(e)] are depicted. Again, even in this case, all images were optimized to have the best contrast, as indicated by the scale

bar below each sub-figure. The dI/dU- CITS maps were extracted at $-1\,V$, $0\,V$, and $1\,V$ voltages because they provide better contrast to distinguish various regions that are present at the surface of the film. The map is featureless at $-1\,V$ [Fig. 7.1(b)] and shows a small variation in the contrast over the surface at $0\,V$ [Fig. 7.1(c)]. No strong variation of the density of states within individual grains, from grain to grain as well as across the grain boundaries is observed. The results exhibited no changes in the density of states across the GB/grain interface, suggesting that grain boundaries might be passivated. At $U = 1\,V$ two main regions can be identified. One with the

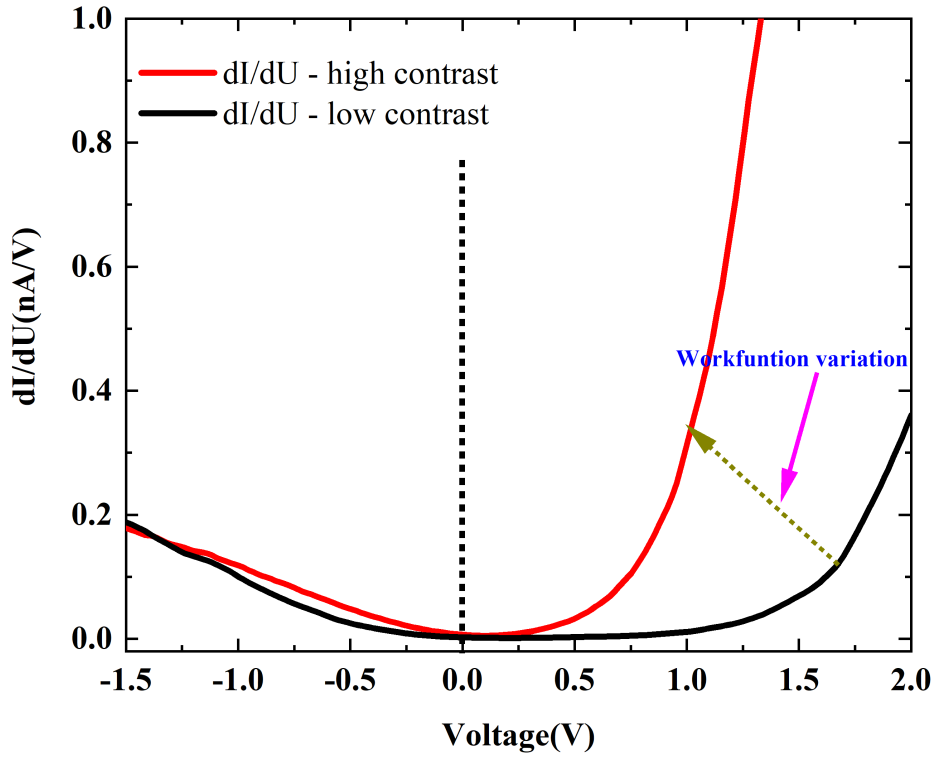

Figure 7.2: Average dI/dU curve extracted from the regions with the higher and lower contrasts. The onset between the two curves observed at the positive voltages is ascribed to difference in workfunction between the two domains. The measurements were carried out with the V-gap of $-2V$, the current setpoint of 0.2 nA and the ramp voltage was from $-2\,V$ to $2\,V$.

higher contrast and another with the lower contrast representing in total $\sim 55\%$ of the analysis area. These two different contrasts can be assigned to a difference in density of defects states at the surface of the film or to a change in workfunction. To disentangle this, some KPFM measurements were also performed, and will be discussed in the following. In Fig. 7.1(e), the average dI/dU from the region with

lower contrast presents a semiconducting like-characteristic with a bandgap of $\sim 1.2\,\text{eV}$ and the Fermi energy position close to the valence band. Regarding the region with the higher contrast, the corresponding dI/dU curve (Fig. 7.2) exhibits a semiconducting behavior as well, but this time, with a Fermi energy position close to the conduction band. The onset observed at the positive voltages in Fig. 7.2, is as indicated above and also reported by H. Mönig *et al.* in Ref. [37], ascribed to a difference in workfunction between the region with high and low contrasts. These findings suggest semiconducting properties, and zero finite conductance $[dI/dU(E_f) = 0]$ at the Fermi energy level of the Rf-CIGSe sample surface. It is important to point out that the measurements were repeated at several spots microscopically distinct from one to another using different tips and the results were similar. Only a few grain boundaries have shown a slight increase in the density of defect states. This can be seen in Fig. 7.3 where one of the grain boundaries exhibiting such augmentation of the DOS is highlighted by the green dots circle. The dI/dU map is displayed at $\text{U} = 0\,\text{V}$ only, because, it is the voltage at which the grain boundary was clearly resolved. Alike analysis was performed on CIGSe

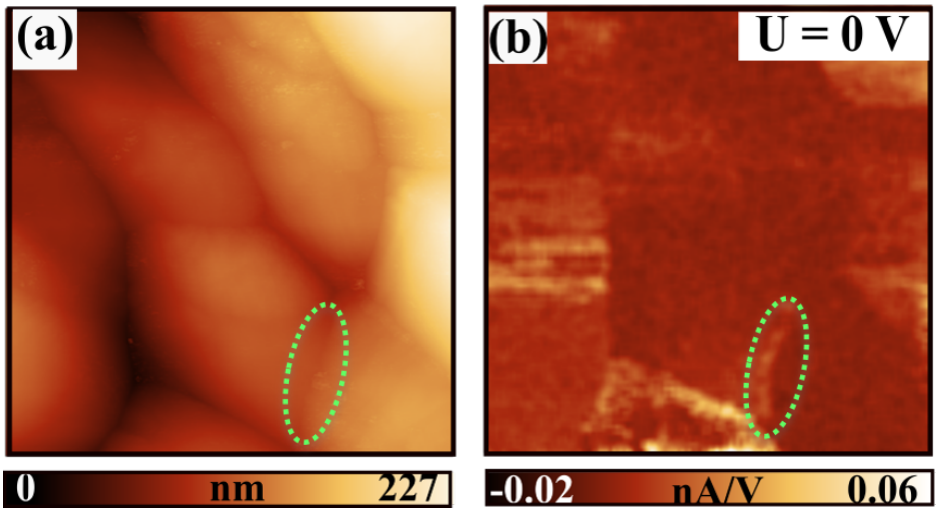

Figure 7.3: STM/STS data of one of the regions of interest studied on Rf-CIGSe surface. (a) STM topography image, (b) dI/dU map at the Fermi level position (U=0 V). The dI/dU map was extracted at U=0 V because at this specific voltage, the grain boundary could be clearly resolved. The GB which exhibits an increase in the density of states compared to the surface of the grains is highlighted by the green dots circle.

samples that were exposed to air and KCN etched [37]. The former authors reported a

strong variation from grain to grain and within grains, and a reduced density of states at grain boundaries. Their results are not in line with the findings presented here. First, most grain boundaries of Rf-CIGSe sample do not show a change in the local density of states as compared to the grains. Besides, the sturdy variation of density of states observed on air exposed/KCN etched samples was ascribed to different degrees of oxidation of the absorber after exposing them to air [38] or to some additional defect states induced by KCN etching [158], which both are absent in the case of the vacuum transferred samples. Therefore, the results acquired from the Rf-CIGSe suggest that the features observed at the surface of the samples after exposing to air or after KCN etching them might not reflect the pristine electronic properties of the film. In contrast to the air exposed/KCN etched absorber, the Rf-CIGSe sample has not shown a strong variation in the density of states across the surface of the film and has exhibited a semiconducting-like characteristic.

In Fig. 7.4, FM-KPFM results performed on the Rf-CIGSe surface are depicted. The KPFM topography image presenting different grains and grain boundaries is displayed in Fig. 7.4(a) and the corresponding workfunction map in Fig. 7.4(b). The

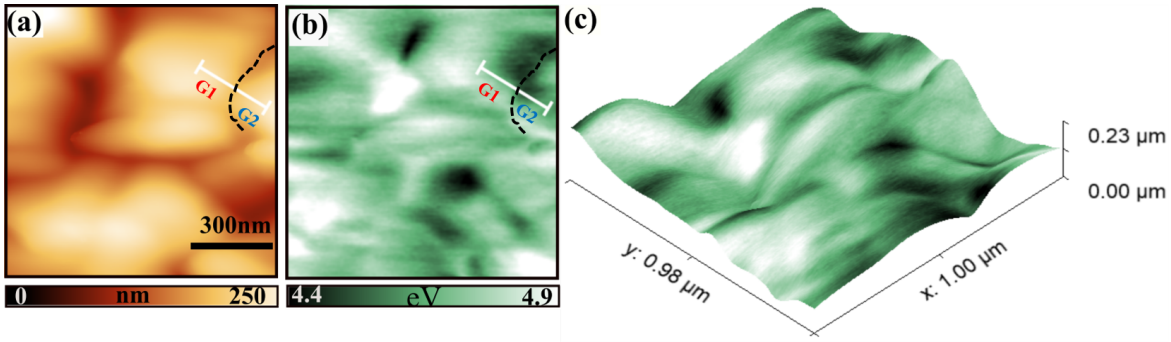

Figure 7.4: Topography and workfunction images of the Rf-CIGSe film adapted from Evandro *et al.* [227]. (a) topography image displaying well-defined grain and grain boundaries; (b) workfunction map showing a workfunction value that varies between 4.4 eV and 4.9 eV; (c) 3D image of the topography overlaid with the workfunction map. The measurements were carried out in UHV using FM mode KPFM. G1 and G2 refer to grain 1 and to grain 2, respectively. The interface between them, as highlighted by the black dots curve, is the so-called grain boundary in polycrystalline CIGSe.

topography image shows a peak to peak height variation of ~ 200 nm. The workfunction map exhibits a strong variation of the workfunction over the surface of the samples

and a smooth variation accross grain boundaries. Interestingly, the map reveals several domains with two main ones, which present a very bright contrast and a very dark contrast exhibiting thus higher and lower workfunction values, respectively. The workfunction difference between these important regions is $\sim 500\,\mathrm{meV}$. As demonstrated in Section 6.1, this workfunction difference of 500 meV between the two patches is 5 times higher than the minimum workfunction (100 meV) which is needed in order to see the effect of the workfunction of a sample in the STS spectra in STM/STS. Therefore, it is concluded that the strong variation observed on the $dI/dU - CITS$ map at U=1 V, in STM/STS data is not linked to difference in bandgap but is due to the variation in workfunction over the surface of the sample.

Following the approach proposed in Ref. [220] both topography and workfunction images are merged onto one three dimensional representation and are shown in Fig. 7.4(c) to check whether there is a link between the change in workfunction and facet contrasts present at the surface of the sample. It is clearly seen that most of the contrast are facets related. To corroborate this and therefore analyze the change in workfunction at the GB/grains interface, line profiles perpendicular to the grain boundaries were investigated. The analyses were done on various regions of interest with the one depicted in Fig. 7.4 included. To illustrate how the investigations were performed, lines profiles extracted from the grain boundary located at the interface between G1 and G2 (see Fig 7.4) are shown in Fig 7.5. G1 and G2 refer to grains 1 and 2. To reduce the noise level, each curve was obtained by averaging fifteen neighbor line profiles across each grain boundary. Fig. 7.5(a) depicts the data recorded while the probe is scanning in the forward direction (line profile trace) and Fig. 7.5(b) the ones acquired when it is scanning in the backward direction (line profile retrace). A similar approach was applied for all grain boundaries present in Fig. 7.4(a). The result is reported in the Appendix (Figs. A.4, A.5 and A.6). The outcomes exhibit that the minima of the grain boundaries do not appear at the same position as the minima/maxima of the workfunction suggesting that the workfunction contrast observed arises mostly from facet contrast and not from the grain boundaries [see Fig. 7.5(a) and retrace Fig. 7.5(b)]. The analyses were reproduced on different other areas of interest and similar observation was seen. It is important to point out that all these observations are opposite to what was measured at the surface of air exposed KCN

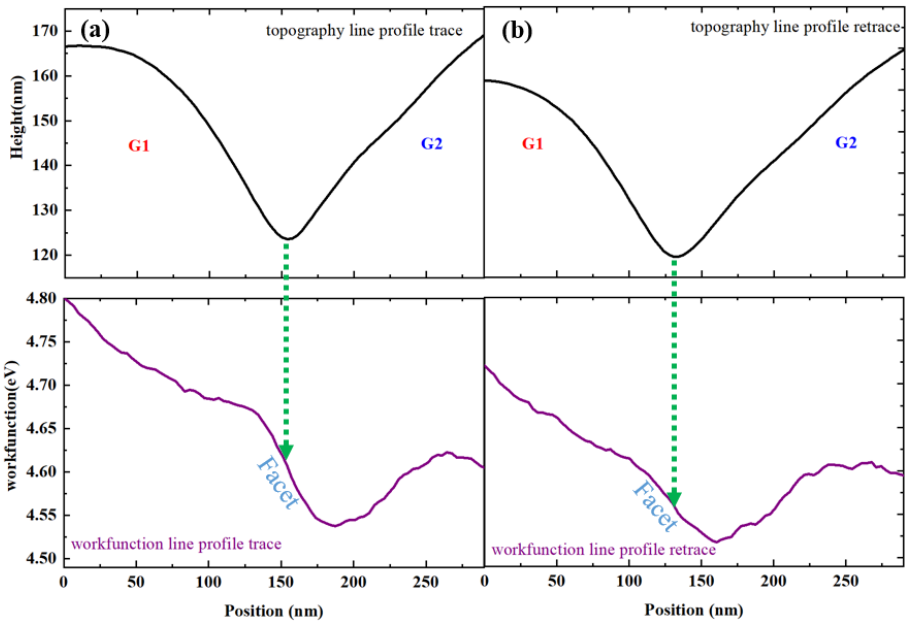

Figure 7.5: Topography and workfunction line profiles extracted from GB located between G1 and G2: (a) line profiles recorded when the probe is scanning in the forward direction, (b) line profiles recorded when it is scanning in the backward direction. G1 and G2 refer to grains 1 and 2.

etched samples [158, 37].

It is shown in the literature [227] that in order to measure an accurate workfunction value of a sample, it has to be cleaned and free of any contamination. In addition, FM mode KPFM that is largely recognized as the KPFM mode that provides a credible accuracy and better lateral resolution needs to be used for measurements [226, 227]. Although those recommendations were respected, *i.e*, FM mode KPFM was used for the analyses and the sample was transferred in UHV to avoid any contamination, the aspect of the UHV cross-contamination was scrutinized. Fig. 7.6 displays topographies (a-c) and workfunction maps (d-f) of the Rf-CIGSe measured immediately after growth [Fig 7.6(a, d)], after keeping it in UHV for a few weeks [Fig 7.6(b, e)] as well as after UHV annealing it at 200° C for 30 minutes [Fig 7.6(c, f)]. Note that the annealing temperature was chosen such as the loss in Se, which is one of the most volatile elements in CIGSe compound could be neglected. The findings exhibit an average workfunction of approximately (5.1 ± 0.1) eV for Rf-CIGS fresh sample which drops to (4.3 ± 0.1) eV after keeping the sample in UHV for a few weeks and completely recovered after UHV annealing steps. The value of the workfunction achieved (5.07 ± 0.01) eV after

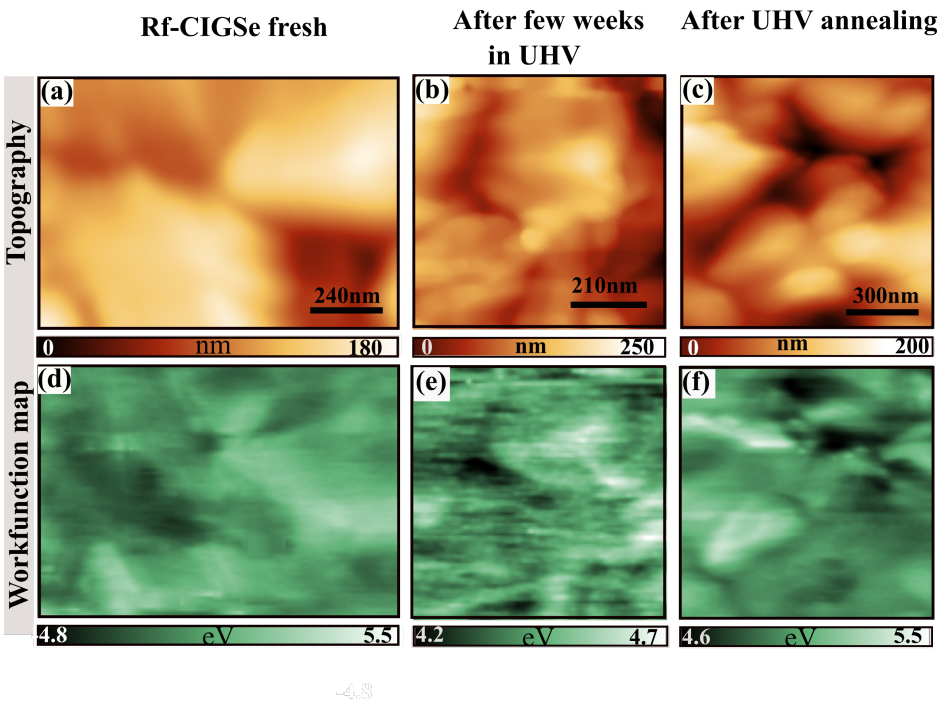

Figure 7.6: Exploration of the UHV cross-contamination of a Rf-CIGSe sample by means of FM-KPFM. (a-c) AFM topography images and (d-f) the corresponding work-function maps. (a-d) represent the data acquired from the Rf-CIGSe fresh sample, *i.e*, the Rf-CIGSe measured directly after introducing it into the SPM machine; (b-e) the data from the same sample after keeping for few weeks in UHV, (c-f) show results after UHV annealing it at 200° C for roughly 30 minutes. The scale below each subfigure was individually optimized with the aim to have better contrast for each image.

UHV annealing is similar to the one of as grown fresh CIGSe sample. This variation in workfunction is also shown in a corresponding histogram depicted in Fig. 7.7. Fig. 7.7 clearly shows that the workfunction of Rf-CIGSe fresh and UHV annealed samples are similar, and are $\sim$ 1.2 times higher than the one of the sample that was kept in UHV for a few weeks. Such a decrease in workfunction after leaving a sample in UHV was also measured at the surface of a single crystal CIGSe sample [227] and was ascribed to change in surface dipole induced by the adsorbates. These results showed that even when the sample is transferred under UHV conditions, its workfunction may be strongly different from the as grown fresh sample workfunction value if one leaves it in UHV for sometime. Nevertheless, after UHV annealing the workfunction recovers to the initial value indicating that changes at the surface of the sample induced by adsorbates have not permanently modified the electrostatic

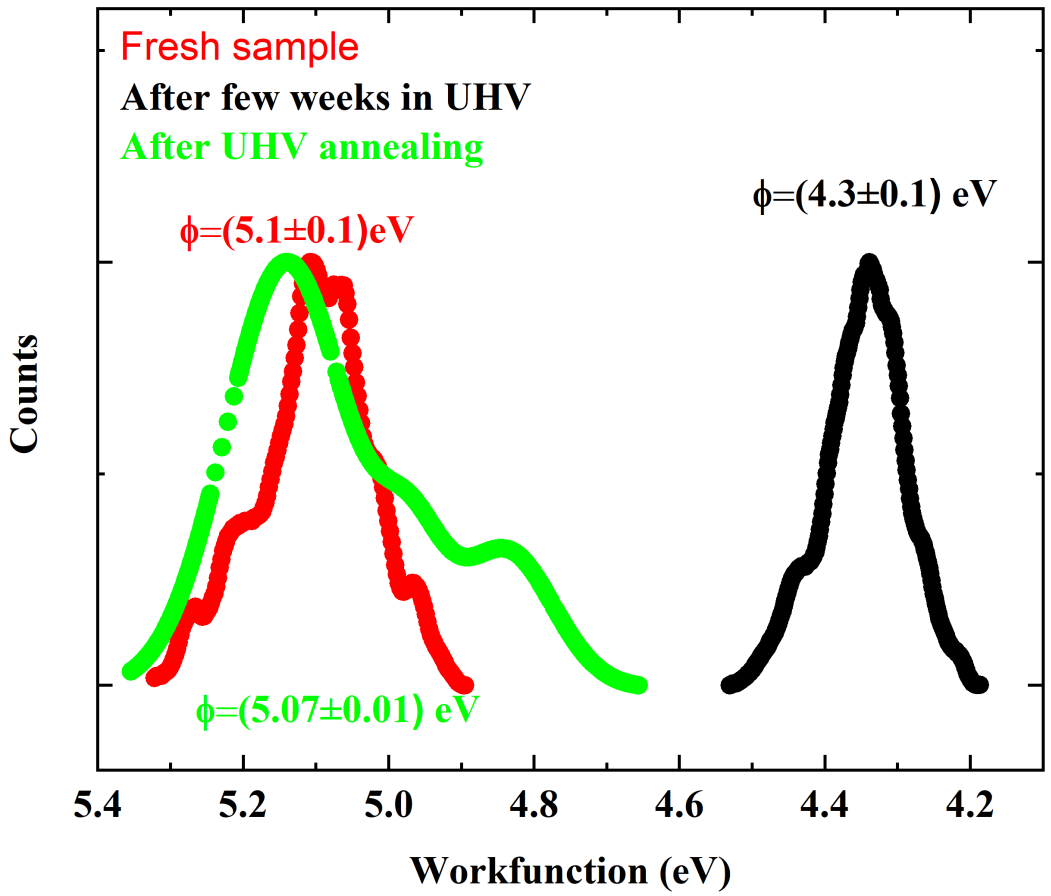

Figure 7.7: Distributed spectra acquired from the Rf-CIGSe fresh sample, the sample that has been kept in UHV for a few weeks as well as from the sample that was UHV annealed at 200^{o}C for 30 minutes. The red, black and green dots curves are extracted from the fresh, the sample kept in UHV and the UHV annealed sample, respectively. The values presented in the graph represent the average workfunction values (ϕ) from different analysis areas, which are microscopically distinct one from the another. Therefore, the errors indicate on those values are the standard deviation errors.

landscape [227] of the polycrystalline CIGSe sample. Thus, annealing in UHV can be considered as an alternative to clean the surface of a sample that initially was not exposed to air and was free of all contamination and moisture, but, which was kept in UHV for sometime.

The following sections will be mainly based on results achieved from the NaF and RbF samples.

7.2 Effect of NaF and RbF PDTs on Cu(In,Ga)Se_2 surface

In this section, the surface properties of the RbF and NaF samples were investigated and critically discussed. The basic idea is to examine how the electronic and chemical properties of the samples vary with respect to the rinsing process. Hence, the samples were analyzed as grown, and after rinsing them with the deionized water (H_2O) and diluted ammonia solution (NH_4OH), respectively. The description of the cleaning procedure is reported in subsection 4.3.1. As indicated earlier, the samples were grown in EMPA using a multistage low-temperature co-evaporation process. Detailed information regarding the growth process can be found in [52]. Immediately after growth, they were shipped in a nitrogen sealed transport box to the scanning probe microscopy (SPM) laboratory of the University of Luxembourg and were introduced into a N_2 filled glove box ($H_2O \leq 1$ ppm, $O_2 \leq 1$ ppm) within the same day to minimize their exposure to air.

7.2.1 Variation of the workfunction of the RbF and NaF samples as a function of the various rinsing process

Fig. 7.8 shows topography and corresponding workfunction maps recorded from the RbF sample after each treatment. All the analyzes were performed in a nitrogen environment to minimize any exposure to air and moisture. In Fig. 7.8(a) the topography image acquired from the as grown sample is presented. The result reveals that the sample is covered with granular structures, which are very densely spread across its surface. Those precipitates represent roughly 45 % of the surface and show lower workfunction (4.9 ± 0.1) eV as compared to the average workfunction value (5.0 ± 0.1) eV of the sample [Fig. 7.8(d)]. With such agglomerations, it is hard to identify the grains or grain boundaries, neither on the topography or on the workfunction map.

After rinsing the sample with deionized water, the topography image shows some CIGSe features [Fig. 7.8(b)], and the workfunction map exhibits a reduction in the low workfunction structures [Fig. 7.8(e)], suggesting thus a partial removal of some surface residues. Approximately 27 % of the precipitates with a workfunction of (4.6 $\pm$ 0.1) eV are still present at the surface of the water rinsed sample. The same results

were observed after cleaning the samples for 30 seconds, 1 minutes and 5 minutes with H_2O. At this point, it is clear that rinsing the RbF sample with only distilled water is not efficient in removing the surface residues.

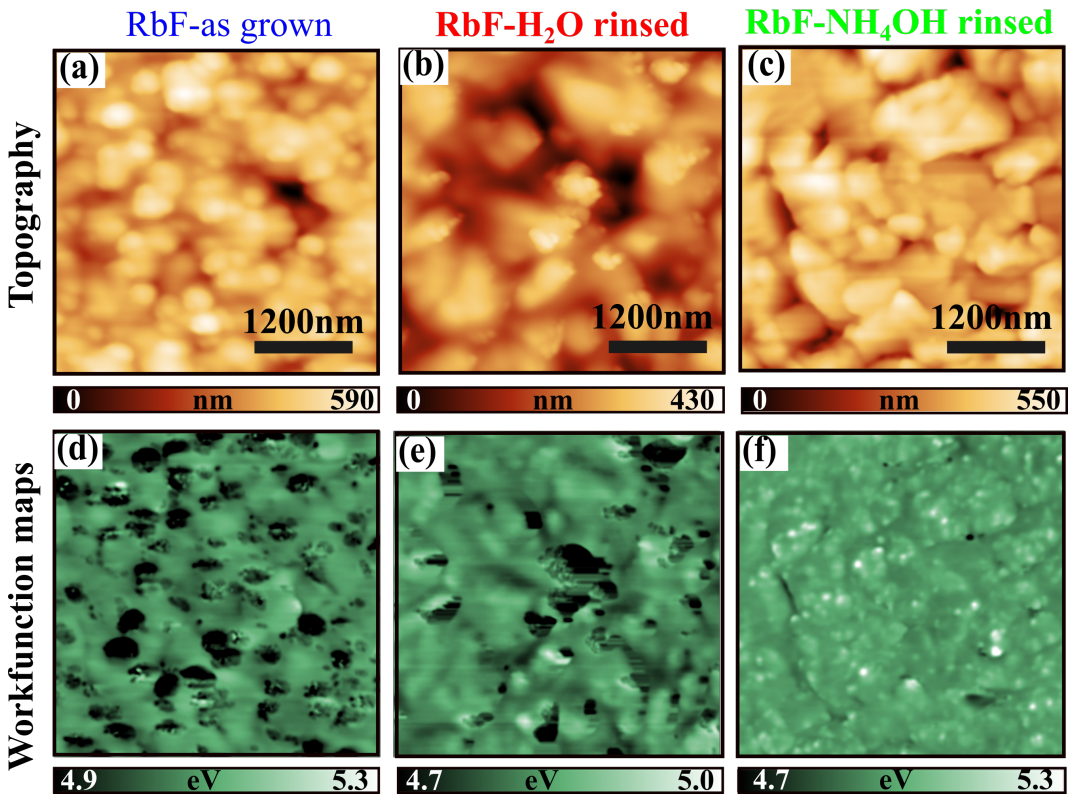

Figure 7.8: FM-KPFM data of RbF sample; (a-d) as grown sample; (b-e) RbF sample after rinsing with the distilled water; (c-f) RbF sample after rinsing with the diluted ammonia solution.

After ammonia rinsing, a clean topography with well known grains and faceted CIGSe surface are observed [Fig. 7.8(c)]. All the surface residues that were found at the surface of as grown and water rinsed samples are not there anymore. In contrast to the results achieved from the as grown sample, the workfunction map [Fig. 7.8(f)] exhibits high workfunction structures of (5.3 ± 0.1) eV with the average workfunction of the surface of (5 ± 0.1) eV. The findings confirm that ammonia cleaning allows removing most of the precipitates with the lower workfunction that was present at the surface of the sample before cleaning the sample with NH_4OH. Hence, it is concluded that ammonia rinsing is an efficient method to remove the surface residues from the surface of the CIGSe samples that were pre-treated with NaF+RbF alkali metal.

Alike measurements were carried out on the NaF sample for comparative purposes.

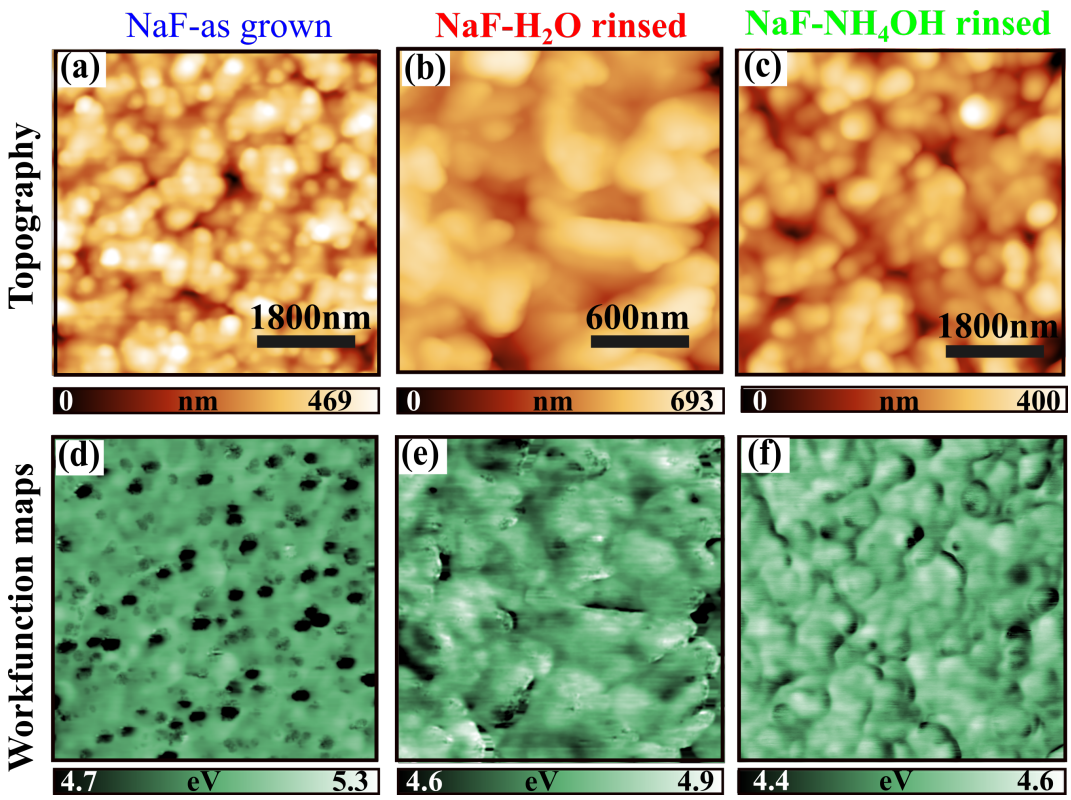

Figure 7.9: FM-KPFM data of NaF sample; (a-d) as grown sample; (b-e) NaF sample after rinsing with the distilled water; (c-f) NaF sample after rinsing with the diluted ammonia solution.

The results are shown in Fig. 7.9. In Fig. 7.9(a)-(d), the KPFM data obtained from the NaF as grown is depicted. The images are similar to the results acquired from the RbF as grown sample. The topography shows that the surface of the NaF sample is also densely covered with granular structures [Fig. 7.9(a)]. The workfunction map [Fig. 7.9(d)] exhibits that the workfunction of those precipitates is lower (4.4 ± 0.3) eV compared to the average workfunction value of the sample (4.9 ± 0.2) eV. Furthermore, the average workfunction of NaF and RbF samples are very close one to another. Although the findings shows a strong correlation between the two samples, it is difficult to say at this stage that the granular structures observed on both sample surfaces have the same origin. The samples were post-treated differently. One sample was treated with NaF only and another one with NaF and RbF.

In contrast to the RbF sample [Fig. 7.8(b)-(e)] where it was shown that rinsing with the distilled water is not enough to remove all the patches from the sample surface, the NaF sample shows a clean topography and workfunction map already after the

H_2O cleaning [Fig. 7.9(b)-(e)]. The precipitates that were found on the as grown sample completely disappeared after rinsing the sample with the purified water. The data become cleaner after NH_4OH washing [Fig. 7.9(c-f)]. Nevertheless, the average workfunction of the NaF NH_4OH rinsed sample (4.5 ± 0.3) eV is lower than that of the RbF NH_4OH rinsed sample (5 ± 0.1) eV. The reason for this difference in workfunction between the two sample is not clear at present, however, will be closely investigated below. Nonetheless, it is speculated that this variation in workfunction can be due to a difference in electron affinity or surface band bending between the two samples.

7.2.2 Changes in surface chemical composition of the film after different cleaning processes

In order to analyze what happened at the surface of samples after each treatment and to investigate whether there is a link between the variation in workfunction presented above and the change in chemical composition, the surface of as grown, the water (H_2O), and ammonia (NH_4OH) rinsed RbF samples were systematically explored with XPS. Their survey spectra are plotted in Fig. 7.10. All curves were normalized for better visualization. Additional to the elements embedded in the CIGSe matrix, it was found that the surface of RbF as grown sample is covered with a lot of sodium, fluorine and a bit of rubidium. The results reveal almost no signature of copper and gallium elements at the surface of the film. This depletion of Cu and Ga after RbF PDT is known and is well documented [32, 232, 255, 233]. After washing the samples with water or ammonia, sodium and fluorine completely disappeared. However, the H_2O rinsed samples still do not exhibit any signature of Cu at the surface although a small signal of Ga is detected. Besides, a tiny amount of rubidium is detected after H_2O and NH_4OH rinsing steps. As the signal from the H_2O rinsed sample has only shown a clear signature of Ga, In, Se, and a little bit of Rb, it is assumed that either the amount of Cu present at its surface is below the detection limit of XPS or its surface is fully covered with a thin layer of $RbInSe_2$ secondary phase as widely reported in the literature [134, 232, 233].

After NH_4OH cleaning a slight signal of Cu is observed, suggesting that the Cu-free compound that was formed at the surface of as grown and water cleaned film is gone. This finding is in good agreement with our KPFM data where it was shown that

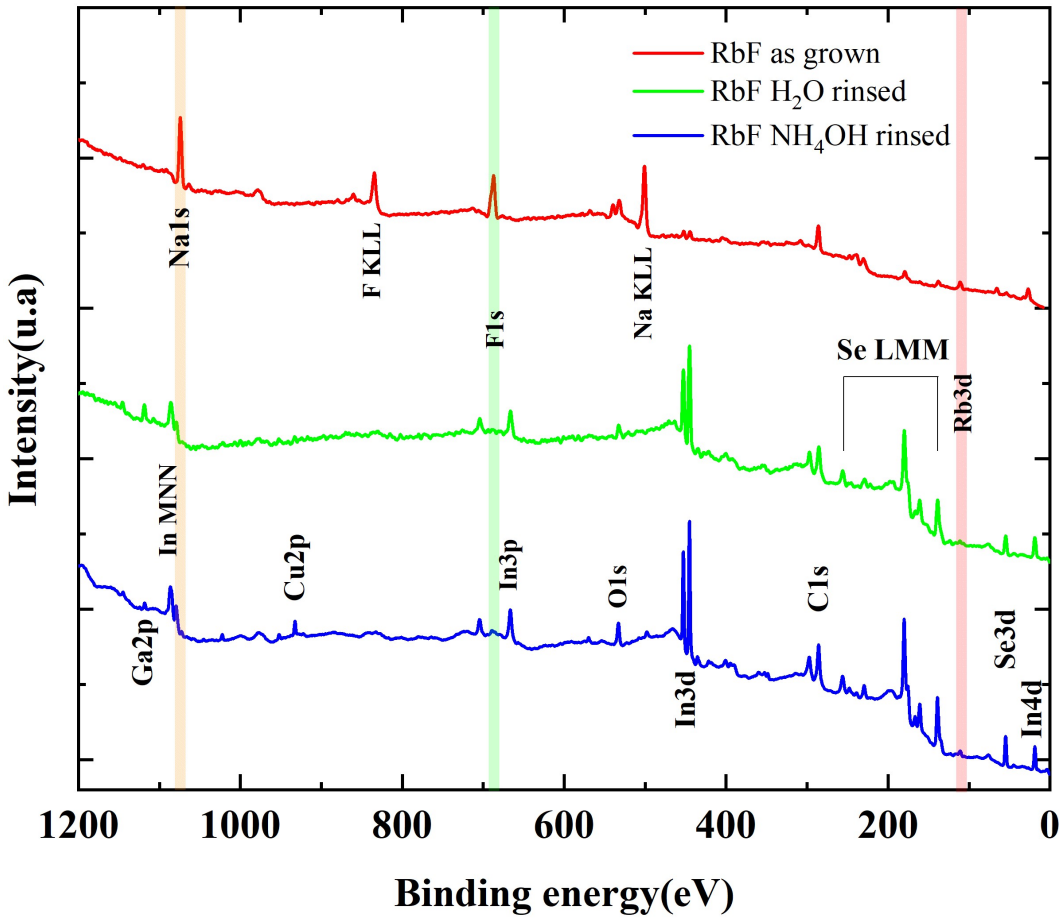

Figure 7.10: Survey spectra of RbF film measured as grown, after water and ammonia rinsing step. All spectra were normalized for better visualization.

removing the residues from the surface of RbF amples required necessarily the use of ammonia. The surface of the ammonia cleaned samples clearly exhibits all elements of CIGSe along with a tiny bit of rubidium. Other than the Cu, In, Ga and Se elements enclosed in the CIGSe compound and the alkali elements and their residual fluoride, a tiny contamination of oxygen was also detected at the surface of the three samples (see Fig. 7.10). This negligible amount of oxygen indicates that the transfer from the PVD to the XPS analysis chamber was successful and will not be further discussed in this work. A similar study was also carried out at the surface of the CIGSe film deposited using the same recipe but which was post-treated with sodium fluoride only (the NaF sample). The result is presented in Fig. 7.11.

Except the fact that a clear signal of Rb was seen on RbF samples, the surface of the two samples looks more or less similar in term of sodium and fluorine contents. A huge amount of sodium and fluorine, which is completely washed away after cleaning

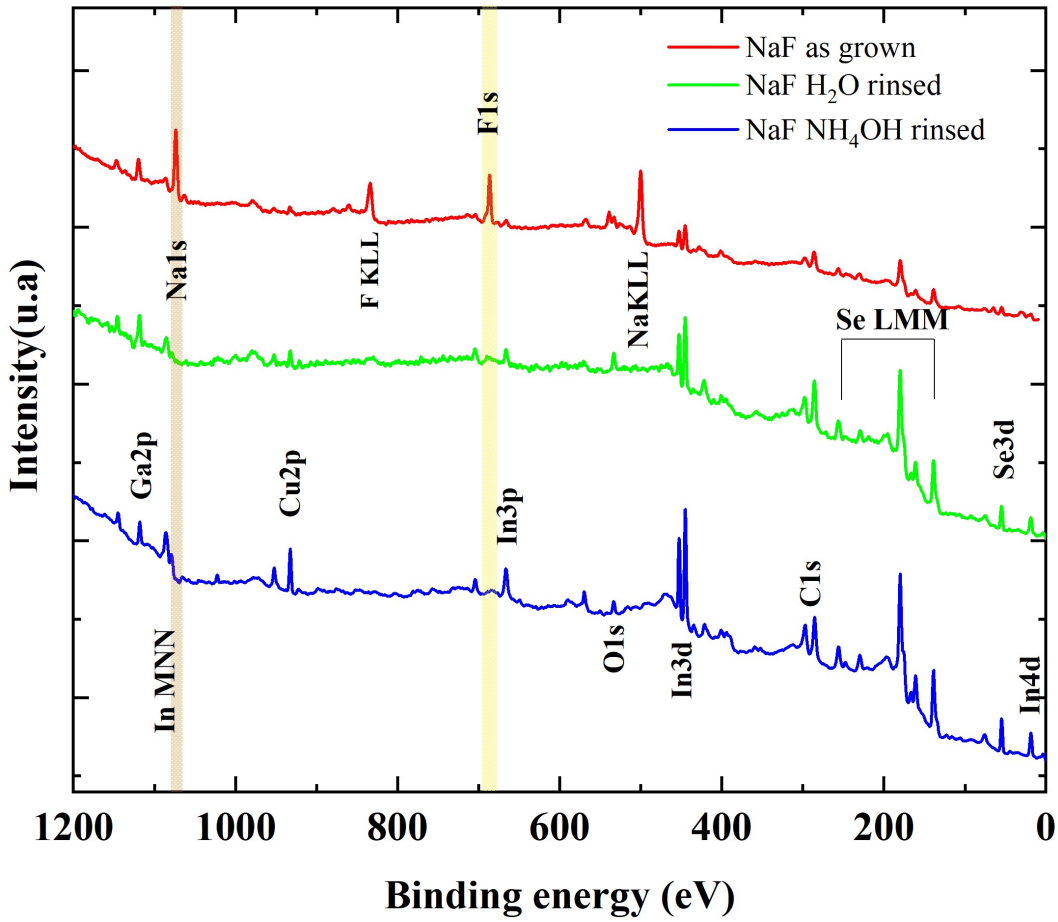

Figure 7.11: Survey spectra of NaF film measured as grown, after water and ammonia rinsing step. All spectra were normalized for better visualization.

was observed. Nevertheless, it is important to emphasize that in this case, a tiny signal of Cu is seen at the surface of non cleaned sample. This small signal of Cu slightly and strongly increases after rinsing the samples with water and ammonia, respectively. To compare the two samples, the survey spectra of both samples acquired as grown and after water, and ammonia cleaning are simultaneously plotted in Fig. 7.12(a), (b), and (c), respectively. The only big change that can be highlighted right now is the difference in Cu content between the two absorbers. The NaF sample exhibits a higher signal of Cu, which is more pronounced after NH_4OH cleaning than the RbF sample. This observation was already reported in literature. It is well-known in the CIGSe community that in contrast to light alkali elements, heavier alkali PDT make the surface of the film to become more Cu-depleted [77, 87, 134, 256, 257].

In Fig. 7.13, high resolution XPS spectra of Rb3d, In3d, and Se3d are presented with the corresponding curve fits. All considered peaks were fitted using the same

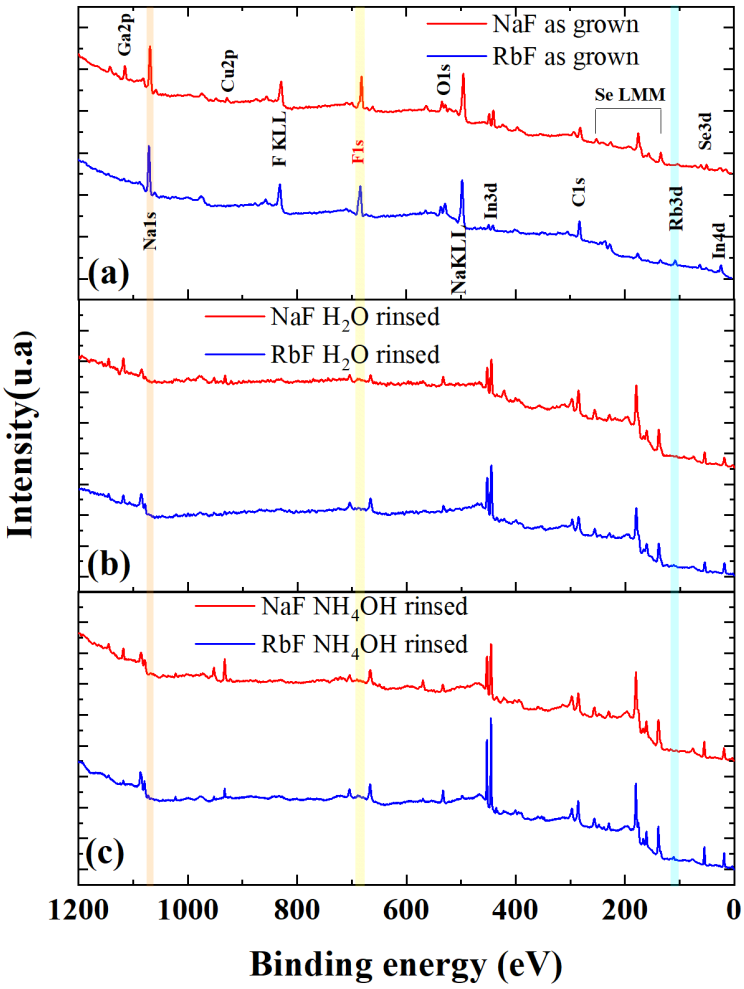

Figure 7.12: Comparative study between NaF and RbF samples. (a) survey spectra of as grown films, (b) and (c) the ones of water and ammonia rinsed samples. All spectra were normalized for better visualization.

Voigt function with a constant full width half maximum and background for each specific element. The first focus was on Rb3d, In3d, and Se3d signals mostly because they exhibit various interesting features after each treatment. In fact, for each of these elements, the results exhibit different chemical environments before the cleaning process, which slightly reduce after water cleaning and collapse to only one environment after ammonia washing. However, the detailed XPS signals of Cu2p, Ga3d as well as the ones of Na1s and F1s were also analyzed and are depicted in the Appendix (Fig. A.7).

On the surface of RbF as grown sample, several dissimilar peaks indicating different chemical environments for Rb, In, and Se are observed. For convenience purposes, they are named I, II, and III. In Fig. 7.13(a) the measured data of Rb is presented. Two different doublet peaks appearing at binding energy (E_B) of 113.0 eV ($Rb3d_{III}$) and

111.05 eV ($Rb3d_{II}$) are seen. The values given here as well as the ones that will be given later in this Chapter refer to the highest peak of the spin-orbit doublet, *i.e.*, the peak located at the total angular momentum 5/2. As suggested in [232, 233] where similar features were observed, the doublet peak at higher binding energy is presumably assigned to RbF and the double peak at lower binding energy to $RbInSe_2$ secondary phase. The first statement is in good agreement with the survey spectra acquired from the same sample where it was found that the surface of the film is more or less entirely covered with sodium and fluorine. The later statement will be thoroughly explored in the following.

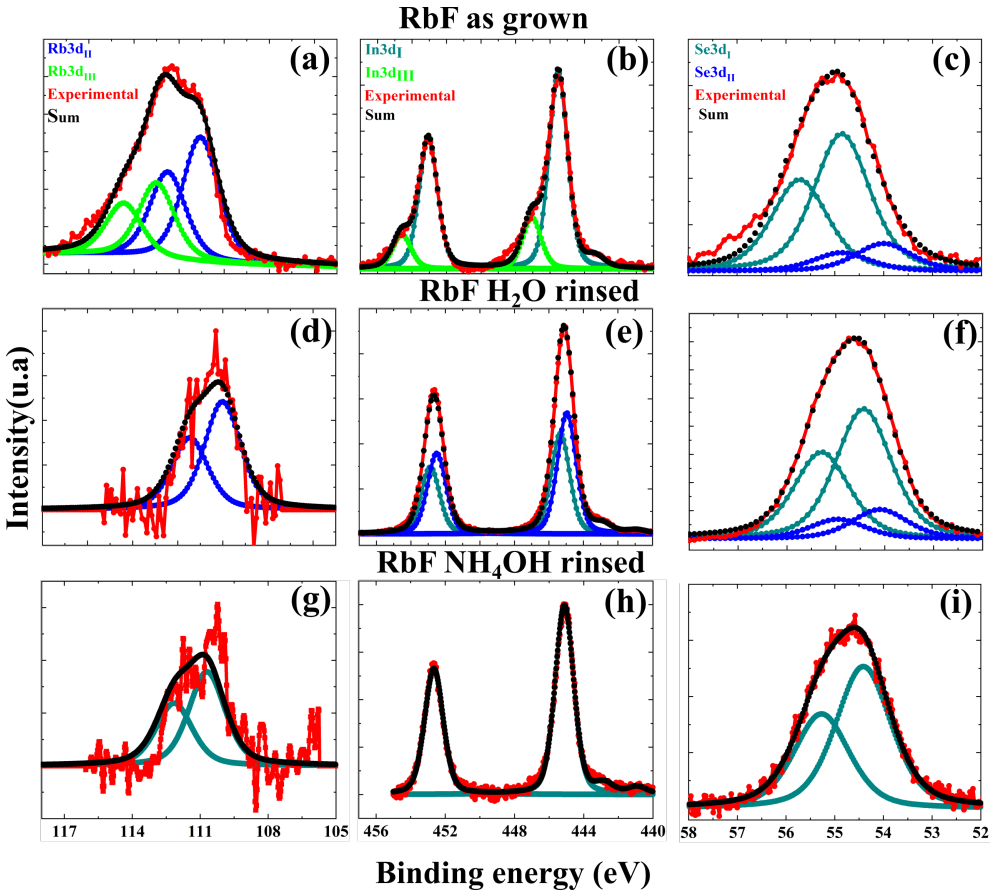

Figure 7.13: High resolution XPS spectra of Rb3d, In3d, and Se3d of RbF as grown, after H_2O and NH_4OH cleaning together with their curves fits, respectively. (a)-(c) show detailed XPS spectra from the as grown sample; (d)-(f) show the data acquired from the H_2O rinsed sample, (g)-(i) show the measured data acquired from the NH_4OH rinsed samples. The detailed XPS signals of Cu2p, Ga3d as well as the ones of Na and F is depicted in the Appendix.

Although the results exhibited several different peaks as reported in the literature,

it is important to point out that the binding energies that are measured are $\sim$ 2.1 eV higher than the ones reported by J. Bombsch *et al* [233] and N. Maticiuc *et al* [232]. Usually, such high binding energy is attributed to surface band bending or the charging effect. But neither of the two speculations is fulfilled here. Although all the signals were acquired in one run and in series, this shift to higher binding energy was observed only for the Rb. In general, to talk about surface band bending or the charging effect in XPS, the peaks of all elements enclosed in a sample should shift in the same direction and with the same energy. Such behavior was not observed suggesting that the feature that is observed for Rb elements in RbF as grown sample is not an XPS artifact and is not due to surface band bending, but, might be associated with a change in the chemical environment of the Rb. It is important to emphasize that the three samples were prepared differently, which might have an effect on the chemical state of the Rb. The measurements presented in this work were performed on RbF as grown sample, whereas the J. Bombsch *et al* and N. Maticiuc *et al*'s results were acquired from the RbF PDT samples that were rinsed with water and ammonia, respectively. Hence, ascribing this difference in the binding energy of Rb to how the sample has been chemical treated makes sense. There were still a lot of alkali metals [Fig. 7.10] and their corresponding residual [Fig. A.6(c), (d)] present at the surface of the sample investigated in our case. However, due to the long duration of measurements, approximately $6h$ in the present case, note that the effect of momentary charging effect when acquiring Rb signal can not be completely excluded.

Fig. 7.13(b) and (c) show the In and Se signals acquired from the same film. The presence of various chemical environments observed illustrates that the sample surface does not only have elements enclosed in the CIGSe. The indium data exhibits two different doublet peaks located at 447.05 eV ($In3d_{III}$) and 445.5 eV ($In3d_{I}$), and Se two distinct doublet peaks positioned at 54.86 eV (Se_{I}) and 54 eV (Se_{II}). As mentioned above, these peaks can help to determine the different segregation phases or compounds present at the surface of the sample. For example, the In binding energy of 445.5 eV and Selenium binding energy of 54.71 eV measured fit well the In and Se E_B values extracted from the bare CIGSe [258]. This indicates that the surface of the sample analyzed may be partly covered with CIGSe. At the same time, the Se peak at 54 eV is close to the ones measured at the surface of RbF PDT absorber

[232]. Furthermore, the indium peak positioned at higher binding energy is close to the tabulated value of In binding energy in the InF_3 compound. Therefore, it is concluded that the surface of as grown RbF sample exhibits three different compounds: the CIGSe, InF_3 and $RbInSe_2$. These findings are also in good agreement with the KPFM findings depicted earlier where different workfunction values were measured over the surface of the sample.

After washing the sample with water, all fluorine-related peaks ($Rb3d_{III}$) and ($In3d_{III}$) completely vanished [Fig. 7.13(d) and (e)]. The water rinsed surface remains only with one Rb doublet peak that in this particular case is assigned to $Rb3d_{II}$, and two more pronounced doublets of In and Se. The binding energy that is measured for $Rb3d_{II}$ (110.01 eV) is close to the values proposed in Ref. [232]. The two indium peaks are located at positions 444.96 eV ($In3d_{II}$) and 445.33 eV ($In3d_{I}$) and the selenium ones at 54.43 eV ($Se3d_{I}$) and 54.10 eV ($Se3d_{II}$). The binding energies values that are measured for $Rb3d_{II}$, ($In3d_{II}$) and $Se3d_{II}$ are in line with the binding energy measured for these elements in $RbInSe_2$ [232]. Additionally, the $In3d_{I}$ and $Se3d_{I}$ binding energies are similar to the reported values on CIGSe absorbers [258]. Therefore, it is deduced that after rinsing the sample with water, the InF_3 phase that was observed on non rinsed completely vanishes leaving behind a surface which is partly composed of CIGSe and $RbInSe_2$ secondary phase as already reported in the literature.

To mimic the standard chemical rinsing process that is commonly conducted prior to the deposition of the buffer and window layers of the CIGSe based solar cell, the sample was thereafter cleaned in 1 molar solution of NH_4OH and was re-explored. Interestingly, in contrast to as grown or water rinsed samples where various chemical surroundings assigned to a mix of a strong Cu-poor CIGSe phase and a $RbInSe_2$ secondary phase were measured, only a single chemical environment was seen after ammonia rinsing [Fig. 7.13(g-i)]. The binding energies of In3d (445.11 eV) and Se3d (54.4 eV) nicely fit the values reported for CIGSe compound, indicating that they are not oxidized. The Rb elements found at a binding energy of 110.70 eV is therefore assumed to be bounded to CIGSe as suggested in [232]. Although there is still a bit of Rb present at the surface of the sample, in line with our KPFM no signature of residual fluoride or $RbInSe_2$ phase was detected after rinsing the sample with ammonia.

The high-resolution XPS signals of the elements enclosed in the NaF sample were

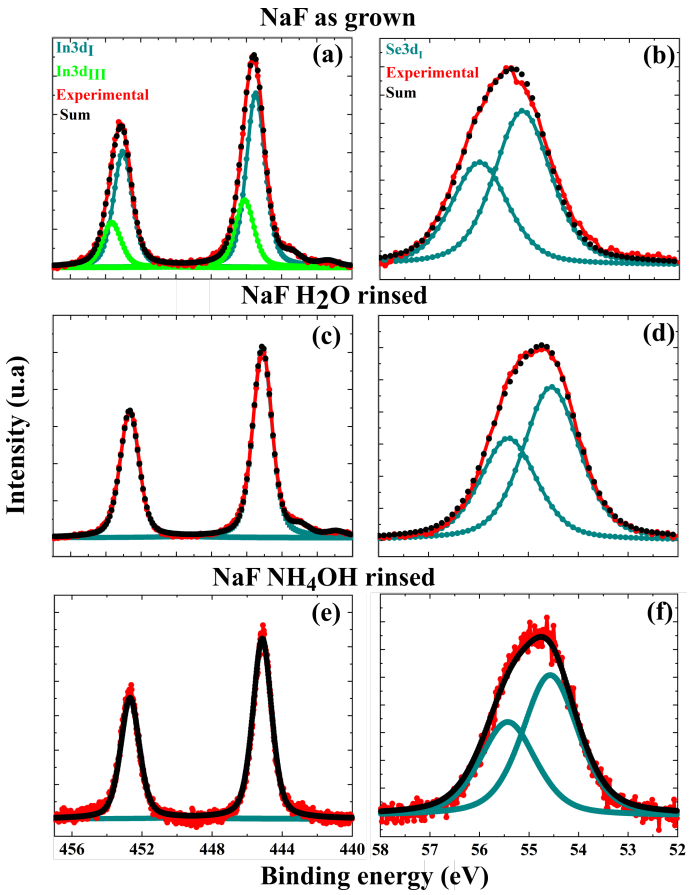

Figure 7.14: High resolution XPS spectra of elements enclosed in NaF sample as grown, after H_2O and NH_4OH cleaning together with their curve fits, respectively. (a)-(b) show detailed XPS spectra from the as grown; (c)-(d) show the data acquired from the H_2O rinsed sample, (e)-(f) show the measured data acquired from the NH_4OH rinsed samples.

also recorded. The data are displayed in Fig 7.14 for the In and Se elements. The rest of the elements, as well as the Na and F signals, are reported in the Appendix (Fig. A.8). The indium signal of as grown NaF [Fig. 7.14(a)] showed two doublet peaks with binding energies similar to the binding energy of $In3d_I$ and $In3d_{III}$ obtained from the RbF sample. The binding energies measured for $In3d_I$ and $In3d_{III}$, in this case, are 445.47 eV and 446.10 eV, which are close to the E_B values extracted from the RbF sample. Therefore, it is deduced that the surface of as grown NaF sample is also partially covered with InF_3 as demonstrated above. This finding is in line with our KPFM data. It was shown that the topography and workfunction map of NaF and RbF samples were both covered with precipitates, which have a reduced workfunction value compared to the average workfunction of the sample. After washing the sample

with H_2O, the fluorine related peak ($In3d_{III}$), as in the case of the RbF sample, completely vanished [Fig. 7.14(c)]. Nevertheless, the E_B of the remaining In signal ($In3d_I$) acquired (445.11 eV) is close to E_B value of In reported in the In_2Se_3 compound [93]. Besides, the Se3d5/2 E_B measured from the NaF distilled H_2O rinsed sample (54.54 eV) is close to one reported for Se in In_2Se_3 phase [93]. The results suggest that although a tiny signal of Cu and Ga was were after rinsing the NaF sample with H_2O, its surface might be dominated by an In_2Se_3 compound. This speculation will be argued using our STM/STS data (see section 7.2.4). After NH_4OH cleaning, the chemical properties of NaF and RbF samples are very similar in term of elements present at the surface of the samples or the binding energy that is measured. This can be seen in the following Table where a summary of the different binding discussed so far is depicted. The binding energy of other elements is reported in the Appendix, in Table A.7. However, note that a clear idea about what we do have at the surface after

Table 7.1: Summary of the binding energy of Rb, In and Se obtained from RbF and NaF as grown, after water and ammonia rinsed samples. The values into brackets are from RbF samples and the ones without brackets from Na samples. The symbol "-" means no elements detected.

specimen	NaF/RbF as grown	NaF/RbF H_2O rinsed	NaF/RbF NH_4OH rinsed
E_B $Rb3d_{II}$ (eV)	- /(111.05)	-/(110.01)	- (110.70)
E_B $Rb3d_{III}$ (eV)	- /(113.0)	-/(-)	-/(-)
E_B $In3d_I$ (eV)	445.47/(445.51)	445.11/(445,33)	445.14/(445.11)
E_B $In3d_{II}$ (eV)	- /(-)	-/(444.96)	- (-)
E_B $In3d_{III}$ (eV)	446.10/(447.05)	(-)/(-)	-/(-)
E_B $Se3d_I$ (eV)	55.14/(54.86)	54.54/(54.43)	54.57/(54.41)
E_B $Se3d_{II}$ (eV)	- /(54.0)	-/(54.10)	-(-)

ammonia cleanning is not known yet. Thus, the next sections will be mainly based on this open question.

7.2.3 Elemental mapping of the RbF sample

In order to corroborate the XPS and KPFM data, the distribution of Rb and In across the surface of the RbF sample was examined with the Helium Ion Microscopy-Secondary Ion Mass Spectrometry (HIM-SIMS). In Fig. 7.15, the map of Rb and In signals acquired from the water rinsed [Fig. 7.15(b-c)] and ammonia rinsed samples [Fig. 7.15(e-f)] as well as their respective SEM images [Fig. 7.15(a)] and [Fig. 7.15(d)] are depicted. The color bar corresponds to the intensity where the regions with the higher contrast indicate the stronger signal of the element of interest.

The SEM images nicely present the characteristic of a polycrystalline CIGSe with grains randomly oriented and grain boundaries. However, compared to the findings reported in Ref. [33] where pinholes were observed after rinsing the RbF PDT absorbers with NH_4OH, smooth SEM images are measured [Fig. 7.15(a) and (d)]. The origin of this difference in surface morphology is not clear at this point. Nevertheless, it is speculated that that can be due to differences in elemental composition between the two samples. The CGI and GGI of the sample explored in this thesis are approximately 0.96 and 0.43, whereas the ones of the sample investigated in Ref. [33] were 0.90 and 0.30.

Regarding the SIMS maps, the results revealed as in the case of XPS that there is a significant amount of Rb on the surface after water rinsing, which is then removed after ammonia etching. As highlighted by the areas underneath the blue circles in [Fig. 7.15(b)] some regions on water rinsed sample map present high concentration of Rb which is not seen after ammonia etching [Fig. 7.15(e)]. These patches can possibly be the low workfunction regions observed on the KPFM map. Although, it is hard to nicely identify the Rb on the grain boundary as the distribution seems to be random and spread across the surface, some preferential segregation of Rb at the GBs on water rinsed sample was observed (see red circles in [Fig. 7.15(b)]). The map of Rb signal recorded after ammonia rinsing is featureless in agreement with the XPS results where it was shown that after rinsing with diluted ammonia the amount of Rb reduced. In addition, pronounced In distribution is seen from the water rinsed sample as compared to the ammonia etching.

For further investigation, the Pearson correlation coefficient between the two elements was calculated. The analytical formula of the Pearson correlation coefficient

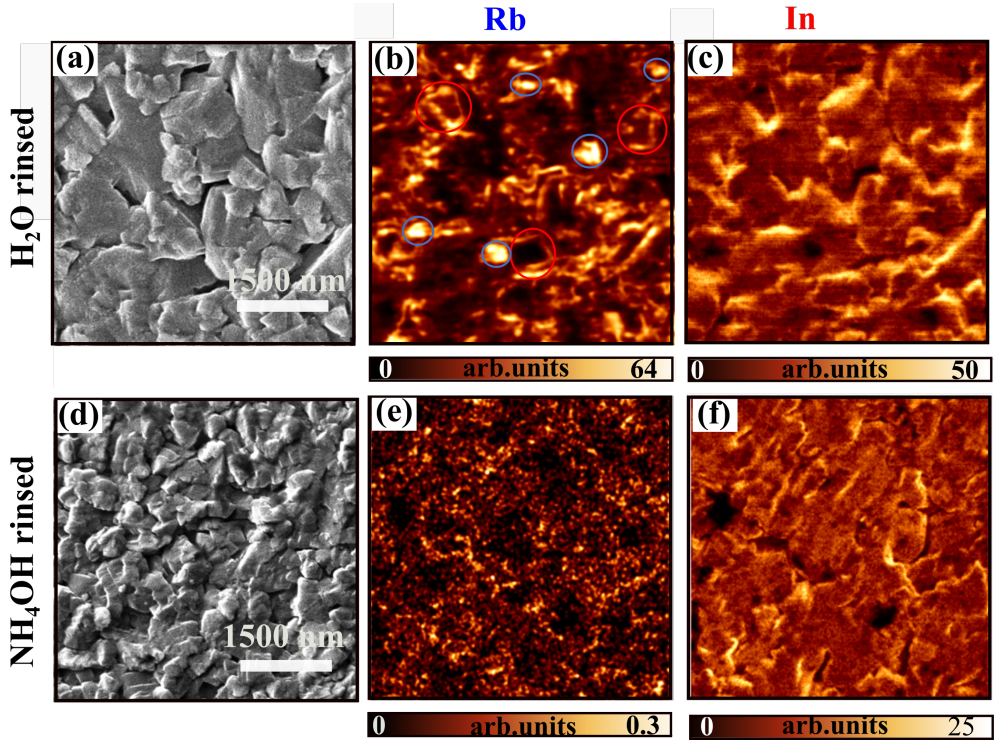

Figure 7.15: HIM-SIMS maps of Rb and In showing surface distribution with the corresponding SEM images. Top row represents water rinsed sample and bottom row represents ammonia rinsed sample.

can be found in the Appendix. The findings exhibited that the correlation between Rb and In distribution for water rinsed sample is approximately 1.43 times higher than in ammonia film, indicating therefore a strong correlation between Rb and In in water cleaned sample compared to ammonia washed sample. Consequently, similar to the KPFM and XPS measurements discussed above, the SIMS results confirmed the formation of two different phases at the surface of the sample after water rinsing, which collapse to a single phase after rinsing the sample with ammonia.

7.2.4 Surface density of states of RbF and NaF samples

Fig. 7.16 depicts STM topography images of the RbF film after water [Fig. 7.16(a)] and after ammonia [Fig. 7.16(e)] cleaning. The corresponding surface density of states (dI/dU-CITS) maps at different specific applied voltages are displayed in Figs. 7.16(b)-(d) for the water rinsed and in Figs. 7.16(f)-(h) for ammonia washed sample. The scale bar below each subfigure indicates how the topography and local-dI/dU vary across the map. Two key arguments explained the reason why the dI/dU-CITS

maps were displayed only at -1, 0, and 1 V. The first motivation is to explore the distribution of the local density of state of the water and ammonia rinsed samples at the Fermi energy level, *i.e*, at U= 0V, in order to compare the results to our KPFM data. The second reason is that the dI/dU-CITS maps of the ammonia rinsed samples are featureless for all voltages below -1V and above 1V.

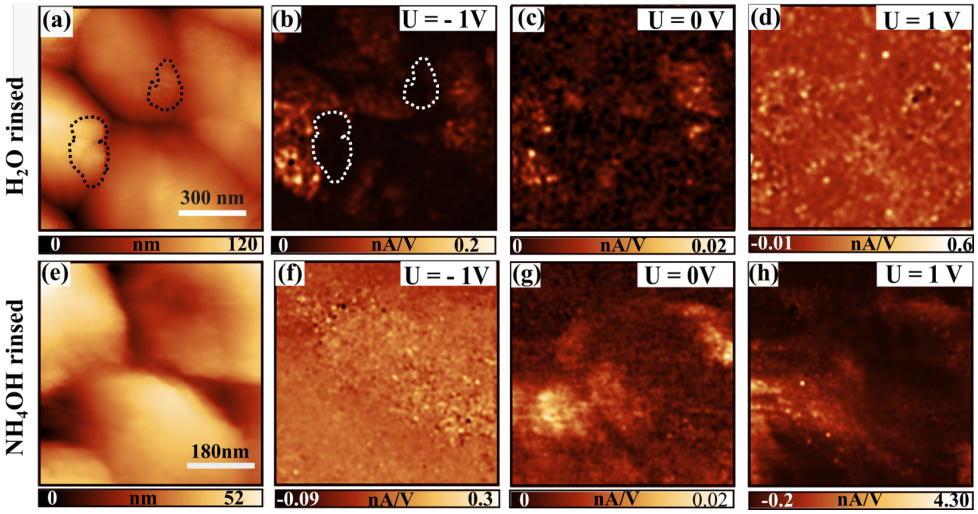

Figure 7.16: (a) STM topography image of the RbF water cleanned sample; (b)-(d) dI/dU-CITS of the same spot at -1, 0 and 1V; (e) STM topography image of the ammonia washed sample; (f)-(h) corresponding dI/dU-CITS at -1, 0 and 1V. The scale bar below each subfigure was optimized to have the best possible contrast for each analysis area. The dI/dU-CITS maps were extracted at 0, -1 and 1V because we would like first to investigate the distribution of the density of states of the water and ammonia at the Fermi position in the aim to compare the results to KPFM findings and also the dI/dU-CITS maps were featureless for all voltages below -1 V and above 1V.

Similar to the KPFM findings conducted on the water washed film, the STM topography images do also exhibit some precipitates at the surface of the sample. Those agglomerations are highlighted by the black dot curve on the surface of the water rinsed sample [Fig. 7.16(a)] and again are absent after ammonia treatment, consolidating thereby the idea that rinsing the sample only with the deionized water is not sufficient to remove all the surface residues from the surface of the film. In Fig 7.16(b)-(d) and (f)- (h) the dI/dU-CITS maps of the water rinsed as well as the ones of the

ammonia rinsed are depicted. Qualitatively speaking, the two results look similar. In both maps, most grains do not show a variation in the density of states at the GB/grain interface. The map only shows a small variation in the contrast between grains and within individual grains. Note that to the best of my knowledge these results are the very first STM/STS findings acquired from the CIGSe surface that were post-treated with alkali-metals. Most of the CIGSe STM/STS data reported heretofore in literature were from the non PDT treated samples [37, 38, 39, 40, 158]. The former authors reported a reduced density of defect states on grain boundaries and strong variation of the density of states over the surface of the sample [37], which are not seen here. Those changes in DOS at GBs and across the surface previously relayed were ascribed to different degrees of oxidation [38] of the absorber after exposing them to air or to some additional defect states induced by KCN etching [158]. The effect of KCN etching on the surface electronic properties of CIGSe was also widely discussed in Chapter 5. In the present study, less variation in the DOS is obtained from the surface of the RbF sample. In addition, almost no change in density of states between grain boundaries and grain interiors are measured. The surface seems to be highly passivated after ammonia cleaning. Nevertheless, the precipitates observed at negative voltages after rinsing the sample with the purified water do reveal lower density of states, which are highlighted by the fuzzy regions (white curve) in Fig. 7.16(b). These features are totally gone after ammonia cleaning. To thoroughly analyse this observation, the average dI/dU curve of these specific regions along with the average dI/dU curve of the entire image were extracted and are presented in Fig. 7.17(a). In addition, as the measurements were repeated for a number of different spots using different tips, the dI/dU curves of the region with low contrast of all the spots acquired from each sample are depicted in Fig. 7.17(b) and (c) for a comparative study. Fig. 7.17(b) displays the data from the water rinsed sample, and Fig. 7.17(c) presents the ones from the ammonia rinsed sample. Only the dI/dU curves of the region with low contrast are shown since they represent the majority of the surface. They represent in total ~ 75 % of areas that were analyzed.

In line with the dI/dU-CITS map presented in Fig. 7.16(b), the results show that the surface of the water rinsed sample is semiconducting and the fuzzy regions exhibit an enlarged bandgap as compared to the rest of the surface [Fig 7.17(a)]. After re-

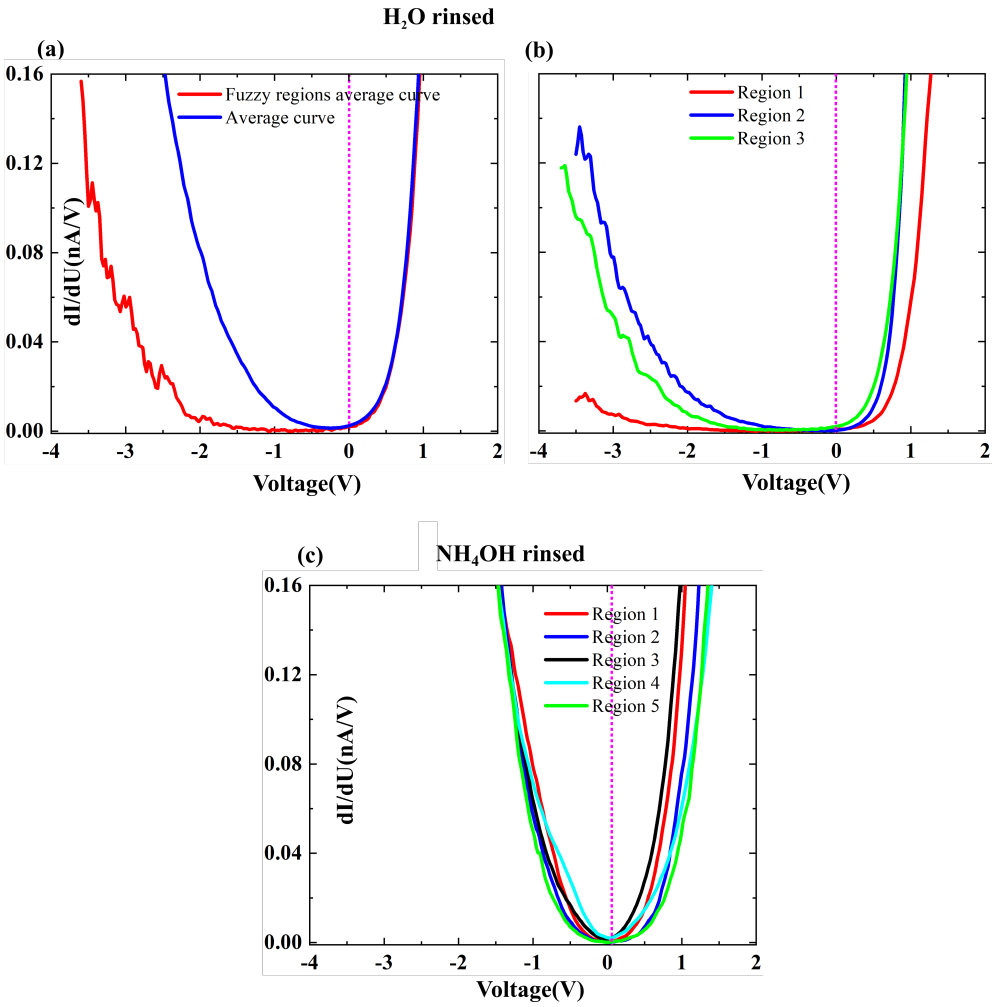

Figure 7.17: (a) dI/dU curve of the fuzzy regions highlighted by the white curves in Fig. 7.16(b) along with the average dI/dU curve of the entire image, (b) and (c) dI/dU curves from various spots using different tips and after water and ammonia rinsing, respectively.

producing the measurements on different regions using different tips, similar features were observed [Fig. 7.17(b)]. Consequently, it is speculated that the surface of the water rinsed sample is partly covered with regions with higher bandgap and regions with lower bandgap. As the same tip was used to acquire the spectra displayed in Fig. 7.17(a), its density of states is assumed to be constant during the whole measurements. Thus, the changes that are observed at the negative voltages can be assigned to difference in bandgap between the two regions. Therefore, it is concluded that the surface of the water rinsed sample do have two different compounds as already suggested by our KPFM and XPS. One with an enlarged bandgap which in this study is assigned to $RbInSe_2$ and another with low bandgap which is ascribed to CIGSe. Similar behavior

was also observed in Fig. 7.17(b). However, the assumption adopted above can not work out here. As various tips were used on different areas, the density of states of the tip might be very different between measurements. Consequently, in this case, it makes sense to attribute the feature observed to a slight variation in density of states of the tip.

Furthermore, as widely reported in literature, an inverted surface is also measured [42]. As can clearly be seen in Fig. 7.17(a) and (b), the Fermi energy position of the water rinsed sample is close to the conduction band. After washing the sample with ammonia, we did not see the fuzzy regions anymore. In addition, a reduced bandgap that is not compatible with a $RbInSe_2$ secondary phase is measured and the Fermi energy position is shifted to the middle of the bandgap [Fig. 7.17(c)]. The $RbInSe_2$ phase which was still present at the surface of the sample after water rinsing is gone. The result is consistent with all the results discussed above, *i.e*, the KPFM, the XPS and SIMS analyses.

For further investigations, the surface density of states of the NaF sample was also examined. The measurements were carried out after H_2O and NH_4OH rinsing, respectively. Figs. 7.18(a) and (b) show the topographies images, and Figs. 7.18(b)-(d) and (f)-(h) the corresponding dI/dU-CITS maps. In agreement with the KPFM topographical image recorded from the same sample [Fig. 7.9(b)], the STM topography [Fig. 7.18(a)] also reveals a clean surface after water rinsing *i.e*, an image without granular structures on top. Both topographies obtained from two different techniques show that the surface of the NaF film is already cleaned after distilled H_2O rinsing. Consequently, it is deduced that in contrast to the RbF sample where it was shown earlier that only NH_4OH washing can help to completely remove the residues from its surface, H_2O rinsing is enough to clean the surface of the NaF sample. The dI/dU-maps depicted in Figs 7.18 (b-d) and (f-h)) are qualitatively similar, and are also similar to the results recorded from RbF sample [Figs. 7.16 (b-d) and (f-h)]. The maps exhibit less variation of the DOS over the surface and almost no changes in DOS at the GBs/grain interface.

To compare the surface density of states of the two samples, the dI/dU curves extracted from the region with the reduced contrast are displayed in Fig. 7.19. As previously indicated, the reason is that those regions represent the major part of

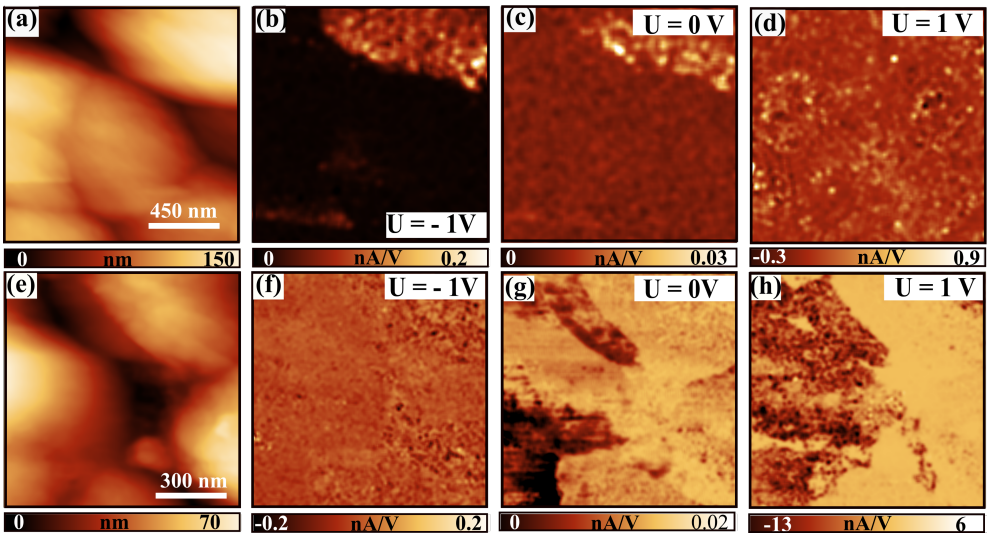

Figure 7.18: (a) STM topography image of the NaF water cleanned sample; (b)-(d) dI/dU-CITS of the same spot at -1, 0 and 1V; (e) STM topography image of the ammonia washed sample; (f)-(h) corresponding dI/dU-CITS at -1, 0 and 1V. The scale bar below each subfigure was optimized to have the best possible contrast for each analysis area. The dI/dU-CITS maps were extracted at 0, -1 and 1V because we would like first to investigate the distribution of the density of states of the water and ammonia at the Fermi position in the aim to compare the results to KPFM findings and also the dI/dU-CITS maps were featureless for all voltages below -1 V and above 1V.

the analyzed areas. Each curve represents the average curve recorded from different spots of each sample and is acquired after water and ammonia washing. Interestingly, although the samples were post-treated differently, their dI/dU curves look really similar after water cleaning, and also after ammonia cleaning. An enlarged band gap, which strongly reduced after ammonia washing, is obtained from the surface of the NaF and RbF samples after H_2O cleaning. This result is supported by our XPS data where it was shown that the surface of NaF sample might be, after water cleaning, partly covered with an In_2Se_3 compound and the one of RbF sample with a $RbInSe_2$ secondary phase. The energy bandgap of the In_2Se_3 compound (2.5 eV [256]) and the one of $RbInSe_2$ (2.57 eV [259]) phase are very close one to another. By using the linear extrapolation method similar energy bandgap can be approximated from the curves presented here. Hence, a combination of the XPS and STS results indicates a partial formation of the In_2Se_3 compound on the surface of NaF film, and a $RbInSe_2$

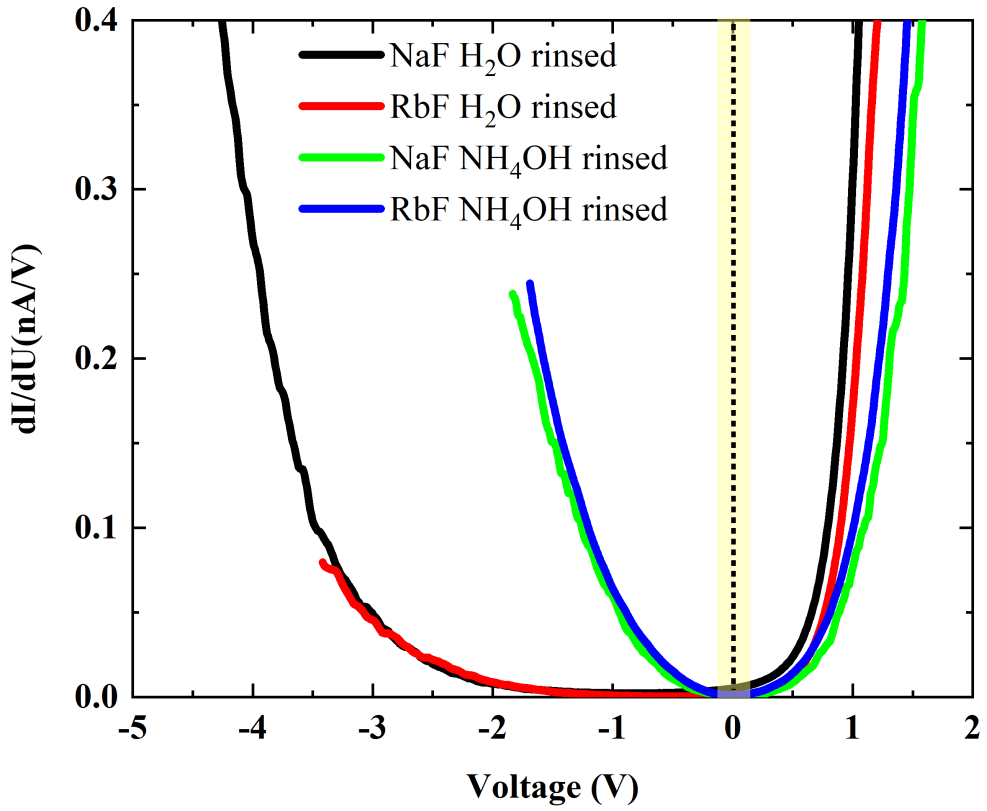

Figure 7.19: Average dI/dU curve extracted from the NaF and RbF samples after H_2O and NH_4OH rinsing. The dark and red curves are extracted after H_2O rinsing, and are from the NaF and RbF samples, respectively. The green and blue curves are extracted after NH_4OH rinsing, and are from the NaF and RbF samples, respectively.

secondary phase on RbF sample after water cleaning. But now raise the question about what type of surface is formed after ammonia rinsing. The ammonia rinsed surfaces show a reduced bandgap compared to the water rinsed surfaces.

To address this open question Raman spectroscopy, which is one of the more powerful techniques that can be used to determine the different compounds that exist at the surface of a sample was used at ambient temperature to further analyze the sample. The results are presented in Fig. 7.20.

Interestingly, the findings nicely fit the CIGSe and their corresponding ordered defect compound peaks reported in Refs. [138, 237] confirming thereby no trace of $RbInSe_2$ phase at the surface of the film after ammonia rinsing as already exhibited by the XPS, the STM/STS, and the SIMS data. The spectra acquired here also exhibit six peaks appearing at the same positions as the ones reported for CIGSe film in Ref. [237] with three of them that are more intense [Fig. 7.20(b)]. Hence, as suggested in the

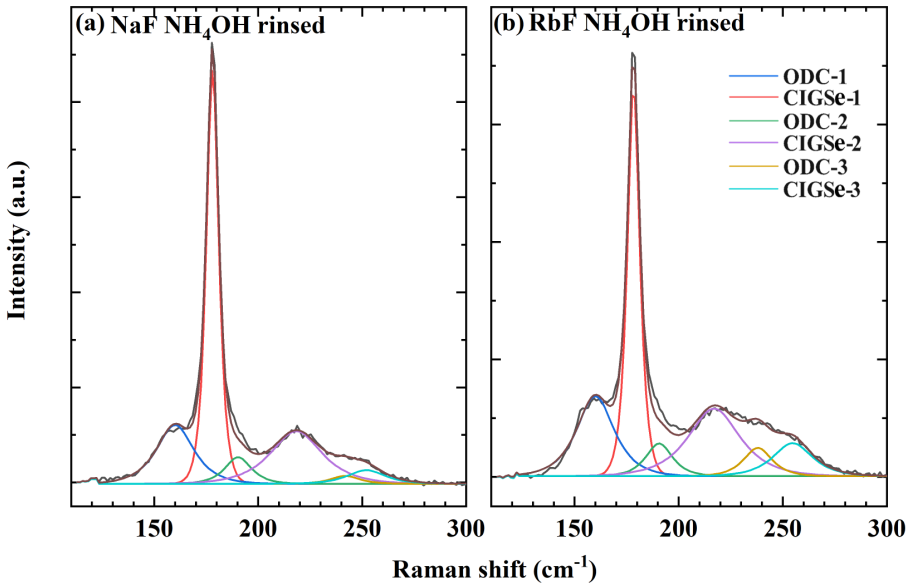

Figure 7.20: Raman spectra of the (a) purely NaF PDT and ammonia rinsed sample surface and the (b) RbF PDT and ammonia rinsed sample. Each peak was fitted with six peaks representing the CIGSe A_1 (CIGSe-1) and the B_2/E modes (CIGSe-2 and CIGSe-3) and their respective peaks due ordered defect compounds (ODC-1, ODC-2 and ODC-3), representing copper depleted regions.

former paper, the three more intense peaks measured from the sample analyzed in the present case are assigned to the CIGSe A_1 (CIGSe-1) and the B_2/E modes (CIGSe-2 and CIGSe-3), whereas the other three are ascribed to the respective peaks due to the copper depleted regions, generally called, ordered defect compounds (ODC-1, ODC-2, and ODC-3).

Furthermore, M. Guc *et al* [260] report for $RbInSe_2$ three main Raman peaks at 114.3, 179.7 and 238 cm^{-1}. Nevertheless, although the same 442 nm excitation wavelength was used to acquire the spectra presented in this study the outcomes have not displayed any peak at or around 114.7 cm^{-1}. The peaks located at 179 and 238 cm^{-1} that are observed are as stated before rather related to the CIGSe A_1 and the ODC-3 modes and not to Raman modes of $RbInSe_2$ secondary phases. The finding is promoted by comparing the Raman signal of the ammonia rinsed RbF sample [see Fig. 7.20(b)] with the signal from the ammonia rinsed NaF sample [see Fig. 7.20(a)]. The ODC-1 peak, which does not match the Raman modes of $RbInSe_2$ [260] shows an increased intensity with respect to the CIGSe A_1 mode, with a ratio of 0.62 for the RbF sample compared to NaF sample where this ratio is 0.43, suggesting thus an enhanced

Cu-depleted surface for the RbF sample. Alike characteristic is also observed for the ODC-2 and ODC-3 modes regarding the CIGSe-2 and the CIGSe-3 mode, respectively. Thereby, as the same properties are measured in the NaF sample where no signatures of $RbInSe_2$ compound was expected, the possibility of not having Raman peaks related to $RbInSe_2$ for the positions 179 and 238 cm^{-1} in the Raman spectrum in Fig. 7.20(b) can be anticipated. Consequently, the Raman data also suggest that the ammonia rinsing completely removed the Rb from the $RbInSe_2$ phases, leaving only copper depleted regions behind. In contrast to the water rinsed RbF sample where a clear signature of $RbInSe_2$ was found, the ammonia rinsed sample does not show any trace of this compound. This suggests that in a final CIGSe device where the absorber was post-treated with the RbF alkali metals, the surface of the film that interacts directly with the buffer is partly covered with ODC and not with a $RbInSe_2$ secondary phase as widely reported in the literature.

7.3 Discussion and summary

KPFM measurements revealed as already reported in [33] that the surface of RbF-PDT treated films is completely covered with residues. In addition, the results also exhibited that rinsing the sample with deionized water which is the cleaning procedure commonly employed for CIGSe post-treated with RbF is not enough to clean the sample and that only ammonia can remove all the surface residues from the film. After washing the sample with ammonia, it is found that some precipitates that were left at the surface of the film after water rinsing are gone. The topography image is clean and presents well known features of CIGSe. The regions with a lower workfunction that were seen in the workfunction map before and after water cleaning are fully disappeared. In agreement with the KPFM results, our XPS measurements do present different chemical environments for In, Se and Rb before and after water rinsing, which collapse to only one environment after ammonia washing. In the case of a water rinsed sample the binding energies achieved for these elements fit well the ones reported in [232] suggesting as already reported the existence of two compounds at the surface of the sample analyzed here as well. These findings are supported by the STS where two main domains with enlarged and low bandgaps were measured. Combining the XPS

and STM as well as the SIMS data where a strong Pearson correlation coefficient was measured between Rb and In in water rinsed sample, the domain with an enlarged bandgap corresponds to $RbInSe_2$ secondary phase and the domain with low bandgap to CIGSe, confirming thus results reported heretofore in literature. After ammonia rinsing, in contrast to non rinsed or water rinsed samples where various chemical surroundings assigned to a mix of a strong Cu-poor CIGSe and a $RbInSe_2$ secondary phase were measured, only a single chemical environment is detected. The binding energies of In3d (445.11 eV) and Se3d (54.4 eV) acquired fit well their values in CIGSe compound, indicating that they are not oxidized. The Rb elements found at a binding energy of 110.70 eV is assumed to be bounded to CIGSe as suggested in Ref. [232]. The results showed that although there was still a bit of Rb present at the surface of the sample, in line with our KPFM, no signature of residual fluoride or $RbInSe_2$ phase are detected after cleaning the absorbers with ammonia. Besides, the STS data exhibits clean topography images and a reduced bandgap, which is not compatible with a $RbInSe_2$ secondary phase. Hence, it is deduced that the surface of the sample is cleaned and free of $RbInSe_2$ phase or residual fluoride after ammonia washing. To examine what type of surface is formed after the ammonia cleaning process, some Raman spectroscopy measurements were performed. Intriguingly, the findings nicely fit the CIGSe and their corresponding ordered defect compound (ODC) peaks reported in Refs. [138, 237] confirming thereby no trace of $RbInSe_2$ phase at the surface of the film after ammonia rinsing as discussed above. Consequently, it is concluded that in contrast to a partial covering of the surface of the CIGSe with a thin layer of $RbInSe_2$ previously reported [232, 233] rather a layer of ODC is found at the CIGSe/air interface of the RbF PDT sample after ammonia cleaning. Moreover, the STS and KPFM do not exhibit a variation in density of states and workfunction across the GB/grain interior interface, suggesting that GBs might be passivated. Although, the dI/dU maps have shown a variation in the density of states from grain to grain, and within the individual grains, no changes in the DOS were observed at GBs. Similarly, KPFM measurements have shown a smooth transition across the GB interfaces. The results are in agreement with the study proposed by Siebentritt *et al.* [259] where it was shown that the GBs band bending is significantly reduced after treating the sample with RbF. The former authors ascribed this reduction in band bending to the accumulation of Rb at the

GB, which passivate most of the defects that were present there. Although the results presented here fit well the ones reported in Refs. [259], it is important to highlight that our SIMS measurements do not reveal any preferential segregation of Rb at the GBs. The map of rubidium showed that Rb is rather randomly distributed and spread across the surface of the samples.

As implications for solar cell devices, the benign properties of GBs (section 3.3.1) and the presence of an ODC layer at the CIGSe/CdS interface are known as good ingredients to significantly improve the performances of the solar cells [139]. With its lower Cu content as compared to the CIGSe, the existence of its thin layer at the utmost layer of CIGSe creates a valence band offset (ΔE_V) at the ODC/CIGSe interface, which acts as a hole barrier in CIGSe solar cells [139], leading to a suppression of carrier recombination by reduction of hole concentration near the hetero-interface.

In summary, it was shown that distilled water rinsing is not an efficient way to clean the CIGSe samples after RbF PDT, and that in order to remove all the surface residues generated after this chemical treatment the use of ammonia is crucial. In line with the literature, it was demonstrated that the surface of distilled water rinsed is partially covered with $RbInSe_2$ secondary phase and ordered defect compound (ODC) layer. However, the results showed that after washing the sample with ammonia the $RbInSe_2$ phase completely vanished leaving behind only an ODC layer at the CIGSe/CdS hetero-interface, which is known to be a good ingredient to significantly improve the CIGSe solar cell performances. Moreover, our findings do not exhibit an accumulation of Rb or change in electronic properties across the GB/grain interface after rinsing the RbF PDTs with ammonia.

Chapter 8

Conclusion and Outlook

CISe and CIGSe absorbers exhibit excellent properties for high power conversion efficiency solar cell devices. However, absorbers that are grown under Cu excess perform worse in the complete devices. This low performance of the absorbers deposited with a final Cu-rich composition has been assigned to an increase of the interface recombination at the surface. It is widely reported in the literature that over stoichiometric absorbers exhibit a precipitate-free bulk with copper selenide secondary phase on top, which can be washed away via KCN cleaning. The first objective of this thesis was to systematically investigate how washing away Cu_xSe secondary phases with KCN modifies the Cu concentration at the front surface of the Cu-rich films. The second objective was to elucidate the impact of Cd in-diffusion on the surface and grain boundary electronic properties of the films. Besides, to compare the results acquired from the front surface to the ones of the rear surface, and hence to investigate the surface of the Cu-rich film which was not KCN etched, the samples were mechanically exfoliated from their substrates and their rear surfaces were examined. The third focus was to thoroughly investigate the surface electronic properties of the pristine absorbers as well as the influence of the cleaning process on the surface properties of the absorbers which were post-treated with NaF and RbF alkali metals.

Since the effect of washing or KCN etching steps happens right at the very near-surface of the absorbers, highly surface-sensitive characterization techniques had to be used. Therefore, combined scanning probe microscopy and X-ray photoelectron spectroscopy was employed as the main tools to scrutinize the sample surface.

The findings show that the surface of KCN etched (10 wt% KCN in H_2O, 300

seconds) Cu-rich absorbers exhibit a Cu-poor feature with a stoichiometric bulk composition. This suggests that a KCN etching step can be used as an alternative way to form a Cu-depleted surface on top of the absorbers grown under Cu excess. Furthermore, a Cu-depleted surface measured after etching the Cu-rich film with KCN has been recognized as one of the crucial ingredients for high performance CISe devices. In addition, in line with the reported STS results on Cu-poor absorbers, the measured samples exhibited a metallic *I(U)* characteristic and a reduced density of defect states at the grain boundaries.

After the cadmium pre-electrolyte treatment, the surface properties of the absorbers significantly improved. The metallic behavior that was observed at the surface of the KCN etched sample was gone leaving behind a semiconducting surface with well-defined conduction and valence band onsets. Furthermore, the change in density of states observed at the grain boundaries completely vanished after the treatment. The improvement of the surface of the absorber after the Cd^{2+} treatment was ascribed to the passivation of Cu vacancies by Cd^{2+}. The Cd^{2+}_{Cu} acts as a donor-like defect state inverting thereby the near-surface of the sample similar to the UHV annealing treatment, which was already discussed in the literature. Therefore, as already reported from the Cu-poor grown absorbers, the results showed a similar positive impact of the cadmium in-diffusion on the surface properties of the CISe sample synthesized with a final Cu-rich composition.

The measurements carried out on the rear surface of the same absorbers have shown a formation of Cu_xSe secondary phase at the back contact interface. The results indicate that for the absorbers grown under Cu excess, a detrimental Cu_xSe precipitate does not only form on the front surface but also at the back. This is in opposition to the reported results on Cu-poor absorbers where no signs of such precipitate were found [151]. We also did not observe such precipitates on Cu-poor samples. With KPFM, a slight increase in work function ($\sim 40\,\mathrm{meV}$) was measured at the grain boundaries of our Cu-rich absorbers. Furthermore, it was shown that such a small change in workfuntion across the grain boundary cannot be resolved with STS. This result should be considered when debating why the Cu-rich absorber presents a reduced performance in final solar cell devices compared to Cu-poor films. The harmful Cu_xSe phase that precipitates on top of the Cu-rich film and which is widely reported

in the community to be washed away with KCN also exists at the back contact. The presence of this highly conductive material at the Mo/absorber interface will increase the back contact recombination velocity and consequently could be very detrimental for the solar cell performance.

The analyses performed on the pristine CIGSe sample have shown a semiconducting surface with a bandgap of ~ 1.2 eV as well as a slight variation in the density of states from grain to grain and within the individual grain. The findings are not in line with the published results on air-exposed and KCN etched absorbers. The metallic surface and high surface inhomogeneity that they exhibited were ascribed to different degrees of oxidation after exposing the absorber to air or to some additional defect states induced by KCN, which are all absent in this particular case. Here, the sample was not KCN etched and was transferred from the PVD to the SPM using a suitable UHV suitcase to minimize any contamination from the atmosphere. In addition, the workfunction map from the same sample has shown several workfunction domains with two main ones, which present a very bright contrast and a very dark contrast exhibiting thus higher [(4.9 ± 0.1) eV] and lower [(4.4 ± 0.1) eV] workfunction values. A thorough analysis of the workfuntion map has revealed that most of those domains arise mostly from the facet contrast and not from the grain boundaries. After keeping the sample in UHV for a few weeks, it was found that its workfunction strongly decreased (for ~ 1.2 times lower than the one of the pristine absorber) due to the presence of adsorbates. Nevertheless, after UHV annealing the workfunction recovers to the initial value indicating that changes at the surface of the sample induced by adsorbates have not permanently modified the electrostatic landscape of the polycrystalline CIGSe sample. Thus, annealing in UHV can be considered as an alternative to clean the surface of a sample that initially was not exposed to air and was free of all contamination and moisture, but, which was kept in UHV for some time.

Regarding the PDTs absorbers, it was found that the way the sample is rinsed after the treatment is extremely important to understand the physical and chemical changes of the absorber surface properties. The samples were analyzed as grown and after distilled water and ammonia rinsing. It was shown that roughly 45% of as grown absorbers surface is covered with granular structures, which exhibit lower workfunction (4.9 ± 0.1) eV as compared to the average workfunction value (5.0 ± 0.1)

eV. This feature was observed at the surface of both NaF and RbF absorbers. Hence, in agreement with the XPS data obtained from the same samples, those precipitates were ascribed to the residual fluorides, which are formed at the surface of the film after the PDT process. However, after rinsing the sample with deionized water, the NaF samples have exhibited a clean topography and workfuntcion map, suggesting that rinsing the sample with distilled H_2O is enough to remove all the patches that were seen at the surface of as grown samples. In contrast, the RbF samples have shown only partial removal of the surface residues. Approximately 27% of the precipitates with a workfunction value of (4.6 ± 0.1) eV was still present at the surface of the water rinsed RbF absorber. The results suggest that purified H_2O rinsing is not an efficient way to clean the CIGSe samples after RbF PDT and that in order to remove all the surface residues generated after this chemical treatment the use of ammonia is crucial. In agreement with the literature, it was found that the surface of purified H_2O cleaning samples is partially covered with $RbInSe_2$ secondary phase and ordered defect compound layer. However, the results showed that after washing the sample with ammonia the $RbInSe_2$ phase completely vanished leaving behind only an ODC layer at the CIGSe/CdS hetero-interface, which is known to be a good ingredient to significantly improve the CIGSe solar cell performances. Moreover, our findings do not exhibit an accumulation of Rb or change in electronic properties across the GB/GIs interface after RbF PDTs.

Outlook

The study carried out in the framework of this thesis helped in understanding chemical and electronic changes at the very near-surface of the CIGSe absorbers after various surface treatments. However, as with any research topic, not all open questions could be thoroughly scrutinized. In the following paragraphs, the list of those topics that could not be studied to their full extent will be proposed.

- **Rear surface of Cu-rich absorbers**

  SEM measurements have shown a substantial change at the grain boundaries after etching the rear surface of the absorbers with KCN. The grain boundaries exhibited brighter contrast as compared to the grain surface, suggesting that

the etching had different effect at the grain boundary (GB) with respect to the grain interior (GI). KPFM measurements confirmed that the brighter contrast observed at GB is due to a change in workfunction across the GB/GI interface after KCN etching. At this stage, the question about whether or not this increase in workfunction at the GB is due to the accumulation of a larger amount of Cu_xSe is accumulated there is still unclear. Additional atom probe tomography analysis should be done in order to clarify it.

- **Cu-poor CIGSe pristine absorbers**

  Since the Cu-poor CIGSe pristine absorbers have exhibited excellent surface properties *i.e*, a smooth surface density of states presenting semiconducting characteristic-like properties with a bandgap of around 1.2 eV, it will be important to fabricate a solar cell device on such absorbers. This is to compare the efficiency that will be achieved to the one obtained from the air-exposed or KCN etched absorbers. Such a comparative study could improve the community's knowledge regarding the impact of air exposure or KCN on CIGSe solar cell devices.

- **PDTs absorbers**

  Although it was found as already reported in the literature that the surface of the distilled H_2O rinsed RbF treated absorbers is partially covered with a $RbInSe_2$ secondary phase and an ODC layer, the study presented here did not show any preferential segregation of Rb and $RbInSe_2$ phases at the grain boundaries. The SIMS measurements have only displayed a surface, which is more or less entirely covered with Rb. As the study was mainly focused on the surface properties, the SIMS tool was set up such as only a few layers of materials from the surface were analyzed. Therefore, in order to investigate if this observation is similar to the one that exists in the bulk of the absorber, some additional depth SIMS measurements are needed.

Appendix

A.1 Heat induced surface passivation

As discussed in chapter 5, the annealed samples measured here show a similar passivation effect as the one reported in Ref. [40]. In Fig. A.1, a topography image and the corresponding dI/dU-CITS map at U=0 V are depicted. As can well be seen, com-

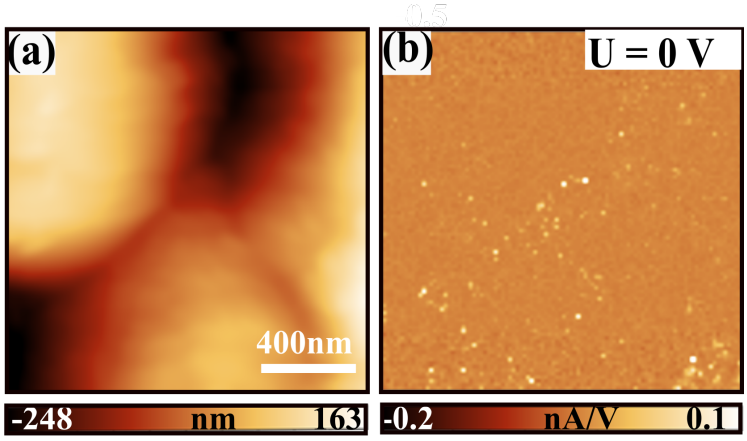

Figure A.1: (a) STM topography of the annealed CISe absorber, (b) dI/dU-CITS maps of the annealed Cu-rich CIS absorber at U=0 V. The sample has been annealed in-situ to 280°C.

pared to the KCN etched case, the map reveals less surface inhomogeneities, a strong reduction of the surface density of states, and no distinct grain boundary contrast. In order to compare the contrast to the KCN treated sample presented in Figure 5.2 of Chapter 5, the scaling of the images needs to be compared. In the present case, a reduction of the dI/dU value from ~ 5 nA/V to 0.3 nA/V at E_F, which is comparable to the passivation effect of the CPE treatment and very similar to the results presented in Ref. [40] is observed.

A.2 XPS and UPS measurements

XPS analysis, compositional measurements

In the following, 3 different tables with the XPS quantification results are presented. In Table A.1, the complete XPS intensity for each element has been used for the etched, Cd treated and sputtered films. In Table A.2, the metallic contribution of Indium after sputtering has not been considered since it is assumed that the indium enrichment is due to preferential sputtering of Selenium and Copper. This makes sense due to the fact that Cu and Se are lighter elements and are closer to Ar in the periodic system compared to Indium. In Table A.3, the XPS quantification in the case of the Cu $2p$ is compared to the Cu $3p$ as done in Chapter 5. The findings exhibit a slightly lower Cu content which is however still within the error of the measurement taking into account that the information depth is different.

Total indium contribution:

Table A.1: Elemental compositions of the CISe samples after various treatments, as measured via XPS. The following peaks have been used for the quantification: Cd $3d$, Cu $3p$, In $3d$, O $1s$, Se $3d$. The total number of Indium counts have been used, including the metallic contribution after sputtering.

sample	Cd [at%]	Cu [at%]	In [at%]	O [at%]	Se [at%]
CISe KCN etched	0.0	17	26	6	51
etched & sputtered	0.0	22	27	0.0	51
CISe Cd^{2+}	10	16	18	7	49
Cd^{2+} & sputtered	1	22	25	0.0	52

Removal of metallic indium

Table A.2: Same quantification as for Table A.1, except that only the Indium in the CISe chemical environment has been used for the quantification.

sample	Cd [at%]	Cu [at%]	In [at%]	O [at%]	Se [at%]
CISe KCN etched	0.0	17	26	6	51
etched & sputtered	0.0	22	26	0.0	52
CISe Cd^{2+}	10	16	18	7	49
Cd^{2+} & sputtered	1	23	24	0.0	52

Removal of metallic indium and Cu3p

Table A.3: Same quantification as for Table A.2 except that the Cu $2p$ has been used instead of the Cu $3p$.

sample	Cd [at%]	Cu [at%]	In [at%]	O [at%]	Se [at%]
CISe KCN etched	0.0	14	26	7	53
etched & sputtered	0.0	24	25	0.0	51
CISe Cd^{2+}	11	11	19	7	52
Cd^{2+} & sputtered	1	22	24	0.0	53

Auger parameters for Cu and In after various surface treatments

Table A.4: Auger parameters (α') for Cu and In after various surface treatments. The different values are compared to the published results in the literature. The values in brackets are from the literature.

sample	Cu [α']	In [α']
CISe KCN etched	1849.3 eV (1849.4 eV-1849.5 eV [261, 262])	852.5 eV (852.7 eV - 852.5 eV [261, 262])
CISe Cd^{2+}	1849.3 eV (1849.4 eV -1849.5 eV [261, 262])	852.6 eV (852.7 eV - 852.5 eV [261, 262]

Valence band offsets: the impact of UHV annealing

The valence band position of the KCN and CPE treated samples are shown in Fig A.2 and compared to the values after UHV annealing. The annealing has been carried out at a nominal temperature of 280°C. In accordance with the discussion in Chapter 5, a type inversion of the KCN etched film after UHV annealing is observed. The valence band position of the UHV treated KCN etched sample is identical to the sample after the CPE treatment. In accordance with the proposed model, STS measurements carried on this sample revealed a passivated surface, confirming the idea that the passivation observed is directly linked to the type inversion.

In table Table A.5, the XPS measurements carried out with an Alkα source are compared to UPS measurements achieved with a HeII source. We do find the same value for both techniques. The small deviations are within the error of the measurement techniques.

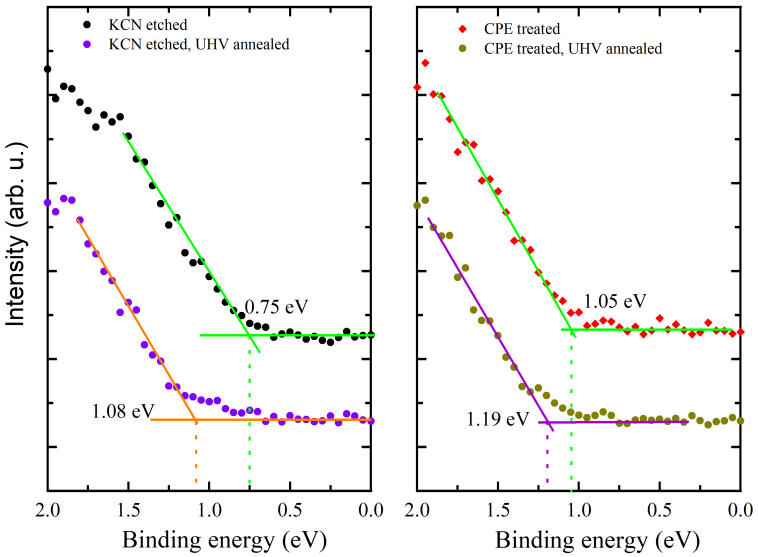

Figure A.2: XPS measurements carried out with an Alkα excitation source after KCN and CPE treatments of a CISe absorber followed by UHV annealing.

Table A.5: Comparison of the valence band position measurements with XPS and UPS. The XPS measurements have been carried out with an Alkα source and the UPS measurement with an He-II source. The values denote the distance of the Fermi-level to the onset of the valence band as deduced via linear extrapolation.

sample	XPS-Alkα	UPS-HeII
KCN etched	0.75 eV	0.77 eV
KCN UHV annealed	1.08 eV	1.06 eV
CPE treated	1.05 eV eV	1.06 eV
CPE treated UHV annealed	1.19 eV	1.13 eV

A.3 Optical and morphological properties of Rf-CIGSe

PL spectrum and SEM image

In Fig. A.3, the PL spectrum and SEM top view image of the Rf-CIGSe are displayed. The SEM micrograph shows that the absorber is polycrystalline with an average grain size of $\sim$ 1000 nm. The PL spectrum exhibits a broad asymmetric peak with a quasi-Fermi energy splitting of $\sim$ 697 meV, revealing the Cu-poor nature of the sample. This Cu-poor characteristic of the film is supported by the EDX data acquired from the same sample. As can be seen in Table A.6 where a CGI of $\sim$ 0.9 was measured.

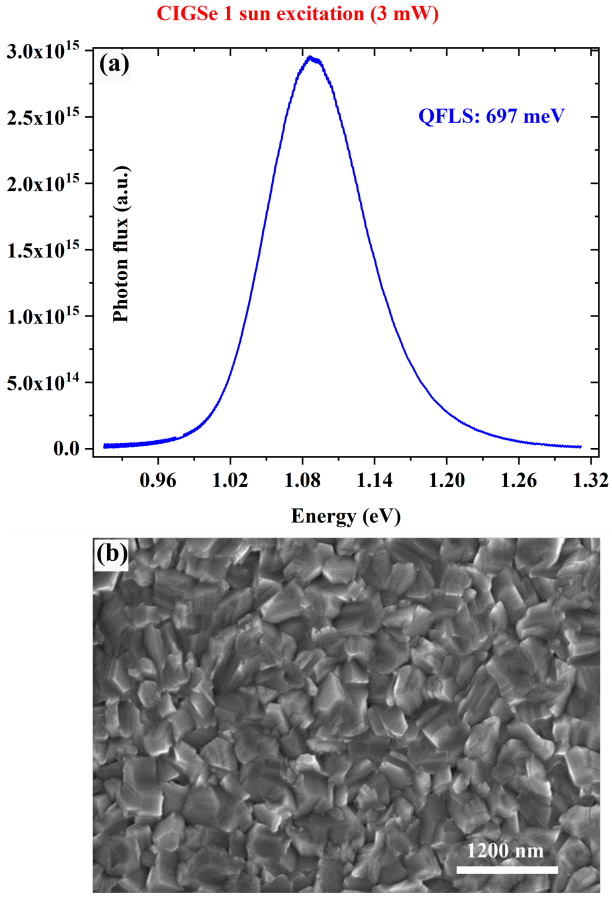

Figure A.3: (a) PL spectrum and (b) SEM recorded from the Rf-CIGSe absorber.

Elemental composition

Table A.6: Elemental composition of Rf-CIGSe along with the corresponding CGI and GGI

Rf-CIGSe	Cu [at%]	In [at%]	Ga [at%]	Se [at%]	CGI /	GGI /
Elemental composition	22.3	18.2	8	51.5	0.9	0.3

A.4 Workfunction and topography line profiles

Fig. A.4 shows the topography and the workfunction map where the different line profiles are extracted. The idea is to investigate the correlation between the work-function contrast and the different facets on the film's surface. In Fig. A.5, the line profiles extracted from the images when the tip was scanning in the forward direction are displayed, while in Fig. A.6 the ones when it was moving in the backward direction are depicted.

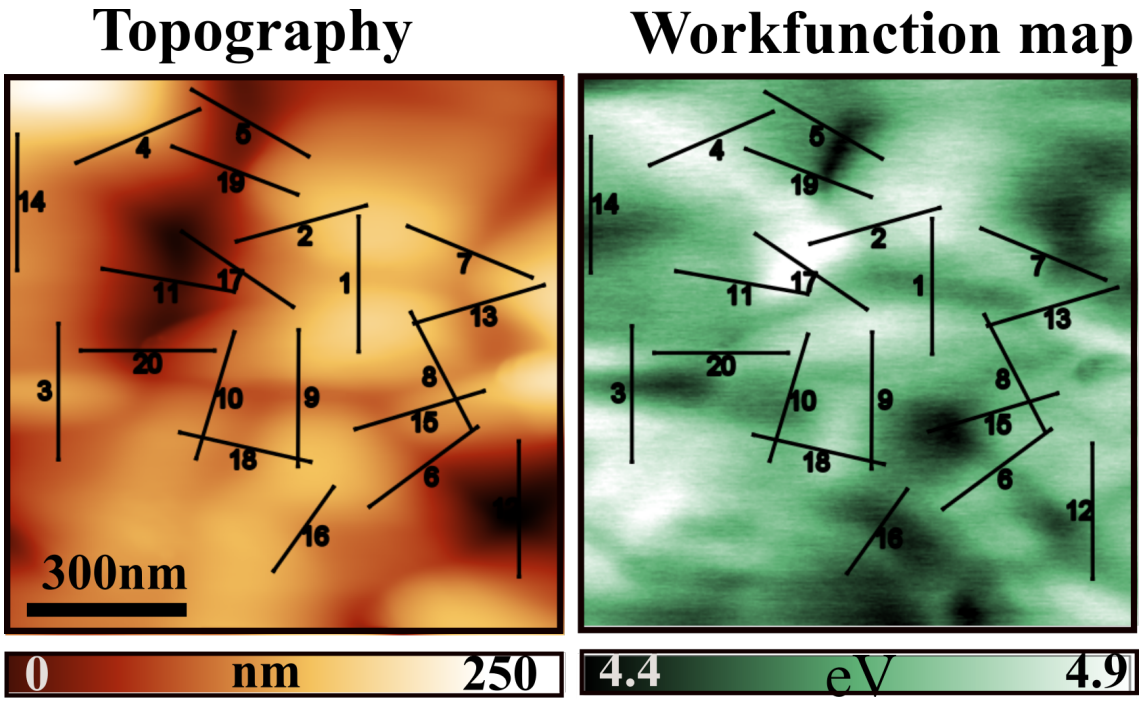

Figure A.4: Topography and workfunction images. The black lines are the regions where line profiles presented in Figs A.5 and A.6 were extracted

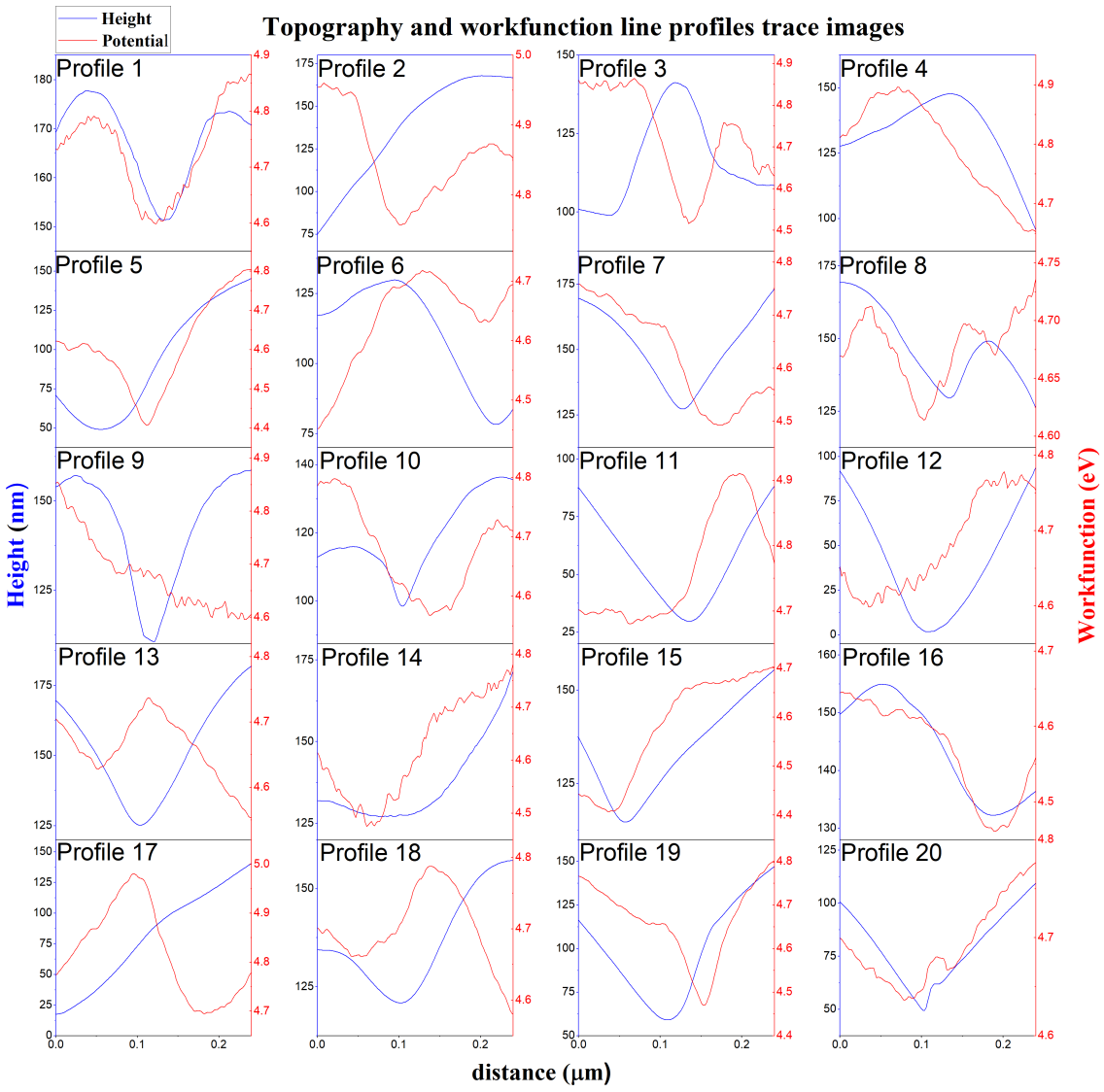

Figure A.5: Trace workfunction and topography lines profiles.

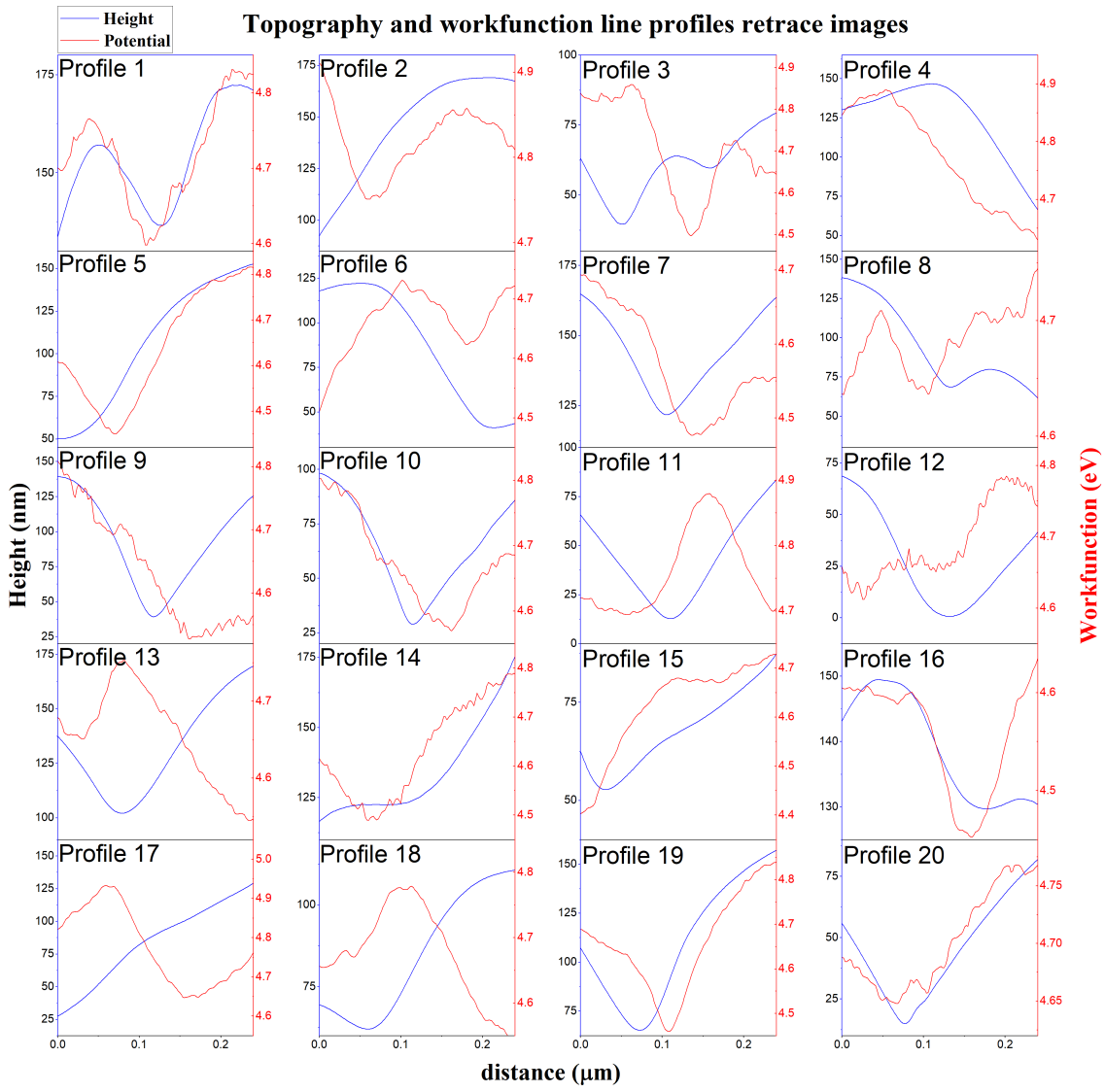

Figure A.6: Retrace workfunction and topography lines profiles.

A.5 High resolution XPS spectra of other elements enclosed in NaF and RbF along with the corresponding binding energies

In the following, the high resolution XPS signals of Cu, Ga, Na, and F obtained from the RbF and NaF treated absorbers as well as their respective curves fits are depicted. The corresponding binding energies are summarized in Table A.7. The two samples exhibited no signature of Na and F after distilled water and ammonia rinsing.

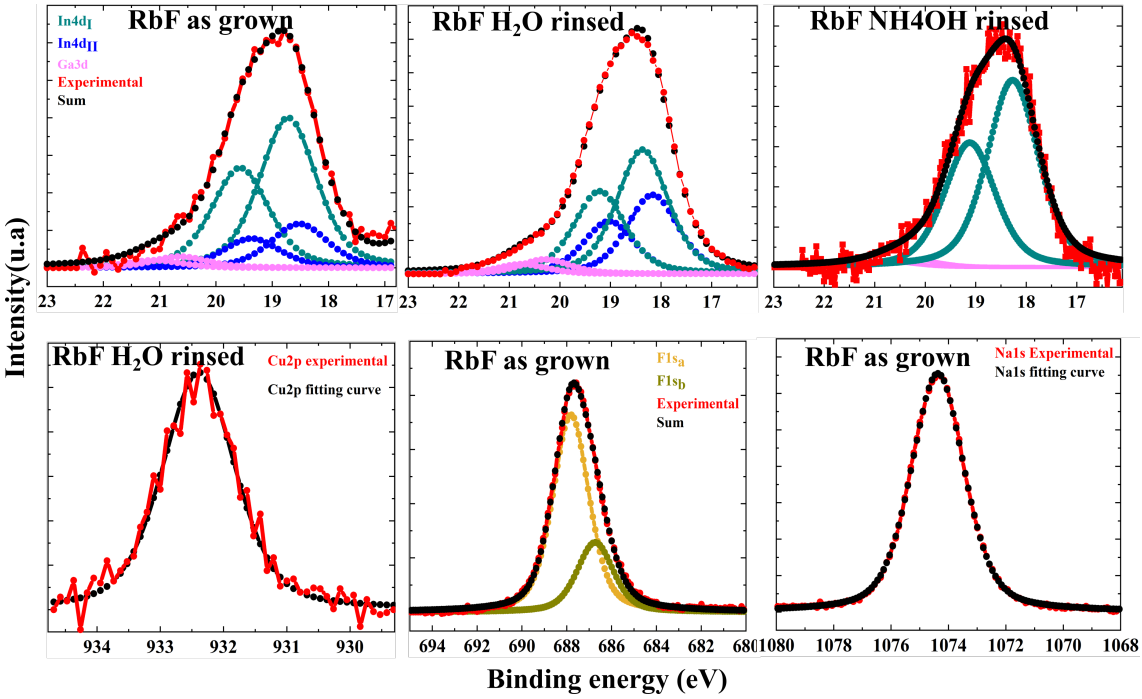

Figure A.7: High resolution XPS signals of Cu, Ga, Na, and F obtained from the RbF treated absorbers. The different binding energies are summarized in Table A.7. The spectra are recorded from as grown, the H_2O rinsed and NH_2OH rinsed samples. No Na and F signals were detected after rinsing the sample with water or ammonia. The two F peaks, $F1s_a$ and $F1s_b$ are assigned to F that are bonded to Rb and Na, respectively (see table A.7 where the binding energies are summarized).

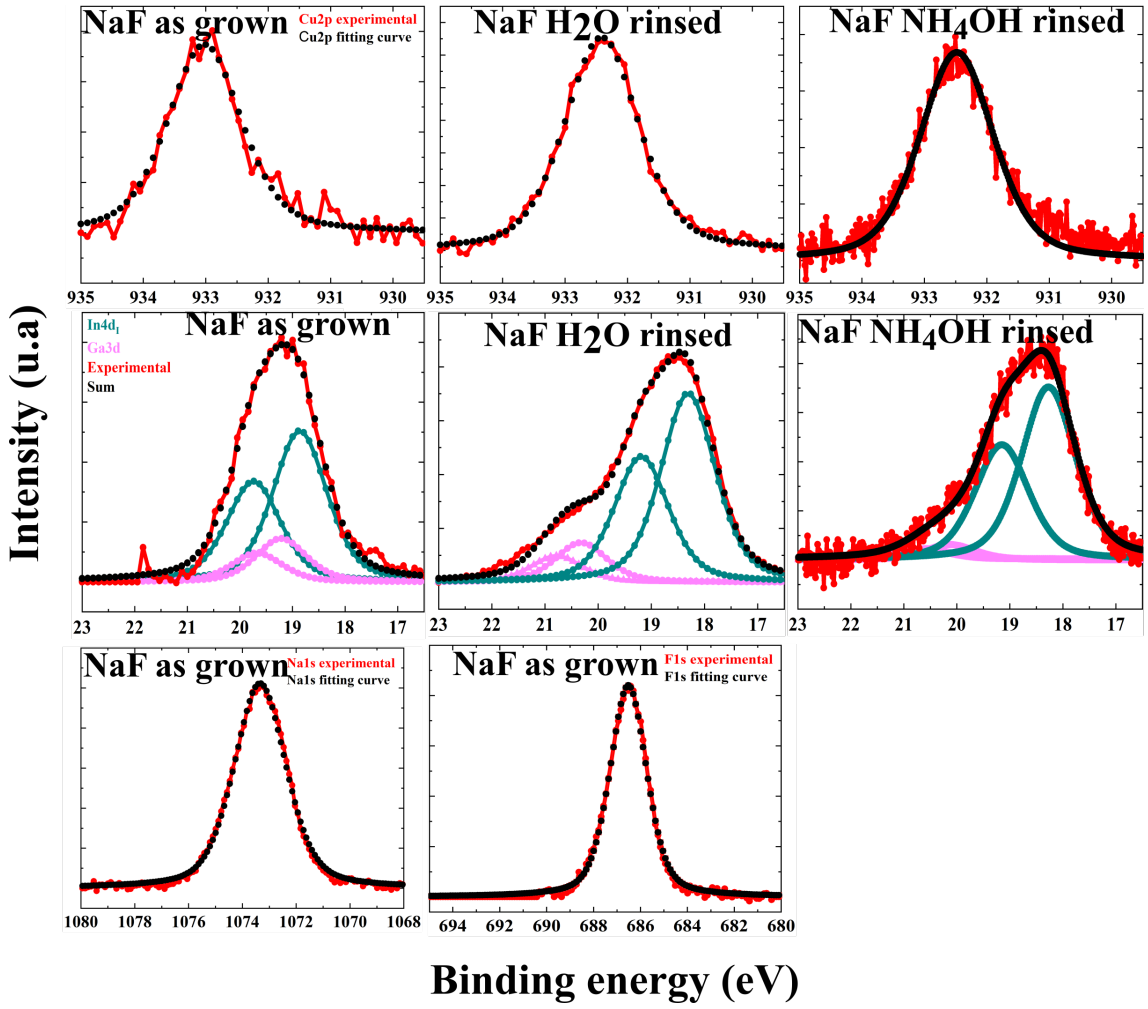

Figure A.8: High resolution XPS spectra of Cu and Ga elements enclosed in NaF sample as grown, after H_2O and NH_4OH cleaning together with their fitting curves, respectively. The different binding energies are summarized in Table A.7. No Na and F signals were detected after rinsing the sample with water or ammonia.

Table A.7: Summary of the binding energy of Cu, Ga, Na and F obtained from NaF and RbF as grown, after water and ammonia rinsed samples. The values into brackets are from RbF samples and the ones without brackets from Na samples. $F1s_a$ and $F1s_b$ are assigned to F present at the surface of the NaF and RbF samples, repectively.

specimen	NaF/RbF as grown	NaF/RbF H_2O rinsed	NaF/RbF NH_4OH rinsed
Cu2p (eV)	933.02/(-)	932.41/(932.39)	932.48 (932.45)
E_B Ga3d (eV)	19.22/(20.64)	20.32/(20.28)	20.13/(20.19)
E_B $In4d_I$ (eV)	18.86/(18.72)	18.31/(18.36)	18.27/(18.27)
E_B $In4d_{II}$ (eV)	-/(18.52)	-/(18.16)	-/(-)
E_B $F1s_a$ (eV)	686.52/(687.77)	-/(-)	- (-)
E_B $F1s_b$ (eV)	-/(686.66)	-/()	- (-)
E_B Na1s (eV)	1073.34/(1074.38)	-/(-)	-/(-)

A.6 Pearson correlation equation

$$r = \frac{n(\sum XY) - (\sum X)(\sum Y)}{\sqrt{[n\sum X^2 - (\sum X)^2][n\sum Y^2 - (\sum Y)^2]}} \quad (1)$$

- r = Pearson Coefficient
- n = number of the pairs of the pixel
- $\sum XY$ = sum of products of the paired pixels
- $\sum X$ = sum of the X pixels
- $\sum Y$ = sum of the Y pixels
- $\sum X^2$ = sum of the squared X pixels
- $\sum Y^2$ = sum of the squared Y pixels

Publications and Presentations

List of publications

First author

C. K. Boumenou, A. Elizabeth, F. Babbe, A. Debot, H. Mönig, A. Redinger, Electronic and compositional properties of the rear-side of stoichiometric $CuInSe_2$ absorbers, Prog. Photovolt: Res. Appl., 29, 775, 2021.

C. K. Boumenou, F. Babbe, A. Elizabeth, M. Melchiorre, C. Spindler, J. Guillot, H. Mönig, S. Siebentritt, A. Redinger, Passivation of the $CuInSe_2$ surface via cadmium pre-electrolyte treatment, Phys. Rev. Mater., 4, 045405, 2020.

C. K. Boumenou *et al.*, the first draft of the paper focuses on PDT treated CIGSe samples is ready and will be submitted to the reviewers very soon.

Second author

E. M. Lanzoni, T. Gallet, C. Spindler, O. R. Sanchez, **C. K. Boumenou**, S. Siebentritt, A. Redinger, The impact of Kelvin probe force microscopy operation modes and environment on grain boundary band bending in perovskite and $Cu(In,Ga)Se_2$ solar cells, Nano Energy, 88, 106270, 2021.

M. Sood, A. Urbaniak, **C. K. Boumenou**, T. P. Weiss, H. Elanzeery, F. Babbe, F. Werner, M. Melchiorre, S. Siebentritt, Near surface defects: Cause of deficit between internal and external open-circuit voltage in solar cells, Prog. Photovolt: Res. Appl., 30, 263, 2022.

List of presentations

C. K. Boumenou, A. Elizabeth, F. Ehre, F. Babbe, H. Mönig, S. Siebentritt, A. Redinger, Surface characterization of polycristalline $Cu(In,Ga)Se_2$ absorbers, EU

PVSEC 2020, Lisbon (Online), Portugal, Oral presentation

C. K. Boumenou, T. Gallet, E. Lanzoni, F. Babbe, M. Melchiorre, C. Spindler, J. Guillot, S. Siebentritt, A. Redinger, Ultra high vacuum scanning tunneling spectroscopy on $CuInSe_2$ thin film solar cell absorber layers, MRS Spring Meeting, Phoenix, Arizona, 2019 & EXHIBIT, Oral presentation

H. Phirke, **C. K. Boumenou**, J. N. Audinot, T. Wirtz, A. Redinger, Effect of Post-Deposition Treatment on optical, electrical and compositional properties of $Cu(In,Ga)Se_2$ thin film solar cell, Maseena 2021, Luxembourg, Poster presentation

Acknowledgments

The completion of this project would perhaps not be possible without the presence of some people who helped and supported me while carrying it out. I would like to take this opportunity to thank and express my sincere gratitude to them.

The first person I would like to thank is my supervisor, Prof. Alex Redinger, who allowed me to work at the Scanning Probe Microscopy (SPM) laboratory in Luxembourg and who supported and encouraged me throughout the full completion of this project. Over the last four years that I spent with him, Alex has always been there to listen and engage heartily and endlessly in serious research-related discussions, and also for issues not directly related to my research project despite his busy calendar. For all that, I would like to deeply thank him and express my perpetual gratitude. Without a doubt, Alex is the kind of supervisor that all PhD students would dream to have. He knows how to motivate you when you are down and how to kindly push you if necessary.

I would like to thank Prof. Thomas Schmidt and Dr. Sascha Sadewasser for being part of my PhD committee and mainly for the useful advice and support throughout my PhD journey. Furthermore, many thank you to Prof. Phillip Dale and Dr. Romain Carron who accepted to be part of my defense committee. Once again, thank you Romain for providing some of the samples that I investigated within this project.

Special thank you to Prof. Susanne Siebentritt for providing some of the samples analyzed in the framework of this thesis and to Dr. Michel Melchiorre for the countless KCN etches.

I would like to thank Amala Elizabeth and Dr. Harry Mönig from the Center for Nanotechnology and Physikalisches Institut, Westfälische Wilhelms-Universität Münster, Münster, in Germany, for the nice collaboration and for carrying out some of my XPS measurements.

I would like to thank Dr. Jerôme Guillot and Dr. Jean-Nicolas Audinot from the Luxembourg Institute of Science and Technology (LIST) for the nice collaboration. Jerôme a big thank you for introducing me to the LIST XPS lab and also for the fruitful discussions we held while carrying my very first XPS measurements. Similarly, thank you so much Jean Nicolas for the SIMS measurements and for your availability. I enjoyed working with you.

A big thank you to our technical staff : Dr. Ulrich Siegel, Dr. Bernd Uder, Robert Himelrick and Robert Wagener for their availability. You were always ready to help with big smiles on your faces, and I was never disappointed even once when I come to see you. The same appears to Astrid Tobias concerning the administrative stuff. Spending these last years with you guys was a great pleasure.

Besides, I would like to thank all my SPM colleagues for their enormous support and a well conducive atmosphere in the lab. Additionally, I would like also to thank all my colleagues from the Laboratory for Photovoltaics and Laboratory for Energy Materials for the fruitful discussions held during our different join photovoltaic seminars.

I would like to thank my all family members and family in law, friends, specially Dr. Stive Roussel Tankio and Dr. Zelalem Urgressa, for their encouragement and support.

Finally, and most importantly, I would like to thank my special lovely wife, Linda, and our two kids Christian Junior and Leo for their understanding and real love. You have always been there for me every single moment besides encouraging and motivating me when I was down. “Madame K”, as I use to call you, big thank you for taking care of our kids and more, even over the weekend, when I had to be in the Lab. I know that it was not easy but you successfully managed it. For that, thank you so much. I love you.

Bibliography

[1] Climate change widespread, rapid, and intensifying – IPCC — IPCC. URL https://www.ipcc.ch/2021/08/09/ar6-wg1-20210809-pr/.(accessed: 2022-03-28).

[2] Greenhouse Effect 101 — NRDC. URL https://www.nrdc.org/stories/greenhouse-effect-101.(accessed:2022-03-28).

[3] International Renewable Energy Agency. *World Energy Transitions Outlook 2022: 1.5°C Pathway*. URL www.irena.org.(accessed:28-03-2022).

[4] A. G. Olabi and A. M. Ali. Renewable energy and climate change. *Renewable and Sustainable Energy Reviews*, vol. 158, p. 112111, 2022.

[5] N. M. Haegel, H. Atwater, T. Barnes, C. Breyer, A. Burrell, Y. M. Chiang, S. De Wolf, B. Dimmler, D. Feldman, S. Glunz, J. C. Goldschmidt, D. Hochschild, R. Inzunza, I. Kaizuka, B. Kroposki, S. Kurtz, S. Leu, R. Margolis, K. Matsubara, A. Metz, W. K. Metzger, M. Morjaria, S. Niki, S. Nowak, I. M. Peters, S. Philipps, T. Reindl, A. Richter, D. Rose, K. Sakurai, R. Schlatmann, M. Shikano, W. Sinke, R. Sinton, B. J. Stanbery, M. Topic, W. Tumas, Y. Ueda, J. Van De Lagemaat, P. Verlinden, M. Vetter, E. Warren, M. Werner, M. Yamaguchi, and A. W. Bett. Terawatt-scale photovoltaics: transform global energy improving costs and scale reflect looming opportunities. *Science*, vol. 364, no. 6443, pp. 836-838, 2019.

[6] C. Philibert. *Solar energy perspectives*. Organisation for Economic Cooperation and Development (OECD), 2011.

[7] How a solar cell works - American Chemical Society. URL https://www.acs.org/content/acs/en/education/resources/highschool/

chemmatters/past-issues/archive-2013-2014/how-a-solar-cell-works.html#.(accessed:2022-03-28).

[8] B. L. Miravet-Sánchez, A. E. García-Rivero, R. A. Yuli-Posadas, L. A. Inostroza-Ruiz, V. Fernández-Guzmán, Y. A. Chávez-Juanito, J. M. Rutti-Marin, and J. A. Apesteguia-Infantes. Solar photovoltaic technology in isolated rural communities in Latin America and the Caribbean. *Energy Reports*, vol. 8, pp. 1238-1248, 2022.

[9] Renewable Power Generation Costs in 2019. URL https://www.irena.org/publications/2020/Jun/Renewable-Power-Costs-in-2019.(accessed:2022-03-29).

[10] Y. Xu, J. Li, Q. Tan, A. L. Peters, and C. Yang. Global status of recycling waste solar panels: a review. *Waste Management*, vol. 75, pp. 450-458, 2018.

[11] M. A. Franco and S. N. Groesser. A systematic literature review of the solar photovoltaic value chain for a circular economy. *Sustainability*, vol. 13, no. 17, p. 9615, 2021.

[12] L. Stolt, J. Hedström, J. Kessler, M. Ruckh, K. O. Velthaus, and H. W. Schock. ZnO/CdS/$CuInSe_2$ thin-film solar cells with improved performance. *Applied Physics Letters*, vol. 62, no. 6, pp. 597-599, 1993.

[13] R. Scheer and H. W. Schock. *Chalcogenide Photovoltaics*. Wiley-VCH, 2012.

[14] M. Powalla, S. Paetel, D. Hariskos, R. Wuerz, F. Kessler, P. Lechner, W. Wischmann, and T. M. Friedlmeier. Advances in cost-efficient thin-Film photovoltaics based on Cu(In, Ga)Se_2. *Engineering*, vol. 3, no. 4, pp. 445-451, 2017.

[15] T. Feurer, P. Reinhard, E. Avancini, B. Bissig, J. Löckinger, P. Fuchs, R. Carron, T. P. Weiss, J. Perrenoud, S. Stutterheim, S. Buecheler, and A. N. Tiwari. Progress in thin film CIGS photovoltaics – research and development, manufacturing, and applications. *Progress in Photovoltaics: Research and Applications*, vol. 25, no. 7, pp. 645-667, 2017.

[16] T. Kawashima, S. Adachi, H. Miyake, and K. Sugiyama. Optical constants of $CuGaSe_2$ and $CuInSe_2$. *Journal of Applied Physics*, vol. 84, no. 9, pp. 5202-5209, 1998.

[17] Y. J. Jang, J. Lee, K. B. Lee, D. Kim, and Y. Lee. Quantitative analysis and band Gap determination for CIGS Absorber Layers using Surface techniques. *Journal of Analytical Methods in Chemistry*, vol. 2018, pp. 1-9, 2018.

[18] S. Siebentritt, L. Gütay, D. Regesch, Y. Aida, and V. Deprédurand. Why do we make Cu(In, Ga)Se_2 solar cells non-stoichiometric? *Solar Energy Materials and Solar Cells*, vol. 119, pp. 18-25, 2013.

[19] M. A. Green, E. D. Dunlop, J. Hohl-Ebinger, M. Yoshita, N. Kopidakis, and X. Hao. Solar cell efficiency tables (Version 58). *Progress in Photovoltaics: Research and Applications*, vol. 29, no. 7, pp. 657-667, 2021.

[20] Best Research-Cell Efficiency Chart — Photovoltaic Research — NREL. URL `https://www.nrel.gov/pv/cell-efficiency.html.(accessed: 2022-04-06)`.

[21] Multicrystalline silicon solar cell with 21.9% efficiency: Fraunhofer ISE Again holds world record - Fraunhofer ISE. URL `https://www.ise.fraunhofer.de/en/press-media/press-releases/2017/multicrystalline-silicon-solar-cell-with-21-point-9-%-efficiency-fraunhofer-ise-again-holds-world-record.html.(accessed:2022-03-30)`.

[22] M. Nakamura, K. Yamaguchi, Y. Kimoto, Y. Yasaki, T. Kato, and H. Sugimoto. Cd-Free Cu(In, Ga)(Se, S)$_2$ thin-film solar cell with record efficiency of 23.35%. *IEEE Journal of Photovoltaics*, vol. 9, no. 6, pp. 1863-1867, 2019.

[23] B. Ümsür. *Surface Engineering of Cu(In, Ga)Se_2 by KF and CdS – a Study by High-Energy Photoemission Spectroscopy.* PhD thesis, 2017.

[24] L. Weinhardt, M. Bär, H. J. Muffler, C. H. Fischer, M. C. Lux-Steiner, T. P. Niesen, F. Karg, T. Gleim, C. Heske, and E. Umbach. Impact of Cd^{2+}-treatment on the band alignment at the ILGAR-ZnO/CuIn(S, Se)$_2$ heterojunction. *Thin Solid Films*, vol. 431, pp. 272-276, 2003.

[25] M. Morkel, L. Weinhardt, B. Lohmüller, C. Heske, E. Umbach, W. Riedl, S. Zweigart, and F. Karg. Flat conduction-band alignment at the CdS/$CuInSe_2$

thin-film solar-cell heterojunction. *Applied Physics Letters*, vol. 79, no. 27, pp. 4482-4484, 2001.

[26] K. Ramanathan, H. Wiesner, S. Asher, R. N. Bhattacharya, J. Keane, M. A. Contreras, and R. Noufi. Junction formation in $CuInSe_2$-based thin-film devices. AIP Conference Proceedings, vol. 462, no. 1, pp. 9-16, 2009.

[27] F. Werner, F. Babbe, J. Burkhart, C. Spindler, H. Elanzeery, and S. Siebentritt. Interdiffusion and doping gradients at the buffer/absorber interface in thin-film solar cells. *ACS Applied Materials and Interfaces*, vol. 10, no. 34, pp. 28553-28565, 2018.

[28] P. W. Yu, S. P. Faile, and Y. S. Park. Cadmium-diffused $CuInSe_2$ junction diode and photovoltaic detection. *Applied Physics Letters*, vol. 26, no. 7, pp. 384-385, 1975.

[29] K. Ramanathan, F. S. Hasoon, S. Smith, D. L. Young, M. A. Contreras, P. K. Johnson, A. O. Pudov, and J. R. Sites. Surface treatment of $CuInGaSe_2$ thin films and its effect on the photovoltaic properties of solar cells. *Journal of Physics and Chemistry of Solids*, vol. 64, no. 9-10, pp. 1495-1498, 2003.

[30] P. Jackson, R. Wuerz, D. Hariskos, E. Lotter, W. Witte, and M. Powalla. Effects of heavy alkali elements in Cu(In, Ga)Se_2 solar cells with efficiencies up to 22.6%. *Physica Status Solidi - Rapid Research Letters*, vol. 10, no. 8, pp. 583-586, 2016.

[31] R. Wuerz, W. Hempel, and P. Jackson. Diffusion of Rb in polycrystalline Cu(In, Ga)Se_2 layers and effect of Rb on solar cell parameters of Cu(In, Ga)Se_2 thin-film solar cells. *Journal of Applied Physics*, vol. 124, no. 16, p. 165305, 2018.

[32] E. Avancini, R. Carron, T. P. Weiss, C. Andres, M. Bürki, C. Schreiner, R. Figi, Y. E. Romanyuk, S. Buecheler, and A. N. Tiwari. Effects of rubidium fluoride and potassium fluoride postdeposition treatments on Cu(In, Ga)Se_2 thin films and solar cell performance. *Chemistry of Materials*, vol. 29, no. 22, pp. 9695-9704, 2017.

[33] S. Ishizuka, N. Taguchi, J. Nishinaga, Y. Kamikawa, S. Tanaka, and H. Shibata. Group III elemental composition dependence of RbF postdeposition treatment

effects on Cu(In, Ga)Se_2 thin films and solar cells. *Journal of Physical Chemistry C*, vol. 122, no. 7, pp. 3809-3817, 2018.

[34] D. Hauschild, D. Kreikemeyer-Lorenzo, P. Jackson, T. M. Friedlmeier, D. Hariskos, F. Reinert, M. Powalla, C. Heske, and L. Weinhardt. Impact of a RbF postdeposition treatment on the electronic structure of the CdS/Cu(In, Ga)Se_2 heterojunction in high-efficiency thin-film solar cells. *ACS Energy Letters*, vol. 2, no. 10, pp. 2383-2387, 2017.

[35] M. D. Heinemann, T. Kodalle, C. Hages, M. Klupsch, D. Greiner, L. Korte, S. Levcenco, T. Unold, R. Schlatmann, and C. A. Kaufmann. Evaluation of recombination losses in thin film solar cells using an LED sun simulator - the effect of RbF post-deposition on CIGS solar cells. *EPJ Photovoltaics*, vol. 9, p. 9, 2018.

[36] S. Karki, P. Paul, G. Rajan, B. Belfore, D. Poudel, A. Rockett, E. Danilov, F. Castellano, A. Arehart, and S. Marsillac. Analysis of recombination mechanisms in RbF-treated cigs solar cells. *IEEE Journal of Photovoltaics*, vol. 9, no. 1, pp. 313-318, 2019.

[37] H. Mönig, Y. Smith, R. Caballero, C. A. Kaufmann, I. Lauermann, C. M. Lux-Steiner, and S. Sadewasser. Direct evidence for a reduced density of deep level defects at grain boundaries of Cu(In, Ga)Se_2 thin films. *Physical Review Letters*, vol. 105, no. 11, p. 116802, 2010.

[38] A. Elizabeth, S. K. Sahoo, D. Lockhorn, A. Timmer, N. Aghdassi, H. Zacharias, T. D. Kühne, S. Siebentritt, H. Mirhosseini, and H. Mönig. Oxidation/reduction cycles and their reversible effect on the dipole formation at $CuInSe_2$ surfaces. *Physical Review Materials*, vol. 4, no. 6, p. 063401, 2020.

[39] S. Bröker, D. Kück, A. Timmer, I. Lauermann, B. Ümsür, D. Greiner, C. A. Kaufmann, and H. Mönig. Correlating the local defect-level density with the macroscopic composition and energetics of chalcopyrite thin-film Surfaces. *ACS Applied Materials and Interfaces*, vol. 7, no. 23, pp. 13062–13072, 2015.

[40] H. Mönig, D. Lockhorn, N. Aghdassi, A. Timmer, C. A. Kaufmann, R. Caballero, H. Zacharias, and H. Fuchs. Heat induced passivation of $CuInSe_2$ surfaces: a

strategy to optimize the efficiency of chalcopyrite thin film solar cells? *Advanced Materials Interfaces*, vol. 1, no. 2, p. 1300040, 2014.

[41] J. Hedstrom, M. Bodegbd, A. Kylner, L. Stolt, D. Hariskos, M. Ruckh, and H. W. Schock. ZnO/CdS/Cu(In, Ga)Se_2 thin film solar cells with improved performance. *Conference Record of the Twenty Third IEEE Photovoltaic Specialists Conference - 1993 (Cat. No.93CH3283-9)*, 1993.

[42] F. Pianezzi, P. Reinhard, A. Chirilă, B. Bissig, S. Nishiwaki, S. Buecheler, and A. N. Tiwari. Unveiling the effects of post-deposition treatment with different alkaline elements on the electronic properties of CIGS thin film solar cells. *Physical Chemistry Chemical Physics*, vol. 16, no. 19, pp. 8843-8851, 2014.

[43] D. H. Cho, K. S. Lee, Y. D. Chung, J. H. Kim, S. J. Park, and J. Kim. Electronic effect of Na on Cu(In, Ga)Se_2 solar cells. *Applied Physics Letters*, vol. 101, no. 2, p. 023901, 2012.

[44] A. Czudek, A. Eslam, A. Urbaniak, P. Zabierowski, R. Wuerz, and M. Igalson. Evolution of the electrical characteristics of Cu(In, Ga)Se_2 devices with sodium content. *Journal of Applied Physics*, vol. 128, no. 17, p. 173102, 2020.

[45] L. Kronik, D. Cahen, H. W. Schock, and H. W. Schock. Effects of sodium on polycrystalline Cu(In, Ga)Se_2 and its solar cell performance. *Advanced Materials*, vol. 10, no. 1, pp. 31-36, 1998.

[46] O. Cojocaru-Mirédin, M. Raghuwanshi, R. Wuerz, and S. Sadewasser. Grain boundaries in Cu(In, Ga)Se_2: a review on composition–electronic property relationships by atom probe tomography and correlative microscopy. *Advanced Functional Materials*, vol. 31, no. 41, p. 2103119, 2021.

[47] Z. K. Yuan, S. Chen, Y. Xie, J. S. Park, H. Xiang, X. G. Gong, and S. H. Wei. Na-diffusion enhanced p-type conductivity in Cu(In, Ga)Se_2: a new mechanism for efficient doping in semiconductors. *Advanced Energy Materials*, vol. 6, no. 24, p. 1601191, 2016.

[48] N. Nicoara, R. Manaligod, P. Jackson, D. Hariskos, W. Witte, G. Sozzi, R. Menozzi, and S. Sadewasser. Direct evidence for grain boundary passivation

in Cu(In, Ga)Se_2 solar cells through alkali-fluoride post-deposition treatments. *Nature Communications*, vol. 10, no. 1, pp. 1-8, 2019.

[49] U. Rau, K. Taretto, and S. Siebentritt. Grain boundaries in Cu(In, Ga)(Se, S)$_2$ thin-film solar cells. *Applied Physics A: Materials Science and Processing*, vol. 96, no. 1, pp. 221-234, 2009.

[50] C. A. Kaufmann, A. Neisser, R. Klenk, and R. Scheer. Transfer of Cu(In, Ga)Se_2 thin film solar cells to flexible substrates using an in situ process control. *Thin Solid Films*, vol. 480, pp. 515-519, 2005.

[51] N. G. Dhere. Toward GW/year of CIGS production within the next decade. *Solar Energy Materials and Solar Cells*, vol. 91, no. 15-16, pp. 1376-1382, 2007.

[52] R. Carron, S. Nishiwaki, T. Feurer, R. Hertwig, E. Avancini, J. Löckinger, Shih C. Yang, S. Buecheler, and A. N. Tiwari. Advanced alkali treatments for high-efficiency Cu(In, Ga)Se_2 solar cells on flexible substrates. *Advanced Energy Materials*, vol. 9, no. 24, p. 1900408, 2019.

[53] P. Reinhard, A. Chirilă, P. Blösch, F. Pianezzi, S. Nishiwaki, S. Buecheler, and A. N. Tiwari. Review of progress toward 20% efficiency flexible CIGS solar cells and manufacturing issues of solar modules. *IEEE Journal of Photovoltaics*, vol. 3, no. 1, pp. 572-580, 2013.

[54] M. Bär, S. Nishiwaki, L. Weinhardt, S. Pookpanratana, W. N. Shafarman, and C. Heske. Electronic level alignment at the deeply buried absorber/Mo interface in chalcopyrite-based thin film solar cells. *Applied Physics Letters*, vol. 93, no. 4, p. 042110, 2008.

[55] D. Abou-Ras, G. Kostorz, D. Bremaud, M. Kälin, F. V. Kurdesau, A. N. Tiwari, and M. Döbeli. Formation and characterisation of $MoSe_2$ for Cu(In,Ga)Se_2 based solar cells. *Thin Solid Films*, vol. 480, pp. 433-438, 2005.

[56] S. Siebentritt. Alternative buffers for chalcopyrite solar cells. *Solar Energy*, vol. 77, no. 6, pp. 767-775, 2004.

[57] D. Liao and A. Rockett. Epitaxial growth of Cu(In,Ga)Se_2 on GaAs(110). *Journal of Applied Physics*, vol. 91, no. 4, pp. 1978-1983, 2002.

[58] D. Liao and A. Rockett. Cu depletion at the $CuInSe_2$ surface. *Applied Physics Letters*, vol. 82, no. 17, pp. 2829-2831, 2003.

[59] A. Bernard. Cadmium & its adverse effects on human health. *The Indian Journal of Medical Research*, vol. 128, no. 4, p. 557, 2008.

[60] N. Naghavi, D. Abou-Ras, N. Allsop, N. Barreau, S. Bücheler, A. Ennaoui, C. H. Fischer, C. Guillen, D. Hariskos, J. Herrero, R. Klenk, K. Kushiya, D. Lincot, R. Menner, T. Nakada, C. Platzer-Björkman, S. Spiering, A. N. Tiwari, and T. Törndahl. Buffer layers and transparent conducting oxides for chalcopyrite Cu(In, Ga)(S, $Se)_2$ based thin film photovoltaics: present status and current developments. *Progress in Photovoltaics: Research and Applications*, vol. 18, no. 6, pp. 411-433, 2010.

[61] A. Niemegeers, M. Burgelman, R. Herberholz, U. Rau, D. Hariskos, and H.W. Schock. Model for electronic transport in Cu(In, Ga)Se_2 solar cells. *Progress in Photovoltaics: Research and Applications*, vol. 6, no. 6, pp. 407-421, 1998.

[62] M. Gloeckler and J. R. Sites. Efficiency limitations for wide-band-gap chalcopyrite solar cells. *Thin Solid Films*, vol. 480, pp. 241-245, 2005.

[63] H. Elanzeery. *The cause of interface recombination in Cu-rich CIS thin film solar cells.* PhD thesis, 2017.

[64] R. Baier. *Electronic grain boundary properties in polycrystalline Cu(In, Ga)Se_2 semiconductors for thin film solar cells.* PhD thesis, 2012.

[65] D. Abou-Ras, R. Caballero, C. A. Kaufmann, M. Nichterwitz, K. Sakurai, S. Schorr, T. Unold, and H. W. Schock. Impact of the Ga concentration on the microstructure of $CuIn_{1-x}Ga_xSe_2$. *Physica Status Solidi - Rapid Research Letters*, vol. 2, no. 3, pp. 135-137, 2008.

[66] J. AbuShama, R. Noufi, S. Johnston, S. Ward, and X. Wu. Improved performance in $CuInSe_2$ and surface-modified $CuGaSe_2$ solar cells. *Conference Record of the IEEE Photovoltaic Specialists Conference*, pp. 299-302, 2005.

[67] P. Jackson, D. Hariskos, E. Lotter, S. Paetel, R. Wuerz, R. Menner, W. Wischmann, and M. Powalla. New world record efficiency for Cu(In, Ga)Se_2 thin-film

solar cells beyond 20%. *Progress in Photovoltaics: Research and Applications*, vol. 19, no. 7, pp. 894-897, 2011.

[68] A. J. Wooten, D. J. Werder, D. J. Williams, J. L. Casson, and J. A. Hollingsworth. Solution-liquid-solid growth of ternary Cu-In-Se semiconductor nanowires from multiple- and single-source precursors. *Journal of the American Chemical Society*, vol. 131, no. 44, pp. 16177-16188, 2009.

[69] B. J. Stanbery. Copper indium selenides and related materials for photovoltaic devices. *Critical Reviews in Solid State and Materials Sciences*, vol. 27, no. 2, pp. 73-117, 2002.

[70] S. C. Abrahams and J. L. Bernstein. Piezoelectric nonlinear optic $CuGaSe_2$ and $CdGeAs_2$: crystal structure, chalcopyrite microhardness, and sublattice distortion. *The Journal of Chemical Physics*, vol. 61, no. 3, pp. 1140-1146, 1974.

[71] S. Schuler, S. Nishiwaki, J. Beckmann, N. Rega, S. Brehme, S. Siebentritt, and M. C. Lux-Steiner. Charge carrier transport in polycrystalline $CuGaSe_2$ thin films. *Conference Record of the IEEE Photovoltaic Specialists Conference*, pp. 504-507, 2002.

[72] T. Eisenbarth, T. Unold, R. Caballero, C. A. Kaufmann, and H. W. Schock. Interpretation of admittance, capacitance-voltage, and current-voltage signatures in Cu(In, Ga)Se_2 thin film solar cells. *Journal of Applied Physics*, vol. 107, no. 3, p. 034509, 2010.

[73] S. H. Wei, S. B. Zhang, and A. Zunger. Effects of Ga addition to $CuInSe_2$ on its electronic, structural, and defect properties. *Applied Physics Letters*, vol. 72, no. 24, pp. 3199-3201, 1998.

[74] C. Persson, Y. J. Zhao, S. Lany, and A. Zunger. n-type doping of $CuInSe_2$ and $CuGaSe_2$. *Physical Review B*, vol. 72, no. 3, p. 035211, 2005.

[75] S. B. Zhang, S. H. Wei, A. Zunger, and H. Katayama-Yoshida. Defect physics of the $CuInSe_2$ chalcopyrite semiconductor. *Physical Review B*, vol. 57, no. 16, p. 9642, 1998.

[76] S. B. Zhang, S. H. Wei, and A. Zunger. Stabilization of ternary compounds via ordered arrays of defect pairs. *Physical review letters*, vol. 78, no. 21, p. 4059, 1997.

[77] A. Chirilă, P. Reinhard, F. Pianezzi, P. Bloesch, A. R. Uhl, C. Fella, L. Kranz, D. Keller, C. Gretener, H. Hagendorfer, D. Jaeger, R. Erni, S. Nishiwaki, S. Buecheler, and A. N. Tiwari. Potassium-induced surface modification of Cu(In, Ga)Se_2 thin films for high-efficiency solar cells. *Nature Materials*, vol. 12, no. 12, pp. 1107-1111, 2013.

[78] K. Hiepko, J. Bastek, R. Schlesiger, G. Schmitz, R. Wuerz, and N. A. Stolwijk. Diffusion and incorporation of Cd in solar-grade Cu(In, Ga)Se_2 layers. *Applied Physics Letters*, vol. 99, no. 23, p. 234101, 2011.

[79] T. Nakada and A. Kunioka. Direct evidence of Cd diffusion into Cu(In, Ga)Se_2 thin films during chemical-bath deposition process of CdS films. *Applied Physics Letters*, vol. 74, no. 17, pp. 2444-2446, 1999.

[80] J. E. Jaffe and A. Zunger. Electronic structure of the ternary chalcopyrite semiconductors $CuAls_2$, $CuGaS_2$ $CuInS_2$, $CuAlse_2$, $CuGaSe_2$, and CuInSe2. *Physical Review B*, vol. 28, no. 10, p. 5822, 1983.

[81] T. Nakada. CIGS-based thin film solar cells and modules: unique material properties. *Electronic Materials Letters*, vol. 8, no. 2, pp. 179-185, 2012.

[82] S. Chichibu, T. Mizutani, K. Murakami, T. Shioda, T. Kurafuji, H. Nakanishi, S. Niki, P. J. Fons, and A. Yamada. Band gap energies of bulk, thin-film, and epitaxial layers of $CuInSe_2$ and $CuGaSe_2$. *Journal of Applied Physics*, vol. 83, no. 7, pp. 3678-3689, 1998.

[83] M. I. Alonso, K. Wakita, J. Pascual, M. Garriga, and N. Yamamoto. Optical functions and electronic structure of $CuInSe_2$, $CuGaSe_2$, $CuInS_2$, and $CuGaS_2$. *Physical Review B - Condensed Matter and Materials Physics*, vol. 63, no. 7, p. 075203, 2001.

[84] C. Persson. Anisotropic hole-mass tensor of $CuIn_{1-x}Ga_x(S, Se)_2$: presence of

free carriers narrows the energy gap. *Applied Physics Letters*, vol. 93, no. 7, p. 072106, 2008.

[85] M. Turcu, I. M. Kötschau, and U. Rau. Composition dependence of defect energies and band alignments in the $Cu(In_{1-x}Ga_x)(Se_{1-y}S_y)_2$ alloy system. *Journal of Applied Physics*, vol. 91, no. 3, pp. 1391-1399, 2002.

[86] S. H. Wei and A. Zunger. Band offsets and optical bowings of chalcopyrites and Zn-based II-VI alloys. *Journal of Applied Physics*, vol. 78, no. 6, pp. 3846-3856, 1995.

[87] P. Pistor, D. Greiner, C. A. Kaufmann, S. Brunken, M. Gorgoi, A. Steigert, W. Calvet, I. Lauermann, R. Klenk, T. Unold, and M. C. Lux-Steiner. Experimental indication for band gap widening of chalcopyrite solar cell absorbers after potassium fluoride treatment. *Applied Physics Letters*, vol. 105, no. 6, p. 063901, 2014.

[88] U. Rau and H. W. Schock. Electronic properties of $Cu(In,Ga)Se_2$ heterojunction solar cells-recent achievements, current understanding, and future challenges. *Applied Physics A*, vol. 69, no. 2, pp. 131-147, 1999.

[89] M. Bär, S. Nishiwaki, L. Weinhardt, S. Pookpanratana, O. Fuchs, M. Blum, W. Yang, J. D. Denlinger, W. N. Shafarman, and C. Heske. Depth-resolved band gap in $Cu(In, Ga)(S, Se)_2$ thin films. *Applied Physics Letters*, vol. 93, no. 24, p. 244103, 2008.

[90] M. Bär, S. Pookpanratana, L. Weinhardt, R. G. Wilks, B. A. Schubert, B. Marsen, T. Unold, M. Blum, S. Krause, Y. Zhang, A. Ranasinghe, K. Ramanathan, I. Repins, M. A. Contreras, S. Nishiwaki, X. Liu, N. R. Paudel, O. Fuchs, T. P. Niesen, W. Yang, F. Karg, A. D. Compaan, W. N. Shafarman, R. Noufi, H. W. Schock, and C. Heske. Soft X-rays shedding light on thin-film solar cell surfaces and interfaces. *Journal of Electron Spectroscopy and Related Phenomena*, vol. 190, pp. 47-53, 2013.

[91] A. A. Luque and S. Hegedus. *Handbook of photovoltaic science and engineering*. Wiley, 2003.

[92] H. Rodriguez-Alvarez, A. Weber, J. Lauche, C. A. Kaufmann, T. Rissom, D. Greiner, M. Klaus, T. Unold, C. Genzel, H. W. Schock, and R. Mainz. Formation of $CuInSe_2$ and $CuGaSe_2$ thin-films deposited by three-stage thermal co-evaporation: a real-time X-ray diffraction and fluorescence study. *Advanced Energy Materials*, vol. 3, no. 10, pp. 1381-1387, 2013.

[93] L. L. Kazmerski, O. Jamjoum, P. J. Ireland, S. K. Deb, R. A. Mickelsen, and W. Chen. Initial oxidation of $CuInSe_2$. *Journal of vacuum science and technology*, vol. 19, no. 3, pp. 467-471, 1981.

[94] U. Rau, D. Braunger, R. Herberholz, H. W. Schock, J.F. Guillemoles, L. Kronik, and D. Cahen. Oxygenation and air-annealing effects on the electronic properties of Cu(In, Ga)Se_2 films and devices. *Journal of Applied Physics*, vol. 86, no. 1, pp. 497-505, 1999.

[95] A. Loubat, M. Bouttemy, S. Gaiaschi, D. Aureau, M. Frégnaux, D. Mercier, J. Vigneron, P. Chapon, and A. Etcheberry. Chemical engineering of Cu(In, Ga)Se_2 surfaces: an absolute deoxidation studied by X-ray photoelectron spectroscopy and Auger electron spectroscopy signatures. *Thin Solid Films*, vol. 633, pp. 87-91, 2017.

[96] D. Regesch, L. Gütay, J. K. Larsen, V. Deprédurand, D. Tanaka, Y. Aida, and S. Siebentritt. Degradation and passivation of $CuInSe_2$. *Applied Physics Letters*, vol. 101, no. 11, p. 112108, 2012.

[97] D. Hauschild, F. Meyer, S. Pohlner, R. Lechner, R. Dietmüller, J. Palm, C. Heske, L. Weinhardt, and F. Reinert. Impact of environmental conditions on the chemical surface properties of Cu(In,Ga)(S, $Se)_2$ thin-film solar cell absorbers. *Journal of Applied Physics*, vol. 115, no. 18, p. 183707, 2014.

[98] H. Mönig, C. H. Fischer, R. Caballero, C. A. Kaufmann, N. Allsop, M. Gorgoi, R. Klenk, H. W. Schock, S. Lehmann, M. C. Lux-Steiner, and I. Lauermann. Surface Cu depletion of Cu(In, Ga)Se_2 films: An investigation by hard X-ray photoelectron spectroscopy. *Acta Materialia*, vol. 57, no. 12, pp. 3645-3651, 2009.

[99] R. Würz, A. Meeder, D. Fuertes Marrón, T. Schedel-Niedrig, A. Knop-Gericke, and K. Lips. Native oxidation of $CuGaSe_2$ crystals and thin films studied by electron paramagnetic resonance and photoelectron spectroscopy. *Physical Review B - Condensed Matter and Materials Physics*, vol. 70, no. 20, p. 205321, 2004.

[100] F. Babbe, L. Choubrac, and S. Siebentritt. Quasi Fermi level splitting of Cu-rich and Cu-poor Cu(In, Ga)Se_2 absorber layers. *Applied Physics Letters*, vol. 109, no. 8, p. 082105, 2016.

[101] D. W. Niles, K. Ramanathan, F. Hasoon, R. Noufi, B. J. Tielsch, and J. E. Fulghum. Na impurity chemistry in photovoltaic CIGS thin films: Investigation with x-ray photoelectron spectroscopy. *Journal of Vacuum Science & Technology A: Vacuum, Surfaces, and Films*, vol. 15, no. 6, pp. 3044-3049, 1997.

[102] R. Hunger, T. Schulmeyer, A. Klein, W. Jaegermann, K. Sakurai, A. Yamada, P. Fons, K. Matsubara, and S. Niki. An option for the surface science on Cu chalcopyrites: the selenium capping and decapping process. *Surface Science*, vol. 557, no 1-3, pp. 263-268, 2004.

[103] J. Lehmann, S. Lehmann, I. Lauermann, T. Rissom, C. A. Kaufmann, M. C. Lux-Steiner, M. Bär, and S. Sadewasser. Reliable wet-chemical cleaning of natively oxidized high-efficiency Cu(In, Ga)Se_2 thin-film solar cell absorbers. *Journal of Applied Physics*, vol. 116, no. 23, p. 233502, 2014.

[104] A. Loubat, S. Béchu, M. Bouttemy, J. Vigneron, D. Lincot, J. F. Guillemoles, and A. Etcheberry. Cu depletion on Cu(In, Ga)Se_2 surfaces investigated by chemical engineering: an x-ray photoelectron spectroscopy approach. *Journal of Vacuum Science and Technology A*, vol. 37, no. 4, p. 041201, 2019.

[105] F. Babbe, H. Elanzeery, M. Melchiorre, A. Zelenina, and S. Siebentritt. Potassium fluoride postdeposition treatment with etching step on both Cu-rich and Cu-poor $CuInSe_2$ thin film solar cells. *Physical Review Materials*, vol. 2, no. 10, p. 105405, 2018.

[106] H. Elanzeery, M. Melchiorre, M. Sood, F. Babbe, F. Werner, G. Brammertz, and

S. Siebentritt. Challenge in Cu-rich $CuInS_2$ thin film solar cells: defect caused by etching. *Physical Review Materials*, vol. 3, no. 5, p. 055403, 2019.

[107] C. D. Lokhande and G. Hodes. Preparation of $CuInSe_2$ and $CuInS_2$ films by reactive annealing in H_2Se or H_2S. *Solar Cells*, vol. 21, no. 1-4, pp. 215-224, 1987.

[108] C. S. Jiang, R. Noufi, K. Ramanathan, H. R. Moutinho, and M. M. Al-Jassim. Electrical modification in Cu(In, Ga)Se_2 thin films by chemical bath deposition process of CdS films. *Journal of Applied Physics*, vol. 97, no. 5, p. 053701, 2005.

[109] H. Mönig, R. Caballero, C. A. Kaufmann, T. L. Schmidt, M. C. Lux-Steiner, and S. Sadewasser. Nanoscale investigations of the electronic surface properties of Cu(In, Ga)Se_2 thin films by scanning tunneling spectroscopy. *Solar Energy Materials and Solar Cells*, vol. 95, no. 6, pp. 1537-1543, 2011.

[110] O. Cojocaru-Miŕdin, P. Choi, R. Wuerz, and D. Raabe. Atomic-scale characterization of the CdS/$CuInSe_2$ interface in thin-film solar cells. *Applied Physics Letters*, vol. 98, no. 10, p. 103504, 2011.

[111] C. Lei, M. Duch, I. M. Robertson, and A. Rockett. Effects of solution-grown CdS on Cu(In, Ga)Se_2 grain boundaries. *Journal of Applied Physics*, vol. 108, no. 11, p. 114908, 2010.

[112] J. Kiss, T. Gruhn, G. Roma, and C. Felser. Theoretical study on the structure and energetics of Cd insertion and Cu depletion of $CuIn_5Se_8$. *Journal of Physical Chemistry C*, vol. 117, no. 21, pp. 10892-10900, 2013.

[113] J. Kiss, T. Gruhn, G. Roma, and C. Felser. Theoretical study on the diffusion mechanism of Cd in the Cu-poor phase of $CuInSe_2$ solar cell material. *Journal of Physical Chemistry C*, vol. 117, no. 49, pp. 25933-25938, 2013.

[114] R. Baier, C. Leendertz, D. Abou-Ras, M. C. Lux-Steiner, and S. Sadewasser. Properties of electronic potential barriers at grain boundaries in Cu(In, Ga)Se_2 thin films. *Solar Energy Materials and Solar Cells*, vol. 130, pp. 124-131, 2014.

[115] D. Azulay, D. Abou-Ras, I. Popov, I. Balberg, and O. Millo. The effect of Na on the electronic properties of Cu(In, Ga)Se_2 thin films: a local-probe study. *Physica Status Solidi - Rapid Research Letters*, vol. 10, no. 6, pp. 448-452, 2016.

[116] M. A. Mayer, L. B. Ruppalt, D. Hebert, J. Lyding, and A. A. Rockett. Scanning tunneling microscopic analysis of Cu(In, Ga)Se_2 epitaxial layers. *Journal of Applied Physics*, vol. 107, no. 3, p. 034906, 2010.

[117] S. A. Jensen, S. Glynn, A. Kanevce, P. Dippo, J. V. Li, D. H. Levi, and D. Kuciauskas. Beneficial effect of post-deposition treatment in high-efficiency Cu(In, Ga)Se_2 solar cells through reduced potential fluctuations. *Journal of Applied Physics*, vol. 120, no. 6, p. 063106, 2016.

[118] T. Feurer, F. Fu, T. P. Weiss, E. Avancini, J. Löckinger, S. Buecheler, and A. N. Tiwari. RbF post deposition treatment for narrow bandgap Cu(In, Ga)Se_2 solar cells. *Thin Solid Films*, vol. 670, pp. 34-40, 2019.

[119] R. Caballero, C. A. Kaufmann, T. Eisenbarth, A. Grimm, I. Lauermann, T. Unold, R. Klenk, and H. W. Schock. Influence of Na on Cu(In, Ga)Se_2 solar cells grown on polyimide substrates at low temperature: impact on the Cu(In, Ga)Se_2/Mo interface. *Applied Physics Letters*, vol. 96, no. 9, p. 092104, 2010.

[120] R. Caballero, C. A. Kaufmann, T. Eisenbarth, M. Cancela, R. Hesse, T. Unold, A. Eicke, R. Klenk, and H. W. Schock. The influence of Na on low temperature growth of CIGS thin film solar cells on polyimide substrates. *Thin Solid Films*, vol. 517, no. 7, pp. 2187-2190, 2009.

[121] C. A. Kaufmann, R. Caballero, A. Eicke, T. Rissom, T. Eisenbarth, T. Unold, S. Schorr, C. Stephan, R. Klenk, and H. W. Schock. Aspects for the optimization of CIGSe growth at low temperatures for application in thin film solar cells on polyimide foil. *2009 34th IEEE Photovoltaic Specialists Conference (PVSC)*, pp. 000670-000675, 2009.

[122] D. Rudmann, D. Brémaud, H. Zogg, and A. N. Tiwari. Na incorporation into Cu (In, Ga)Se_2 for high-efficiency flexible solar cells on polymer foils. *Journal of Applied Physics*, vol. 97, no. 8, p. 084903, 2005.

[123] R. Wuerz, A. Eicke, F. Kessler, P. Rogin, and O. Yazdani-Assl. Alternative sodium sources for Cu(In, Ga)Se_2 thin-film solar cells on flexible substrates. *Thin Solid Films*, vol. 519, no. 21, pp. 7268-7271, 2011.

[124] K. Granath, M. Bodega, and L. Stolt. The effect of NaF on Cu(In, Ga)Se_2 thin film solar cells. *Solar Energy Materials and Solar Cells*, vol. 60, no. 3, pp. 279-293, 2000.

[125] R. Würz, D. Fuertes Marron, A. Meeder, A. Rumberg, SM Babu, T. Schedel-Niedrig, U. Bloeck, P. Schubert-Bischoff, and M. C. Lux-Steiner. Formation of an interfacial $MoSe_2$ layer in CVD grown $CuGaSe_2$ based thin film solar cells. *Thin Solid Films*, vol. 431, pp. 398-402, 2003.

[126] D. W. Niles, M. Al-Jassim, and K. Ramanathan. Direct observation of Na and O impurities at grain surfaces of $CuInSe_2$ thin films. *Journal of Vacuum Science and Technology A: Vacuum, Surfaces, and Films*, vol. 17, no. 1, pp. 291-296, 1999.

[127] M. A. Contreras, B. Egaas, P. Dippo, J. Webb, J. Granata, K. Ramanathan, S. Swartzlander A. Asher, and R. Noufi. On the role of Na and modifications to Cu(In,Ga)Se_2 absorber materials using thin-MF (M=Na, K, Cs) Precursor Layers. *Conference Record of the Twenty Sixth IEEE Photovoltaic Specialists Conference*, 1997.

[128] M. Ruckh, D Schmid, M. Kaiser, R. Schäffler, T. Walter, and H. W. Schock. Influence of substrates on the electrical properties of Cu(In, Ga)Se_2 thin films. *Proceedings of 1994 IEEE 1st World Conference on Photovoltaic Energy Conversion - WCPEC (A Joint Conference of PVSC, PVSEC and PSEC)*, 1994.

[129] T. Maeda, A. Kawabata, and T. Wada. First-principles study on alkali-metal effect of Li, Na, and K in $CuInSe_2$ and $CuGaSe_2$. *Japanese Journal of Applied Physics*, vol. 54, no. 8S1, p. 08KC20, 2015.

[130] E. Ghorbani, J. Kiss, H. Mirhosseini, G. Roma, M. Schmidt, J. Windeln, Thomas D. Kühne, and C. Felser. Hybrid-functional calculations on the incorporation of Na and K impurities into the $CuInSe_2$ and $CuIn_5Se_8$ solar-cell

materials. *Journal of Physical Chemistry C*, vol. 119, no. 45, pp. 25197-25203, 2015.

[131] M. A. Bodeg, K. Granath, and L. Stolt. Growth of Cu(In, Ga)Se_2 thin films by coevaporation using alkaline precursors. *Thin Solid Films*, vol. 361, pp. 9-16, 2000.

[132] T. P. Weiss, S. Nishiwaki, B. Bissig, R. Carron, E. Avancini, J. Löckinger, S. Buecheler, and A. N. Tiwari. Injection current barrier formation for RbF postdeposition-treated Cu(In, Ga)Se_2-based solar cells. *Advanced Materials Interfaces*, vol. 5, no. 4, p. 1701007, 2018.

[133] T. Kodalle, T. Bertram, R. Schlatmann, and C. A. Kaufmann. Effectiveness of an RbF post deposition treatment of CIGS Solar cells in dependence on the Cu Content of the absorber layer. *IEEE Journal of Photovoltaics*, vol. 9, no. 6, pp. 1839-1845, 2019.

[134] N. Maticiuc, T. Kodalle, B. Ümsür, T. Bertram, R. Wenisch, Y. Wang, I. Majumdar, H. A. Yetkin, D. Abou-Ras, N. Schäfer, C. A. Kaufmann, R. Schlatmann, and I. Lauermann. Depth-resolved analysis of the effect of RbF post deposition treatment on CIGSe with two different Cu concentrations. *Solar Energy Materials and Solar Cells*, vol. 226, p. 111071, 2021.

[135] N. Taguchi, S. Tanaka, and S. Ishizuka. Direct insights into $RbInSe_2$ formation at Cu(In, Ga)Se_2 thin film surface with RbF postdeposition treatment. *Applied Physics Letters*, vol. 113, no. 11, p. 113903, 2018.

[136] M. Malitckaya, H. P. Komsa, V. Havu, and M. J. Puska. Effect of alkali metal atom doping on the $CuInSe_2$-based solar cell absorber. *Journal of Physical Chemistry C*, vol. 121, no. 29, pp. 15516-15528, 2017.

[137] W. Witte, D. Abou-Ras, and D. Hariskos. Chemical bath deposition of Zn(O, S) and CdS buffers: Influence of Cu(In, Ga)Se_2 grain orientation. *Applied Physics Letters*, vol. 102, no. 5, p. 051607, 2013.

[138] T. Kodalle, L. Choubrac, L. Arzel, R. Schlatmann, N. Barreau, and C. A. Kaufmann. Effects of KF and RbF post deposition treatments on the growth of

the CdS buffer layer on CIGS thin films - a comparative study. *Solar Energy Materials and Solar Cells*, vol. 200, p. 109997, 2019.

[139] T. M. Friedlmeier, P. Jackson, D. Kreikemeyer-Lorenzo, D. Hauschild, O. Kiowski, D. Hariskos, L. Weinhardt, C. Heske, and M. Powalla. A closer look at Initial CdS growth on high-efficiency Cu(In, Ga)Se_2 absorbers using surface-sensitive methods. *2016 IEEE 43rd Photovoltaic Specialists Conference (PVSC)*, pp. 0457-0461, 2016.

[140] L. Weinhardt, O. Fuchs, D. Groß, G. Storch, E. Umbach, N. G. Dhere, A. A. Kadam, S. S. Kulkarni, and C. Heske. Band alignment at the CdS Cu(In, Ga)S_2 interface in thin-film solar cells. *Applied Physics Letters*, vol. 86, no. 6, p. 062109, 2005.

[141] P. Schöppe, S. Schönherr, R. Wuerz, W. Wisniewski, G. Martínez-Criado, M. Ritzer, K. Ritter, C. Ronning, and C. S. Schnohr. Rubidium segregation at random grain boundaries in Cu(In, Ga)Se_2 absorbers. *Nano Energy*, vol. 42, pp. 307-313, 2017.

[142] M. Raghuwanshi, A. Vilalta-Clemente, C. Castro, S. Duguay, E. Cadel, P. Jackson, D. Hariskos, W. Witte, and P. Pareige. Influence of RbF post deposition treatment on heterojunction and grain boundaries in high efficient (21.1%) Cu(In,Ga)Se_2 solar cells. *Nano Energy*, vol. 60, pp. 103-110, 2019.

[143] P. Pistor, D. Greiner, C. A. Kaufmann, S. Brunken, M. Gorgoi, A. Steigert, W. Calvet, I. Lauermann, R. Klenk, T. Unold, and M. C. Lux-Steiner. Experimental indication for band gap widening of chalcopyrite solar cell absorbers after potassium fluoride treatment. *Applied Physics Letters*, vol. 105, no. 6, p. 063901, 2014.

[144] A. Laemmle, R. Wuerz, and M. Powalla. Efficiency enhancement of Cu(In, Ga)Se_2 thin-film solar cells by a post-deposition treatment with potassium fluoride. *Physica Status Solidi - Rapid Research Letters*, vol. 7, no. 9, pp. 631-634, 2013.

[145] T. Dullweber, O. Lundberg, J. Malmstrom, M. Bodegard, L. Stolt, U. Rau,

H. W. Schock, and J.H. Werner. Back surface band gap gradings in Cu(In,Ga)Se solar cells. *Thin Solid Films*, vol. 387, no. 1-2, pp. 11-13, 2001.

[146] M. Gloeckler and J. R. Sites. Band-gap grading in Cu(In, Ga)Se_2 solar cells. *Journal of Physics and Chemistry of Solids*, vol. 66, no. 11, pp. 1891-1894, 2005.

[147] J. Kavalakkatt, D. Abou-Ras, J. Haarstrich, C. Ronning, M. Nichterwitz, R. Caballero, T. Rissom, T. Unold, R. Scheer, and H. W. Schock. Electron-beam-induced current at absorber back surfaces of Cu(In,Ga)Se_2 thin-film solar cells. *Journal of Applied Physics*, vol. 115, no. 1, p. 014504, 2014.

[148] B. Vermang, J. T. Wätjen, V. Fjällström, F. Rostvall, M. Edoff, R. Gunnarsson, I. Pilch, U. Helmersson, R. Kotipalli, F. Henry, and D. Flandre. Highly reflective rear surface passivation design for ultra-thin Cu(In, Ga)Se_2 solar cells. *Thin Solid Films*, vol. 582, pp. 300-303, 2015.

[149] T. Feurer, B. Bissig, T. P. Weiss, R. Carron, E. Avancini, J. Löckinger, S. Buecheler, and A. N. Tiwari. Single-graded CIGS with narrow bandgap for tandem solar cells. *Science and Technology of Advanced Materials*, vol. 19, no. 1, pp. 263-270, 2018.

[150] R. Scheer and H. J. Lewerenz. Formation of secondary phases in evaporated $cuins_2$ thin films: a surface analytical study. *Journal of Vacuum Science and Technology A: Vacuum, Surfaces, and Films*, vol. 13, no. 4, pp. 1924-1929, 1995.

[151] M. Bär, L. Weinhardt, C. Heske, S. Nishiwaki, and W. N. Shafarman. Chemical structures of the Cu(In, Ga)Se_2/Mo and Cu (In, Ga) (S, $Se)_2$ /Mo interfaces. *Physical Review B - Condensed Matter and Materials Physics*, vol. 78, no. 7, p. 075404, 2008.

[152] T. Wada, N. Kohara, S. Nishiwaki, and T. Negami. Characterization of the Cu(In, Ga)Se_2/Mo interface in CIGS solar cells. *Thin Solid Films*, vol. 387, no. 1-2, pp. 118-122, 2001.

[153] J. Keller, R. Schlesiger, I. Riedel, J. Parisi, G. Schmitz, A. Avellan, and T. Dalibor. Grain boundary investigations on sulfurized Cu(In, Ga)(S, $Se)_2$ solar cells

using atom probe tomography. *Solar Energy Materials and Solar Cells*, vol. 117, pp. 592-598, 2013.

[154] V. Nadenau, D. Hariskos, H. W. Schock, M. Krejci, F. J. Haug, A. N. Tiwari, H. Zogg, and G. Kostorz. Microstructural study of the CdS/$CuGaSe_2$ interfacial region in $CuGaSe_2$ thin film solar cells. *Journal of Applied Physics*, vol. 85, no. 1, pp. 534-542, 1999.

[155] V. Alberts, R. Swanepoel, and M. J. Witcomb B. Material properties of $CuInSe_2$ prepared by H_2Se treatment of CuIn alloys. *Journal of materials science*, vol. 33, no. 11, pp. 2919-2925, 1998.

[156] D. F. Marrón, A. Meeder, S. Sadewasser, R. Würz, C. A. Kaufmann, T. Glatzel, T. Schedel-Niedrig, and M. C. Lux-Steiner. Lift-off process and rear-side characterization of $CuGaSe_2$ chalcopyrite thin films and solar cells. *Journal of Applied Physics*, vol. 97, no. 9, p. 094915, 2005.

[157] C. Spindler, F. Babbe, M. H. Wolter, F. Ehré, K. Santhosh, P. Hilgert, F. Werner, and S. Siebentritt. Electronic defects in Cu(In, Ga)Se_2: towards a comprehensive model. *Physical Review Materials*, vol. 3, no. 9, p. 090302, 2019.

[158] C. K. Boumenou, F. Babbe, A. Elizabeth, M. Melchiorre, C. Spindler, J. Guillot, H. Mönig, S. Siebentritt, and A. Redinger. Passivation of the $CuInSe_2$ surface via cadmium pre-electrolyte treatment. *Physical Review Materials*, vol. 4, no. 4, p. 045405, 2020.

[159] H. J. Msller. Structure and defect chemistry of grain boundaries in $CuInSe_2$. *Solar Cells*, vol. 31, no. 1, pp. 77-100, 1991.

[160] S. S. Schmidt. *Microscopic properties of grain boundaries in Cu(In, Ga)Se_2 and CuInS2 thin-film solar cells studied by transmission electron microscopy.* PhD thesis, 2011.

[161] J. Y. W. Seto. The electrical properties of polycrystalline silicon films. *Journal of Applied Physics*, vol. 46, no. 12, pp. 5247-5254, 1975.

[162] T. I. Kamins. Hall mobility in chemically deposited polycrystalline silicon. *Journal of Applied Physics*, vol. 42, no. 11, pp. 4357-4365, 1971.

[163] M. E. Cowher and T. O. Sedgwick. Chemical vapor deposited polycrystalline silicon. *Journal of The Electrochemical Society*, vol. 119, no. 11, p.1565, 1972.

[164] W. Siegel, G. Kuhnel, and H. A. Suhneider. On the determination of the carrier concentration in large-grain polycrystalline InP, GaAs, and GaP by Hall effect measurements. *phys. stat. sol. (a)*, vol. 87, no. 2, pp. 673-681, 1985.

[165] M. K. Sharma and D. P. Joshi. Electrical conduction model for polycrystalline GaAs films. *Journal of Applied Physics*, vol. 102, no. 3, p. 033704, 2007.

[166] Y. Yan, Wan J. Yin, Y. Wu, T. Shi, N. R. Paudel, C. Li, J. Poplawsky, Z. Wang, J. Moseley, H. Guthrey, H. Moutinho, S. J. Pennycook, and M. M. Al-Jassim. Physics of grain boundaries in polycrystalline photovoltaic semiconductors. *Journal of Applied Physics*, vol. 117, no. 11, p. 112807, 2015.

[167] C. Persson and A. Zunger. Anomalous grain boundary physics in polycrystalline : the existence of a hole barrier. *Physical Review Letters*, vol. 91, no. 26, p. 266401, 2003.

[168] D. F. Marrón, S. Sadewasser, A. Meeder, T. Glatzel, and M. C. Lux-Steiner. Electrical activity at grain boundaries of Cu(In, Ga)Se_2 thin films. *Physical Review B - Condensed Matter and Materials Physics*, vol. 71, no. 3, p. 033306, 2005.

[169] Y. Yan, C. S. Jiang, R. Noufi, S. H. Wei, H. R. Moutinho, and M. M. Al-Jassim. Electrically benign behavior of grain boundaries in polycrystalline $CuInSe_2$ films. *Physical Review Letters*, vol. 99, no. 23, p. 235504, 2007.

[170] M. Hafemeister, S. Siebentritt, J. Albert, M. C. Lux-Steiner, and S. Sadewasser. Large neutral barrier at grain boundaries in chalcopyrite thin films. *Physical Review Letters*, vol. 104, no. 19, p. 196602, 2010.

[171] Y. Yan, M. M. Al-Jassim, and K. M. Jones. Structure and effects of double-positioning twin boundaries in CdTe. *Journal of Applied Physics*, vol. 94, no. 5, pp. 2976-2979, 2003.

[172] Y. Yan, M. M. Al-Jassim, and K. M. Jones. Passivation of double-positioning twin boundaries in CdTe. *Journal of Applied Physics*, vol. 96, no. 1, pp. 320-326, 2004.

[173] C. Persson and A. Zunger. Compositionally induced valence-band offset at the grain boundary of polycrystalline chalcopyrites creates a hole barrier. *Applied Physics Letters*, vol. 87, no. 21, p. 211904, 2005.

[174] J. E. Jaffe and A. Zunger. Defect-induced nonpolar-to-polar transition at the surface of chalcopyrite semiconductors. *Physical Review B - Condensed Matter and Materials Physics*, vol. 64, no. 24, p. 241304, 2001.

[175] I. Visoly-Fisher, S. R. Cohen, and D. Cahen. Direct evidence for grain-boundary depletion in polycrystalline CdTe from nanoscale-resolved measurements. *Applied Physics Letters*, vol. 82, no. 4, pp. 556-558, 2003.

[176] I. Visoly-Fisher, S. R. Cohen, A. Ruzin, and D. Cahen. How polycrystalline devices can outperform single-crystal ones: Thin film CdTe/CdS solar cells. *Advanced Materials*, vol. 16, no. 11, pp. 879-883, 2004.

[177] M. J. Romero, K. Ramanathan, M. A. Contreras, M. M. Al-Jassim, R. Noufi, and P. Sheldon. Cathodoluminescence of Cu(In,Ga)Se_2 thin films used in high-efficiency solar cells. *Applied Physics Letters*, vol. 83, no. 23, pp. 4770-4772, 2003.

[178] C. S. Jiang, R. Noufi, J. A. AbuShama, K. Ramanathan, H. R. Moutinho, J. Pankow, and M. M. Al-Jassim. Local built-in potential on grain boundary of Cu(In, Ga)Se_2 thin films. *Applied Physics Letters*, vol. 84, no. 18, pp. 3477-3479, 2004.

[179] C. S. Jiang, R. Noufi, K. Ramanathan, J. A. AbuShama, H. R. Moutinho, and M. M. Al-Jassim. Does the local built-in potential on grain boundaries of Cu(In, Ga)Se_2 thin films benefit photovoltaic performance of the device? *Applied Physics Letters*, vol. 85, no. 13, pp. 2625-2627, 2004.

[180] L. Kronik and Y. Shapira. Surface photovoltage phenomena: theory, experiment, and applications. *Surface Science Reports*, vol. 37, no. 1-5, pp. 1-206, 1999.

[181] V. J. Lee and D. R. Mason. Analytic expressions relating surface charge and potential profiles in the space-charge region in semiconductors. *Journal of Applied Physics*, vol. 34, no. 9, pp. 2660-2667, 1963.

[182] D. Azulay, O. Millo, I. Balberg, H. W. Schock, I. Visoly-Fisher, and D. Cahen. Current routes in polycrystalline $CuInSe_2$ and Cu(In, Ga)Se_2 films. *Solar Energy Materials and Solar Cells*, vol. 91, no. 1, pp. 85-90, 2007.

[183] S. Siebentritt, M. Igalson, C. Persson, and S. Lany. The electronic structure of chalcopyrites - bands, point defects and grain boundaries. *Progress in Photovoltaics: Research and Applications*, vol. 18, no. 6, pp. 390-410, 2010.

[184] S. Siebentritt and S. Schuler. Defects and transport in the wide gap chalcopyrite $CuGaSe_2$. *Journal of Physics and Chemistry of Solids*, vol. 64, no. 9-10, pp. 1621-1626, 2003.

[185] S. Sadewasser, T. Glatzel, S. Schuler, S. Nishiwaki, R. Kaigawa, and M. Ch Lux-Steiner. Kelvin probe force microscopy for the nanoscale characterization of chalcopyrite solar cell materials and devices. *Thin Solid Films*, vol. 431, pp. 257-261, 2003.

[186] K. Taretto, U. Rau, and J. H. Werner. Numerical simulation of grain boundary effects in Cu(In, Ga)Se_2 thin-film solar cells. *Thin Solid Films*, vol. 480, pp. 8-12, 2005.

[187] K. Taretto and U. Rau. Can grain boundaries improve the performance of Cu(In,Ga)Se_2 solar cells? *MRS Online Proceedings Library (OPL) : Symposium Y – Thin-Film Compound Semiconductor Photovoltaics-2007*, vol. 1012, p. 309, 2007.

[188] K. Taretto and U. Rau. Numerical simulation of carrier collection and recombination at grain boundaries in Cu (In, Ga)Se_2 solar cells. *Journal of Applied Physics*, vol. 103, no. 9, p. 094523, 2008.

[189] M. Gloeckler, J. R. Sites, and W. K. Metzger. Grain-boundary recombination in Cu(In, Ga)Se_2 solar cells. *Journal of Applied Physics*, vol. 98, no. 11, p. 113704, 2005.

[190] W. K. Metzger and M. Gloeckler. The impact of charged grain boundaries on thin-film solar cells and characterization. *Journal of Applied Physics*, vol. 98, no. 6, p. 063701, 2005.

[191] Y. Yan, R. Noufi, and M. M. Al-Jassim. Grain-boundary physics in polycrystalline $CuInSe_2$ revisited: experiment and theory. *Physical Review Letters*, vol. 96, no. 20, p. 205501, 2006.

[192] Y. Yan, K. M. Jones, C. S. Jiang, X. Z. Wu, R. Noufi, and M. M. Al-Jassim. Understanding the defect physics in polycrystalline photovoltaic materials. *Physica B: Condensed Matter*, vol. 401, pp. 25-32, 2007.

[193] M. Kawamura, T. Yamada, N. Suyama, A. Yamada, and M. Konagai. Grain boundary evaluation of $Cu(In_{1-x}Ga_x)Se_2$ solar cells. *Japanese Journal of Applied Physics*, vol. 49, no. 6R, p. 062301, 2010.

[194] S. Sadewasser, D. Abou-Ras, D. Azulay, R. Baier, I. Balberg, D. Cahen, S. Cohen, K. Gartsman, K. Ganesan, J. Kavalakkatt, W. Li, O. Millo, T. Rissom, Y. Rosenwaks, H. W. Schock, A. Schwarzman, and T. Unold. Nanometer-scale electronic and microstructural properties of grain boundaries in Cu(In, Ga)Se_2. *Thin Solid Films*, vol. 519, no. 21, pp. 7341-7346, 2011.

[195] S. Sadewasser. Surface potential of chalcopyrite films measured by KPFM. *Physica Status Solidi (A) Applications and Materials Science*, vol. 203, no. 11, pp. 2571-2580, 2006.

[196] S. Sadewasser. Microscopic characterization of individual grain boundaries in Cu-III-VI_2 chalcopyrites. *Thin Solid Films*, vol. 515, no. 15, pp. 6136-6141, 2007.

[197] G. Hanna, T. Glatzel, S. Sadewasser, N. Ott, H. P. Strunk, U. Rau, and J. H. Werner. Texture and electronic activity of grain boundaries in Cu(In,Ga)Se_2 thin films. *Applied Physics A: Materials Science and Processing*, vol. 82, no. 1, pp. 1-7, 2006.

[198] M. J. Romero, C. S. Jiang, R. Noufi, and M. Al-Jassim. Lateral electron trans-

port in Cu(In, Ga)Se_2 investigated by electro-assisted scanning tunneling microscopy. *Applied Physics Letters*, vol. 87, no. 17, p. 172106, 2005.

[199] G. Binnig and H. Rohrer. Scanning tunneling microscopy from birth to adolescence. *Reviews of Modern Physics*, vol. 59, no. 3, p. 615, 1986.

[200] K. Bian, C. Gerber, A. J. Heinrich, Daniel J. Müller, S. Scheuring, and Y. Jiang. Scanning probe microscopy. *Nature Reviews Methods Primers*, vol. 1, no. 1, pp. 1-29, 2021.

[201] C. Davisson and L .H. Ghrmer. Diffraction of Electrons by a Crystal of Nickel. *Physical Review*, 30, 1927.

[202] B. Voigtländer. *Scanning probe microscopy: atomic force microscopy and scanning tunneling microscopy*. Springer, 2015.

[203] C. J. CHEN. *Introduction to Scanning Tunneling Microscopy*. Oxford University Press, USA, 2021.

[204] G. Binnig, H. Rohrer, C. Gerber, and E. Weibel. Tunneling through a controllable vacuum gap. *Applied Physics Letters*, vol. 40, no. 2, pp. 178-180, 1982.

[205] C. Wagner, R. Franke, and T. Fritz. Evaluation of I (V) curves in scanning tunneling spectroscopy of organic nanolayers. *Physical Review B - Condensed Matter and Materials Physics*, vol. 75, no. 23, p. 235432, 2007.

[206] J. Bardeen. Tunnelling from a many-particle point of view. *Physical Review Letters*, vol. 6, no. 2, p. 57, 1961.

[207] J. Tersoff and D .R. Hamann. Theory and application for the scanning tunneling microscope. *Physical review letters*, vol. 50, no. 25, p. 1998, 1985.

[208] C. K. Boumenou, A. Elizabeth, F. Babbe, A. Debot, H. Mönig, and A. Redinger. Electronic and compositional properties of the rear-side of stoichiometric $CuInSe_2$ absorbers. *Progress in Photovoltaics: Research and Applications*, vol. 29, no. 7, pp. 775-785, 2021.

[209] G. Binnig, C. F. Quate, and C. h. Gerber. Atomic Force Microscope. *Physical Review Letters*, vol. 56, no. 9, p. 930, 1986.

[210] G. Binnig, C. H. Gerber, E. Stoll, T. R. Albrecht, and C. F. Quate. Atomic resolution with atomic force microscope. *Europhysics Letters*, vol. 3, no. 12, p. 1281, 1987.

[211] T. R. Albrecht and C. F. Quate. Atomic resolution imaging of a nonconductor by atomic force microscopy. *Journal of Applied Physics*, vol. 62, no. 7, pp. 2599–2602, 1987.

[212] L. Liu, N. Xi, G. Li, and H. Chen. Atomic force microscope-based nanorobotic system for nanoassembly. *Nano Optoelectronic Sensors and Devices*, pp. 51-79, 2012.

[213] R. Garcõ Âa, R. Ân, and P. Ârez. Dynamic atomic force microscopy methods. *Surface Science Reports*, vol. 49, pp. 197-301, 2022.

[214] U. Zerweck, C. Loppacher, T. Otto, S. Grafström, and L. M. Eng. Accuracy and resolution limits of Kelvin probe force microscopy. *Physical Review B - Condensed Matter and Materials Physics*, vol. 71, no. 12, p. 125424, 2005.

[215] T. Glatzel, S. Sadewasser, and M. C. Lux-Steiner. Amplitude or frequency modulation-detection in Kelvin probe force microscopy. *Applied Surface Science*, vol. 210, no. 1-2, pp. 84-89, 2003.

[216] Y. Martin, C. C. Williams, and H. K. Wickramasinghe. Atomic force microscope-force mapping and profiling on a sub 100 Å scale. *Journal of Applied Physics*, vol. 61, no. 10, pp. 4723-4729, 1987.

[217] T. R. Albrecht, P. Grütter, D. Horne, and D. Rugar. Frequency modulation detection using high-Q cantilevers for enhanced force microscope sensitivity. *Journal of Applied Physics*, vol. 69, no. 2, pp. 668-673, 1991.

[218] M. Nonnenmacher, M. P. O'Boyle, and H. K. Wickramasinghe. Kelvin probe force microscopy. *Applied Physics Letters*, vol. 58, no. 25, pp. 2921-2923, 1991.

[219] F. Streicher, S. Sadewasser, and M. C. Lux-Steiner. Surface photovoltage spectroscopy in a Kelvin probe force microscope under ultrahigh vacuum. *Review of Scientific Instruments*, vol. 80, no. 1, p. 013907, 2009.

[220] S. Sadewasser, T. Glatzel, M. Rusu, A. Jäger-Waldau, and M. C. Lux-Steiner. High-resolution work function imaging of single grains of semiconductor surfaces. *Applied Physics Letters*, vol. 80, no. 16, pp. 2979-2981, 2002.

[221] C. Sommerhalter, S. Sadewasser, T. Glatzel, T. Matthes, and M. C. Lux-Steiner. Kelvin probe force microscopy for the characterization of semiconductor surfaces in chalcopyrite solar cells. *Surface Science*, vol. 482, pp. 1362-1367, 2001.

[222] F. Robin, H. Jacobs, O. Homan, A. Stemmer, and W. Bächtold. Investigation of the cleaved surface of a p-i-n laser using Kelvin probe force microscopy and two-dimensional physical simulations. *Applied Physics Letters*, vol. 76, no. 20, pp. 2907-2909, 2000.

[223] T. Glatzel, D. F. Marrón, T. Schedel-Niedrig, S. Sadewasser, and M. C. Lux-Steiner. $CuGaSe_2$ solar cell cross section studied by Kelvin probe force microscopy in ultrahigh vacuum. *Applied Physics Letters*, vol. 81, no. 11, pp. 2017-2019, 2002.

[224] W. Melitz, J. Shen, A. C. Kummel, and S. Lee. Kelvin probe force microscopy and its application. *Surface Science Reports*, vol. 66, no. 1, pp. 1-27, 2011.

[225] S. Sadewasser and T. Glatzel. *Kelvin probe force microscopy. measuring and compensating electrostatic forces*. Springer, 2011.

[226] T. Wagner, H. Beyer, P. Reissner, P. Mensch, H. Riel, B. Gotsmann, and A. Stemmer. Kelvin probe force microscopy for local characterisation of active nanoelectronic devices. *Beilstein Journal of Nanotechnology*, vol. 6, no. 1, pp. 2193-2206, 2015.

[227] E. M. Lanzoni, T. Gallet, C. Spindler, O. Ramírez, C. K. Boumenou, S. Siebentritt, and A. Redinger. The impact of Kelvin probe force microscopy operation modes and environment on grain boundary band bending in perovskite and Cu(In, Ga)Se_2 solar cells. *Nano Energy*, vol. 88, p. 106270, 2021.

[228] T. Gallet. *Co-evaporation and scanning probe microscopy characterizations of hybrid halide perovskite thin films for solar cells*. PhD thesis, 2021.

[229] H. Siegfried. *Auger- and X-Ray photoelectron spectroscopy in materials science.* Springer Science and Business Media, 2013.

[230] F. A. Stevie and C. L. Donley. Introduction to x-ray photoelectron spectroscopy. *Journal of Vacuum Science and Technology A*, vol. 38, no. 6, p. 063204, 2020.

[231] E. Janocha. *Electronic properties of ALD zinc oxide interfaces and its implication for chalcopyrite absorber materials.* PhD thesis, 2012.

[232] N. Maticiuc, T. Kodalle, J. Lauche, R. Wenisch, T. Bertram, C. A. Kaufmann, and I. Lauermann. In vacuo XPS investigation of Cu(In, Ga)Se_2 surface after RbF post-deposition treatment. *Thin Solid Films*, vol. 665, pp. 143-14, 2018.

[233] J. Bombsch, E. Avancini, R. Carron, E. Handick, R. Garcia-Diez, C. Hartmann, R. Félix, S. Ueda, R. G. Wilks, and M. Bär. NaF/RbF-treated Cu(In, Ga)Se_2 thin-film solar cell absorbers: distinct surface modifications caused by two different types of rubidium chemistry. *ACS Applied Materials and Interfaces*, vol. 12, no. 31, pp. 34941-34948, 2020.

[234] A. Benninghoven. Surface investigation of solids by the statical method of secondary ion mass spectroscopy (sims). *Surface Science*, vol. 35, pp. 427-457, 1973.

[235] A. Benninghoven. Developments in secondary ion mass spectroscopy and applications to surface studies. *Surface Science*, vol. 53, no. 1, pp. 596-625, 1975.

[236] D. Cialla-May, M. Schmitt, and J. Popp. Theoretical principles of Raman spectroscopy. *Physical Sciences Reviews*, vol. 4, no. 6, pp. 1-9, 2019.

[237] C. Rincón, S. M. Wasim, G. Marín, J. M. Delgado, J. R. Huntzinger, A. Zwick, and J. Galibert. Raman spectra of the ordered vacancy compounds $CuIn_3Se_5$ and $CuGa_3Se_5$. *Applied Physics Letters*, vol. 73, no. 4, pp. 441-443, 1998.

[238] S. Nishiwaki, T. Feurer, B. Bissig, E. Avancini, R. Carron, S. Buecheler, and A. N. Tiwari. Precise Se-flux control and its effect on Cu(In, Ga)Se_2 absorber layer deposited at low substrate temperature by multi stage co-evaporation. *Thin Solid Films*, vol. 633, pp. 18-22, 2017.

[239] V. Deprédurand, T. Bertram, and S. Siebentritt. Influence of the Se environment on Cu-rich CIS devices. *Physica B: Condensed Matter*, vol. 439, pp. 101-104, 2014.

[240] J. I. Goldstein, Dale E. Newbury, Joseph R. Michael, Nicholas W.M. Ritchie, John Henry J. Scott, and David C. Joy. *Scanning electron microscopy and x-ray microanalysis*. Springer New York, 2017.

[241] J.N. Audinot, P. Philipp, O. De Castro, A. Biesemeier, H. Q. Hoang, and T. Wirtz. Highest resolution chemical imaging based on secondary ion mass spectrometry performed on the helium ion microscope. *Reports on Progress in Physics*, vol. 84, p. 105901, 2021.

[242] Y. Yan. Understanding of defect physics in polycrystalline photovoltaic materials. *2011 37th IEEE Photovoltaic Specialists Conference*, 2011.

[243] NIST XPS Database. URL `https://srdata.nist.gov/xps/elm_Spectra_query.aspx?Elm1=Se&LD1=3d&Elm2=&LD2=&Elm3=&LD3=&Elm4=&LD4=&sType=PE`.

[244] R. Hunger, T. Schulmeyer, A. Klein, W. Jaegermann, M. V. Lebedev, K. Sakurai, and S. Niki. SXPS investigation of the Cd partial electrolyte treatment of $CuInSe_2$ absorbers. *Thin Solid Films*, vol. 480, pp. 218-223, 2005.

[245] C. Persson, Y. J. Zhao, S. Lany, and A. Zunger. n-type doping of $CuInSe_2$ and $CuGaSe_2$. *Physical Review B - Condensed Matter and Materials Physics*, vol. 72, no. 3, p. 035211, 2005.

[246] A. Redinger and T. Unold. High surface recombination velocity limits quasi-Fermi level splitting in kesterite absorbers. *Scientific Reports*, vol. 8, no. 1, pp. 1-9, 2018.

[247] R. T. Ross. Some thermodynamics of photochemical systems. *The Journal of Chemical Physics*, vol. 46, no. 12, pp. 4590-4593, 1967.

[248] W. Shockley and H. J. Queisser. Detailed balance limit of efficiency of p-n junction solar cells. *Journal of Applied Physics*, vol. 32, no. 3, pp. 510-519, 1961.

[249] S. Rühle. Tabulated values of the Shockley-Queisser limit for single junction solar cells. *Solar Energy*, vol. 130, pp. 139-147, 2016.

[250] T. Kirchartz, J. A. Márquez, M. Stolterfoht, and T. Unold. Photoluminescence-based characterization of halide perovskites for photovoltaics. *Advanced Energy Materials*, vol. 10, no. 26, p. 1904134, 2020.

[251] Y. Zhao, H. Lee, W. Choi, W. Fei, and C. J. Lee. Large-area synthesis of monolayer $MoSe_2$ films on SiO_2/Si substrates by atmospheric pressure chemical vapor deposition. *RSC Advances*, vol. 7, no. 45, pp. 27969-27973, 2017.

[252] E. V. C. Robert, J. De Wild, and P. J. Dale. Reaction chemistry of group IV containing copper chalcogenide semiconductors Cu_2MX_3(M = Sn, Ge and X = S, Se). *Journal of Alloys and Compounds*, vol. 695, pp. 1307-1316, 2017.

[253] Polyxeni T. *Local inhomogeneities in polycrystalline wide-bandgap CuIn1-xGaSe2 thin-films*. PhD thesis, 2019.

[254] T. Schwarz, A. Lomuscio, S. Siebentritt, and B. Gault. On the chemistry of grain boundaries in $CuInS_2$ films. *Nano Energy*, vol. 76, p. 105081, 2020.

[255] T. Kodalle, M. D. Heinemann, D. Greiner, Hasan A. Yetkin, M. Klupsch, C. Li, P. A. van Aken, I. Lauermann, R. Schlatmann, and C. A. Kaufmann. Elucidating the mechanism of an RbF post deposition treatment in CIGS thin film solar cells. *Solar RRL*, vol. 2, no. 9, p. 1800156, 2018.

[256] E. Handick, P. Reinhard, J. H. Alsmeier, L. Köhler, F. Pianezzi, S. Krause, M. Gorgoi, E. Ikenaga, N. Koch, R. G. Wilks, S. Buecheler, A. N. Tiwari, and M. Bär. Potassium postdeposition treatment-induced band gap widening at Cu(In, Ga)Se_2 surfaces - reason for performance leap? *ACS Applied Materials and Interfaces*, vol. 7, no. 49, pp. 27414-27420, 2015.

[257] M. Mezher, L. M. Mansfield, K. Horsley, M. Blum, R. Wieting, L. Weinhardt, K. Ramanathan, and C. Heske. KF post-deposition treatment of industrial Cu(In, Ga)(S, $Se)_2$ thin-film surfaces: modifying the chemical and electronic structure. *Applied Physics Letters*, vol. 111, no. 7, p. 071601, 2017.

[258] W. Calvet, B. Ümsür, A. Steigert, K. Prietzel, D. Greiner, C. A. Kaufmann, T. Unold, M. Lux-Steiner, and I. Lauermann. In situ investigation of as grown Cu(In,Ga)Se_2 thin films by means of photoemission spectroscopy. *Journal of Vacuum Science and Technology A*, vol. 37, no. 3, p. 031510, 2019.

[259] S. Siebentritt, E. Avancini, M. Bär, J. Bombsch, E. Bourgeois, S. Buecheler, R. Carron, C. Castro, S. Duguay, R. Félix, E. Handick, D. Hariskos, V. Havu, P. Jackson, H. P. Komsa, T. Kunze, M. Malitckaya, R. Menozzi, M. Nesladek, N. Nicoara, M. Puska, M. Raghuwanshi, P. Pareige, S. Sadewasser, G. Sozzi, A. N. Tiwari, S. Ueda, A. Vilalta-Clemente, T. P. Weiss, F. Werner, R. G. Wilks, W. Witte, and M. H. Wolter. Heavy alkali treatment of Cu(In, Ga)Se_2 solar cells: surface versus bulk effects. *Advanced Energy Materials*, vol. 10, no. 8, p. 1903752, 2020.

[260] M. Guc, T. Kodalle, R. Kormath Madam Raghupathy, H. Mirhosseini, T. D. Kühne, I. Becerril-Romero, A. Pérez-Rodríguez, C. A. Kaufmann, and V. Izquierdo-Roca. Vibrational Properties of $RbInSe_2$: Raman scattering spectroscopy and first-principle calculations. *Journal of Physical Chemistry C*, vol. 124, no. 2, pp. 1285-1291, 2019.

[261] D. Cahen, P. J. Ireland, L. L. Kazmerski, and F. A. Thiel. X-ray photoelectron and Auger electron spectroscopic analysis of surface treatments and electrochemical decomposition of $CuInSe_2$ photoelectrodes. *Journal of Applied Physics*, vol. 57, no. 10, pp. 4761-4771, 1985.

[262] E. Niemi and L. Stolt. Characterization of $CuInSe_2$ thin films by XPS. *Surface and Interface Analysis*, vol. 15, no. 7, pp. 422-426, 1990.